Spectral SP: A New Approach to Mapping Reservoir Flow and Permeability

FOA522_5517

Donald M. Thomas

Principal Investigator

University of Hawaii

SUMMARY

The primary Phase I project milestones are listed below with details on secondary milestones provided in Table S. We present a summary of the accomplishments under each milestone here, with substantially more detail in the Phase I Technical Project Report following.

S.1 Plan First Field Surveys

Initially, significant delays in the project schedule were encountered due to the time required for finalization of our contract and release of the funds by DOE. Upon release of the funding, and under guidance from our Berkeley collaborators, field MT equipment, supplied by KMS Technologies, was selected for the project. Evaluation of leasing costs versus purchase led us to the conclusion that purchase of the equipment, using State funds, would provide the project with greater flexibility. Hence a purchase was made rather than leasing directly from the company; this process entailed significantly more time and delayed field operations but proved to be essential due to much longer required field survey time than was initially anticipated. Arranging access to the field sites at Kilauea were complicated by their location in a recently defined hazard zone around Halema'uma'u crater but access was granted with the proviso that USGS staff were required to accompany the field teams. All other required equipment was procured as planned.

S.2 First Field Surveys

Equipment from KMS was delivered to Berkeley for testing and approval by our collaborators; some delays due to scheduling conflicts arose that further delayed arrival of the equipment in Hawaii. Upon delivery of the equipment, the Berkeley collaborators arrived in Hawaii and assisted in the initial deployment of the equipment at the Kilauea summit. A number of challenges were encountered in identifying a quiet remote site and in the initial summit

deployment; those were addressed and the Hawaii team was able to acquire extended MT/Spectral SP data sets from 18 stations at the Kilauea summit and subsequently relocate the array to Puna where extended MT/SSP data sets were acquired from 18 stations on the Middle and Lower East Rift Zone of Kilauea.

S.3 Data Processing Modeling and Inversion

Initial data quality checks identified a number of issues that required modification to our remote stations and additional data acquisition program; access to University-owned MT array proved to be essential to the success of that effort. In processing of the data, a major impediment was encountered with the KMS system due to the poor utility and user interface of the vendor's proprietary software. As discussed below, we were forced to develop our own data processing system to allow us to efficiently pre-process and conduct the Spectral SP analysis using a Robust Multivariate Errors in Variables (RMEV) approach and canonical correlations. That effort required considerably more time than was initially anticipated. The Kilauea summit data set that had been collected in 2002 and 2003 was reprocessed by our Berkeley collaborators and Spectral SP signals were identified at a limited number of sites. The new project data were processed and analyzed using both the frequency domain RMEV approach as well as in the time domain using our newly developed software package. The RMEV analysis identified Spectral SP signals at several of the recent stations and the time domain analysis identified several episodes of Spectral SP signals, and identified a number of other E-field signals that, although not directly related to fluid flow processes, may be of scientific interest. Analysis of the Puna data in the time domain identified an array of environmental and anthropogenic E-field variations present in the time domain data sets that have interfered with computation of stable apparent resistivity and phase curves and completion of the frequency domain RMEV analysis. Work is continuing on those data.

S.4 Data Visualization Software Development

The data visualization effort developed an initial software package for visualization of the resistivity distributions that were to be derived from the MT/Spectral SP analysis. However, as the effort to pre-process and analyze the raw MT data encountered problems using the KMS proprietary software, software development efforts were redirected toward capabilities for analyzing and visualization of the time domain MT and Spectral SP data. That work resulted in the *MTPlot* package, developed by an added team member, Dr. Lienert, that allowed us to more efficiently process the raw MT H- and E-field data; equally important, it provided an efficient method of conducting time domain review and analysis of the processed data and to distinguish among E-field signals that were irrelevant (e.g sferics, and anthropogenic signals) to local geologic processes, those that were associated with geologic processes but not relevant to fluid flow, and those Spectral SP signals of interest to our investigation. The new software package will be invaluable to our continuing analysis of the Spectral SP data in Phase II of the project.

Table S. Summary table of Spectral SP Research Plan

S.1	**Plan First Field Surveys**
S.1.1	Prepare/issue bid package for equipment
S.1.2	Issue PO and schedule delivery of equipment
S.1.3	Plan survey sites
S.1.4	Arrange access to survey areas
S.1.5	Begin purchasing supplies

S.2	**First Field Surveys**
S.2.1	Schedule travel/lodging etc. for LBL
S.2.2	Take delivery of equipment and check out
S.2.3	Deploy network at Kilauea Summit
S.2.4	Collect data from Kilauea Network
S.2.5	Transfer field stations to Puna
S.2.6	Additional Field Time as Needed
S.2.7	LBL Team returns to Mainland
S.2.8	Return rental equipment to vendor

S.3	**Data Processing Modeling and Inversion**
S.3.1	Data quality check and validation
S.3.2	Processing of Kilauea Field Data
S.3.3	Initial model of MT data Kilauea
S.3.4	Processing of SSP data Kilauea
S.3.5	Initial model of SSP data Kilauea
S.3.6	Meet/Review Models for Kilauea Data
S.3.7	Processing of KERZ Data Set
S.3.8	Initial model of KERZ MT Data Set
S.3.9	Processing SSP data KERZ
S.3.10	Initial model of SSP data KERZ
S.3.11	Review model for KERZ MT/SSP Data set
S.3.12	Modify modeling parameters; rerun model
S.3.13	Compile/Review Results develop Ph.1 Report

S.4	**Data Visualization Software Development**
S.4.1	Interface with LBL staff on Model output
S.4.2	Begin developing software representation of resistivity mapping and flow mapping
S.4.3	Develop initial visualization of Kilauea Data
S.4.4	Review and modify initial visualization
S.4.5	Develop initial visualization of KERZ Data
S.4.6	Review and modify initial visualization KERZ
S.4.7	Finalize and complete report on visualization module

TECHNICAL REPORT

Spectral SP: A New Approach to Mapping Reservoir Flow and Permeability

Prepared for: US DOE Geothermal Technologies Office, FOA 522_5517

Donald M. Thomas *Principal Investigator*

Barry R. Lienert

Erin L. Wallin

University of Hawaii

Appendix F

Analysis of 2002-2003 MT Data

Erika Gasperikova

Lawrence Berkeley National Laboratory

27 May 2014

INTRODUCTION

The over-riding objective of the Spectral SP project has been to investigate the feasibility of using self-potential measurements made during magnetotelluric (MT) surveys to identify and define fluid flow, as a proxy for subsurface permeability, within a geothermal system. In the context of the funding opportunity announcement, DE-FOA-0000522, we were, in the Phase I work, to conduct "a robust feasibility assessment of the proposed technology... … Applicants must propose technologies in Technology Readiness Levels (TRLs) 2 and 3 for Phase I." DOE guidance for TRL2 technologies includes this definition "Once basic principles are observed, practical applications can be invented. Applications are speculative, and there may be no proof or detailed analysis to support the assumptions." Guidance for TRL 3 includes "Active research and development (R&D) is initiated. This includes analytical studies and laboratory-scale studies to physically validate the analytical predictions…".

To greatly simplify a complex set of relationships, the basic concepts being investigated are:

(1) MT surveys collect magnetic and electric field variations in order to infer subsurface resistivity distributions; in a static, geological environment, the magnetic source-field variations will induce currents and electric potential variations, within geological media that will depend on the media's electrical conductivity. In the absence of noise, the electric field variations will be perfectly correlated with the magnetic field variations. Field studies conducted in a limited number of areas have, however, detected electric field variations induced by variable anthropogenically-sourced currents in the ground (for example, DC trains [Egbert, 2000; Kappler et al, 2010] that do not correlate with the regional magnetic field.

(2) A separate natural source of subsurface current also exists, and arises from the self-potential (SP) effect that results from charge separation associated with fluid flow [Zablocki, 1976; Aizawa, 2008]. The electric field induced by the regional magnetic field can be predicted and removed and the remaining electric field will contain the SP variations which can then be used to map subsurface fluid flow.

Hence, our task, in the Phase I work, is to demonstrate that, through innovative application of the MT survey technique and a detailed analysis of the data, that we can isolate these naturally occurring SP-induced field variations if they are present and use these signals to infer subsurface flow distributions. At a minimum, our intent is to advance the technology to

TRL 4, namely: “The basic technological components are integrated to establish that the pieces will work together. This is relatively "low fidelity" compared with the eventual system... The goal of TRL 4 should be the narrowing of possible options in the complete system.” ,or to TRL 5: “The basic technological components are integrated so that the system configuration is similar to (matches) the full application in almost all respects…. Scientific risk should be retired at the end of TRL 5. Results presented should be statistically relevant.” Ultimately, the objective of this work is to develop SP isolation as a technique that can be used to map subsurface fluid flow in a geothermal field and provide guidance in exploration and development programs in a way that will reduce drilling costs associated with non-productive boreholes.

In order to achieve these objectives, we proposed to re-evaluate an existing MT data set, collected in 2002 and 2003 at the Kilauea summit by our LBNL collaborators, and to supplement that data set using more modern equipment with a more limited suite of measurements made at the Kilauea summit and the East Rift Zone of Kilauea where a known geothermal system exists. The new data was to be collected using simultaneous field stations at Kilauea, with multiple remote stations located at several tens of kilometers distant from Kilauea, and to collect data for more extended durations than a typical MT resistivity survey would entail. The analysis of the prior and new data was to apply Egbert’s (1997) multivariate statistical software package to separate coherent signals of varying spatial scales and to attempt to identify anomalous electric (and SP) and magnetic field variations.

In practice, we were able to collect a substantial data set for the Kilauea summit and a more limited data set for the Kilauea East Rift Zone using a recently-developed MT survey system supplied by KMS Technologies. Our analysis applied Egbert’s code to the data set; to facilitate that analysis, we also developed additional software to allow us to process and analyze the magnetic and electric field data in an alternative way that allows a more intuitive identification of anomalous data within our records and facilitate identification of likely Spectral SP signals in the data sets. In both analytical approaches, we have identified evidence of anomalous Spectral SP signals that we believe are associated with subsurface fluid flow. The following report will detail the equipment used and the field methods applied as well as the data analysis methods and results obtained.

Equipment Used

The backbone of our field monitoring equipment was the KMS Technologies (Houston, TX) MT recording station consisting of the KSM-820 acquisition system. These units were recommended by our Berkeley collaborators based on the higher sensitivity and broader dynamic range of the KMS instruments than other commercial units. They also allowed more direct user control of sampling frequency and recording intervals. The latter feature allowed us to collect continuous sequences of data for longer periods of time and at higher sampling rates than are typically used in conventional MT surveys. We used Ag/AgCl electrodes to measure electric field components, rather than copper or lead electrodes, due to their greater stability and lower

noise characteristics. Additionally, the electrolyte used in the silver electrodes consisted of sodium chloride which substantially reduced environmental concerns regarding installation of this equipment in Hawaii Volcanoes National Park. We also incorporated a "bucker-box", fabricated by Berkeley Geophysics (Berkeley, CA), into the E-field electrode circuit in order to reduce the high DC electric field background arising from the greater spread (200 m) of our electrodes, allowing us to increase the gain/sensitivity of the E-field data collection.

Site Selection

The selection of sites in which we are conducting research was, to an extent, driven by the FOA and the requirement that we use data sets that were already available. Our Berkeley colleagues had collected an extensive suite of data from nearly fifty MT stations distributed over the summit and flanks of Kilauea Volcano between 2002 and 2003. Our intent was to use those data sets as a foundation for the study while supplementing those data with additional MT surveys using more modern equipment that would provide greater sensitivity, broader dynamic range, and longer data acquisition times.

The Kilauea summit is, in at least one sense, also an ideal location to conduct research into the SP phenomenon. This region has been extensively studied; its structure is well known; it is intensively monitored by a diverse array of geophysical instruments. It is underlain by extremely high temperatures with an active magmatic conduit that extends from the summit to the middle east rift zone, and there is a diverse assortment of hydrothermal systems within a well constrained area. A number of the early studies of conventional SP were performed at the Kilauea summit where very strong SP anomalies were associated with hydrothermal systems resulting from recent intrusions [Zablocki, 1976; Anderson, 1985]. If we are to test the concept of detecting and characterizing spectral SP signals associated with geothermal activity within an MT data set, then our best opportunity for encountering such signals should be at the Kilauea summit.

We have also expanded the Kilauea data set into Lower Puna, where a known geothermal resource has been demonstrated to extend along much of the Kilauea East Rift Zone. This effort was intended to determine whether we would be able to also see spectral SP signals associated with groundwater/hydrothermal fluid flows around that recognized geothermal field as well.

1. METHODS

Here we present a description of all the procedures and technical details used in accomplishing Phase I goals. This includes specifics of survey design at each location, Kilauea and Puna, and details of the frequency and time domain analysis applied to the data set.

1.1 Survey Design

The Kilauea caldera was chosen as the first study site for Phase I. Its proximity to a known heat source and magmatic and hydrothermal activity provides an ideal testing ground for our methods. Puna is also located in an area of known geothermal potential. The infrastructure present in Puna is the source of cultural noise in some of the data. The Puna data are currently undergoing further analysis and processing.

Figure 1.1.1 Map of East Hawaii County, showing locatin of Kilauea and Puna MT surveys. The Kilauea East rift zone (ERZ), Pung Geothermal Venture power station (PGV) and the *Parker, Lau and hkml* remotes used in the data acquisition.

Kilauea survey design

For the Kilauea survey, we used a combination of 3 remote stations in an effort to select and use the quietest remote data. The locations of the remotes relative to the Kilauea and Puna surveys are shown in Figure 1.1.1. The stations are denoted: *hkml* (located approximately 35 km from the caldera on the Mauna Loa side of the Big Island's Saddle Road) which was used for the first two groups, and *Lau* and *Parker* (50 and 60 km from the survey on the Mauna Kea side of the Saddle Road) which were used with the last four of our MT data groups.

In addition to the 3 remote sites, we collected MT data at 18 stations adjacent to Kilauea Caldera and the uppermost East and Southwest Rift Zones. The station locations are shown on the map in Figure 1.1.2. With the exception of *Parker*, where two orthogonal magnetic coils were installed, each station consisted of two orthogonal magnetic coils and two orthogonal electric dipoles. The orientations of the X and Y components were 135 and 225 degrees, respectively. The Ag/AgCl electrodes were placed in bentonite which was kept fully saturated. The electrodes were kept in place for a minimum of 24 hours prior to data acquisition to allow the self-potential signals of the electrodes to stabilize. The bucker boxes were used to remove ambient DC SP signals in order to increase sensitivity sufficiently to measure the small SP variations that we expected during the several days of data acquisition. For groups 3-6 we also acquired 12-24 hours of synchronous data at a 1 kHz sampling frequency. Groups 1 and 2 have only limited time segments at this higher sampling frequency. At all station groups data were synchronously acquired for 72 hours at a 40 Hz sampling frequency, although data in some recording locations were several hours shorter as a result of instrument problems that occurred at the beginning of some of the recording intervals. The long duration of data acquisition allowed us to split the 72 hour data into 6 hour segments and to process each 6 hour segment independently. This allowed us to determine how the results of our analysis varied over time and to isolate signals of interest using the canonical correlation method described in a subsequent section.

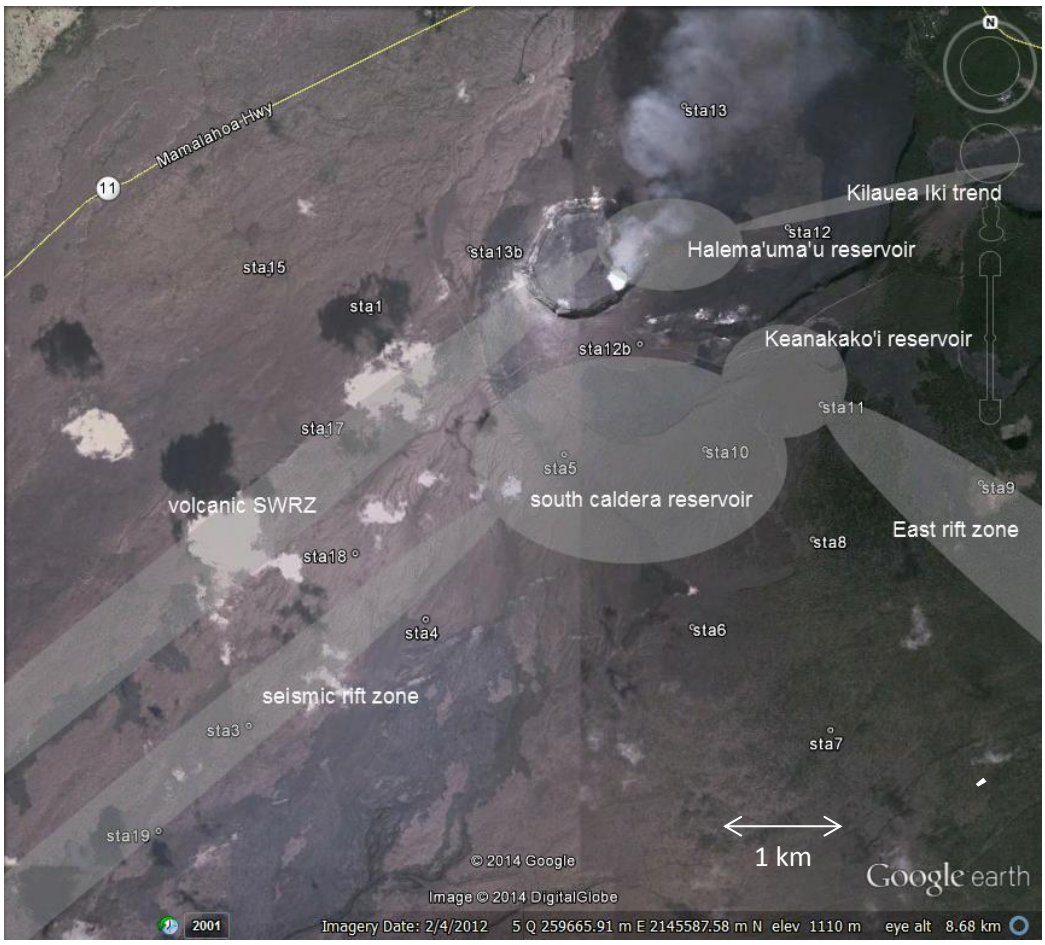

Figure 1.1.2 Map of Kilauea Summit MT station locations (2012-2013) and relevant volcanic features. The south caldera reservoir, east rift zone and southwest seismic zones are at a depth of approximately 3 km. The volcanic SWRZ and Kilauea Iki trend are approximately 1.5 km depth [Poland, 2013].

Table 1 Kilauea MT Stations

Group	Kilauea Stations	Remote
1	*sta3, sta4, sta5, sta19*	*hkml*
2	*sta1, sta12, sta13, sta15*	*hkml*
3	*sta12, sta13, sta12b, sta13b*	*Parker, Lau*
4	*sta1, sta6, sta7, sta8*	*Parker, Lau*
5	*sta7, sta8, sta9, sta11*	*Parker, Lau*
6	*sta9, sta10, sta17, sta18*	*Parker, Lau*

Of the 18 stations we occupied, thirteen were also occupied in an MT survey conducted in 2002-2003. We have impedance values from the early survey, and an analysis of those data is

included in Appendix F. Stations *sta01*, *sta12*, *sta13*, and *sta08* were recorded in two different groups, so we have two sounding curves for each of these three stations.

Puna survey design

In Puna we collected data at 18 stations (Figure 1.1.3, Table 2). When possible both *Lau* and *Parker* were occupied to serve as dual remote reference sites. Due to equipment malfunction we only acquired data at *Parker* for groups 1, 5 and 6. We performed repeat acquisitions at *pun02*, *pun05*, *km01* and *rcc02*. With the exception of *Parker*, where two orthogonal magnetic coils were installed, each station consisted of two orthogonal magnetic coils and two orthogonal electric dipoles. The orientations of X and Y components were 135 and 225 degrees, respectively. Electrodes were of Ag/AgCl type and were emplaced in bentonite that was allowed to stabilize for at least 24 hours prior to data acquisition. Ambient self-potential signals were bucked allowing sufficient sensitivity to measure time varying SP. The data were acquired synchronously in 7 groups. The synchronous acquisition was for 24 hours at a 1 kHz sampling frequency followed by 72 hours at a 40 Hz sampling frequency.

Collection of the Puna data presented a broad variety of challenges that impeded collection of the planned full data set in this region. The field conditions in the more remote areas of Puna were extraordinarily difficult with extremely dense jungle, dangerous, intensely-fractured ground within the surface expression of the rift zone, and high rainfall that affected the reliability of the data recording system. In the more accessible areas of Puna, we encountered high levels of anthropogenic noise: the area is somewhat rural and the great majority of residential water systems consist of catchment cisterns with water pumps; many residential lots are also "off grid" with solar PV (with inverters) and individual generator units for domestic power. Finally, although a number of large land-owners had initially agreed to provide access for our studies, when formal application was made, we encountered extended delays in reviews and approvals and legal wrangling between some of the land-owners and the University regarding liability and indemnification terms of a right of entry. Hence, substantially more time was required for the surveys in Lower Puna and the extent of coverage was considerably more limited than desired.

Table 2 Puna MT Stations

Group	Puna Stations	Remote
1	*pun09, pun11, pun20*	*Parker,Lau*
2	*pun08, pun17, pun19*	*Lau*
3	*pun02, pun05, pun12*	*Lau*
4	*pun02, pun05*	*Lau,*
5	*km01, rcc02*	*Parker,Lau*
6	*km01, rcc02*	*Parker,Lau*
7	*km02, rcc03, rcc04*	*Lau*

Figure 1.1.3 Map of Puna MT station locations (2012-2013), Kilauea's East rift zone (ERZ) and the location of Puna Geothermal Venture (PGV) power station.

1.2 Analysis of the MT Data

In this section we describe our development and use of new and existing software for processing of the raw data for frequency and time domain analysis. The new software provides analytical tools for processing and visualization of the proprietary KMS data format that are neither available from KMS nor from any other commercial software package. This is followed by a description of the time and frequency domain techniques used for analysis of the MT data to detect signals related to fluid flow. The frequency domain analysis consists of the robust multivariate errors in variables (RMEV) approach and canonical correlations. We also include a description of the magnetotelluric phase tensor which is useful for separating local from regional subsurface conductivity structures [Chave and Jones, 2012].

1.2.1 Software development: The *MTPlot* Windows Application

An executable software package based on Egbert's remote reference and single station codes, was provided to us by KMS technologies. This was the only MT processing software that could directly read the proprietary KMS format. In practice, we found that the KMS-provided

package was extremely difficult to use effectively and greatly impeded our progress in processing the raw data. A much more acute issue relevant to the project objectives is that the frequency domain analysis of the E- and H-field data ingests and processes data collected over extended periods of time that may include truly spurious and irrelevant signals (e.g. anthropogenic noise) that we may wish to exclude from the analysis. The long durations of the data segments used for the frequency domain analysis may also obscure important Spectral SO signals that are of short duration, intermittent, or aperiodic. Hence, our need to better control the preprocessing of the data for RMEV and RR analysis, and to have other options of time and frequency domain analysis, led us to develop our own software for examining and applying signal processing techniques to the raw magnetotelluric timeseries generated by the KMS software.

Overview:

The application was written to perform the following tasks

A. Read and display raw magnetotelluric data consisting of two or three orthogonal components of the magnetic field and two of the electric field. Correct analog-to-digital-converter (ADC) gain factors, sensor calibration factors and electrode lengths to display the data in standard units (pT and mV/km). The initial version of *MTPlot* reads data collected in the binary format used by KMS-820 data loggers, but can potentially be adapted to read other formats.
B. Concatenate multiple files, split files into multiple segments and filter and decimate files at lower sample rates
C. Edit and correct header information containing items such as channel identifier, enabled channels, sensor type, electrode length, etc.
D. Digitally filter the data to remove interference from power line noise, etc.
E. Perform Fourier transforms on data sets ranging in size from 1 record (2560 points for KMS data) to 400 records (~1 million points).
F. Cross correlate the electric and magnetic fields to obtain estimates of the magnetotelluric impedance tensor and apparent resistivity which can be used to obtain estimates of the subsurface resistivity structure.
G. Spike Identification

Program Coding Environment:

All the software has been coded in C using the Microsoft Visual Studio 2005 Integrated Development Environment (IDE). This IDE contains a programmer's editor integrated with a compiler, linker and debugger. It also allows straightforward inclusion of the functions needed to create and manage graphical windows and user input, i.e., the Windows Application Programming Interface (the Win32 API). The present version of *MTPlot* was developed to stay

within the 32-bit limit required by Windows 32-bit operating systems which limited its size in memory to less than 3.2 Gbytes. Use of the Win32 API rather than the more commonly used Microsoft Foundation Class Library resulted in a very small executable module (<1 Mbyte) and no additional libraries or ancillary files, making updated versions very fast to download. *MTPlot* runs on any version of Windows from XP onwards (80% of the world's desktops and laptops).

MTPlot uses the traditional "Petzold Style" implementation of the API [Petzold, 1992]. This style contains an initial call in the *WinMain* routine to create a single window and a simple message loop which intercepts the application's interrupts due to user input, passing them to the Windows Procedure *MTPlotWndProc*. This programming technique is non-sequential, i.e., the order in which the code is executed is determined by the user rather than by the programmer.

MTPlotWndProc first calls *InitInstance*, which creates the toolbar and status bar and initializes the *MTPlot* variables. The toolbar provides shortcuts to the most commonly used menu items and the status bar contains important data such as the input file record number. Some program variables such as the last used input directory are loaded from a text file, which, if it does not already exist, is created in the same directory as the executable. *MTPlotWndProc* then processes the user's keyboard and mouse input using another message loop containing case statements that match menu calls such as loading an input file. Since the primary display refreshes very rapidly when changes occur, the single application window is regenerated for different plot types rather than using multiple windows. Although multiple windows are useful for comparison, they would have made the application unnecessarily complex. In any event, any display in the single window can be instantly copied on to the Windows clipboard and pasted into other applications (e.g., MS Word) for subsequent viewing and comparison.

Program Details:

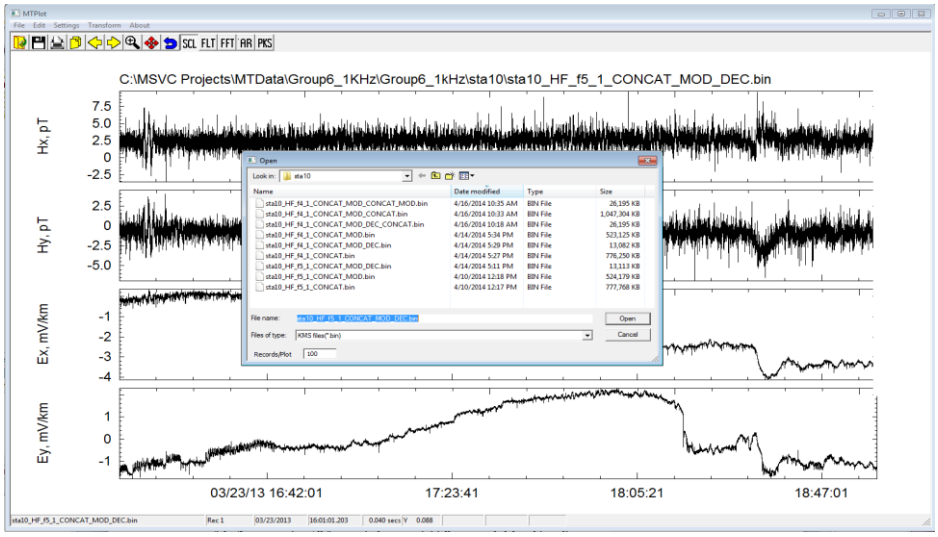

Figure 1.2.1 The MTPlot window showing a data file and the dialog used to load it.

A. Loading and displaying files:

The open file dialog, shown in Figure 1.2.1, is always opened with details enabled which allow easy sorting by date or name. Since the binary data are organized into fixed record lengths of either 2560 or 5120 samples, it proved useful to allow loading of multiple records so longer lengths of data could be viewed and analyzed. A records/plot edit box was added to the file dialog for this purpose. On the lowest x-axis, the time is displayed in 24 hour format with the date displayed on the left of the first annotation. All four vertical axes are initially auto scaled, but this scaling can be enabled or disabled using the SCL toolbar button. Individual scales for each trace can also be manually set in Settings/Plot Scaling. Left clicking the mouse places a cursor on the selected data point in any of the plots with the time and amplitude of the point displayed in the status bar. A zoom control icon also allows selective enlargement of plot regions. To return to the original magnification, the zoom icon must be clicked on again. Because of memory constraints, the number of simultaneously displayed records is presently limited to 500 (about 1 million points).

B. Concatenation:

Concatenating files is done using File/Concatenate (no files need to be loaded). This allows selection of multiple files using the ctrl and shift keys in standard Windows style. Once the input files are selected, a File Save Dialog appears, allowing the output Filename and directory to be specified (the default is the source file directory). Once OK is selected in this second dialog, a wait cursor appears which remains until the concatenation operation is complete.

C. Display and editing of the Input File Header

The KMS binary data consists of a 1024 byte header followed by a block of data consisting of a fixed number of three-byte (24 bit) integers for the enabled channels. The fixed number is set to 2560 data points for older versions of the KMS firmware and 5120 data points for the more recent versions. Each header contains information such as amplifier gains, GPS time settings, etc., which are needed to convert the data to values of the measured fields. Most of these values were converted to readable form by the decode function and are available for inspection in the File/File Information dialog. Since the channels were not labeled in the header, the Settings/File Header, shown in Figure 1.2.2, allows easy inspection and editing of the header values for each channel.

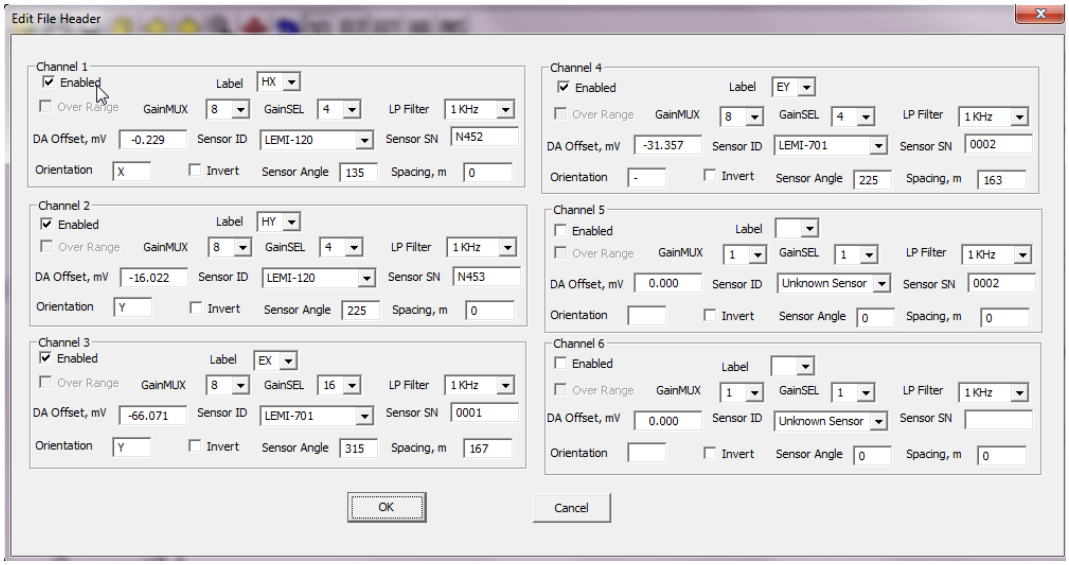

Figure 1.2.2 The dialog used to edit the header values for each input channel.

D. Filtering and Decimation.

Filtering is done by two low-pass recursive digital filter routines and is enabled/disabled using the FLT toolbar button. The filter cutoff is specified in Settings/Filter as the number of samples, e.g., at a 40 Hz sampling rate, 5 samples corresponds to an 8 Hz cutoff. Either an 8-pole routine, *filter8* (<50 samples cutoff) or a 4-pole, *filter4* (>50 samples cutoff) is used. To prevent oscillations at the beginning of each record, the last 200 samples from the previous record are initially loaded into the recursive filter. The decimation factor set in Settings/Decimation is the number by which the present sample rate is divided, which is limited to integral factors of the block size. When decimating, it is essential to filter the data at a number of samples at least double the decimation factor in order to prevent aliasing.

E. Fourier analysis

When a finite section of a time sequence is transformed into the frequency domain using Fourier analysis, it is important to first remove either a linear or polynomial trend to prevent adding large low-frequency components to the resulting spectra. Interactive fitting allows a polynomial up to degree 20 to be fitted and displayed beneath the dialog as the order is changed (Figure 1.2.3). It was also necessary to apply a tapered window to the data in order to reduce spectral leakage (Blackman and Tukey, 1959). Both Hamming and Hanning windows can be selected in the dialog. Transforming the *N* displayed data points is then performed using a Fast Fourier Transform (FFT) contained in the routine *four1*. The result is a set of *N/2* complex coefficients. Their amplitudes are calculated and displayed for all four traces using the FFT toolbar icon as shown in Figure 1.2.4.

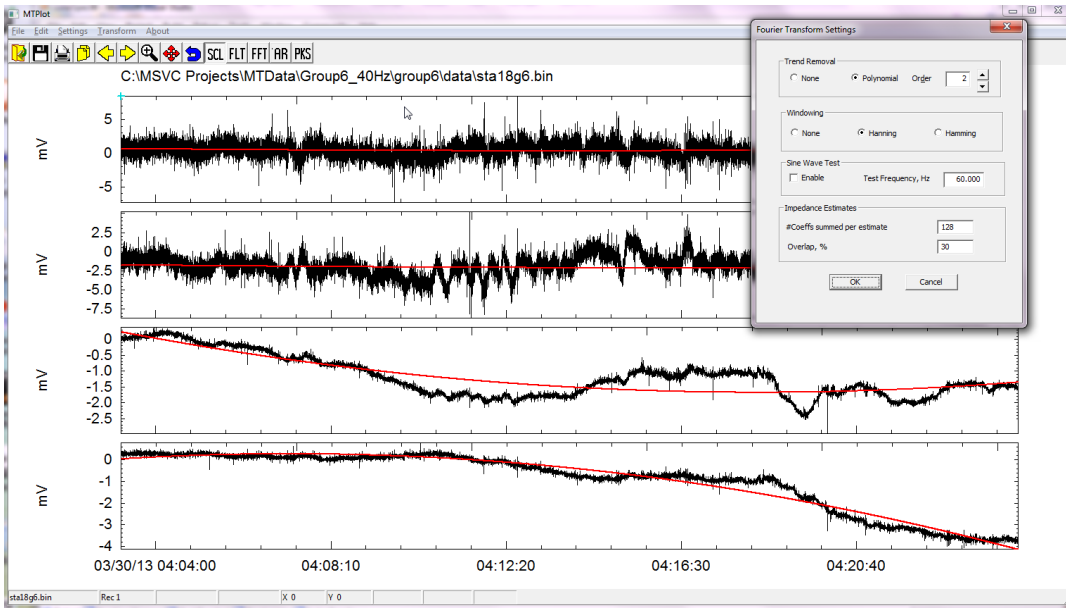

Figure 1.2.3 15 minutes of MT data (black curves) with fitted quadratic polynomials (red curves). The Settings/Fourier Analysis dialog used to interactively change the polynomial order is also shown.

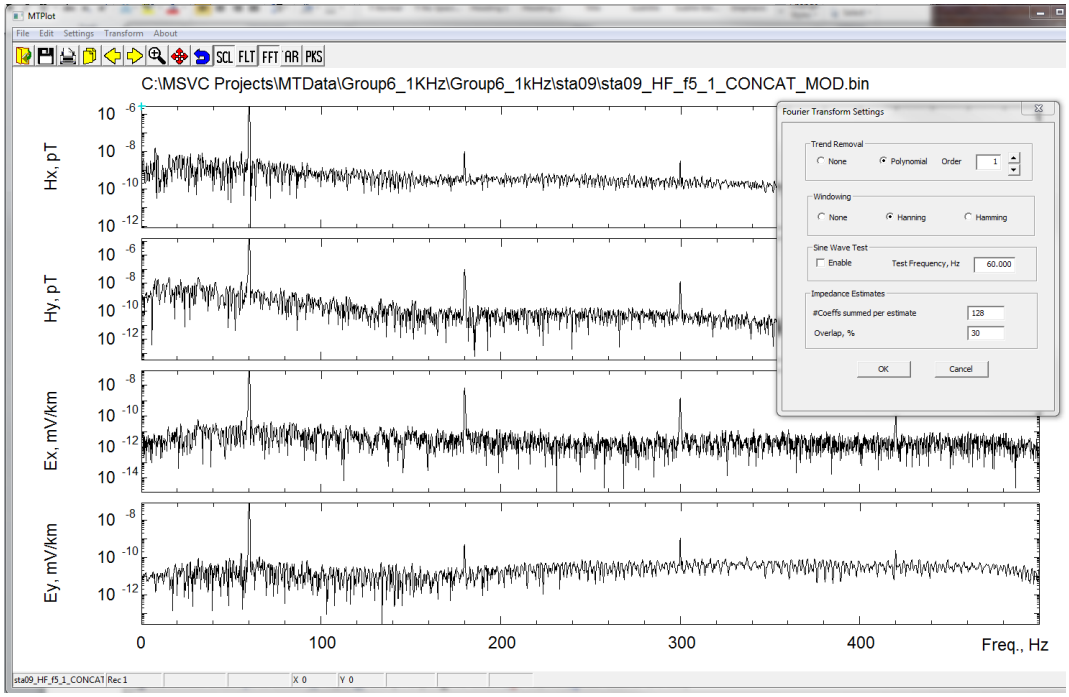

Figure 1.2.4 Fourier transforms of 2.56 seconds of data recorded at 1000 samples/sec on Kilauea summit in 2013. The spikes are due to power line interference at 60 Hz and its harmonics. These plots indicate small spectral leakage resulting from the application of a Hanning Window taper applied to the data set prior to applying the FFT.

F. Impedance and Apparent Resistivity Calculation.

The relationship between the two horizontal magnetic field and two horizontal electric field frequency components can be written

$$E_x = Z_{xx}H_x + Z_{xy}H_y \quad (1)$$

and

$$E_y = Z_{yx}H_x + Z_{yy}H_y \quad (2)$$

Where, H_x, H_y, E_x, E_y are the magnetic and electric fields and $Z_{xx}, Z_{xy}, Z_{yx}, Z_{yy}$ are the four components of the complex symmetric magnetotelluric impedance tensor, Z_{ij}. To solve equations (1) and (2) for Z_{ij} at least two simultaneous estimates of the four complex field components are required [Sims and Bostick, 1971]. In *MTPlot*, the sum of squares,

$$\psi = \sum_{i=1}^{n}\left(E_{xi} - Z_{xx}H_{xi} - Z_{xy}H_{yi}\right).\left(E_{xi}^{*} - Z_{xx}^{*}H_{xi}^{*} - Z_{xy}^{*}H_{yi}^{*}\right) \quad (3)$$

or differences between measured values of Ex and Ey and those predicted by eqns. (1) and (2) are minimized for *n* components of frequency (* represents the complex conjugate). The *n* field components are obtained by assuming that the impedances remain constant over a range on each side of the individual estimates. This range is set in *MTPlot* by "Coeffs Summed per Estimate" in Settings/General. Differentiating eqn. (3) with respect to Z_{xx} and setting the results for both real and imaginary parts to zero results in

$$\sum_{i=1}^{n}\overline{E_{xi}H_{xi}^{*}} = Z_{xx}\sum_{i=1}^{n}\overline{H_{xi}H_{xi}^{*}} + Z_{xy}\sum_{i=1}^{n}\overline{H_{yi}H_{xi}^{*}} \quad (4)$$

where * is the complex conjugate and the over-bars are means. A similar minimization with respect to Z_{xy} results in the equation

$$\sum_{i=1}^{n}\overline{E_{xi}H_{yi}^{*}} = Z_{xx}\sum_{i=1}^{n}\overline{H_{xi}H_{yi}^{*}} + Z_{xy}\sum_{i=1}^{n}\overline{H_{yi}H_{yi}^{*}}. \quad (5)$$

Equations (4) and (5) can then be solved for Z_{xx} and Z_{xy}. It is possible to derive six similar equations, two of which minimize the E-field noise and two minimize the H-field noise. The remaining two are frequently unstable [Sims and Bostick, 1971]. When the AR icon is selected, *MTPlot* initially plots all four of these stable tensor estimates for the tensor element selected in Settings/General. This results in a visual estimate of noise in the E and H-fields. Other Settings/General values allow plotting averages of the four estimates as well as their phases and converted apparent resistivities. An example appears in Figure 1.2.5.

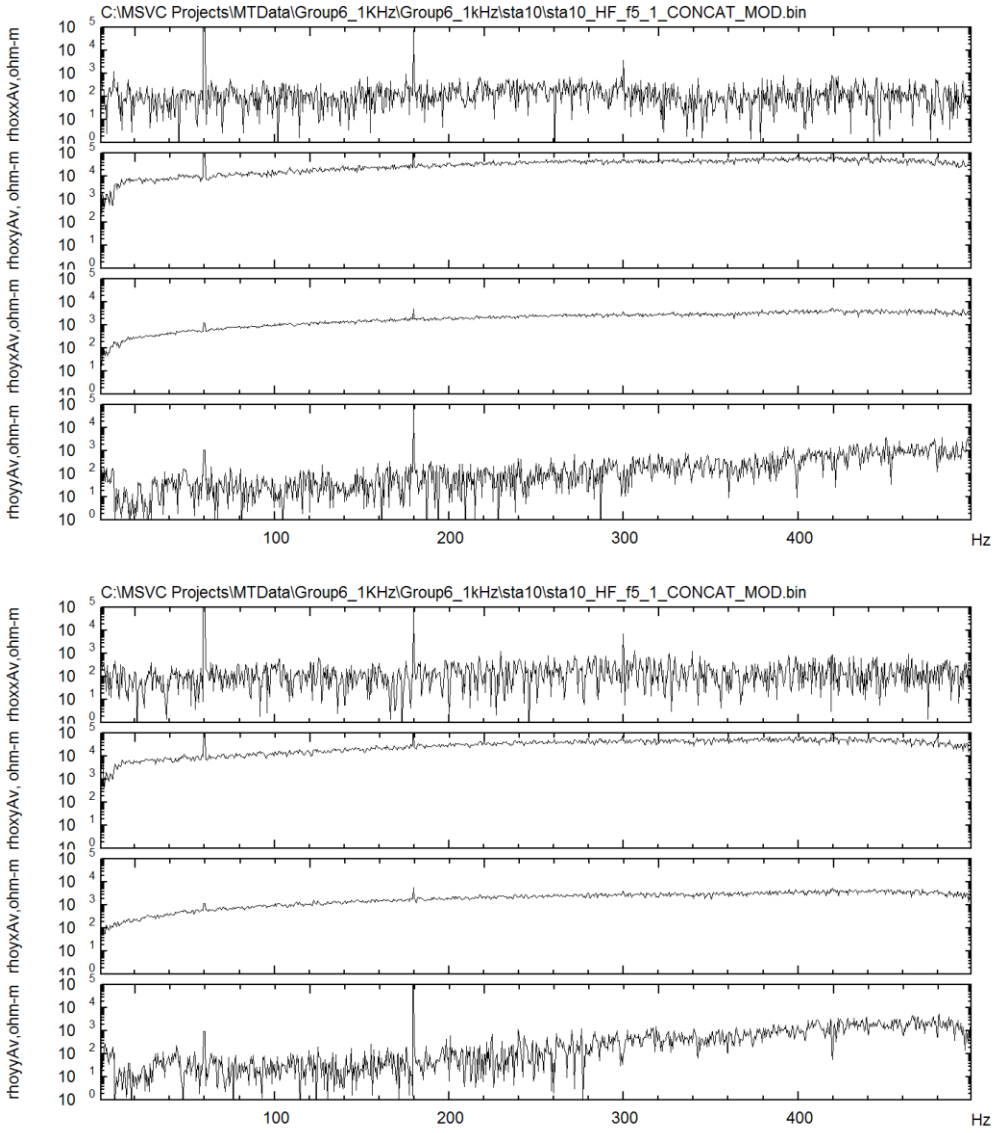

Figure 1.2.5 Apparent resistivities for station 10 near the Kilaeua Summit. The two plots look almost identical, but they are independent results for two sequential 4 minute time segments (100 records each) with 128 coefficients averaged in each plotted point. The spikes at 60, 120 and 180 Hz are power line interference.

G. Spike identification:

All the MT data we have collected contain spikes which appear to be of short duration and are apparent in the example data plotted in Figure 1.2.1. The spikes we observe are usually, but not always, present in both the E and H-fields and occur on average about twice a second. We first examined the length of one of these spikes using data collected at 1000 samples/sec.

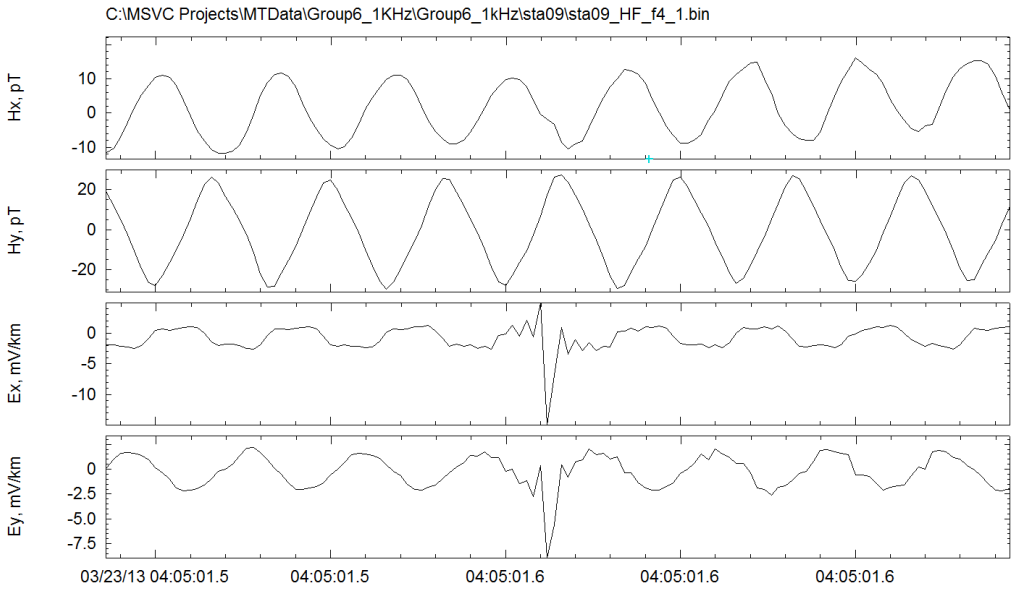

Figure 1.2.6 Spikes in the E-fields observed at sta09, close to the summit of Kilauea. The sinusoidal patterns are due to power line interference.

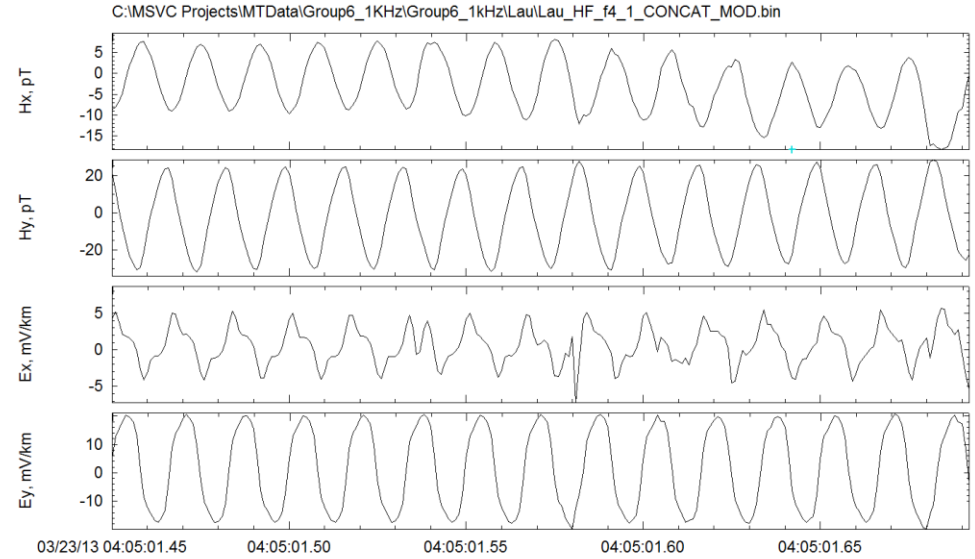

Figure 1.2.7 Same spike observed at the Lau site, about 50 km north of sta09.

Figures 1.2.6 and 1.2.7 show the same spike observed at two sites 50 km apart. The spike is also present in the H-fields but it is smaller and partially obscured by 60 Hz interference. This spike appeared identical at the other three Kilauea sites where MT data were being simultaneously collected, but is of lower amplitude at the Lau site. Its

observation at the Lau site appears to preclude it being due to volcanic activity at Kilauea. In order to better define this noise source and take appropriate measures to distinguish among locally generated signals and those that are irrelevant to our evaluation of the Spectral SP signals, the routine *FindPeaks* was added to *MTPlot* to locate and process these spikes. This method was previously developed by one of us (BRL) for locating peaks in spectral analysis. *FindPeaks* locates each peak by examining successive differences and comparing them with an estimated signal-to-noise ratio. In *MTPlot*, peak location is invoked by the PKS icon. An example is shown in Figure 1.2.8.

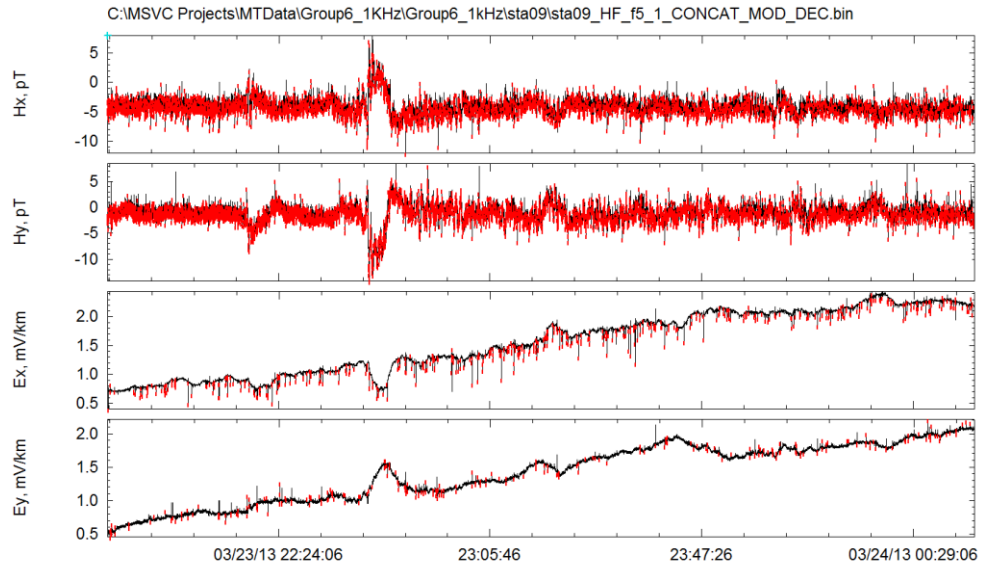

Figure 1.2.8 100 records (~2 hours) of MT data at Kilauea station sta09 re-sampled at 25 samples/sec. The identified spikes are marked by red vertical lines.

1.2.2 RMEV Analysis Method

A spatial array of measurement sites is necessary in order to separate the fields of a 'local' self potential (SP) source from the natural and induced EM fields of the Earth, both external (by currents in the ionosphere) and internal (induced by local sub-surface conductivities). Natural magnetic fields of external origin are coherent over hundreds of kilometers. Since the EM field vectors induced by the external magnetic field at each site are governed by the subsurface conductivity distribution they are not the same at separated sites but can be expressed in terms of local impedance tensors. If it is assumed that the correlated parts of

local magnetic fields are all of external origin, locally and regionally induced EM fields can be predicted by these local impedance tensors.

Subtracting the electric fields predicted by local impedance tensors from the measured fields yields a residual electric field that is highly sensitive to anomalous signals local to the site, and those are the signals of interest in our approach. Hydrothermal activity and fluid flow are some of the mechanisms that would produce these fields. Such anomalous electric field signals would not be correlated with the MT fields induced by external magnetic fields. Egbert's [1997] multivariate statistical approach is used for extracting the electric field residuals. This method is very useful for a better understanding of signal and noise characteristics, and for separating coherent signals of differing spatial scales

Common MT data processing methods use a univariate statistical approach, processing one station with a 2 channel (Hx and Hy) remote reference (referred to herein as RR approach). For this effort, we employ a multivariate processing scheme that utlilizes data from all channels, in the group of stations. This improves signal to noise ratios and diagnose biases due to coherent noise. In our case the number of channels in the array is as many as 20 when we have 4 MT stations and two 2-channel remote reference stations acquiring data synchronously. The RMEV method was developed and presented in Egbert, 1997. It is also described in Kappler, Morrison and Egbert, 2010. In the latter work the authors employed the approach we use here to search for anomalous processes and signals at two MT stations where data were acquired for four years.

The spectral density matrix (SDM) is a multivariate structure of the EM data which contains information about the dimensionality of signal and coherent noise. For the magnetotelluric method, it has been shown previously [Egbert 1989] that the number of non-zero eigenvalues of the SDM will be 2 in the absence of coherent noise. This corresponds to the case where the MT plane wave assumption holds perfectly. One may expect that if EM fields were being produced by some other process, such as hydrothermal activity, that these signals would not be coherent with the solar wind or sferic (lightning-induced) signals. We subject the SDM to an eigenvalue decomposition, and consider only the first four eigenvalues, since the higher values typically correspond to signal levels below the system noise floor. We are interested in the dimensionality of the coherent noise, and how that information can be extracted from our MT data set and utlized.

To estimate the dimensionality of coherent noise we begin with the robust multivariate errors in variables (RMEV) model described in Egbert 1997,

$$\mathbf{X_i} = \mathbf{U}\boldsymbol{\beta_i} + \mathbf{V}\boldsymbol{\gamma_i} = \begin{bmatrix}\mathbf{U} & \mathbf{V}\end{bmatrix}\begin{bmatrix}\boldsymbol{\beta_i} \\ \boldsymbol{\gamma_i}\end{bmatrix} + \boldsymbol{\varepsilon_i} = \mathbf{W}\boldsymbol{\alpha_i} + \boldsymbol{\varepsilon_i} \cdot \qquad (6)$$

where $\mathbf{X_i}$ are the K Fourier Coefficients (FC's) for the ith of L time segments of data $[H_{x,i}(\omega), H_{y,i}(\omega), E_{x,i}(\omega), E_{y,i}(\omega)]$ in K single or multiple station channels at a single frequency, ω, $\mathbf{V}$ is a $K \times N$ matrix whose N columns represent the coherent noise sources in these K channels and $\boldsymbol{\varepsilon}$ represents only incoherent noise. The columns of $\mathbf{U}$ ideally, represent the magnetic and electric fields that would be observed for idealized quasi uniform magnetic sources (the plane wave case). $\boldsymbol{\beta_i}$ and $\boldsymbol{\gamma_i}$ define both linear polarizations of the source magnetic and electric fields and coherent noise. The vectors $\boldsymbol{\varepsilon_i}$ represent only incoherent noise. $\mathbf{U}$ and $\mathbf{V}$ are combined into a single $K \times (L+N)$ matrix, $\mathbf{W}$, of coherent signal/noise vectors, where $M = N + 2$ is the coherence dimension of the data. $N = M - 2$ is the dimensionality of coherent noise. In the case of purely incoherent noise, $M = 2$, $N = 0$, and $\mathbf{W} = \mathbf{U}$, a situation corresponding to the two polarizations of the plane-wave MT source fields. An estimate of $M > 2$ implies evidence for coherent noise.

For our multiple channel synchronized data sets we utilize the robust spectral density matrix (SDM) and use a method similar to that presented in Kappler 2010. The SDM is a table of the cross power spectra between all possible components, a $K \times K$ matrix of complex values averaged over the L time segments, $S_{i,j} = \langle x_i, x_j \rangle$. The i^{th} diagonal elements of the SDM are $S_{i,i}$ the time averaged autopowers of the i^{th} channel, and the cross powers between channels i and j are given by $S_{i,j.}$ The robust SDM is then given by

$$\mathbf{S} = \sum_{i=1}^{L} \mathbf{w_i} \mathbf{X_i} \mathbf{X_i^*} \tag{7}$$

Where the weights, $\mathbf{w_i}$, are one over the noise variances estimated for the data, and * denotes the complex conjugate. The estimate of M is then given by the number of eigenvalues of $\mathbf{S}$ with signal to noise ratios significantly greater than one. Further and detailed descriptions of robust estimation can be found in Kappler et al.,2010 and Egbert, 1997. To determine the coherence dimensionof $\mathbf{S}$ we subject it to an eigen decompositon. At each frequency $\omega = 2\pi f$, the SDM is decomposed as

$$\mathbf{S}(\omega) = \mathbf{P}(\omega)\mathbf{D}(\omega)\mathbf{P}^*(\omega). \tag{8}$$

Where $\mathbf{P}$ is matrix whose columns are eigenvectors of $\mathbf{S}$, and $\mathbf{D}$ is the diagonal matrix of eigenvalues λ. Expressed in units of SNR (dB) the number of third and higher ($M > 2$) eigenvalues significantly greater than 1dB indicates the number of sources of noise unrelated to ambient MT variations, and is an estimate of the number of coherent noise sources (N) affecting the entire station group. It is these that are our target signals of interest. They may be unique to a site or distributed over multiple sites dependent upon subsurface processes.

The RMEV estimator can tell us about the coherence dimension of the array data, but the MT signal and coherent noise must be separated. If we can isolate signals shown as third or higher eigenvalues >>1 that are uncorrelated to at least some stations in the group, we may be able to assert that these signals are related to subsurface processes, not to the plane wave, and not to coherent noise. Because these anomalous signals can vary over time, and are sometimes periodic with higher cultural noise during daylight hours, we split the 72 hour data into 6 hour time segments. The RMEV method [Egbert, 1997] also provides estimates of the magnetotelluric impedances, from which we calculate apparent resistivity. We also calculate apparent resistivity using a traditional remote reference processing method (RR) included with Egbert's processing codes. These codes are available from the *mtnet* website [*mtnet.dias.ie*] and are packaged as *emtf* [Egbert,1997].

Canonical correlation

To determine signals which are common at all sites in a group, or unique to a single site, we employ canonical correlation analysis (CCA) as described in Kappler et al., 2010 and Kappler 2008. The canonical correlation (also called canonical coherency) method is a frequency-dependent measure of the coherence between two timeseries. We use the technique to uncover noise that is correlated between stations, within channels at a single station, or any channel combination from within the array of data channels. If the group was comprised of four stations with four channels each and a remote reference with two channels, then the number of channels in the group is 18. This will create an SDM with dimensions of 18×18. As an example, the first submatrix is given by $\mathbf{S}_{AA}$, where *A* is the index comprised of the four channels that make up an individual MT station. We subject $\mathbf{S}_{AA}$ to an eigen decomposition and consider the third and higher eigenvalues. The remaining channels can be put into index *B*. We then construct the submatrices: $\mathbf{S}_{AA}$, $\mathbf{S}_{AB,}$ $\mathbf{S}_{BA}$ and $\mathbf{S}_{BB}$. From these we calculate the matrix product $\mathbf{S'}$,

$$\mathbf{S'} = \mathbf{S}_{AA}^{-1/2}\mathbf{S}_{AB}\mathbf{S}_{BB}\mathbf{S}_{BA}\mathbf{S}_{AA}^{-1/2}. \qquad (4)$$

The length of *A* plus the length of *B* is less than or equal to *K* (the number of channels in the group). The ordered eigenvalues of $\mathbf{S'}$ yield the canonical correlation coefficients (*CC*) that describe the correlation between the channels of index *A* and those of index *B*. We are searching for channel combinations that produce elevated third or higher eigenvalues at the station of interest ($\mathbf{S}_{AA}$) and exhibit a low correlation (*CC*) with other stations or channel groupings (*B*). The occurrence of such a combination indicates the possibility of subsurface processes in action. The analysis requires looking at many possible combinations of $\mathbf{S}_{AA}$ and $\mathbf{S'}$ to identify the anomalous E-field signals.

Magnetotelluric phase tensor

The magnetotelluric phase tensor allows an interpretation of those parts of the impedance tensor that are not impacted by the interference of shallow heterogeneities that may dominate measured amplitudes in MT data and distort the regional electric fields associated with the geological target of interest. The phase tensor also provides a method for visualizing MT data and determining dimensionality and conductivity gradients present over the period range of the data. It can be calculated quickly prior to modelling and provides an initial look at the properties of the data being analyzed. It also serves as a guide for later interpretation of resistivity models.

The electric and magnetic fields are measured in a cartesian coordinate system providing x and y components of the electric fields and the x and y components of the magnetic field. The Fourier transforms of the x and y components of the two fields are related by a two dimensional complex impedance tensor $\mathbf{Z}(\omega)$ which, in terms of its real and imaginary parts, can be written as: $\mathbf{Z}(\omega) = \mathbf{P}(\omega) + i\mathbf{Q}(\omega)$.

We shall subsequently assume that all tensors are frequency-dependent Fourier transforms of the original field vectors. The observed electric field transform is the sum of the regional and distorted electric field vector transforms, $\mathbf{E}_{obs} = \mathbf{E}_{reg} + \mathbf{E}_{dis}$. If it is assumed that $\mathbf{E}_{dis}$ results from the linear distortion of $\mathbf{E}_{reg}$ by near surface conductive heterogeneities, then the observed electric field transform can be written as the product of a real distortion tensor, $\mathbf{D}$, and the regional electric field vector transform, i.e., $\mathbf{E}_{obs} = \mathbf{D}\,\mathbf{E}_{reg}$. Meanwhile the regional magnetic field vector transform is not affected by near surface conductive heterogeneities and is reasonably approximated by the observed magnetic field vector transform, $\mathbf{H}_{reg} = \mathbf{H}_{obs}$.

The observed and regional complex impedance tensors $\mathbf{Z}_{obs}$ and $\mathbf{Z}_{reg}$ can be obtained by solving the two equations $\mathbf{E}_{obs} = \mathbf{Z}_{obs}\mathbf{H}_{obs}$ and $\mathbf{E}_{reg} = \mathbf{Z}_{reg}\mathbf{H}_{reg}$. From the above equations it follows that $\mathbf{Z}_{obs} = \mathbf{D}\mathbf{Z}_{reg}$. The magnetotelluric phase tensor is defined by the tensor product, $\mathbf{\Phi} = \mathbf{P}^{-1}\mathbf{Q}$ [Caldwell et al., 2004; Chave, A. and Jones, A, 2012 pp.130-136] which has the following properties,

$$\mathbf{\Phi} = \left(\mathbf{D}\cdot\mathbf{P}_{reg}\right)^{-1}\cdot\mathbf{D}\cdot\mathbf{Q}_{reg} = \mathbf{P}_{reg}^{-1}\cdot\mathbf{D}^{-1}\cdot\mathbf{D}\cdot\mathbf{Q}_{reg} = \mathbf{P}_{reg}^{-1}\mathbf{Q}_{reg} = \mathbf{\Phi}_{reg} \quad . \tag{6}$$

The distortion tensor drops out, and the observed phase tensor equals the undistorted regional phase tensor. Therefore, as Caldwell et al. (2004) show, the measured phase tensor is equal to the regional phase under the "distortion-free" period assumption with no restriction on the underlying regional geo-electric structures, even if 3-D. Any 2 x 2 matrix such as $\mathbf{\Phi}$ defines a transformation, and for visualization it is used to transform a unit circle into an ellipse where Φ_{max} and Φ_{min} are the major and minor axes of the ellipse, respectively. When the regional

structure is 1-D the ellipse is a circle and the conventional impedance tensor phase is given by arctangent of the radius of the circle. In the case of two dimensional regional resistivity the 'skew angle' $\beta = 0$; Φ_{max} and Φ_{min} are rotationally invariant, and α is the angle of the semi-major axis and an azimuth of the magnetic field that gives rise to Φ_{max}. For a 3-D regional structure, β is non-zero, and the angle of the semi major axis is skewed from the orientation of the magnetic field.

Unlike the impedance or apparent resistivity, as shown by equation 6, at longer periods $\mathbf{\Phi}$ is relatively independent of the galvanic effect of shallow conductive heterogeneities. The color of the ellipses presented herein represents the geometric mean (Φ_2) of the principal phase values Φ_{max} and Φ_{min} with, $\Phi_2 = \sqrt{(\Phi_{min}\,\Phi_{max})}$. As with magnetotelluric phase, the phase tensor indicates how resistivity changes with depth. $\Phi_2 > 45°$ indicates increasing conductivity with depth [Heise et al., 2012, Caldwell et al., 2004].

2. RESULTS AND DISCUSSION

After applying the methods described above to the Kilauea data set we find that there are E-field variations not associated with electromagnetically induced electric fields present in the electric field that are likely related to subsurface fluid flow. The RMEV and canonical correlation analysis locates signals presenting as an elevated third eigenvalue and low correlation with other stations in the group. We rule out a variety of cultural noise sources providing evidence that these signals may be related to subsurface fluid flow, geothermal and/or volcanic processes. The time domain analysis of the electric fields further aid the interpretation by allowing us to evaluate temporal variations in the E-field not associated with similar variations in the H-fields. The following section presents and discusses results from, first, the frequency domain analysis, including apparent resistivity estimates from both the RMEV and RR method of data processing, the canonical correlation results, the magnetotelluric phase tensor and how it compares with data acquired in 2002-2003, and finally results from the time domain analysis and spike detection.

2.1 RMEV Analysis of 2012-2013 Data

There are several outputs of the RMEV approach. The ones we utilize herein are the apparent resistivity and the spectral density matrix (SDM). The apparent resistivity and phase are compared with the apparent resistivity and phase from standard remote reference (RR) processing output and demonstrate the measure of coherent noise present in the Kilauea data, and not present in the Puna data. We use the SDM, which is comprised of auto and crosspowers of the E and H field channels for the group, in the canonical correlation analysis. We perform an eigen decomposition of the submatrices of the SDM to examine the nature of the correlated and

uncorrelated noise present in the different channels and to look for signals related to fluid flow. Analysis of the 2002-2003 data is provided in APPENDIX F.

Apparent Resistivity

The 1997 paper by Egbert shows how the RMEV approach can improve impedance estimates if coherent noise sources are intermittent, or if at least one site is unaffected by coherent noise. It also describes how the RMEV approach can provide a measure of coherent noise. Appendix A contains the apparent resistivity and phase for the 2002-2003 data compared to the collocated stations acquired in 2012-2013. In some cases, the Kilauea data processed with the RMEV method are noisier near the magnetotelluric deadband in comparison to their 2002-2003 counterparts, which were also processed by the RMEV method, but at long period they are repeatable. The result of RR processing of all 72 hours of 40 Hz Kilauea Station 09 data (2012) is shown in Figure 2.1.1. The deadband is evident in the station 09 RR curves as being between 1 and 10 seconds. We note that, at several frequencies, there are overlapping calculations of apparent resistivity and phase: this frequency overlap is an artifact created in the configuration files for the RR and RMEV processing, and occurs in the event of noisy data. However this doesn't hinder our interpretation. Figure 2.1.2 shows the same station 09 data processed using the RMEV approach. Unrealistic values (> 10,000 Ωm) of apparent resistivity from periods less than 0.2 seconds to several seconds are the norm for 2012 and 2013 RMEV processing, and occur at all stations at Kilauea (See Appendix A). We believe that this is in part due to proximity to the caldera activity and will be discussed in more detail below.

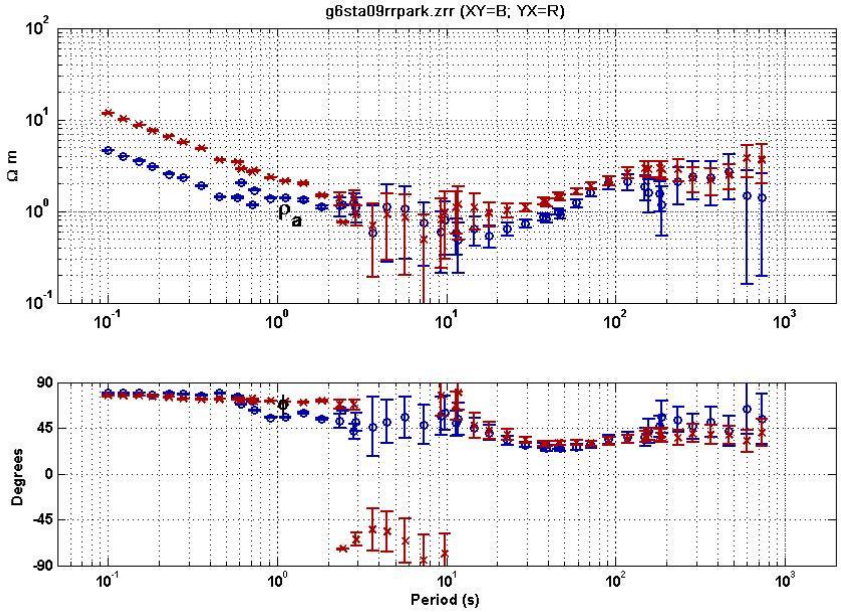

Figure 2.1.1 Apparent resistivity and phase for 2013 Kilauea Station 9 processed with the RR method.

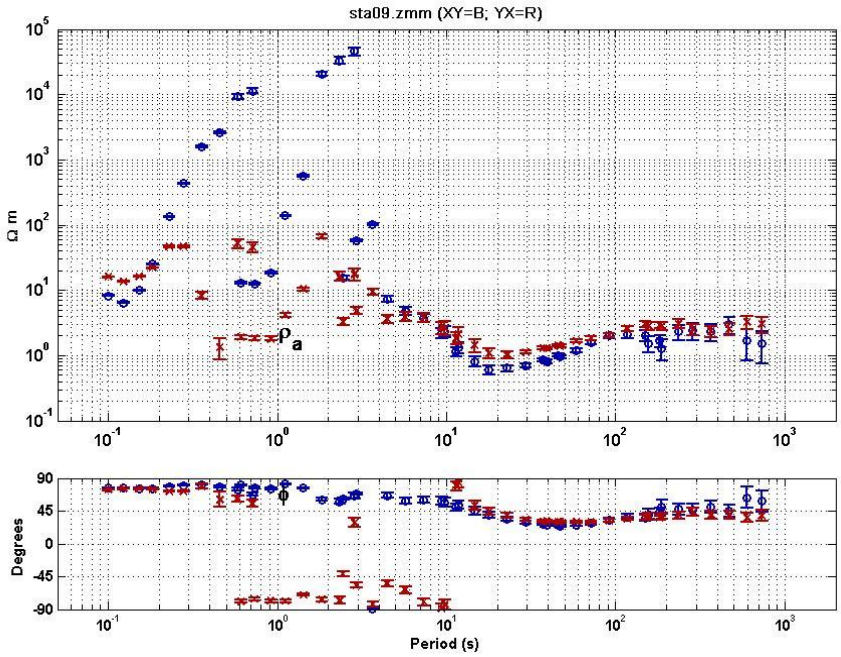

Figure 2.1.2 Apparent resistivity and phase for Kilauea Station 9 processed with the RMEV method.

As further evidence for these assertions, data from Puna do not exhibit this strong noise characteristic. Figure 2.1.3 shows the RR processing result using Puna Station pun02 and a remote reference. Figure 2.1.4 shows pun02 results when using the RMEV approach. In this case the RMEV approach has provided slightly improved impedance estimates. While the RMEV method has improved the estimate of the MT impedance in the Puna data, it has not done so in the Kilauea data, thus demonstrating the sensitivity of the RMEV approach to strong coherent noise contamination of the MT signal at a given suite of stations.

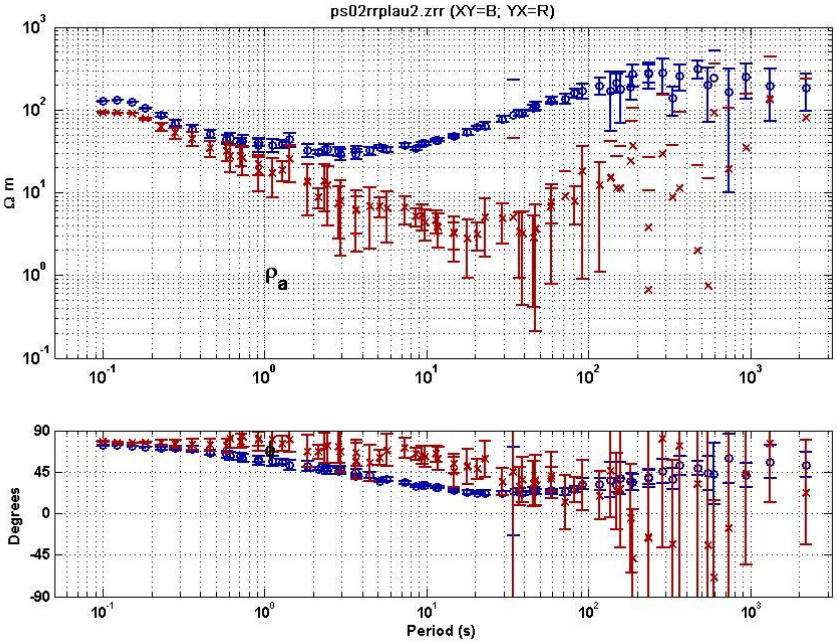

Figure 2.1.3 Apparent resistivity and phase for Puna Station pun02 processed with the RR method.

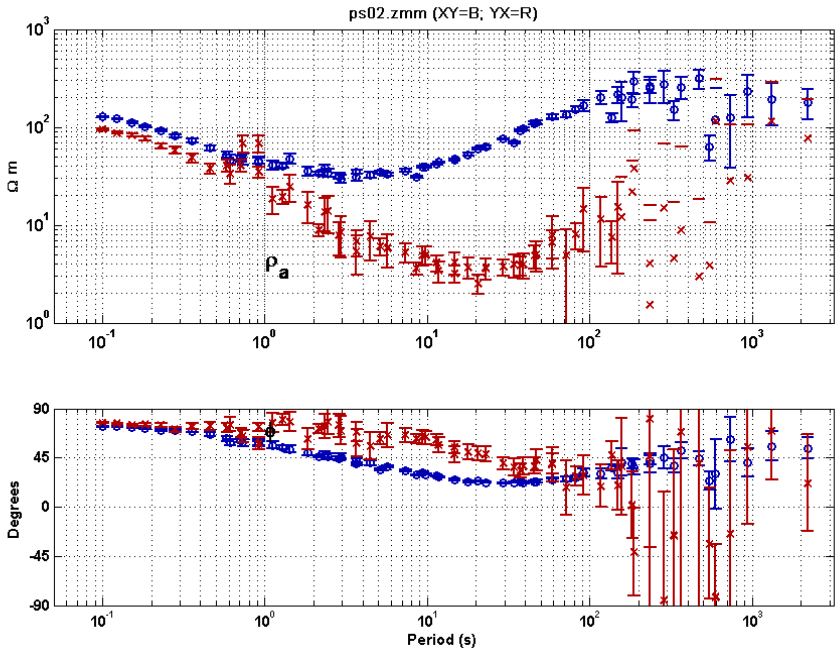

Figure 2.1.4 Apparent resistivity and phase for Puna Station pun02 processed with the RMEV method.

Canonical Correlation

The canonical correlation method allows the comparison of an isolated group of channels (for example, a single station) from the entire group of channels that were simultaneously recorded. We use the data acquired at a 40 Hz sampling rate for this analysis. The 72 hours of data were segmented into 6 hour time bands prior to processing. Figure 2.1.5 shows the first four eigenvalues (top panel is λ_1, bottom panel is λ_4) as a function of time and period for station 18. Orange and red colors represent higher signal to noise ratio (dB). The horizontal axis is the 6 hour time bands and the vertical axis is period. The first two eigenvalues (upper two panels) are associated with the MT response [Egbert, 1989], while the third and fourth are related to noise (or, in our case E-field signals of interest). Figure 2.1.6 is the same time and frequency with color indicating canonical correlation coefficient between station18's magnetic and electric fields with all other channels recorded in group 6. Yellows and reds indicate higher correlation coefficients. Plots of each stations' dominant eigenvalues and canonical correlations are provided in APPENDIX B.

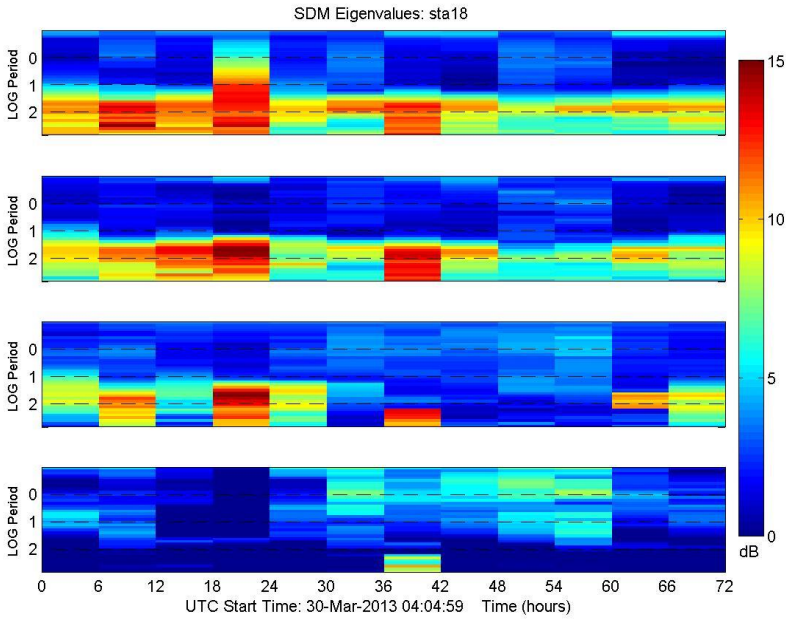

Figure 2.1.5 First four eigenvalues of station 18. Top panel is λ_1, bottom panel is λ_4. There is large signal in the third eigenvalue (third panel down) at periods > 10 seconds in the first 5 timebands, and again from 36-42 hours and during the last twelve hours. Large signals at period of 10 to 1000 seconds in the first and second eigenvalue correspond to the ambient MT signal. Elevated signals in the fourth eigenvalue are at shorter period and overlap the MT deadband, with the exception of the longest period between 36 and 42 hours.

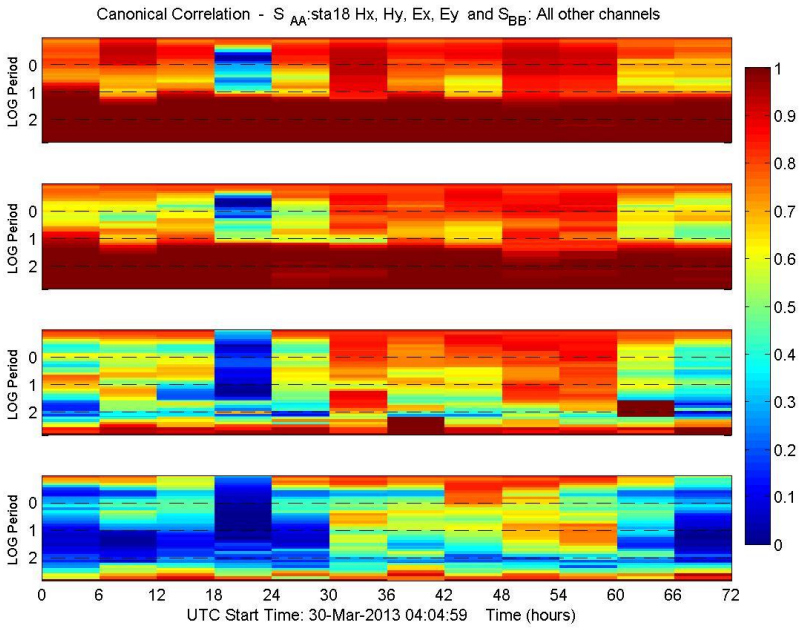

Figure 2.1.6 Canonical correlation coefficients between station 18 H and E channels and all other H and E channels in group 6.

We want to examine the eigenvalue and canonical correlation plots for periods and time bands with both high third eigenvalue and low third correlation coefficient. It is difficult to identify them looking at these plots (2.1.5 and 2.1.6) simultaneously. To aid in this qualitative examination, we normalize the eigenvalues of S_{AA} to range from 0 to 1 and plot λ_3 and CC_3 for each time band. The upper panel of Figure 2.1.7 shows the λ_3 and CC_3 values when station 18 Hx, Hy, Ex and Ey are included in S_{AA} and E channels from the rest of the stations in group 6 are included in index *B*.

We can also subtract the correlation coefficients from λ_3. This provides a single measure of how signals at a given station compare to their correlation with other channels in the group of stations. The values from this differencing operation can range from -1 to 1, and anything larger than 0 is a value with a normalized third eigenvalue larger than the correlation coefficient. Large values from this differencing operation indicate the possibility that the station in S_{AA} is exhibiting the sought-for anomalous E-field contribution, and subsurface fluid flows, we are looking for. An example for station 18 is plotted in the lower panel of Figure 2.1.7.

We consider different sources of noise as we interpret the canonical correlation results to identify signals of interest. The MT deadband (1-10 seconds period) typically exhibits low signals and may also have very low correlation. There can be diurnal fluctuations in electromagnetic fields that create noise in the data, though for the Kilauea data set we are somewhat removed from cultural sources of emf (e.g. power lines, large intermittent electrical

loads, etc.). Small canonical correlation coefficients, that occur during night time hours, subtracted from third or fourth eigenvalues can enhance the diurnal effect. This is more prevalent in examining differences between λ_4 and CC_4. At Lower Puna, proximity to a quarry, the town of Pahoa, and housing subdivisions, resulted in some electromagnetic noise contamination. We also see diurnal temperature changes that impact the electrodes. These are very long period and should not interfere with our interpretations. There is also the potential for a coastal effect to create noise in our data, but it would likely be coherent across all stations in a group. The impact of a coastal effect would be minimal on stations further than a skin depth from the coastline, and would not affect the horizontal components to a great extent [Schmucker, 1970]. Other sources of noise may be related to: deflation and inflation near the Kilauea summit;or to seismic activity, in the form of earthquakes or volcanic tremor (tremor can induce fluid flow and we ought to look for it in our data); and shallow boiling that would be a fluid flow-related signal of interest to us.

While we have tried numerous combinations of channels to isolate signals of interest, our most successful approach has been to initially include the electric and magnetic field channels of a single station in S_{AA}. Friedel [2005] and Fitterman [1978] both discuss the lack of sensitivity of magnetic field to fluid flow and electrokinetic processes. So we believe that any signals that are of interest reside predominantly in the electric fields, and this is what we have found as we apply these methods. In the following results we examine the impact of including electric field channels from other stations in index *B*. We use the stations from group 6 and stations from group 2 as examples. Results for all groups (1 through 6) are included in APPPENDIX C.

Group 6 results

Group 6 results are shown in Figures 2.1.7 – 2.1.10. Group 6 is perhaps one of the most geologically diverse groupings of stations. Station 9 (Figure 2.1.8) is located at the Puhimau thermal feature: a ~5 hectare area of thermal ground overlying a shallow magmatic intrusion that was emplaced in the 1930's. Station 10 (Figure 2.1.9) is proximal to Kilauea's East Rift Zone (ERZ), while stations 17 and 18 (Figures 2.1.10 and 2.1.7 respectively) are near the Southwest Rift Zone (SWRZ). Examining the upper panels of the four figures, there are two large λ_3 and CC_3 evident at all stations. The first is between 36 to 42 hours from 100 to 1000 seconds, and the second is from 60 to 66 hours at 100 seconds. This high λ_3 indicates a large noise source, while the large CC_3 indicates that these events impacted all four stations simultaneously. All four lower panels show the influence of the MT deadband, with light blue colors caused when $0.2 < \lambda_3 < 0.3$ and $CC_3 < 0.05$. These lighter colors actually appear to extend beyond the typical MT deadband of 1 to 10 seconds, going from $10^{-.25}$ to $10^{1.25}$ seconds. Station 18 exhibits a very large difference between λ_3 and CC_3 in the first 30 hours.

We also look at the behavior of λ_4- CC_4 at the stations in group 6. The differences for all four stations in group 6 are shown in Figure 2.1.11. There is evidence of diurnal variation. The transitions at 6 hours, 30 hours and 54 hours, mark the middle of the night. Coherency drops at night creating a large difference between the fourth eigenvalue and canonical correlation

coefficient. Station 9 however appears to exhibit a large difference over multiple time bands, and predominantly at short periods. This could be related to the proximity to Puhimau and the influence of shallow hydrothermal activity including boiling. λ_3- CC_3 and λ_4- CC_4 for all stations are plotted in APPENDIX C and E.

Group 2 results

Figures 2.1.12 – 2.1.15 show the diagnostic plots for the Group 2 (*sta01, sta12, sta13, sta15*). Stations 12 and 13 are within the Kilauea caldera. Station 1 is 2 km southwest of Halema'uma'u, and station 15 another 1 km west (locations are shown in Figure 1.1.2). Figures 2.1.13 and 2.1.14 reveal that, as might be expected, the two caldera stations share similar characteristics. At periods shorter than 10 seconds (frequencies higher than .1 Hz) there is a strong diurnal component lasting from 6 to 24 hours and repeated between 36 and 54 hours at stations 12 and 13. At station 1 the diurnal effect is not as evident. It is present somewhat at station 15. Of course diurnal effects may be due to cultural noise but may also be associated with diurnal meteorological effects (e.g. rainfall) and temperature variation at this location. The start time of this acquisition is 8:30 at night, and the correlations at stations 12 and 13 decrease in the nighttime hours. In spite of any diurnal signals, the large differences at 12 and 13, compared to

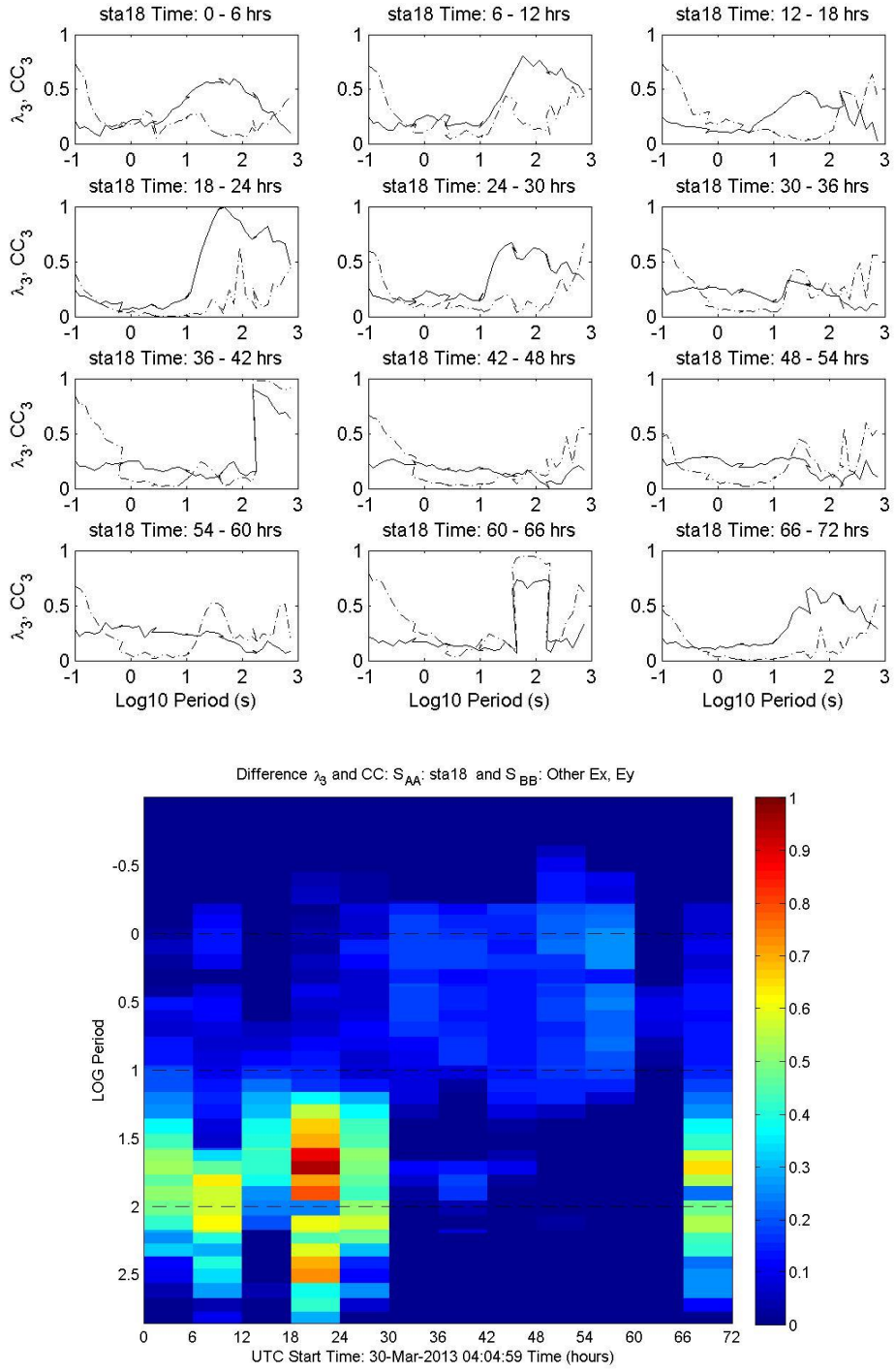

Figure 2.1.7 Normalized λ_3(solid line) station 18 Hx, Hy, Ex and Ey and correlation coefficients (CC, dashed line) between station 18 (S_{AA}) and all other E channels (S_{BB}) in Group 6 are shown for each time band in the upper panel. Plotted in this manner we can identify periods where low correlation coefficients and modest λ_3 could give a large difference. The lower panel shows the difference between normalized λ_3 for station 18 Hx, Hy, Ex and Ey and correlation coefficients (CC) between station 18 and all other E channels in Group 6.

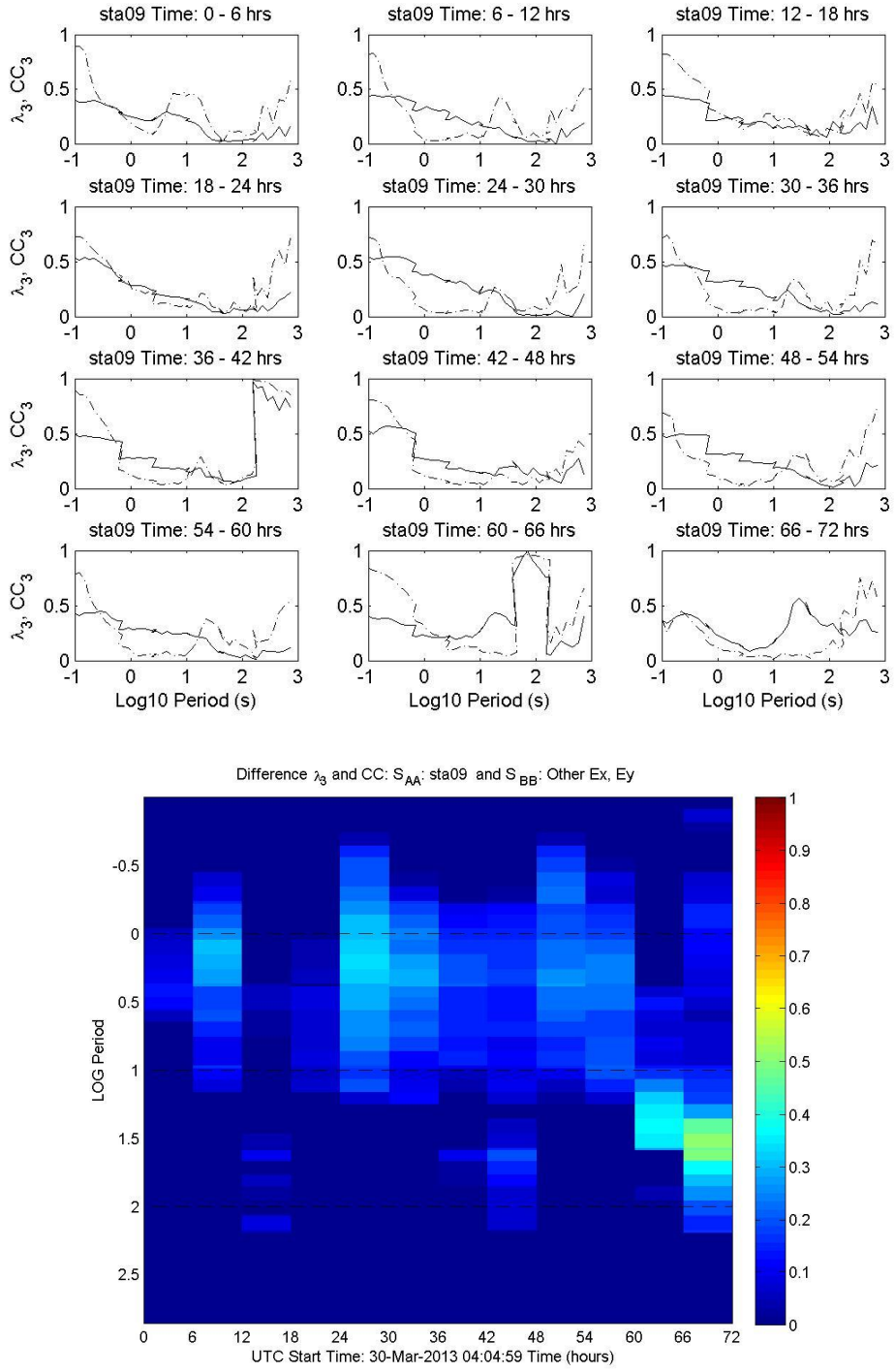

Figure 2.1.8 Normalized λ_3 (solid line) station 09 Hx, Hy, Ex and Ey and correlation coefficients (CC, dashed line) between station 09 (S_{AA}) and all other E channels (S_{BB}) in Group 6 are shown for each time band in the upper panel. Plotted in this manner we can identify periods where low correlation coefficients and modest λ_3 could give a large difference. The lower panel shows the difference between normalized λ_3 for station 09Hx, Hy, Ex and Ey and correlation coefficients (CC) between station 09 and all other E channels in Group 6.

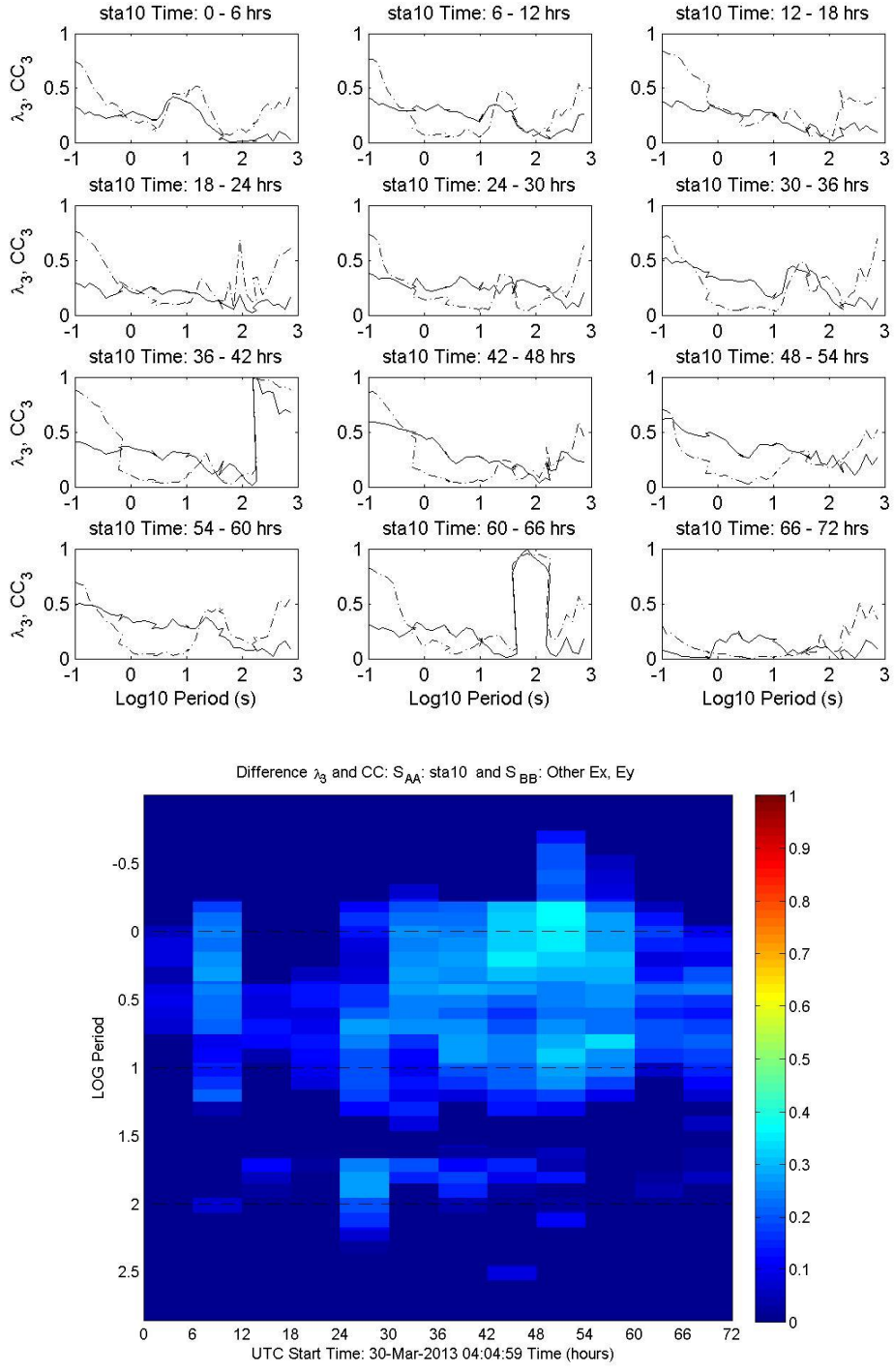

Figure 2.1.9 Normalized λ_3 (solid line) station 10 Hx, Hy, Ex and Ey and correlation coefficients (CC, dashed line) between station 10 (S_{AA}) and all other E channels (S_{BB}) in Group 6 are shown for each time band in the upper panel. Plotted in this manner we can identify periods where low correlation coefficients and modest λ_3 could give a large difference. The lower panel shows the difference between normalized λ_3 for station 10 Hx, Hy, Ex and Ey and correlation coefficients (CC) between station 10 and all other E channels in Group 6.

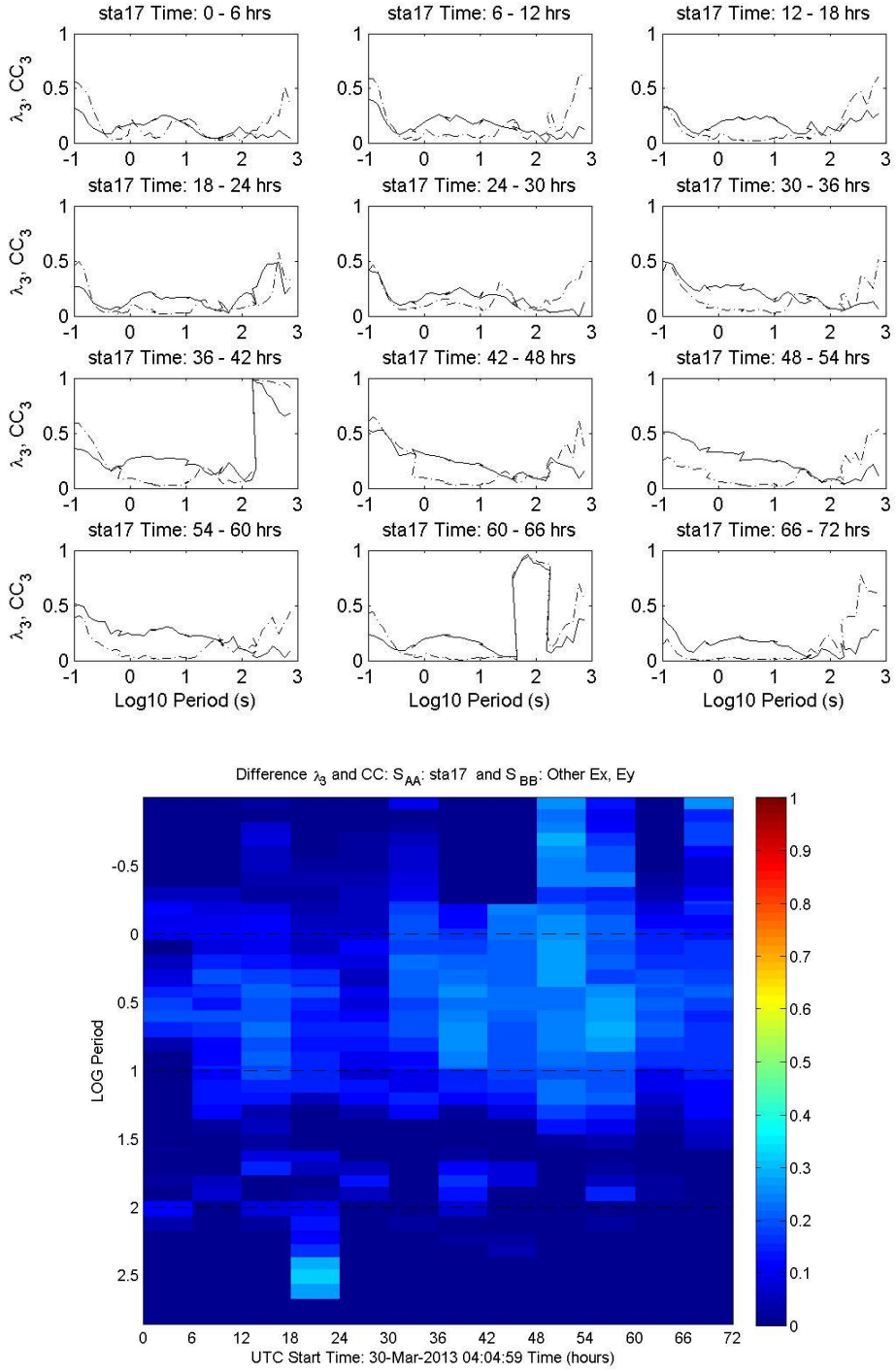

Figure 2.1.10 Normalized λ_3 (solid line) station 17 Hx, Hy, Ex and Ey and correlation coefficients (CC, dashed line) between station 17 (S_{AA}) and all other E channels (S_{BB}) in Group 6 are shown for each time band in the upper panel. Plotted in this manner we can identify periods where low correlation coefficients and modest λ_3 could give a large difference. The lower panel shows the difference between normalized λ_3 for station 17 Hx, Hy, Ex and Ey and correlation coefficients (CC) between station 17 and all other E channels in Group 6.

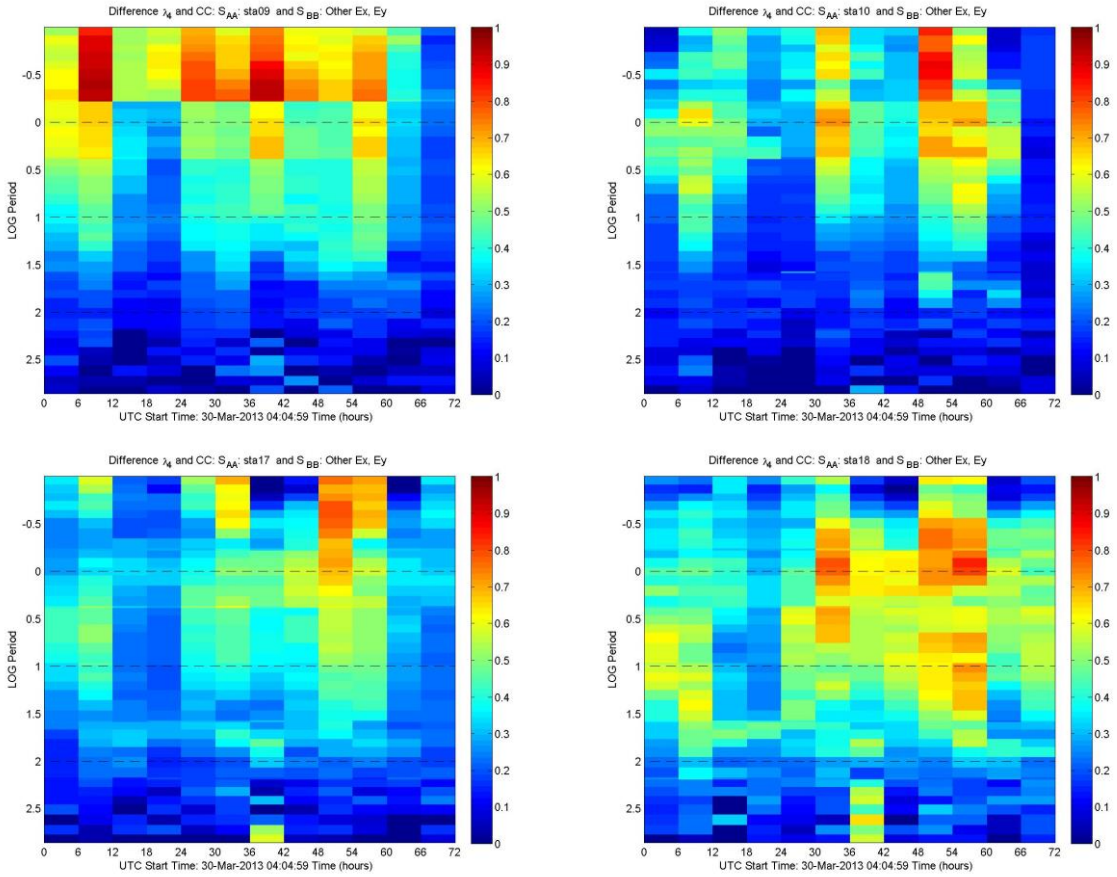

Figure 2.1.11 Normalized λ_4 – CC_4 difference for all stations in group 6. Station 9 exhibits the largest difference and at short periods and across multiple time bands, which we suspect is related to shallow hydrothermal activity at Puhimau. Diurnal fluctuation is evident at short period in stations 10, 17, and 18.

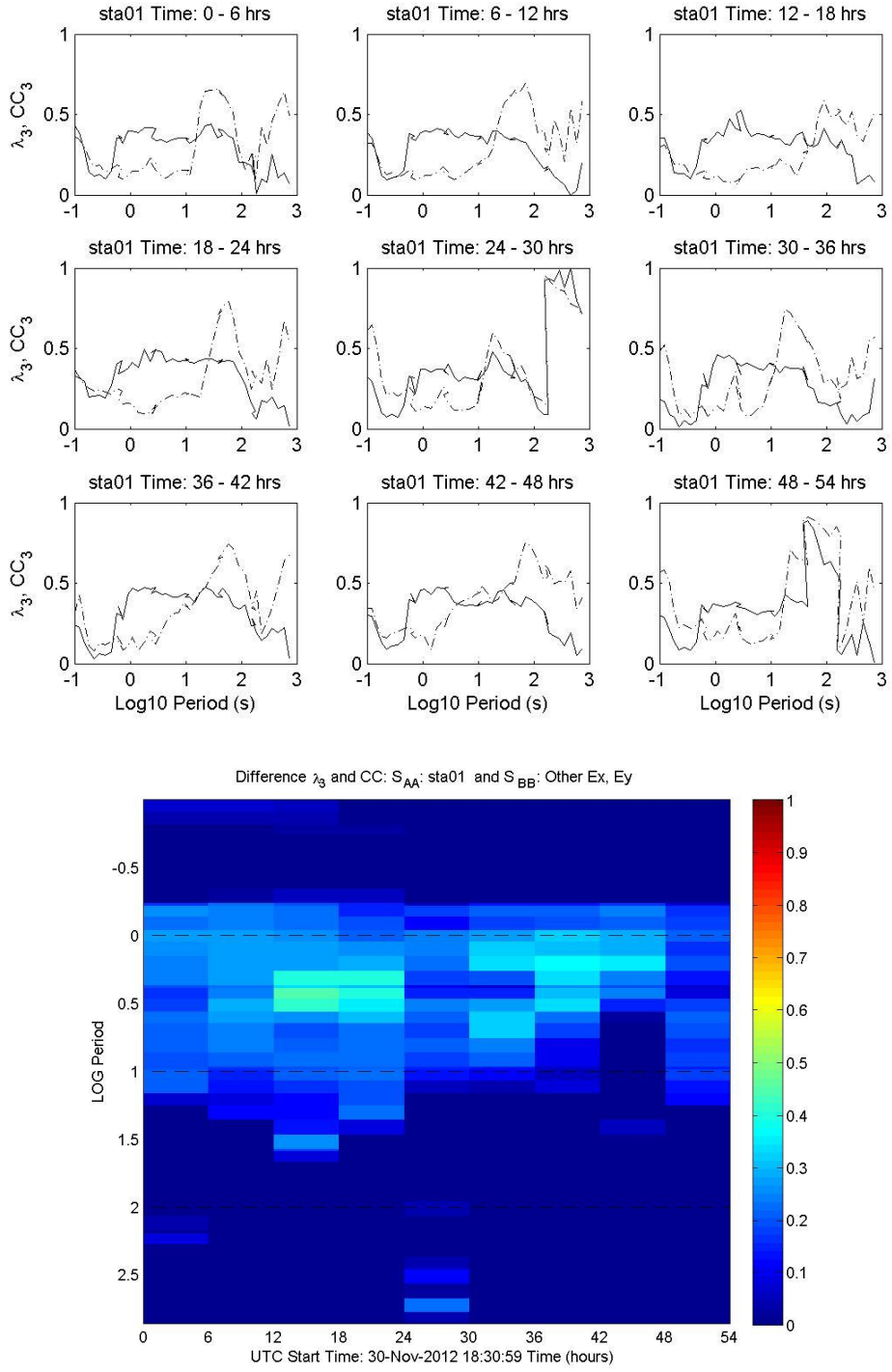

Figure 2.1.12 Normalized λ_3 (solid line) station 01 Hx, Hy, Ex and Ey and correlation coefficients (CC, dashed line) between station 01 (S_{AA}) and all other E channels (S_{BB}) in Group 2 are shown for each time band in the upper panel. Plotted in this manner we can identify periods where low correlation coefficients and modest λ_3 could give a large difference. The lower panel shows the difference between normalized λ_3 for station 01 Hx, Hy, Ex and Ey and correlation coefficients (CC) between station 01and all other E channels in Group 2.

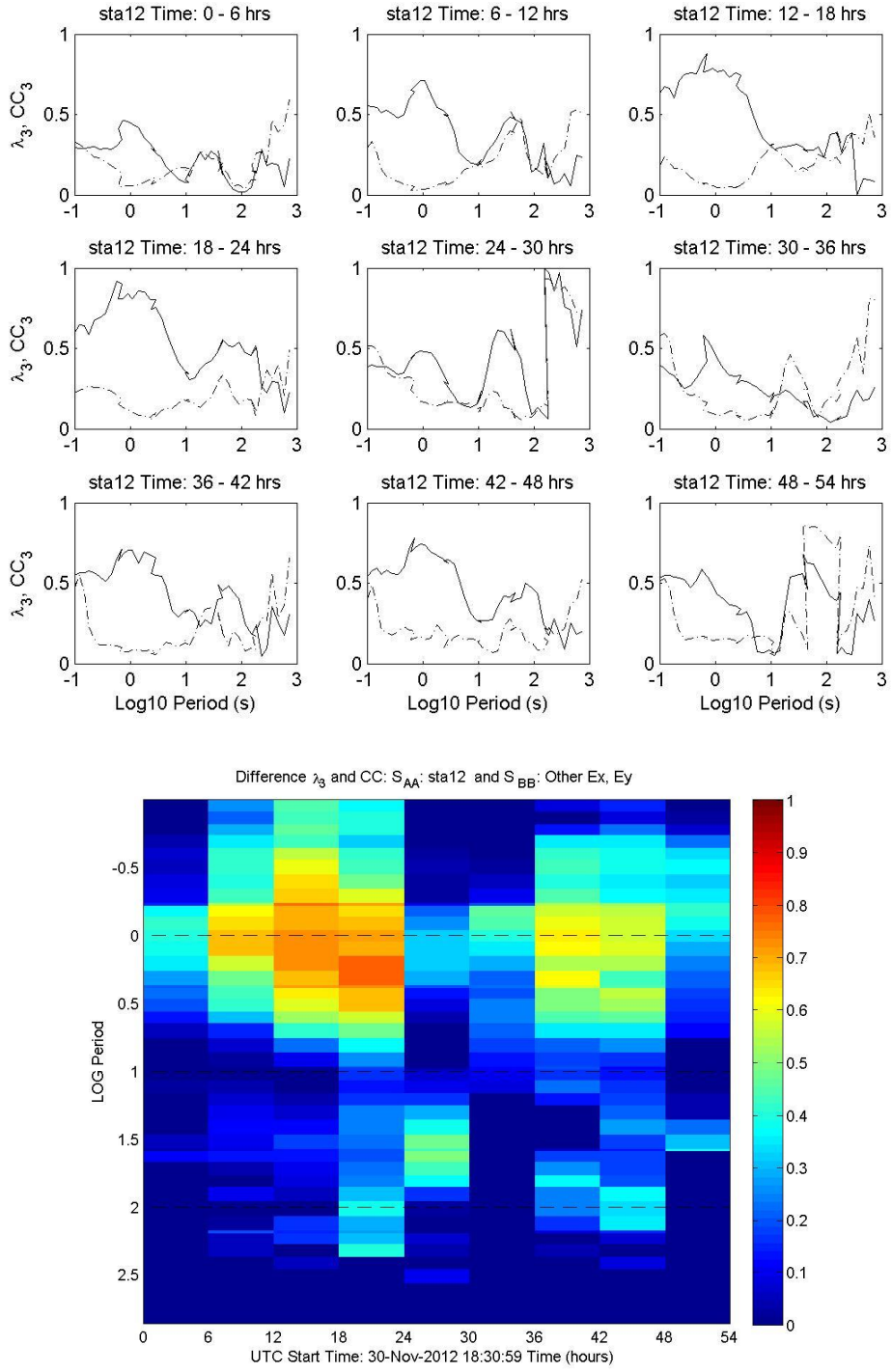

Figure 2.1.13 Normalized λ_3 (solid line) station 12 Hx, Hy, Ex and Ey and correlation coefficients (CC, dashed line) between station 12 (S_{AA}) and all other E channels (S_{BB}) in Group 2 are shown for each time band in the upper panel. Plotted in this manner we can identify periods where low correlation coefficients and modest λ_3 could give a large difference. The lower panel shows the difference between normalized λ_3 for station 12 Hx, Hy, Ex and Ey and correlation coefficients (CC) between station 09 and all other E channels in Group 2.

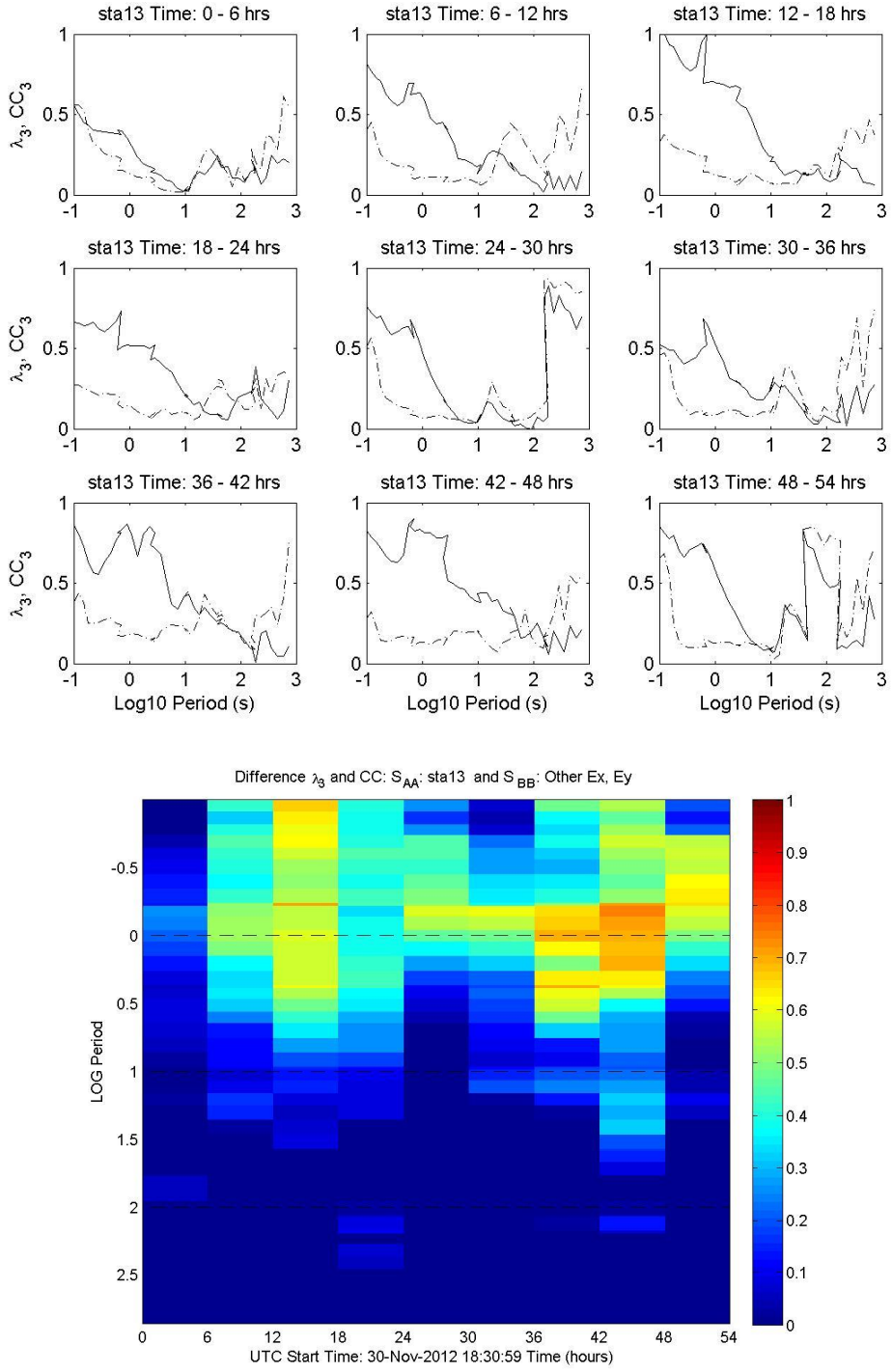

Figure 2.1.14 Normalized λ_3 (solid line) station 13 Hx, Hy, Ex and Ey and correlation coefficients (CC, dashed line) between station 13 (S_{AA}) and all other E channels (S_{BB}) in Group 2 are shown for each time band in the upper panel. Plotted in this manner we can identify periods where low correlation coefficients and modest λ_3 could give a large difference. The lower panel shows the difference between normalized λ_3 for station 13 Hx, Hy, Ex and Ey and correlation coefficients (CC) between station 13 and all other E channels in Group 2.

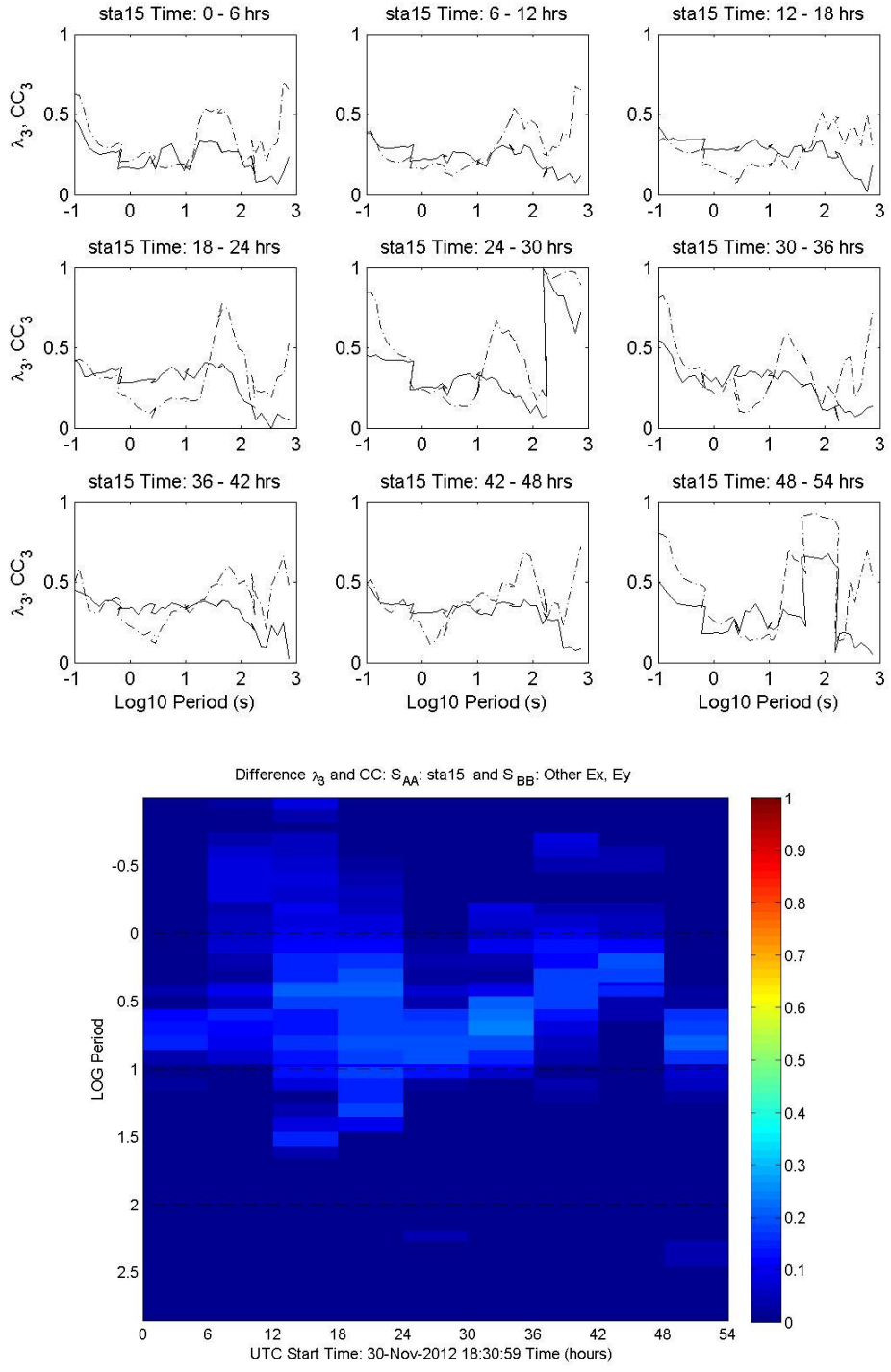

Figure 2.1.15 Normalized λ_3 (solid line) station 15 Hx, Hy, Ex and Ey and correlation coefficients (CC, dashed line) between station 15 (S_{AA}) and all other E channels (S_{BB}) in Group 2 are shown for each time band in the upper panel. Plotted in this manner we can identify periods where low correlation coefficients and modest λ_3 could give a large difference. The lower panel shows the difference between normalized λ_3 for station 15 Hx, Hy, Ex and Ey and correlation coefficients (CC) between station 15 and all other E channels in Group 2.

stations 1 and 15, may indicate the influence of their proximity to Kilauea summit and the influence of magmatic and hydrothermal activity.

Earthquakes and DI Events

To determine if anomalous E-field signals are related to seismogenic activity we use information on earthquake time (UTC), location and magnitude available from

http://quake.geo.berkeley.edu/anss/catalog-search-help.html#datetime

We also obtained timeseries of deflation-inflation (D/I) events for the time period of the Kilauea survey from Hawaiian Volcano Observatory (HVO) scientists (Mike Poland, personal communication).

Between 60 and 66 hours and near 100 seconds period, group six has a large third eigenvalue that is highly correlated between the stations (Figures 2.1.7 – 2.1.10 upper panels). This acquisition was started at 04:04:59 UTC on March 30, 2013. A check of earthquake records indicates that two earthquakes were recorded during the acquisition of group 6, the first corresponding to the timeband 30-36 hours and the second at the time band of 54 to 60 hours. These are the time bands prior to when we see elevated λ_3 and CC values. A check of tiltmeter data that monitors DI events at the Kilauea Summit shows that there are no reversals in tiltmeter readings that correspond to these time bands. For group 2 there is a strong highly correlated λ_3 in the records for 24-30 hours (Upper panel of Figures 2.1.12 – 2.1.15). A check of earthquakes in the vicinity reveals four shallow low magnitude earthquakes that occurred during that time band.

Another observation that we have made regarding the summit caldera data is that many of our computed apparent resistivity values in the frequency range of 1 Hz to 3 Hz are extremely unstable and unrealistically high even though computed values for lower frequency intervals are much more stable and far more reasonable. Although some of this instability may be related to the signals falling within the deadband for our coils, the instability extends beyond the deadband. We have considered a second volcanogenic source for the variable E-field signals: harmonic tremor is a nearly continuous phenomenon within the caldera region of Kilauea; the ground motion associated with harmonic tremor also occurs within a similar frequency range and could very well be responsible for fluid motion, associated with "elastic" cycling of fracture apertures within the saturated subsurface formations in the caldera. In order to confirm this, we would have to conduct a much more focused study on the relationship between harmonic tremor and Spectral SP response that is beyond the scope of our present objectives.

As of now the relationship between earthquakes, tremor and our data are inconclusive. We are in the process of obtaining local seismic records relating to volcanic tremor, including long period events, very long period events and harmonic tremor that may clarify any relationships that exist. These large λ_3 values within a single time band also impact the normalization of λ_3 across all time bands.

Magnetotelluric Phase Tensor

The phase tensors for group 6 (calculated using impedance from the RMEV approach) are shown in Figure 2.1.16. We have seen in the canonical correlation results that station 18 shows a signal of interest, possibly associated with hydrothermal activity. However the phase tensor for station 18 is not markedly different than that of station 17 or 10. Station 9 phase tensor is the station with the unique appearance. The $\Phi_2 << 45°$ indicates a zone of higher resistivity. This is likely associated with the intrusion responsible for the Puhimau hot spot thermal area. The orange colors $\Phi_2 > 45°$ indicate an electrically conductive region. We do not expect the phase tensor to be a useful diagnostic for detecting fluid flow. However it is useful in the case of changing electrical resistivity related to volcanism and geothermal reservoir characterization. The MT phase tensor has been used as a timelapse study of reinjection into a geothermal reservoir [Peacock et al., 2012]. Phase tensors for all 6 groups of 2012-2013 Kilauea data are shown in Appendix D. There they are compared to phase tensors for stations acquired in 2002 and 2003.The 2012-2013 phase tensor plots are comparable with those taken a decade earlier at periods related to deep structure.

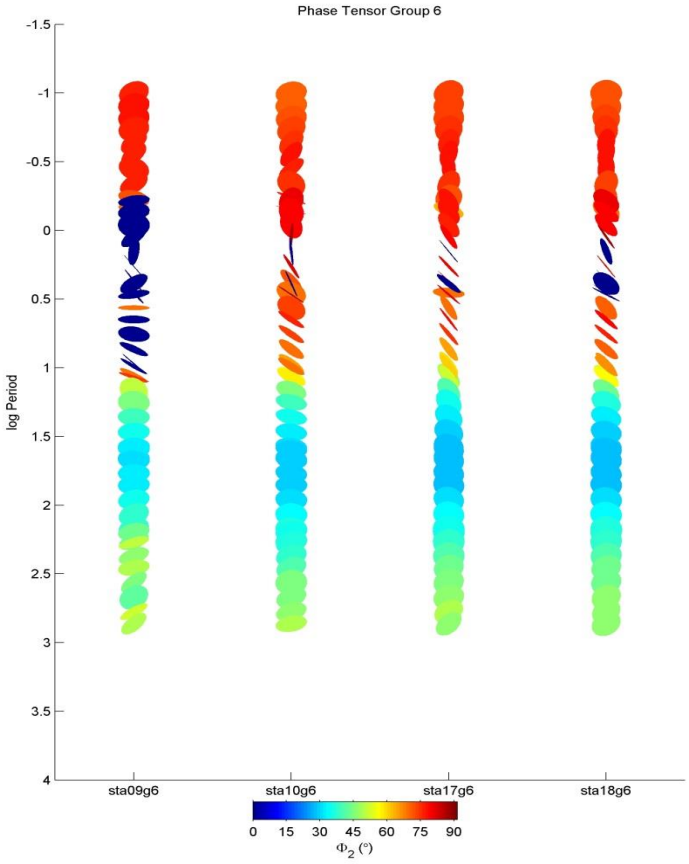

Figure 2.1.16 Phase Tensor plots of group 6 stations 09, 10, 17 and 18.

2.2 Time Domain Analysis

A disadvantage of the frequency domain method is that it requires a frequency analysis (FFT) that effectively integrates long stretches of time-domain data to obtain the frequency components. Although frequency analysis is essential for getting a frequency-dependent MT response, it is less clear that the one-time or irregular events that may characterize geothermal and volcanic processes in a region as dynamic as the Kilauea summit can be well-represented in the frequency domain. Such events easily become buried in the noise when they are non-repetitive. We have addressed this problem in two ways. The first is to perform frequency analyses over relatively short time periods and then to examine the resulting correlations in each period over longer intervals. In this way it is possible to see decreases in correlation resulting from increases in electrical activity due to external noise or hydrothermal/volcanic activity. The second is to examine the time-domain records visually for unusual events that are not correlated with magnetic field variations. The times of these events and their amplitudes can then be used for further analysis.

Long Period Perturbations in the E-field

We used the *MTPlot* software that we developed to examine the time domain data for evidence of E-field activity that was uncorrelated with the H-fields. The first example is shown in Figure 2.2.1, where the Ey data at the sta10 site, located near the caldera boundary faults, shows unusual "saw-tooth" fluctuations having a magnitude of 0.5 mV/km. No similar variation is observed in either Hx, Hy or Ex at this station, nor are they present at sta18, located ~3 km WSW of sta10. The magnitude of the expected MT E-field is well-defined by the large variations in Hy, during the time interval between 02:06:00 and 02:09:00, that correlate well with the variations in Ex. Similar correlations exist between the variations in Hx and those in Ey, but they are obscured by the shorter-period fluctuations. The location of sta10, in a prohibited-access area of the National Park that is several kilometers distant from residential areas, and the timing of the events, ~02:00 local time, is not consistent with an anthropogenic source for these fluctuations.

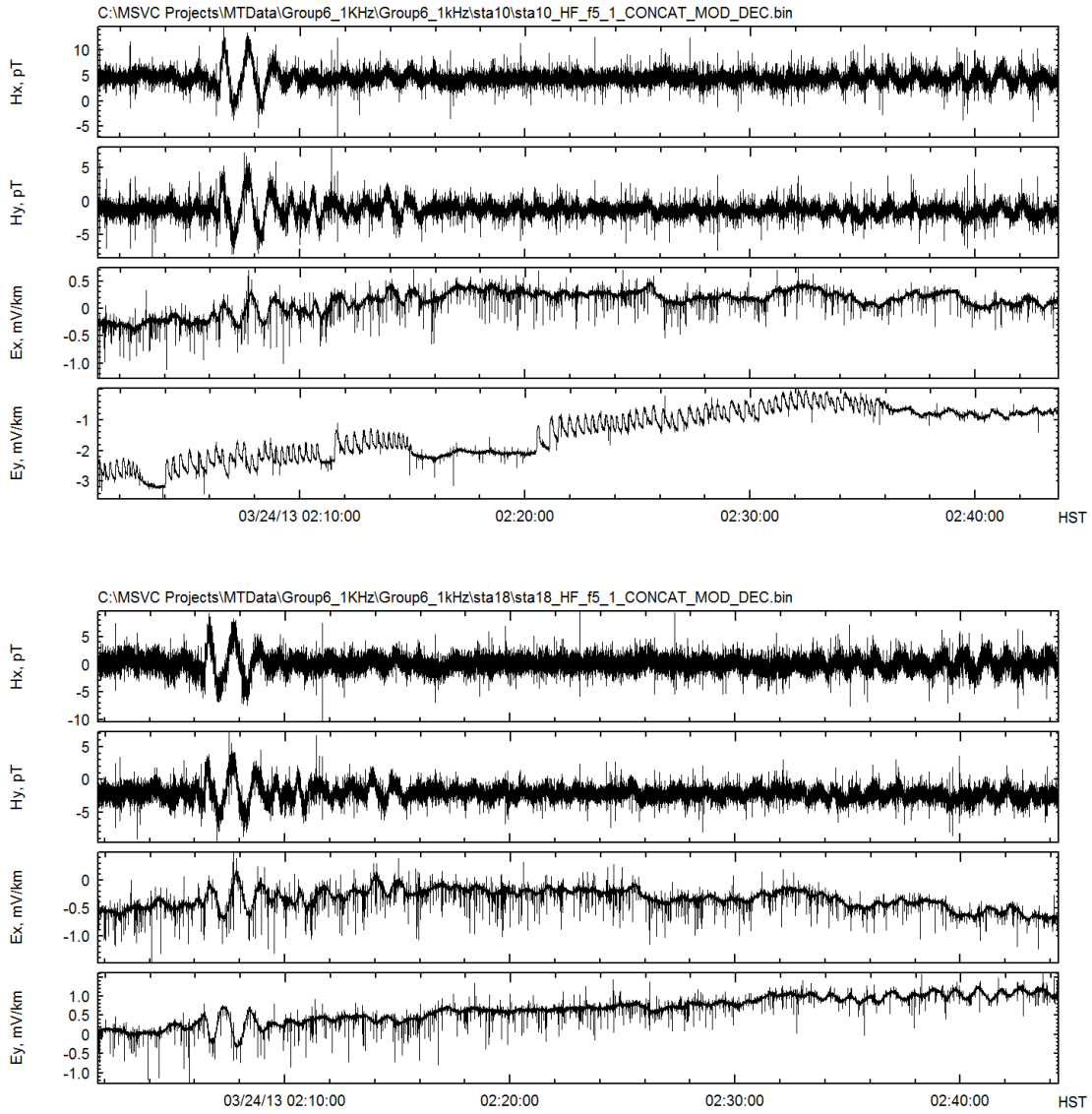

Figure 2.2.1 Upper panel is field data recorded over a 40 minute time interval at sta10; lower panel is field data for sta18 for the same interval. Time code is Hawaii Standard Time (HST).

MTPlot was used to calculate the Fourier spectrum of the data in Figure 2.2.1, and the result is shown in Figure 2.2.2. The MT spectra for sta10 of the H-fields and Ex only extend out to 0.03 Hz, whereas the Ey spectra extend out to nearly 0.1 Hz with the largest peak at 0.05 Hz; the spectra for sta18, although showing nearly identical H-field Ex fields, show no such variation in the Ey field. The period of the anomalous signal is ~20 seconds and is not considered to be consistent with an environmental (e.g. temperature or rainfall) influence on the (buried) electrodes but is within a frequency that is consistent with periodic variations in fumarole discharges observed at Kilauea and elsewhere.

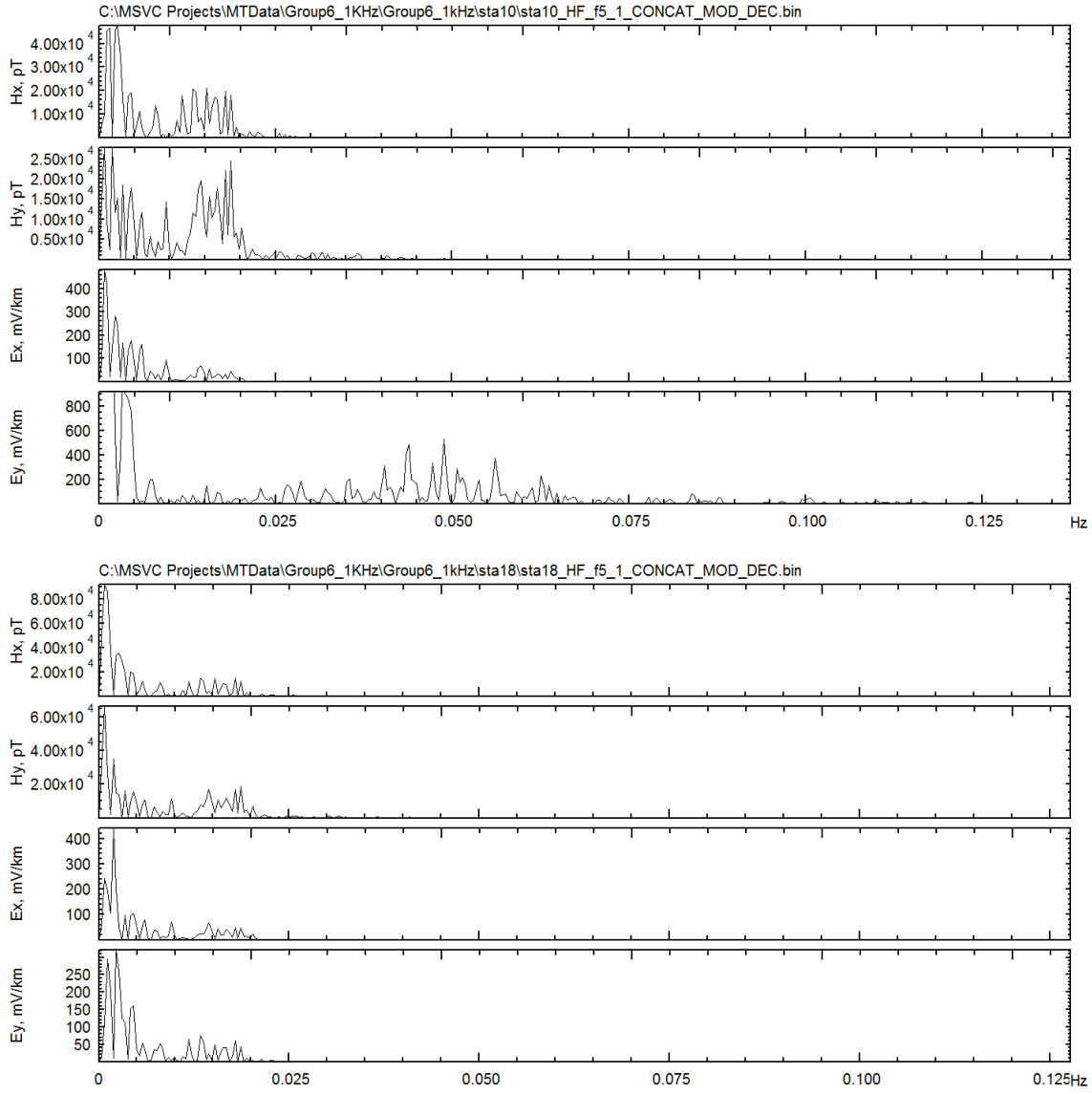

Figure 2.2.2 Upper panel is the Fourier spectrum of the data for sta10; lower panel is the Fourier spectrum of the data from sta18.

We believe that this is an example of a Spectral SP signal generated by subsurface fluid flows that are local to our sta10 site. Our reasoning is as follows:

1) The shape of the individual anomalies, showing an increase followed by a decay, is very similar to the SP responses observed during a deep-hole injection test that was conducted in Nojima [Murikami et al., 2001] in which water was injected at variable rates into a deep geothermal test hole. Even though the injection rate changes in that study were on the order of a few liters per minute, some of the observed SP responses were as large as ~20 mv. Other fluid injection studies have also observed significant variations in surface SP signals

although temporal resolution and depth of injection renders most of them less relevant to the present work [Marquis et al., 2002; Maineult, et al., 2008].

2) sta10 is located near, and possibly over, the magma conduit transporting magma from the summit crater out to the East Rift Zone. The magma conduit is extremely dynamic with flow through the system changing on a nearly continuous basis in response to changes in the level and degassing rate of the lava lake inside Halema'uma'u and with deflation/inflation events (DI) occurring at sporadic intervals. We postulate that expansion and contraction of the magma conduit will likely influence fracture apertures within the rift that could have a throttling effect on water/steam flow within the thermal envelope around the magma conduit.
3) We see these periodic fluctuations in E-field on the Ey electrode pair: this electrode pair is orthogonal to the strike of the rift zone; Zablocki (1976) and many investigators since, have shown that the SP variation is strongest across the strike of a linear thermal feature and weakest along the strike. Hence, our Ex electrode pair is likely to be significantly less sensitive to the inferred flow variations. The absence of similar signals at other stations that were collected simultaneously with sta10 strongly suggests that the source of the variations is within close proximity to this station.

This example demonstrates that time domain analysis can provide valuable guidance in identifying non-MT signals of interest that subsequent spectral analysis is capable of further characterizing.

A second candidate example of a spectral SP signal is shown in Figure 2.2.3 where, at stat10, we have a gradually rising signal that suddenly drops and then undergoes a recovery toward higher values; within the recovery period is an MT-induced E-field dip that recovers to its original upward trend after the H-field stabilizes. Sta18 shows a very clear response to the MT-induced Ex and Ey variations but the longer period oscillation and drop/recovery are absent from the sta18 E-fields. As was the case for the prior example, local time during the anomalous Ey-field variation occurred during late night-time hours when anthropogenic noise would be least likely to generate such variances; similar to the prior example as well, there were no rainfall events in the study area that could reasonably account for the observed changes. Finally, we present a much longer duration data set for stations sta10 and sta18 in Figure 2.2.4. Again, we see quite significant differences between the sta10 Ey data and that for sta18. The longer record is more difficult to interpret: we recognize that electrode effects can present variations similar to those observed on these longer time scales. There is a strong diurnal variation in the data; we have characterized the diurnal temperature effects on our recording instrumentation and found them to be on the order of ~0.2 mv. Temperature effects on the electrodes need to be considered as another source of the diurnal variations observed but, other stations in the region, that were buried to similar depths in similar ashy soils show quite different, and minimal diurnal effects. An alternate, volcanogenic, source of these diurnal SP variations is associated with earth-tidal effects on the eruptive process; an association between earth-tides and eruptive activity at Kilauea has been postulated [Dzurisin, 1980] as well as at other erupting volcanic systems

[Sottili et al., 2012; van Manen, et al., 2012]. Flexing of the Kilauea summit's magmatic plumbing system could well be affecting localized heat-flow and fluid flow within the region and from that, produce the observed variations is E-field that are being observed here.

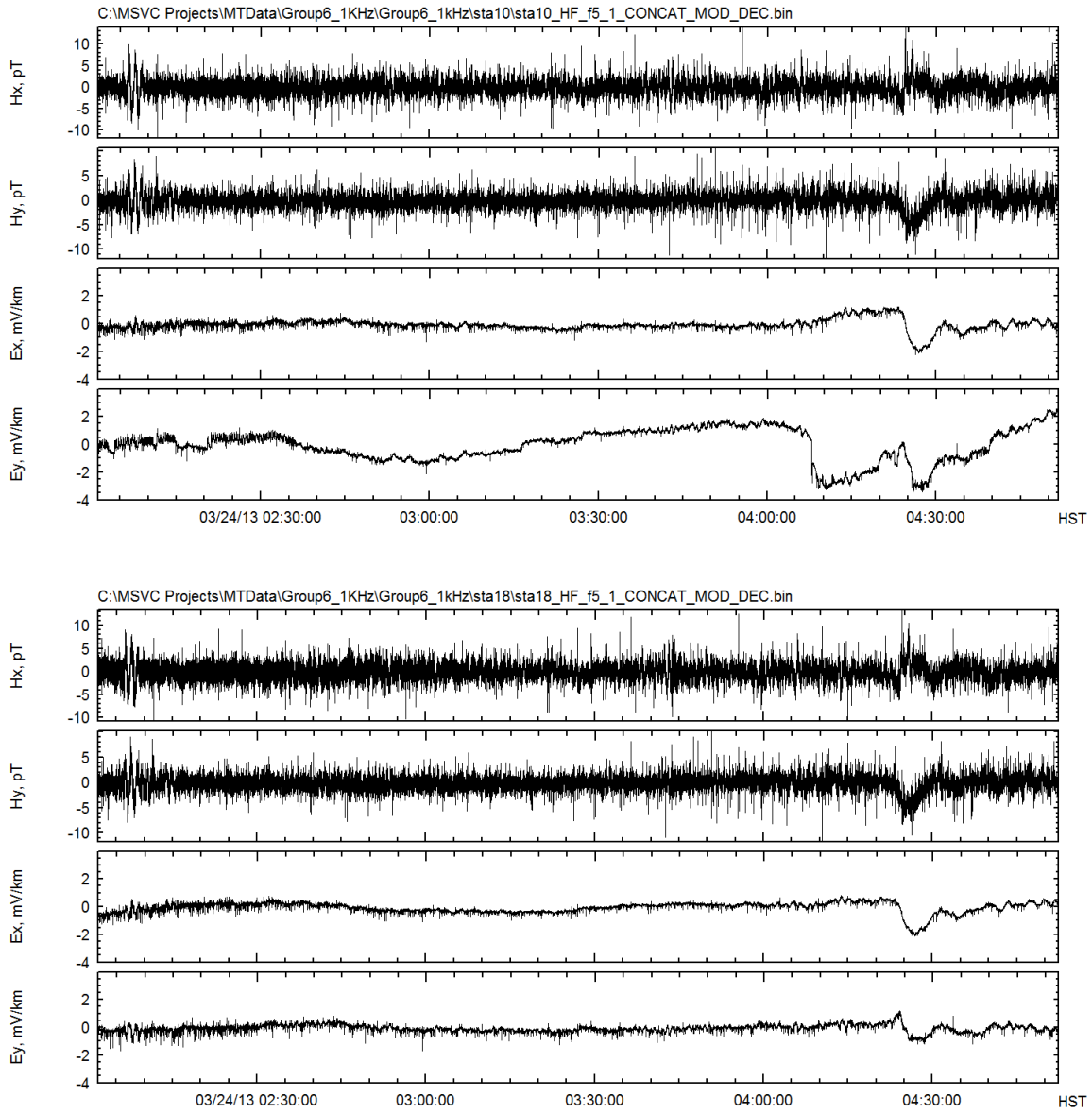

Figure 2.2.3 Upper panel is field data recorded over a 3 hour time interval at sta10; lower panel is field data for sta18 for the same interval. Time code is Hawaii Standard Time (HST).

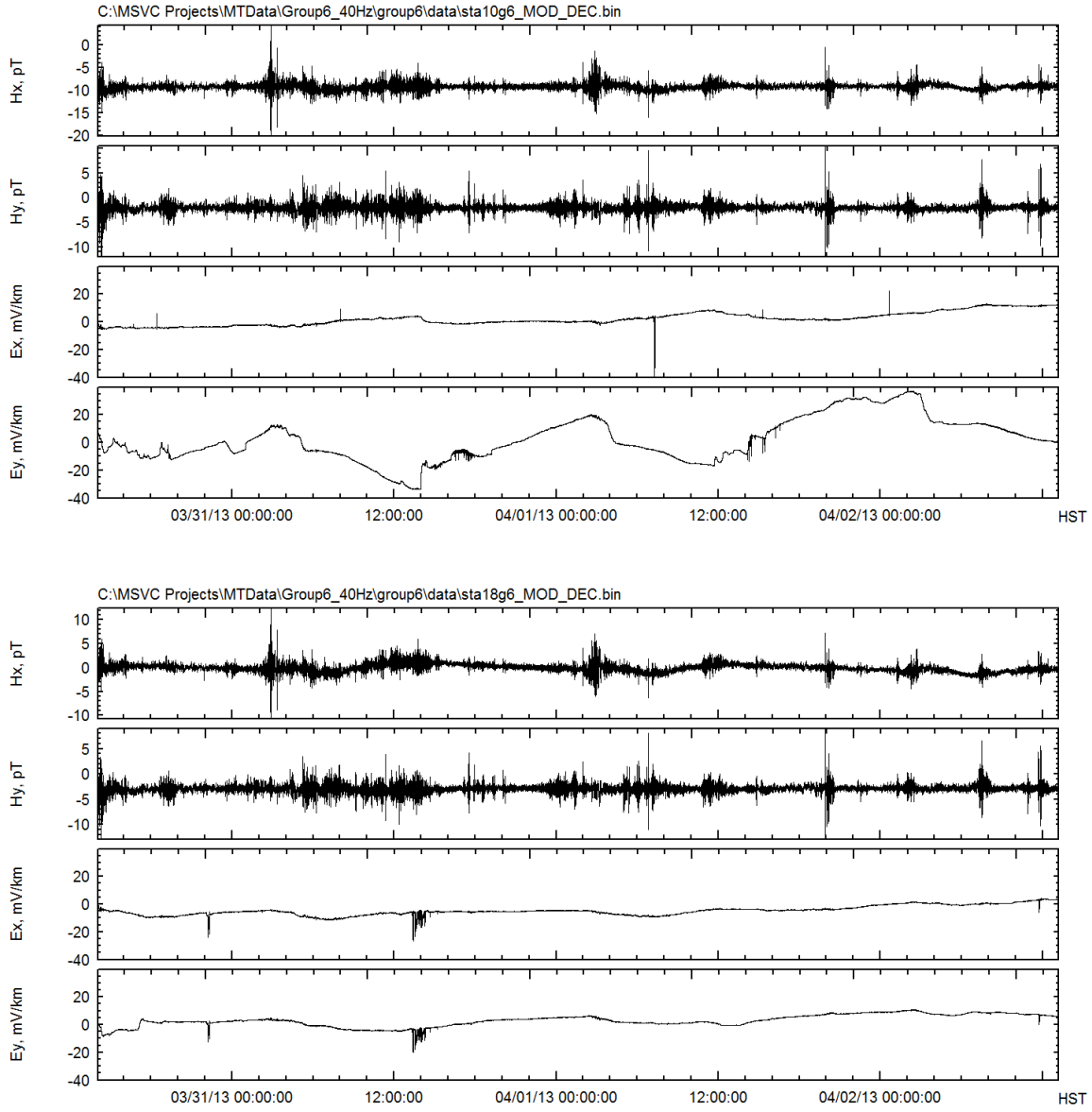

Figure 2.2.4 Upper panel is E- and H-field data recorded over a 72 hour time interval at sta10; lower panel is field data for sta18 for the same interval. Time code is Hawaii Standard Time (HST).

Spike Identification

As is evident from the above time domain plots of the data records, a dominant feature of the data for the Kilauea summit region is the presence of short-duration spikes. One possible source of the observed spikes is sferics, which are pulses of energy 1-2 mS long, generated by lightning, and can travel thousands of km in the earth's ionosphere [Ohkubo et al., 2005; Bianchi and Meloni, 2007]. They are generated about 100 times per second worldwide and their dominant source regions are in central Africa, Southeast Asia and Central America [Levy et al.,, 1996], i.e. at least 4000 km from Hawaii. There are, however, studies that have inferred a

relationship between the spike activity and volcanic/geologic processes associated with eruptive activity [Enomoto, et al., 2006]. Because we suspect that the spikes may be contributing to the poor coherence of the MT data in the frequency range from 0.1-1 Hz a significant effort was invested into their analysis and developing an understanding of sources, and relevance to the hydrothermal/volcanic processes occurring at the Kilauea summit.

Using a routine *FindPeaks* , which was written for *MTPlot*, we examine approximately 2 hours of MT data (sampling frequency = 1 kHz) from Kilauea station 9, re-sampled at 25 samples/sec. The identified spikes are marked by red vertical lines in Figure 1.2.8, above. The occurrence times of peaks located in the Ex channel were used to obtain the simultaneous amplitude of Ey. The Ex and Ey components were then used to calculate the horizontal direction of the E field component and its amplitude. To remove spikes that were correlated with orthogonal H-fields, Ex amplitudes that were less than the Hy amplitude (in pT) were not used. For typical apparent resistivities estimated beneath the Kilauea MT sites, this corresponds to a factor of 10-50 above the MT E-field induced by the H-field.

Figure 2.2.5 shows the directions and amplitudes for the spikes in Figure 1.2.8 satisfying these criteria. They indicate a polarization direction close to the direction of Halema'uma'u caldera, which was active at the time these measurements were made. The same analysis was then performed on the three other Kilauea sites that were operating in the same time interval. The results are plotted in Figures 2.2.6, 2.2.7 and 2.2.8.

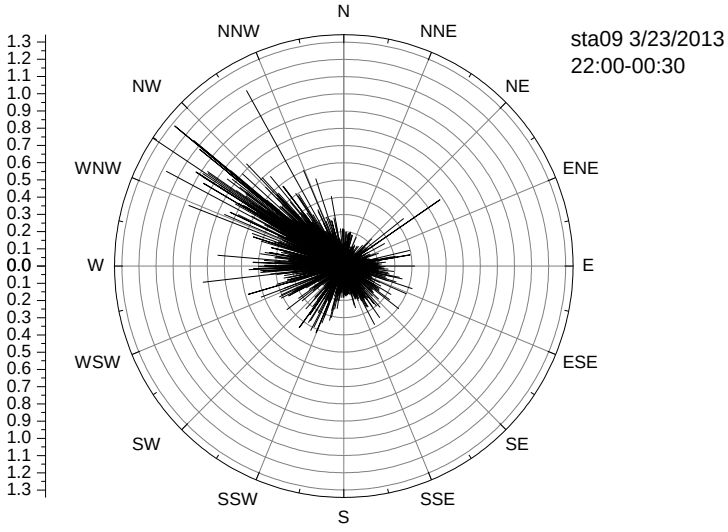

Figure 2.2.5 Polar plot of E-field spike amplitudes (mV/km) and directions (degrees from N) for *sta09*

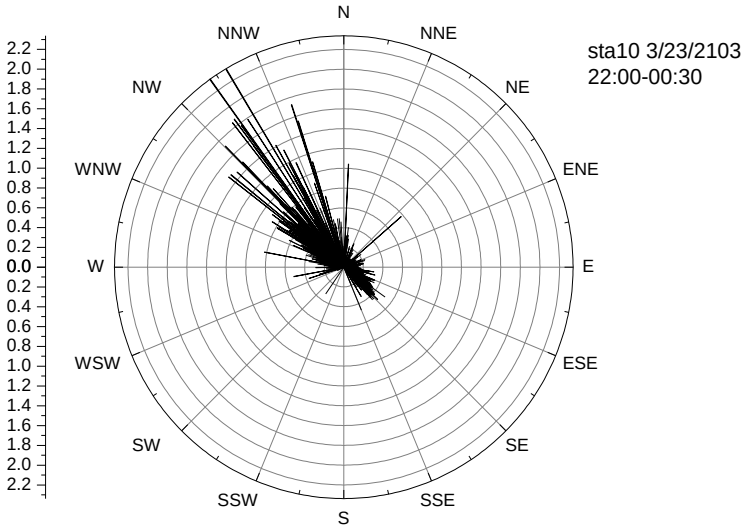

Figure 2.2.6 Polar plot for *sta10.*

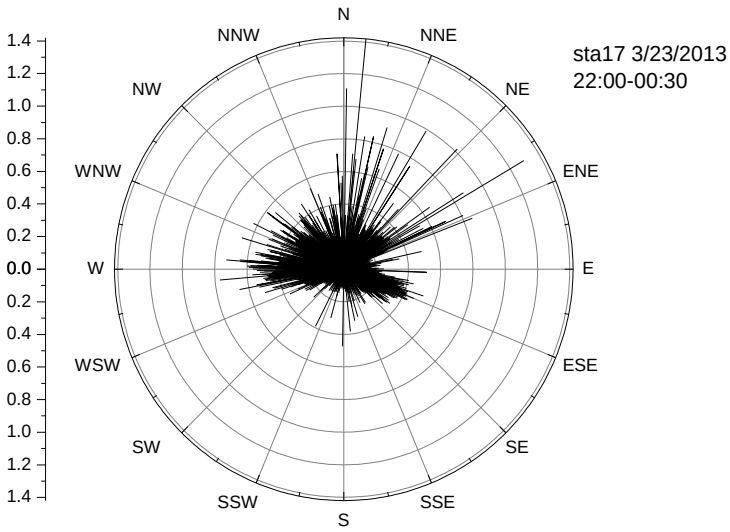

Figure 2.2.7 Polar plot for *sta17*.

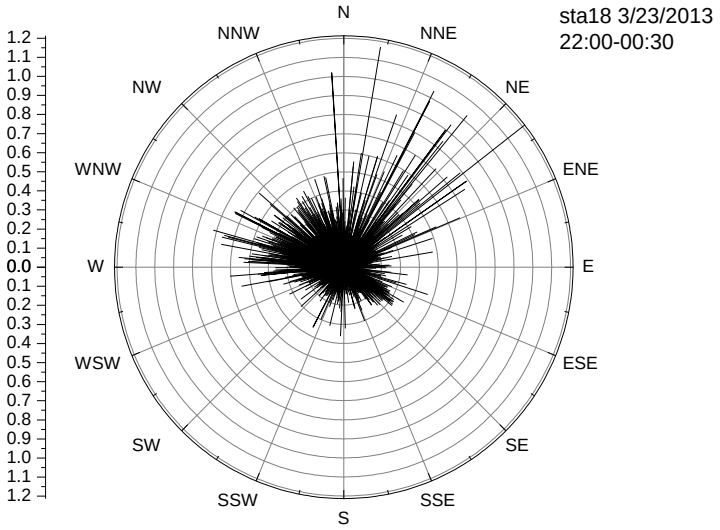

Figure 2.2.8 Polar plot for *sta18.*

The plots in Figures 2.2.5 – 2.2.8 indicate that, although there is considerable scatter in some of the stations, there is a clear directionality to the spike orientations with those spikes having the largest values (>0.6 mV/km) all pointing towards Halemaʻumaʻu crater.

To better visualize the spike identification results, they are plotted as rose diagrams on the Kilauea Summit map in Figure 2.2.9. All four sets of directions are consistent with a source at Halemaʻumaʻu crater. The directions at *sta10,* the site closest to Halemaʻumaʻu are very well grouped and also have double the amplitude of those at the more distant sites. *Sta10* is proximal to the magma conduit feeding Kilauea's East rift zone, and the spikes align with the azimuth of the conduit. We also note that sta10 is thought to be directly over the magma conduit that feeds the Kilauea East Rift zone [D. Swanson, Hawaiian Volcano Observatory, pers. comm.]

We conclude that although our initial analysis suggested that the spikes that are present in both E and H-fields were due to sferics, spikes that do not show a correlation between E and H may be due to volcanic activity. These spikes are of short duration and are unlikely to be associated with fluid flow; their orientation, however, does indicate that they may be associated with some aspect of volcanic activity at Kilauea's summit crater. We believe that the most likely process responsible for these observations is the degassing process occurring within Halemaʻumaʻu: Buttner et al. (1997, 2000) studied lava fragmentation in molten lava under laboratory and field conditions that showed strong E-field pulses of 1 msec. or less duration generated by explosive degassing of magma. Similar E-field pulses were observed by Enomoto et al. (2006) at Mt. Usu during explosive eruptive episodes. Though these data are not demonstrably related to the objective of the current study, these

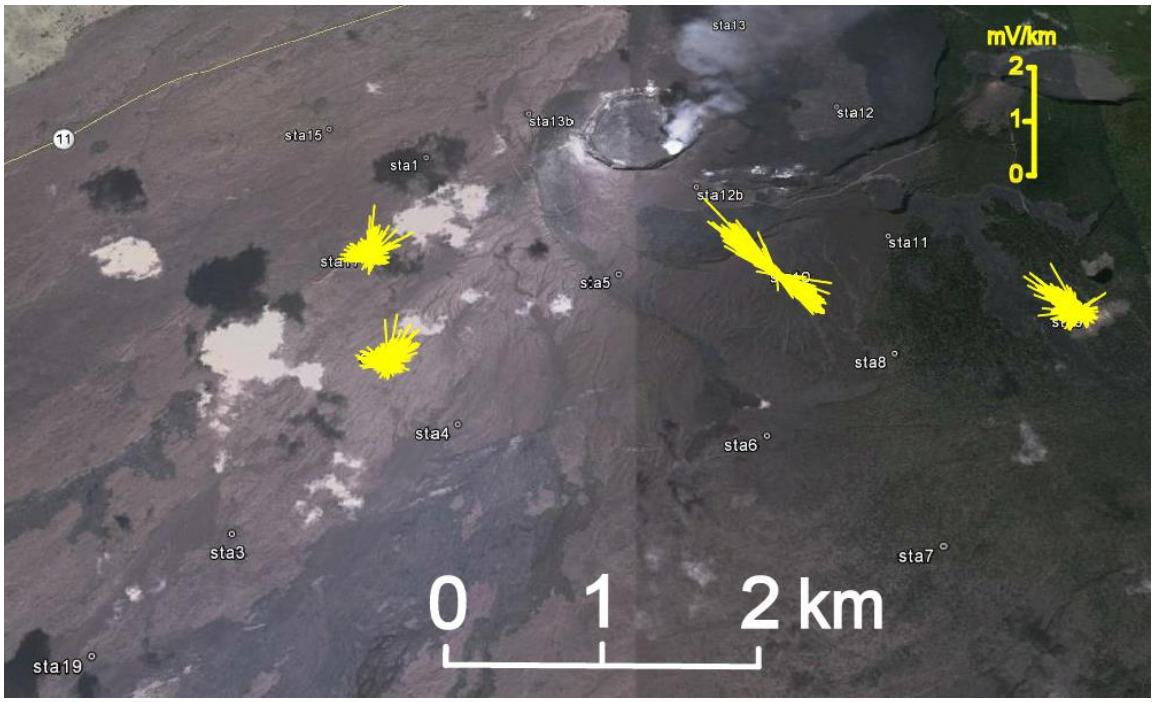

Figure 2.2.9 Rose diagrams (yellow lines) for E-field directions for spikes recorded between 3/23/13 22:00 to 3/24/13 00:30 on the summit of Kilauea.

findings demonstrate the value and power of this software to screen data for the variety of processes that are occurring in a geothermal or volcanic environment and to assist in resolving questions regarding anthropogenic interferences that could impact the interpretation of the MT or Spectral SP signals under analysis.

2.3 Analysis of Lower Puna data

As noted previously, our MT data collection program for Puna was severely impacted by field and environmental conditions as well as significant delays in gaining access to some areas of interest where thermal activity was known to exist. As data was gathered and pre-processed we also found that the data quality was severely impacted by environmental conditions: Figure 2.3.1 shows a data record for starcc2 for a period of approximately 72 hours. There are several notable characteristics: there is a strong diurnal variability in high frequency noise that begins in the early morning hours and continues for much of the day; further, there are significant blocks of time during which one or both of the electrode pairs show significant deviations from the diurnal trend. Although this station is reasonably well removed from the Puna population center of Pahoa, it is surrounded by small residential farm lots and, hence, we believe that the high frequency noise that we are seeing in this record is derived from anthropogenic noise associated with individually grounded domestic power systems. The longer term deviations in E-field are

consistent with SP variations but, in the present case, the most likely explanation for the observed deviations are rainfall events: the region received several tens of mm of rainfall during this interval and, unlike continental environments, precipitation in this area frequently consists of relatively brief intervals of, sometimes intense, rainfall followed by periods of clear skies. Although other Puna stations showed less noisy responses (Figure 2.3.2), evidence of rainfall effects were evident there as well. The result of the anthropogenic and environmental noise on the analysis of these data sets is evident in the apparent resistivity and phase curves shown in Figures 2.3.1. and 2.3.2. Efforts to preprocess and conduct frequency domain analysis of the Puna data have so far proved unsuccessful and will require substantially more effort to filter and characterize the non-MT induced E-field variations and work is continuing on this effort.

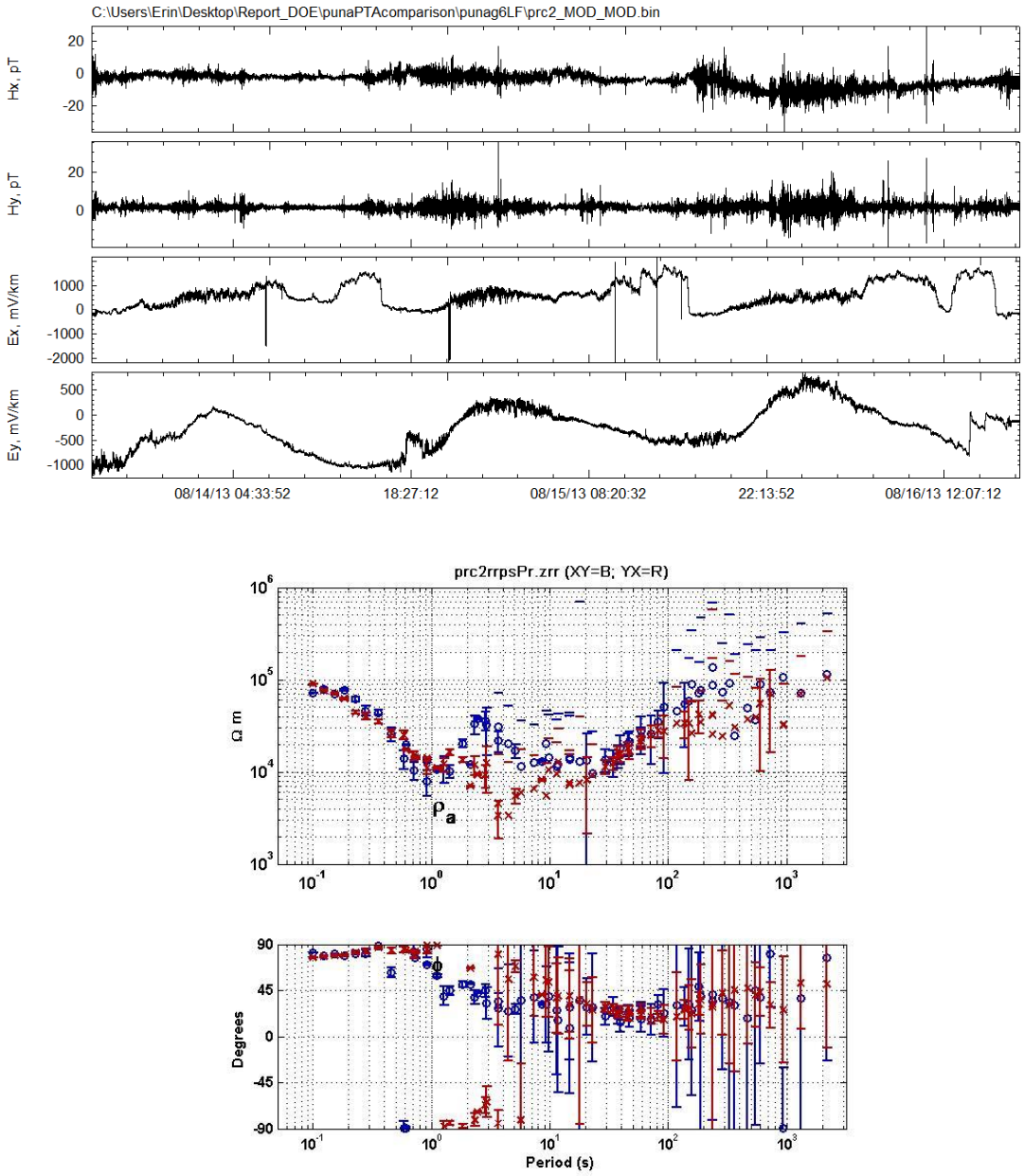

Figure 2.3.1 Upper Panel is time series for Puna station rcc2 acquired with Puna group 6. Time code is UTC or Hawaii Standard Time plus ten hours. Lower panel is unedited apparent resistivity and phase for starcc2.

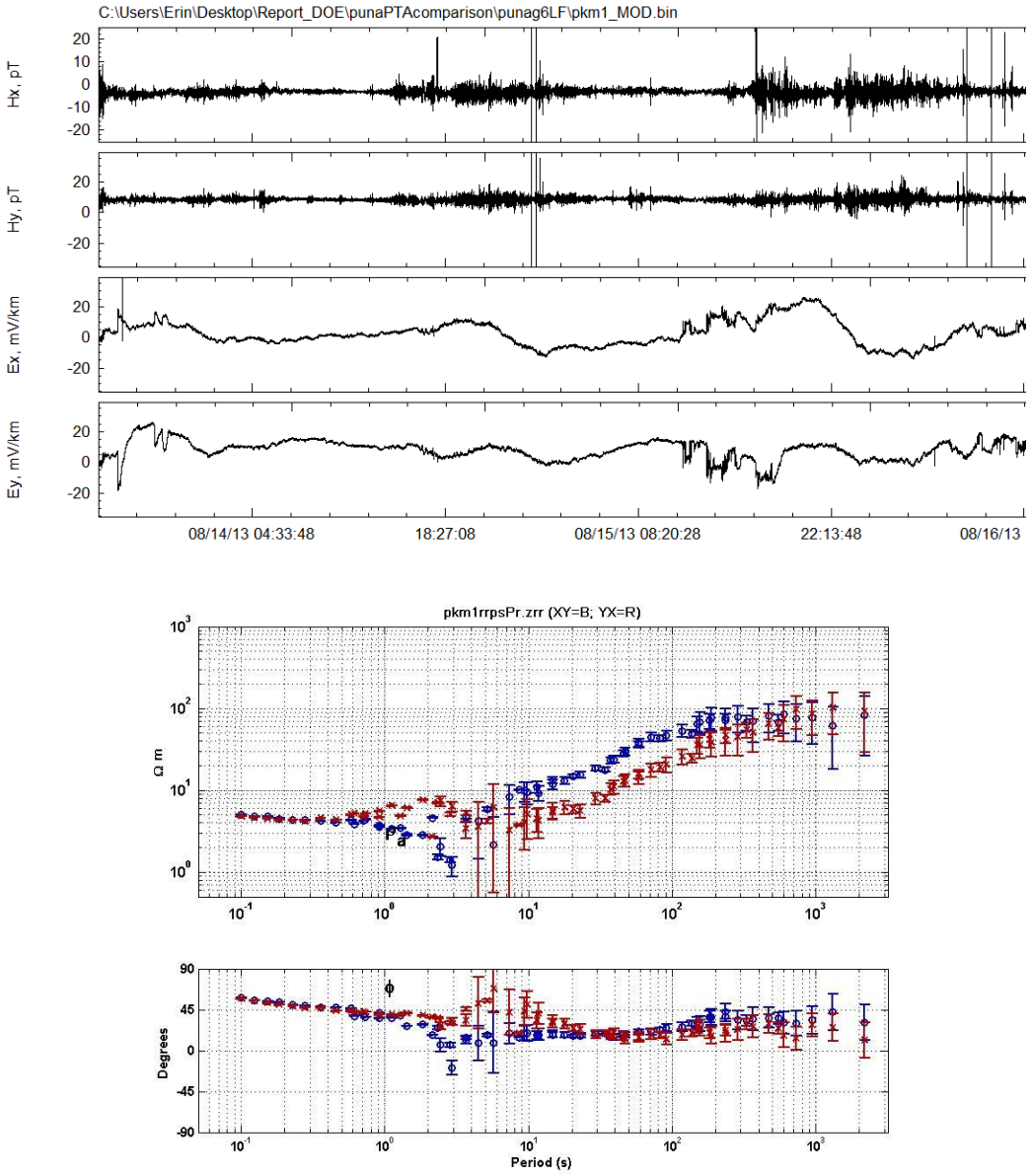

Figure 2.3.2 Upper panel is time series for Puna station station km01 acquired with Puna group 6. Lower panel is the unedited apparent resistivity and phase for the timeseries in the upper panel.

3. CONCLUSIONS

The reanalysis of the 2002 Kilauea data set using the Robust Multivariate Errors in Variables (RMEV) analysis was completed and did show limited evidence of Spectral SP signals

in the original data set (Appendix NN). Those findings were substantially enhanced by the new suite of data collected as part of the Phase I work: RMEV analysis of the Kilauea 40 Hz MT data shows canonical correlation and coherency characteristics that are interpreted to be evidence for Spectral SP signals at stations 12, 13, 4, 18 and 19, and to a lesser extent at 6, 7, 8, and 11, but are less evident at 9, 10, and 17.

In order to efficiently process the KMS data output, we developed specialized software that could ingest the KMS data and allow us to pre-process it prior to applying the RMEV analysis; this effort proved to have an ancillary, and no less valuable, benefit of enabling us to critically evaluate the time-domain data and make more robust inferences about the source of the non-MT induced signals that were presenting in the E-field data. With *MTPlot* we were able to distinguish among: unrelated interferences (sferics and anthropogenic noise); purely volcanogenic processes (E-field spikes generated by fragmentation processes); possible environmental effects (temperature or rainfall influences on the electrodes); and what we believe are Spectral SP signals generated by subsurface flows induced by volcanic/deformation processes occurring at the Kilauea summit.

We have also observed that the apparent resistivity curves from Kilauea are markedly different from those at Puna with noisy and unrealistically high estimates that extend beyond the the periods of the MT deadband. We believe this may be due to proximity to the Kilauea Summit, caldera and shallow rift zones. The geology of the Summit region, the dilatational and compressional perturbations that exist in the presence of magma movement can create fluid movement. We suspect that some of the signals we see in our data are due to volcanic tremor events. This is due to the periods at which we see these spurious signals. Scale of movement inharmonic tremor.

Complete elucidation of these multiple processes, although of interest, is not the purpose of the present study and has not been fully explored. But we believe that we have demonstrated that the Spectral SP signals can be identified using the RMEV approach and can be characterized in the time domain data sets using the *MTPlot* software package that we developed.

Our accomplishments in the Puna geothermal field were more limited: we were able to collect data from a suite of stations over previously unexplored sections of the middle east rift and the flanks of the rift zone. However, we encountered extremely difficult field conditions, limiting our access to the undeveloped areas of the rift, and to high levels of anthropogenic electrical noise in areas where residential development enabled access. Environmental conditions – high rainfall in particular – also limited the success in recovery of multiple sets of simultaneous field data for the RMEV analysis. Analytical work is continuing on this data set, but, as will be discussed below, we believe that other data sets that are now available to us will provide greater probability of success in further analyzing the spectral SP signals.

4. PROJECTED PLANS FOR FUTURE WORK

Substantial progress was made on the overall goals that were originally proposed for this project: our primary objective was to demonstrate that we can identify Spectral SP signals in an MT data set using Egbert's multivariate analysis approach. Reprocessing of the 2002-2003 Kilauea summit data identified coherency and correlation coefficients that were consistent with Spectral SP at a few locations and the collection and analysis of new Kilauea summit data under the present project have identified several other sites where Spectral SP can be inferred; further, we have developed time domain analytical tools that also allow us to better characterize the Spectral SP signals and segregate those most relevant to fluid flow and those that are not. Our efforts in Lower Puna were less successful due to difficult environmental conditions, access issues, and higher than expected levels of anthropogenic noise. Substantial additional analysis of the Puna data will be required in order to segregate environmental and anthropogenic signals from those relevant to Spectral SP and we anticipate continuing that analytical work.

The work plan for Phase II, as originally proposed, was to undertake Spectral SP surveys in three of four other prospective geothermal areas in Hawaii: a Mauna Kea rift zone suspected to be present based on previously conducted MT surveys; Hualalai west flank; Haleakala; and the Mauna Loa Southwest rift. That work was intended to set the stage for follow-on work, under other funding, to undertake a drilling program into one of the favorable prospects, based on the MT/Spectral SP data, to develop ground truth for the subsurface permeability structure and define the relationship between the Spectral SP analysis and subsurface permeability.

However, during the time of the Phase I work, a concurrent project on Mauna Kea has provided us with new information on the geothermal potential there as well as an opportunity to move ahead more rapidly on the project goals. The Principal Investigator was awarded a project through the Cooperative Ecosystems Study Unit, managed by the Army Corps of Engineers, to conduct an assessment of groundwater resources on the southwest flank of Mauna Kea. That project has drilled the first of two continuously-cored observation holes that showed both substantial groundwater resources as well as much higher geothermal gradients (~165 C/km) at depth than had been previously suspected. Recently published gravity data suggests that this area is one of the two dominant dike complexes of Mauna Kea and would be a productive area in which to focus our Spectral SP work for Phase II. Further, there will be a second test hole, to a nominal depth of ~1.5 km to 2 km (depending on the deep temperature gradient), which will be drilled (funding is in hand and permits have been secured) in an area that would be appropriate to conduct our ground-truth testing of the Spectral SP analysis. MT surveys conducted in this region as part of that work show extremely good data quality, Figure 4.1.1, with minimal anthropogenic noise, as well as evidence of Spectral SP signals (Figure 4.1.2). Hence, we would propose to focus our efforts in this region as one of our three Spectral SP survey areas. The other two areas that would provide the most valuable data would be Hualalai's rift systems and that of Haleakala as originally proposed.

We also believe that our efforts will be assisted through an expansion of the expertise on the project team. Due to the challenges in processing and analyzing of the KMS data, we brought Dr. Lienert onto the project team and he was able to develop the *MTPlot* software package and assist in the analysis

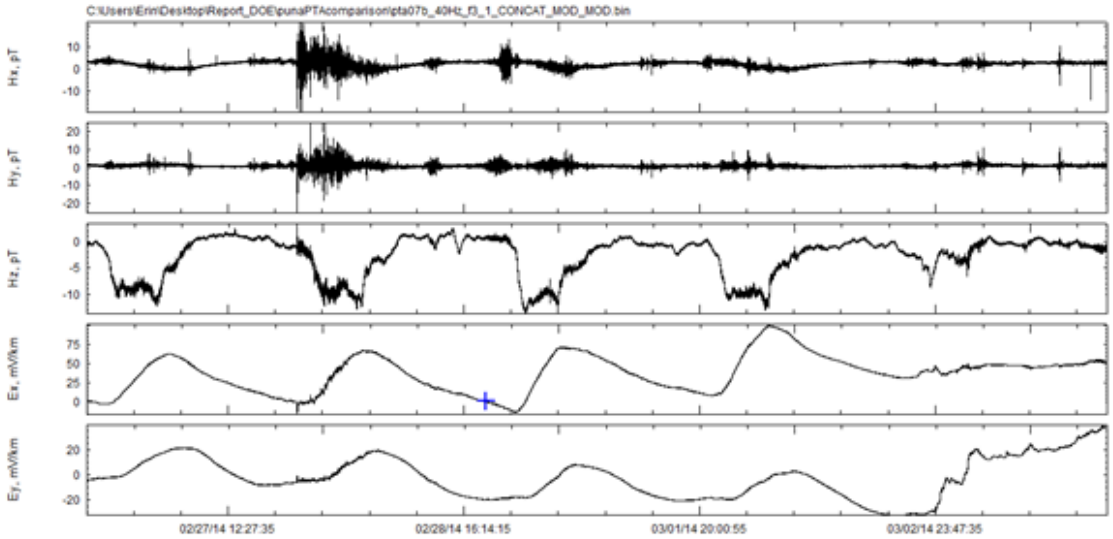

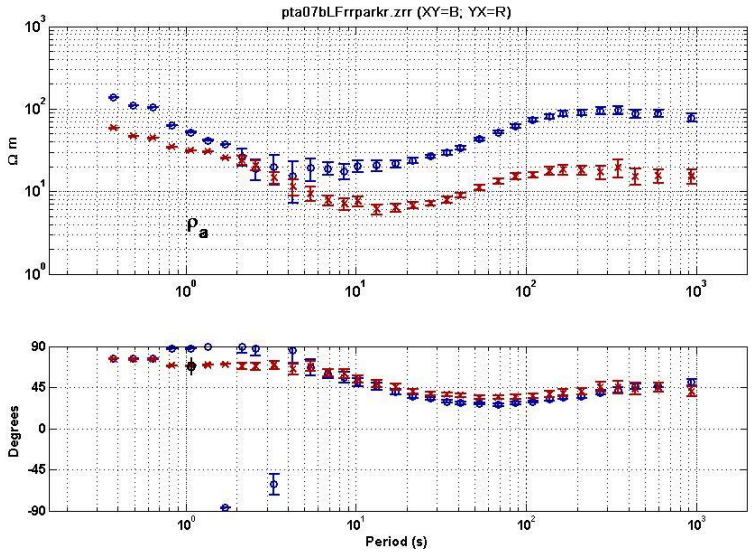

Figure 4.1.1 Upper panel is time series for PTA station pta07b. Time code is UTC or Hawaii Standard Time + 10 hours. Ex and Ey fields are much more regular than anything found in Puna. Lower panel is the unedited apparent resistivity and phase for the timeseries in the upper panel and shows much more stable computed values.

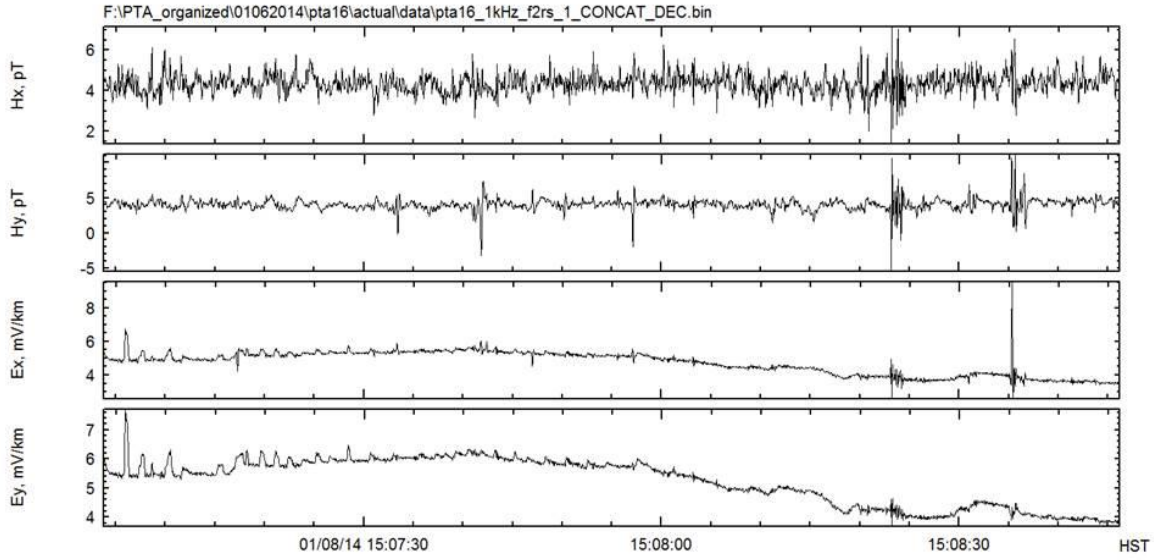

Figure 4.1.2 Time series for PTA station pta16 showing variations that are similar to our time domain observations at the Kilauea summit. Analysis of these signals is continuing.

of the underlying physics and mathematics of processing the data. We would anticipate having him continue as a member of our research team into the second phase of work. With the application of Egbert's code to this technology, we also encountered some uncertainties in the details of the multivariate analysis that may prove to be important in the overall application of this method; although we could, with the current project team, resolve those, we believe that it would be more efficient if we could involve Dr. Egbert to some degree in our efforts. Further, we have been pursuing an informal collaboration with Dr. Andre Revil, at Colorado School of Mines, in the characterization of the physical and electrical properties of the basaltic formations recovered in our initial borehole. We would like to explore the possibility of involving him in undertaking a detailed modeling exercise that would incorporate the physical and electrical properties of the core recovered from the new borehole along with the results of the MT and Spectral SP monitoring data collected.

We believe these proposed changes in approach for Phase II of our project work will yield substantially greater advancement in our analysis of the Spectral SP data and its application to mapping subsurface permeable structures.

5. ACKNOWLEDGMENTS

This work was funded by the US Department of Energy, Geothermal Technologies Office under FOA522_5517. We would also like to thank Hawaiian Volcanoes National Park Natural Resources Management and Hawaiian Volcano Observatory for arranging access, Don Swanson for escorting us during the Kilauea Summit MT survey, and the private landowners who allowed access to MT Sites in Lower Puna.

6. REFERENCES

Anderson, L.A., 1985, Self-potential investigations in the Puhimau thermal Area, Kilauea Volcano, Hawaii, *Geophysics*, **50**(2):274

Battaglia, J. K. Aki, and V. Ferrazzini, 2005, Location of tremor sources and estimation oflava output using tremor source amplitude on the Piton de la fournaise volcano: 1. Location of tremor sources, J. *Volcanology and Geothermal Research*, **147**, 269-290.

Bianchi, C. and A. Meloni, 2007, Natural and man-made terrestrial electromagnetic noise: an outlook, *Annals of Geophysics*, **50**, 3, pp 435-445.

Blackman, R.B. and J.W. Tukey, 1959, *The Measurement of Power Spectra, from the Point of View of Communications Engineering*, New York: Dover Publications.

Büttner, R., H. Röder, and B. Zimanowski, 1997, Electrical effects generated by experimental volcanic explosions, *Appl. Phys. Lett.*, 70, 1903-1905.

Büttner, R. and B. Zimanowski, 2000, Short-time electrical effects during volcanic eruption: Experiments and field measurements, *J. Geophys, Res*., 105, 2819-2827, 2000

Caldwell, T.G., H.M. Bibby, and Brown, C., 2004. The magnetotelluric phase tensor, *Geophys. J. Int*., **158**, 457-173.

Chouet, B., and P. Dawson, 2013, Very long period conduit oscillations induced by rockfalls at Kilauea Volcano, Hawaii, *J. Geophys. Res*., **118**, 5352-5371, doi:10.1002/jgrb/50376,2013.

Dzurisin, D., 1980, Influence of fortnightly earth tides at Kilauea volcano, Hawaii. Geophys. Res. Lett., 7, pp. 925–928.

Egbert, G.D., and J.R. Booker , 1989, Multivariate analysis of geomagnetic array data: 1. The Response Space, *J. Geophys. Res*., **94**, B10, pp 14,227-14,247.

Egbert, G.D. (1997), Robust multiple-station magnetotelluric data processing, *Geophys J. Int*., **130**, 475-496.

Enomoto, Y., Hashimoto, H., Shirai, N., Murakami, Y., Mogi, T., Takada, M., & Kasahara, M. (2006). Anomalous geoelectric signals possibly related to the 2000 Mt. Usu eruption and 2003 Tokachi-Oki earthquakes. *Physics and Chemistry of the Earth, Parts A/B/C*, *31*(4), 319-324.

Fitterman, D.V., 1978, Electrokinetic and magnetic anomalies associated with dilatant regions in a layered earth. *J. Geophys. Res*., **83**:5923-5928.

Friedel, S., 2005, Can subsurface water flow be sensed magnetically? Results from electrokinetic volcano simulations, *COMSOL Multiphysics User's Conference*, Frankfurt, Germany.

Kappler, K.N., 2008, Long-term electromagnetic monitoring at Parkfield, CA, PhD thesis, Univ. of calif., Los Angeles.

Kappler, K.N., H.F. Morrison, and G.D. Egbert (2010), Long-term monitoring of ULF electromagnetic fields at Parkfield, California, *J. Geophys. Res*., **115**, B04406, doi:10.1029/2009JB006421

Konstantinos, I.K., and V. Schlindwein (2002), Nature, wavefield properties and source mechanism of volcanic tremor: a review, *J. of Volcanology and Geothermal Research*, **119**, 161-187

Levy II, H., W.J. Moxim, and P.S. Kasibhatla, 1996, A global three-dimensional time-dependent lightning source of tropospheric NO_x, *J. Geophys. Res*., **101**, D17, pp 22,911-22,922.

Maineult, A., E. Strobach, and J. Renner (2008), Self-potential signals induced by periodic pumping tests, *J. Geophys. Res*., 113, B01203, doi:10.1029/2007JB005193.

Marquis, G., M. Darnet, P. Sailhac et al. (2002), Surface electric variations induced by deep hydraulic stimulation: An example from the Soultz HDR site, *Geophys. Res. Lett*., 29(14), 1662, doi:10.1029/2002GL015046.

Murakami, H., Hashimoto, T., Oshiman, N., Yamaguchi, S., Honkura, Y. and Sumitomo, N. (2001), Electrokinetic phenomena associated with a water injection experiment at the Nojima fault on Awaji Island, Japan. *Island Arc*, 10: 244–251. doi: 10.1111/j.1440-1738.2001.00322.x

Okhubo, A., H. Fukunishi, Y. Takahashi, and T. Adachi, 2005, VLF/ELF sferic evidence for in-cloud discharge activity producing sprites, *Geophys. Res. Lett*., **32**, L04812, doi:10.1029/2004GL021943.

Peacock, J. S. Thiel, P. Reid, and G. Heinson, 2012, Magnetotelluric monitoring of fluid injection: Example from an enhanced geothermal system, *Geophys. Res. Lett*. **39**, L18403, doi:10.1029/2012GL53080.

Petzold, C., 1992, *Programming Windows : The Microsoft guide to Writing Applications for Windows* 3.1, Redmond, WA, Microsoft Press.

Poland, M. 2013, Magma supply and storage at Hawaiian volcanoes, *Large Igneous Provinces Commission*, Dec: http://www.largeigneousprovinces.org

Schmucker, U., 1970, *Anomalies of geomagnetic variations in the southwestern United States, Bulletin of the Scripps Institution of Oceanography of the University of California*. Arrhenius et al., ed. University of California Press. IBN:0-520-09318-6

Sims, W.E., F.X. Bostick Jr., and H.W. Smith, 1971, the estimation of magnetotelluric impedance tensor elements from measured data, *Geophysics*, **36**, 5, pp 938-842.

Sottili, G. and D. Palladino, 2012, Tidal modulation of eruptive activity at open-vent volcanoes: evidence from Stromboli, Italy. *Terra Nova*, Vol. 24, Issue 3, pp.233 -237.

van Manen, S. Kervyn, M. Blake, S., Apparent tidal influence on magmatic activity at Oldoinyo Lengai volcano, Tanzania, as observed in Moderate resolution Imaging Spectroradiometer (MODIS) data. *Jour. Vol. Geoth. Res.*, Vol. 189, Issue: 1-2, pp. 151-157**.**

Zablocki, C. J., 1976, Mapping thermal anomalies on an active volcano by the self-potential method, Kilauea, Hawaii. *In Proceedings of the 2nd UN Symposium on the Development and Use of Geothermal Resources Vol. 2*, pp. 1299-1309.

7. LIST OF APPENDICES

A. Comparison of apparent resistivity and phase curves 2002-2003 and 2012-2013
B. Dominant SDM eigenvalues and canonical coherence for 6 hour data segments
C. λ_3 and CC_3 diagnostic results from Kilauea 2012-2013
D. Comparison of Phase Tensor 2002-2003 and 2012-2013
E. λ_3 and CC_3 and λ_4 and CC_4 differences
F. LBNL Analysis from 2002-2003 and 2012-2013

APPENDIX A

Comparison of apparent resistivity and phase curves 2003 and 2012

Figures 1-12 display plots of apparent resistivity and phase from 2002 or 2003 on the left, with plots of results from 2012-2013 on the right. These data were processed using the RMEV method described in the text. Overall the characteristics are similar between the data acquired a decade apart. There are noisier signals that create anomalously high resistivities at periods from .2 to 10 seconds in the 2012 data. In 2002-2003 this range is reduced to .2 to 4 seconds period. Longer period data are typically less noisy in 2012. The 2012 data are processed at a different frequency scale than 2003. Figures 13-14 display plots of apparent resistivity and phase from additional stations collected in 2012-2013.

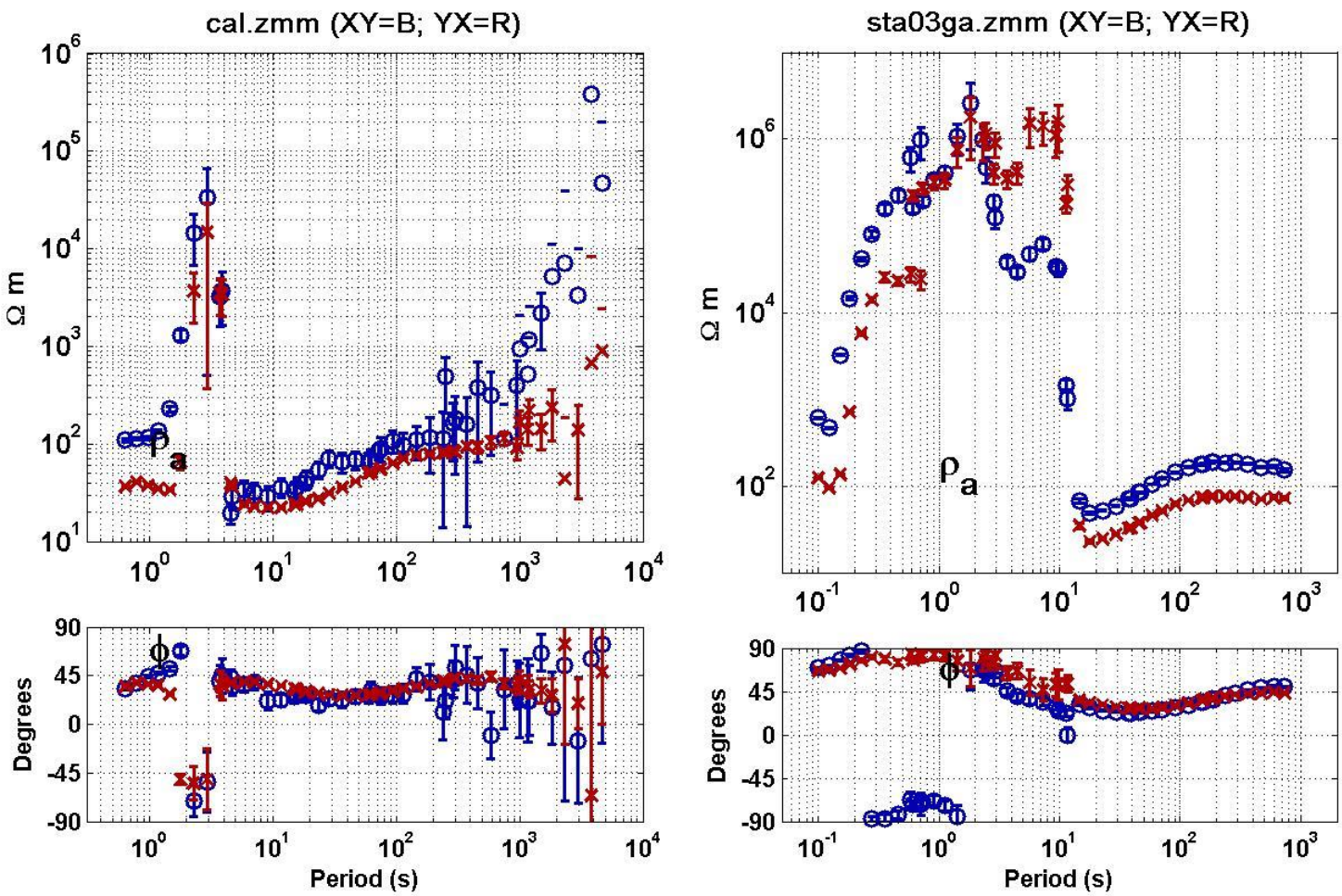

Figure 1 2003 'cal' apparent resistivity and phase from the RMEV method are on left. Apparent resistivity and phase from the RMEV method from collocated 2012 station 03 are on the right.

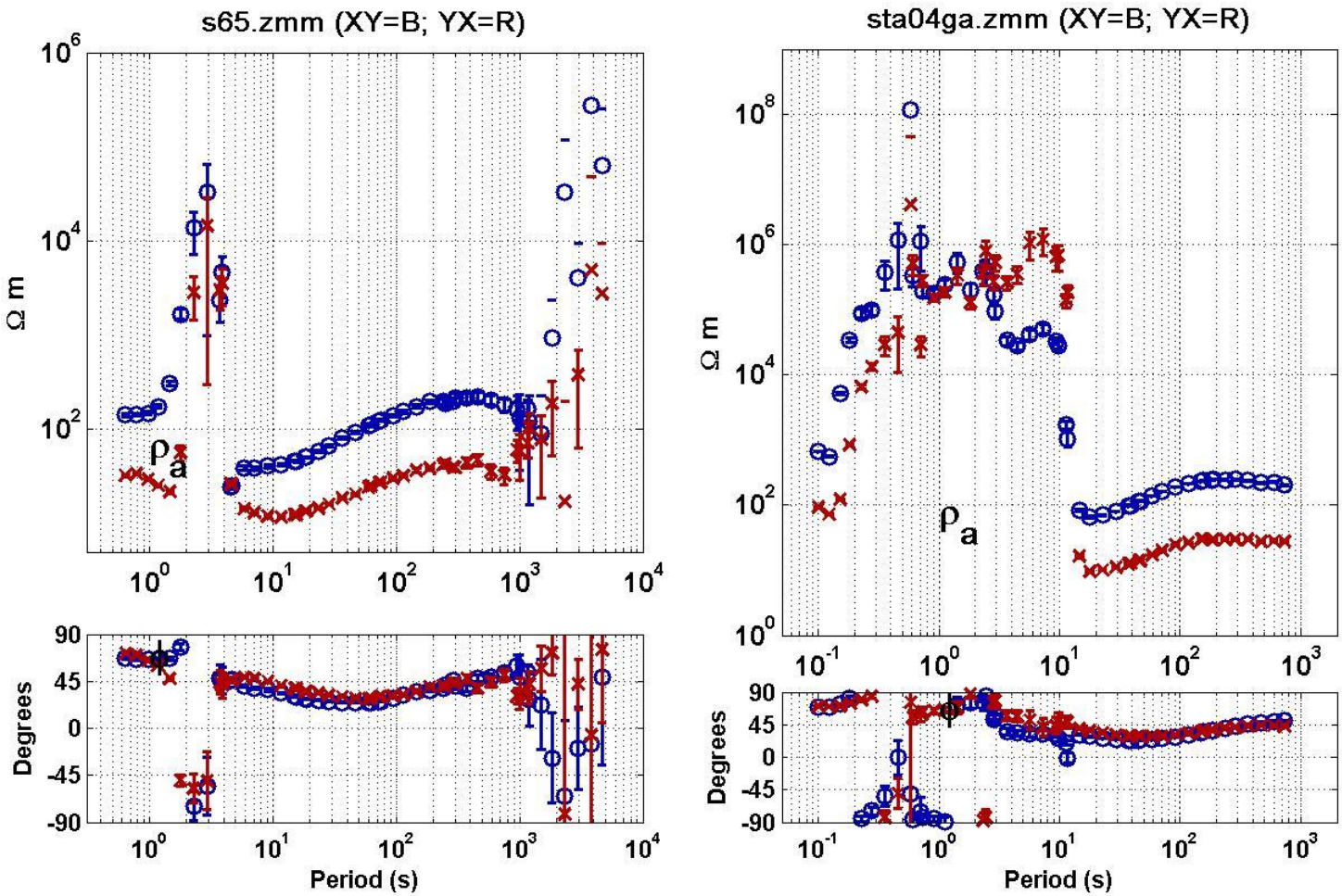

Figure 2 2003 ‘s65’ apparent resistivity and phase from the RMEV method are on left. Apparent resistivity and phase from the RMEV method from collocated 2012 station 04 are on the right.

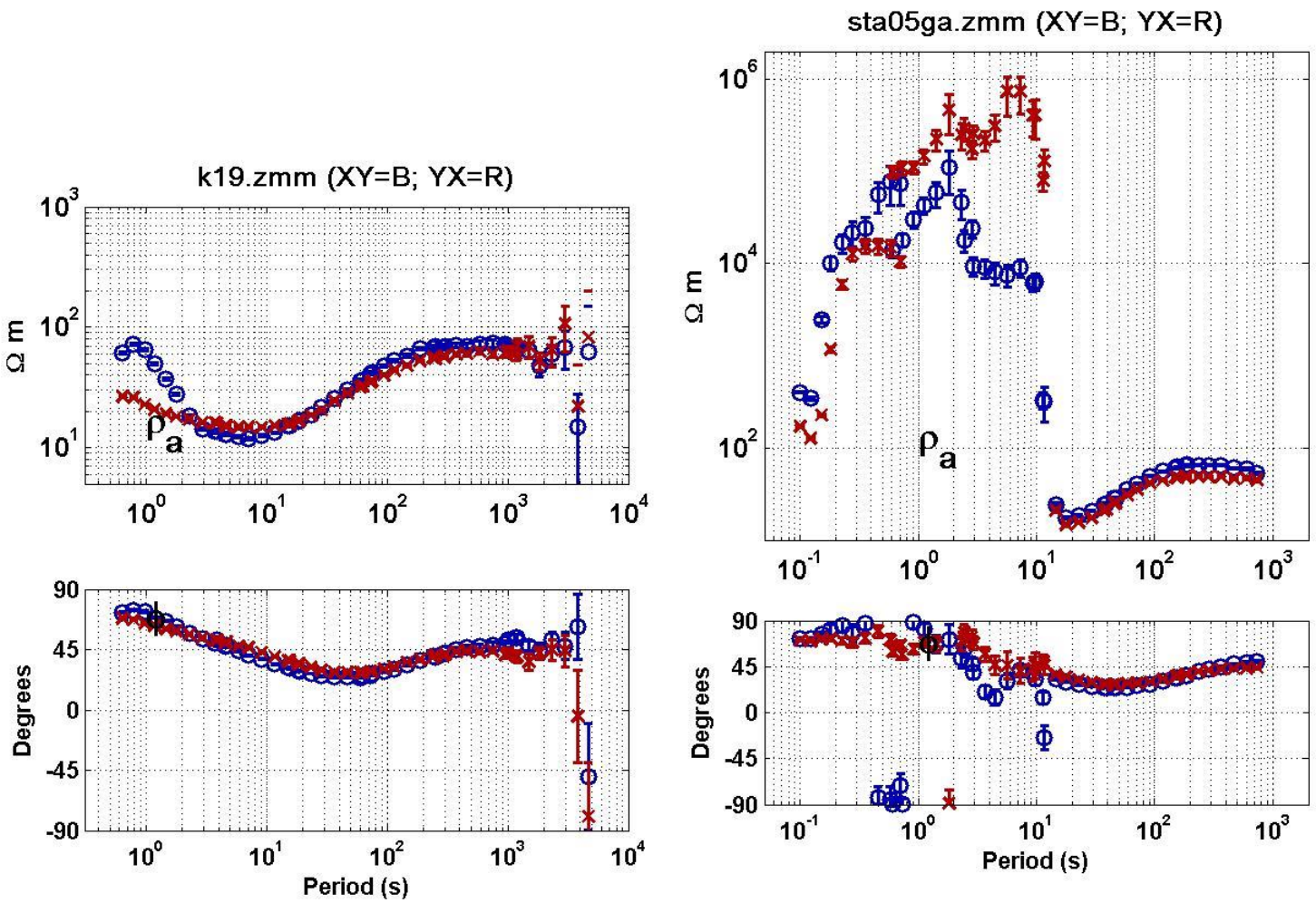

Figure 3 2003 'k19' apparent resistivity and phase from the RMEV method are on left. Apparent resistivity and phase from the RMEV method from collocated 2012 station 05 are on the right.

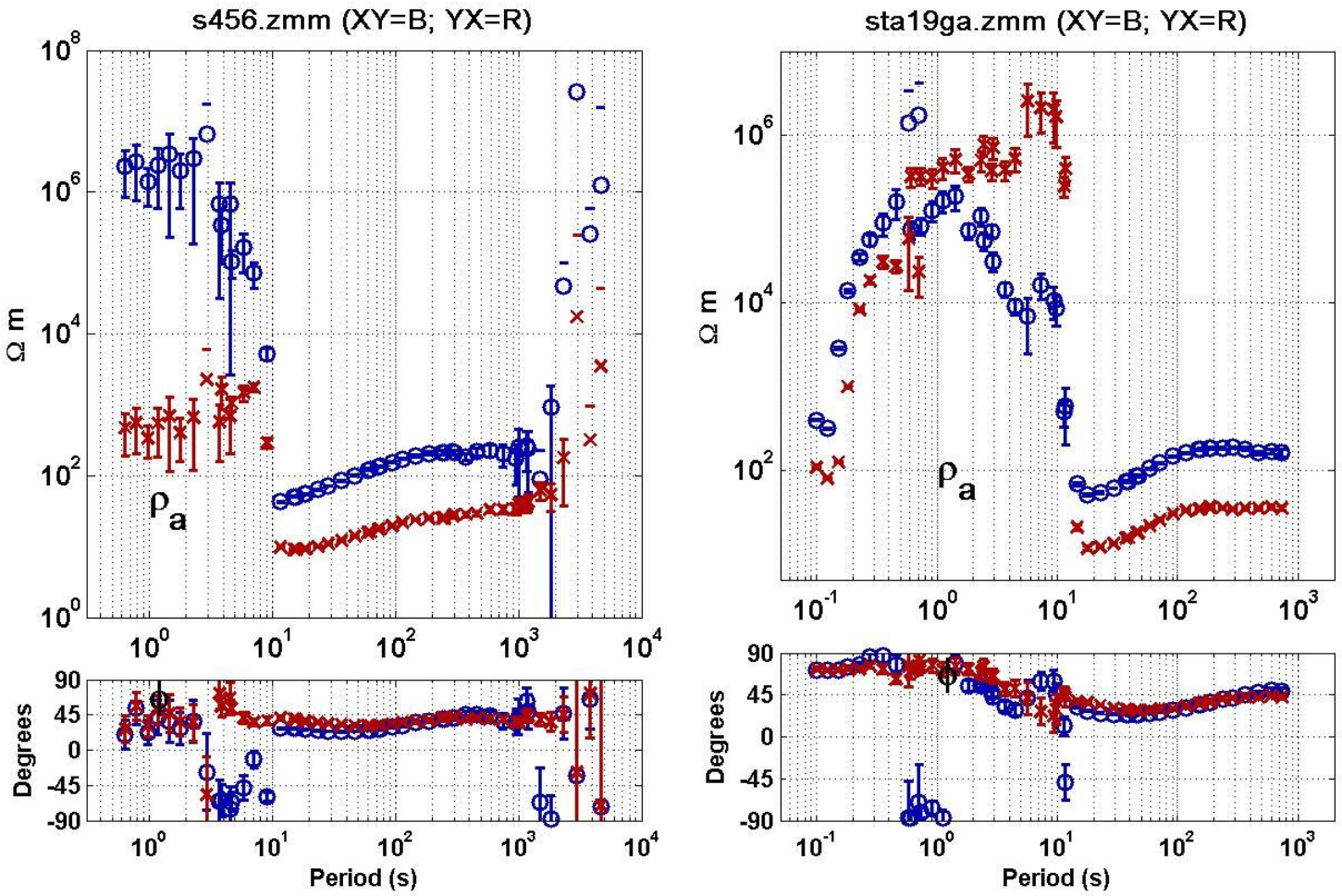

Figure 4 2003 ‘s456’ apparent resistivity and phase from the RMEV method are on left. Apparent resistivity and phase from the RMEV method from collocated 2012 station 19 are on the right.

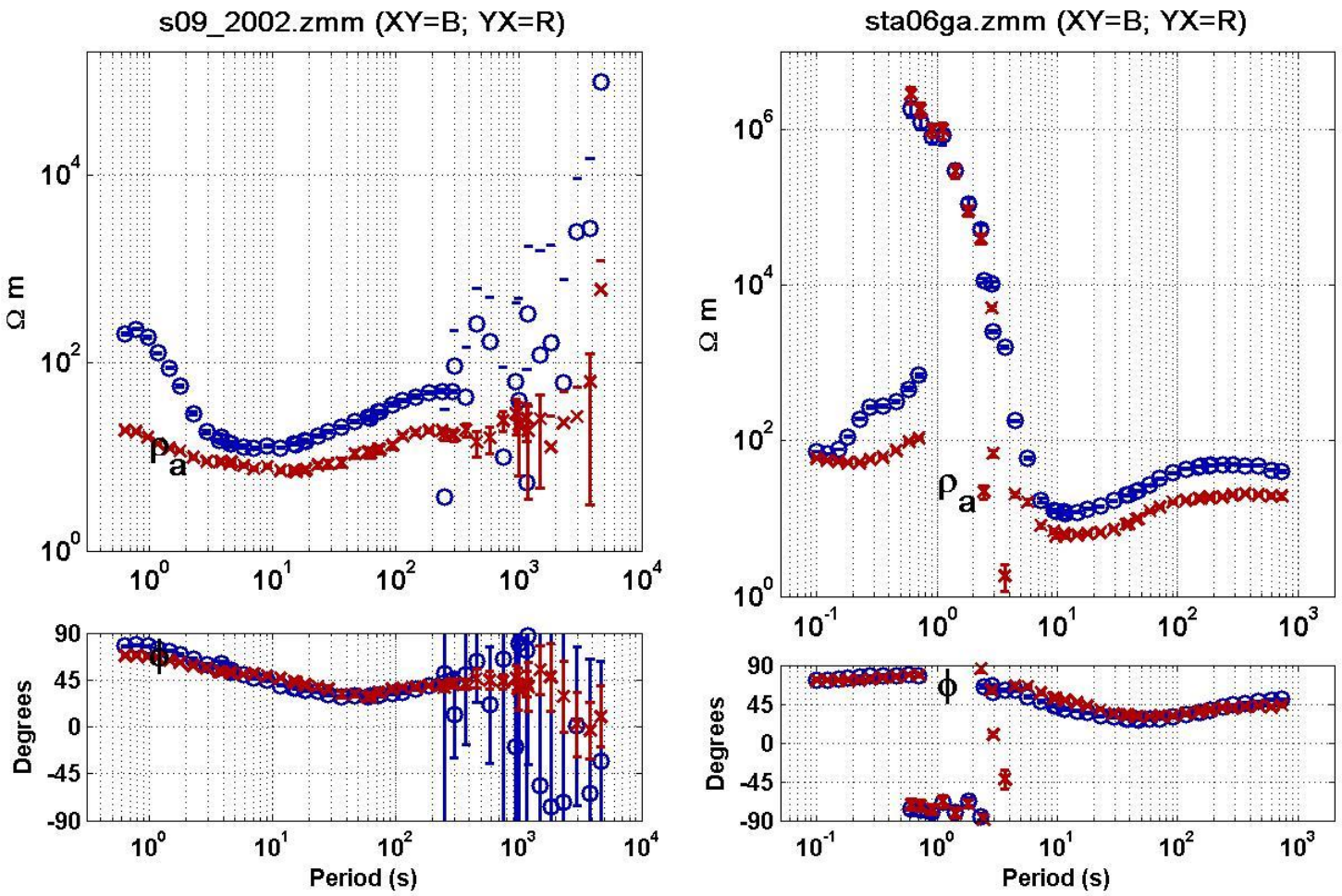

Figure 5 2003 ‘s09_2002’ apparent resistivity and phase from the RMEV method are on left. Apparent resistivity and phase from the RMEV method from collocated 2012 station 06 are on the right.

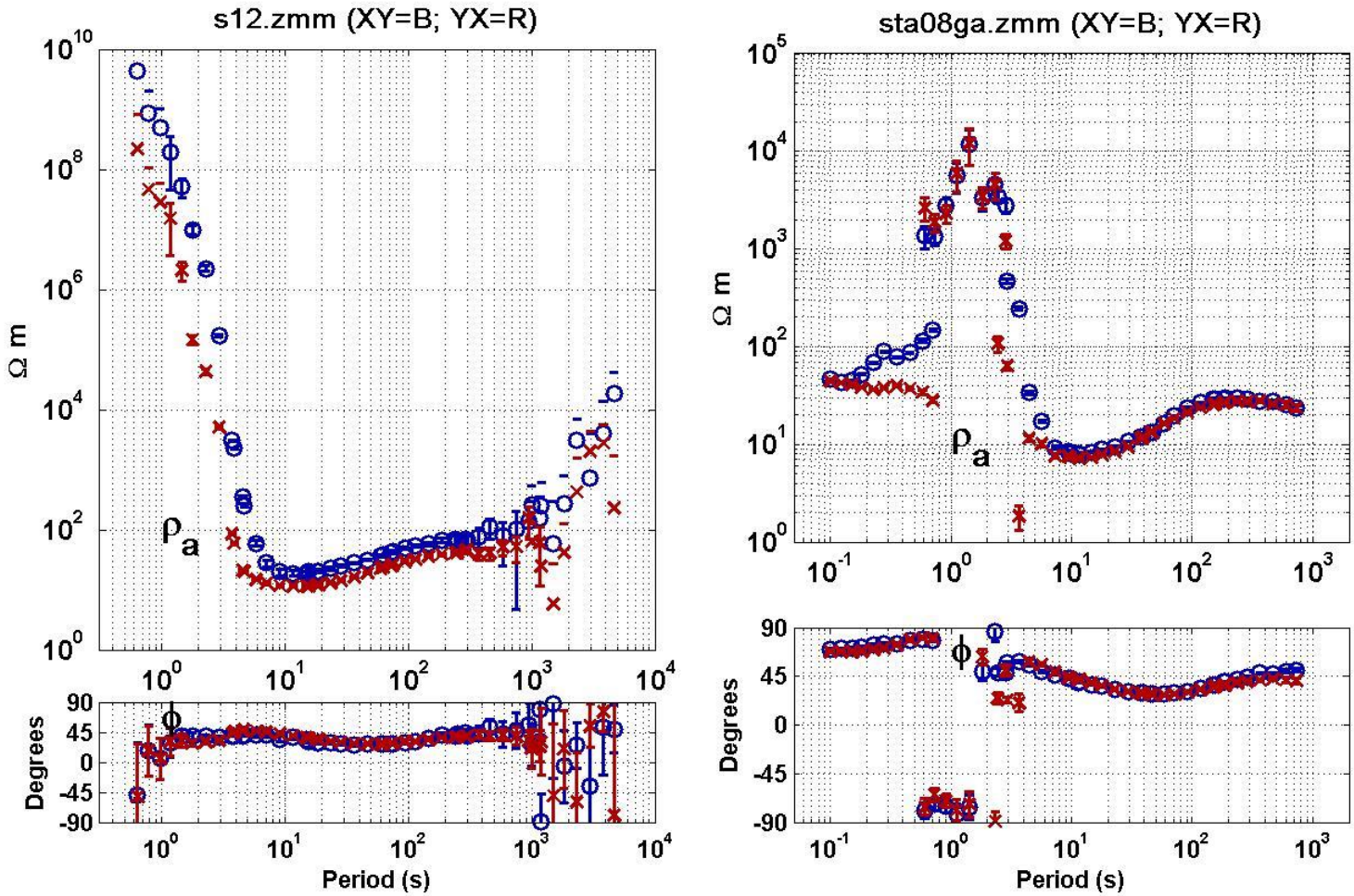

Figure 6 2003 ‘s12’ apparent resistivity and phase from the RMEV method are on left. Apparent resistivity and phase from the RMEV method from collocated 2012 station 08 are on the right.

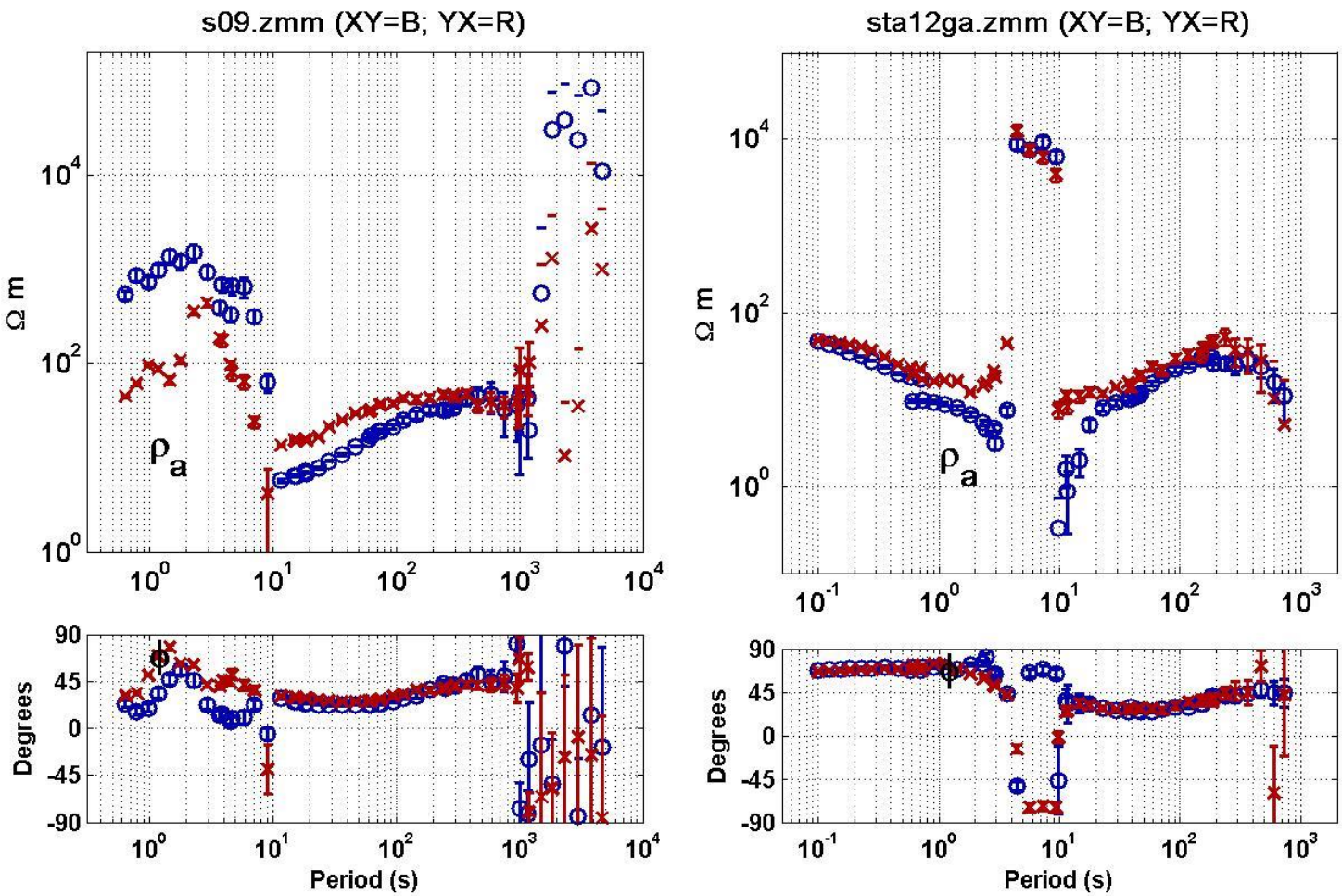

Figure 7 2003 ‘s09’ apparent resistivity and phase from the RMEV method are on left. Apparent resistivity and phase from the RMEV method from collocated 2012 station 12 are on the right.

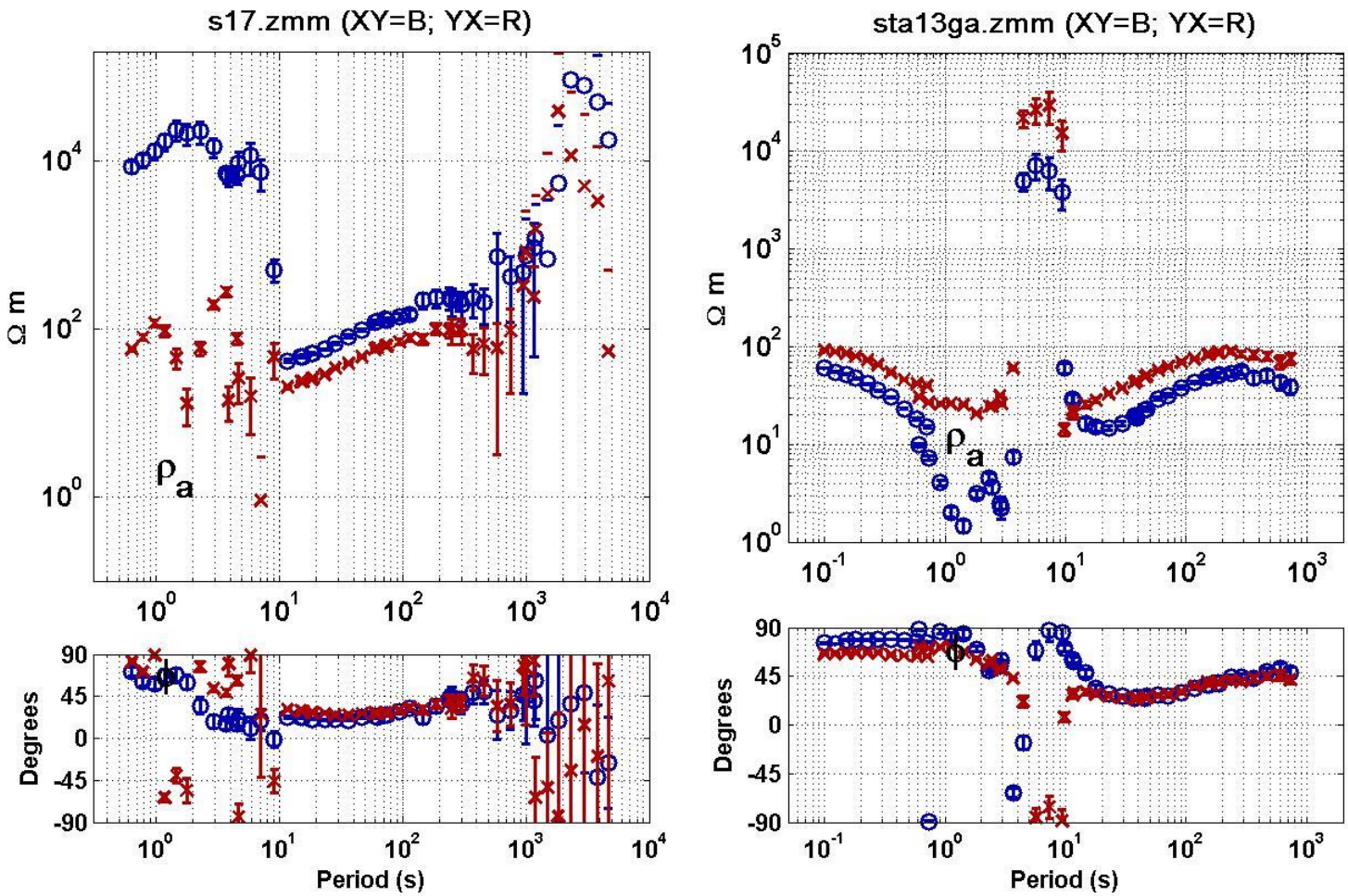

Figure 8 2003 ‘s17’ apparent resistivity and phase from the RMEV method are on left. Apparent resistivity and phase from the RMEV method from collocated 2012 station 13 are on the right. There is a swap in the XY and YX modes between the s17 and sta13 data. The s17 data were processed at LBNL and results provided, so we cannot verify the orientations of the installation.

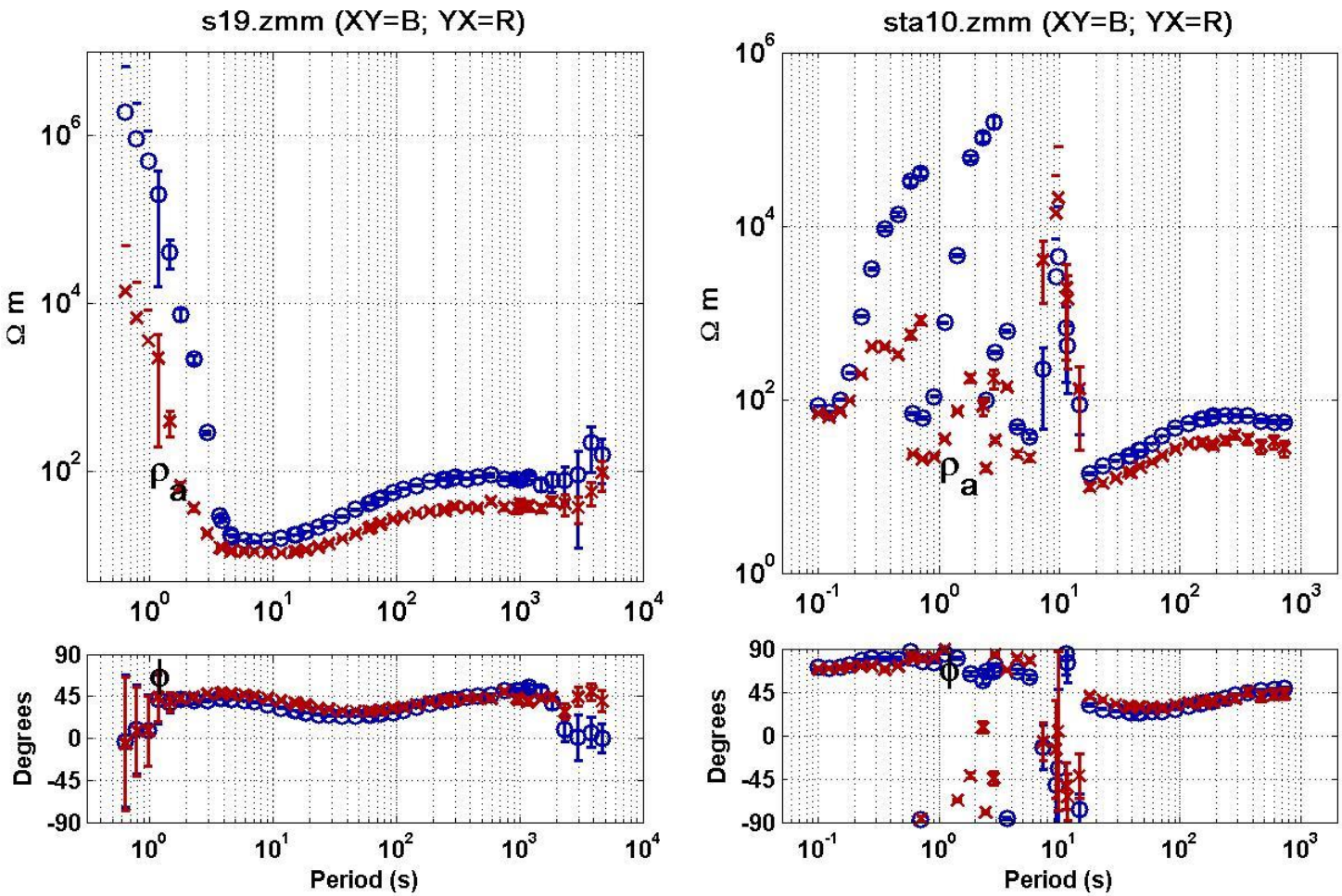

Figure 9 2003 ‘s19’ apparent resistivity and phase from the RMEV method are on left. Apparent resistivity and phase from the RMEV method from collocated 2012 station 10 are on the right.

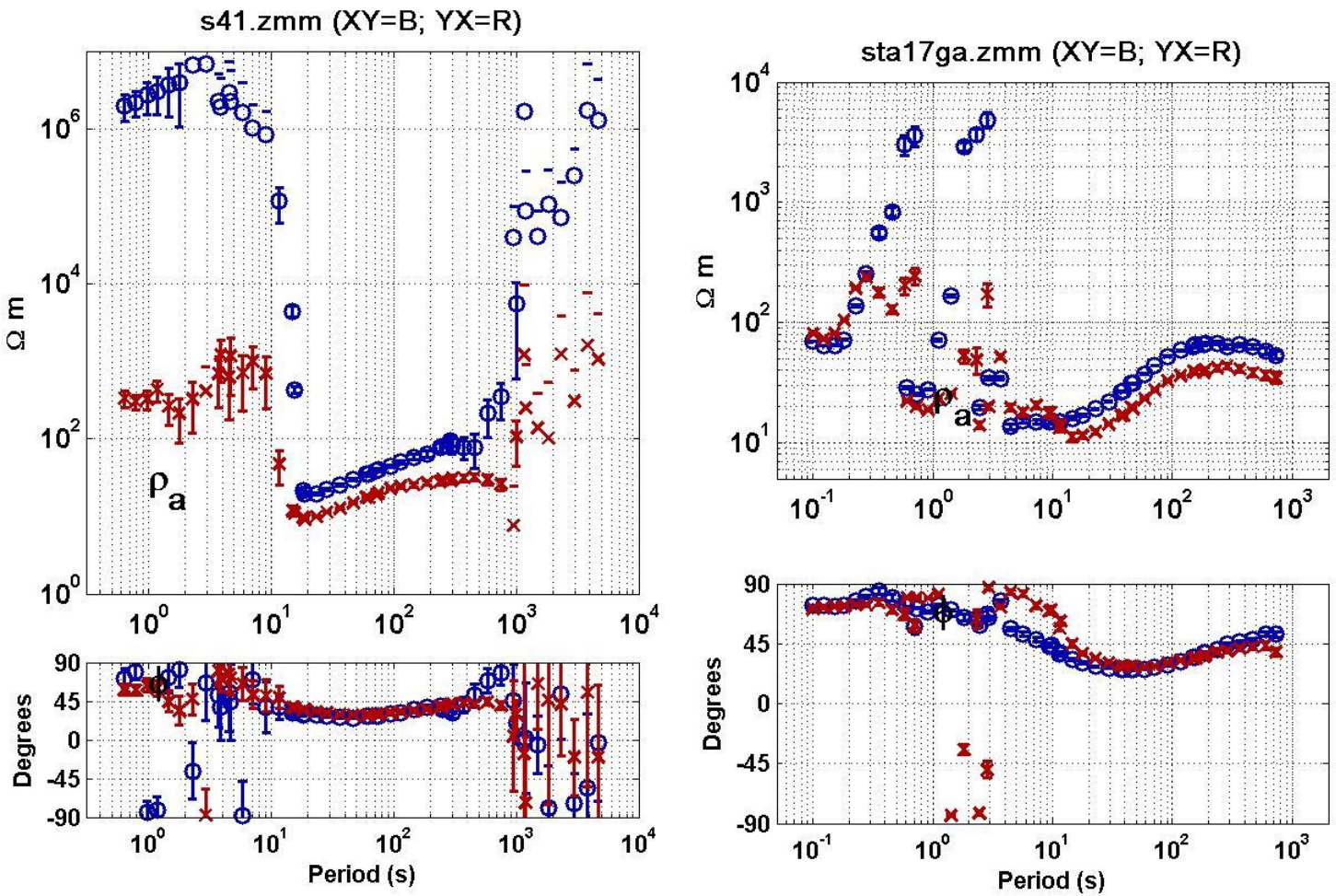

Figure 10 2003 ‘s41’ apparent resistivity and phase from the RMEV method are on left. Apparent resistivity and phase from the RMEV method from collocated 2012 station 17 are on the right. There is a swap in the XY and YX modes between the s41 and sta17 data. The s41 data were processed at LBNL and results provided, so we cannot verify the orientations of the installation.

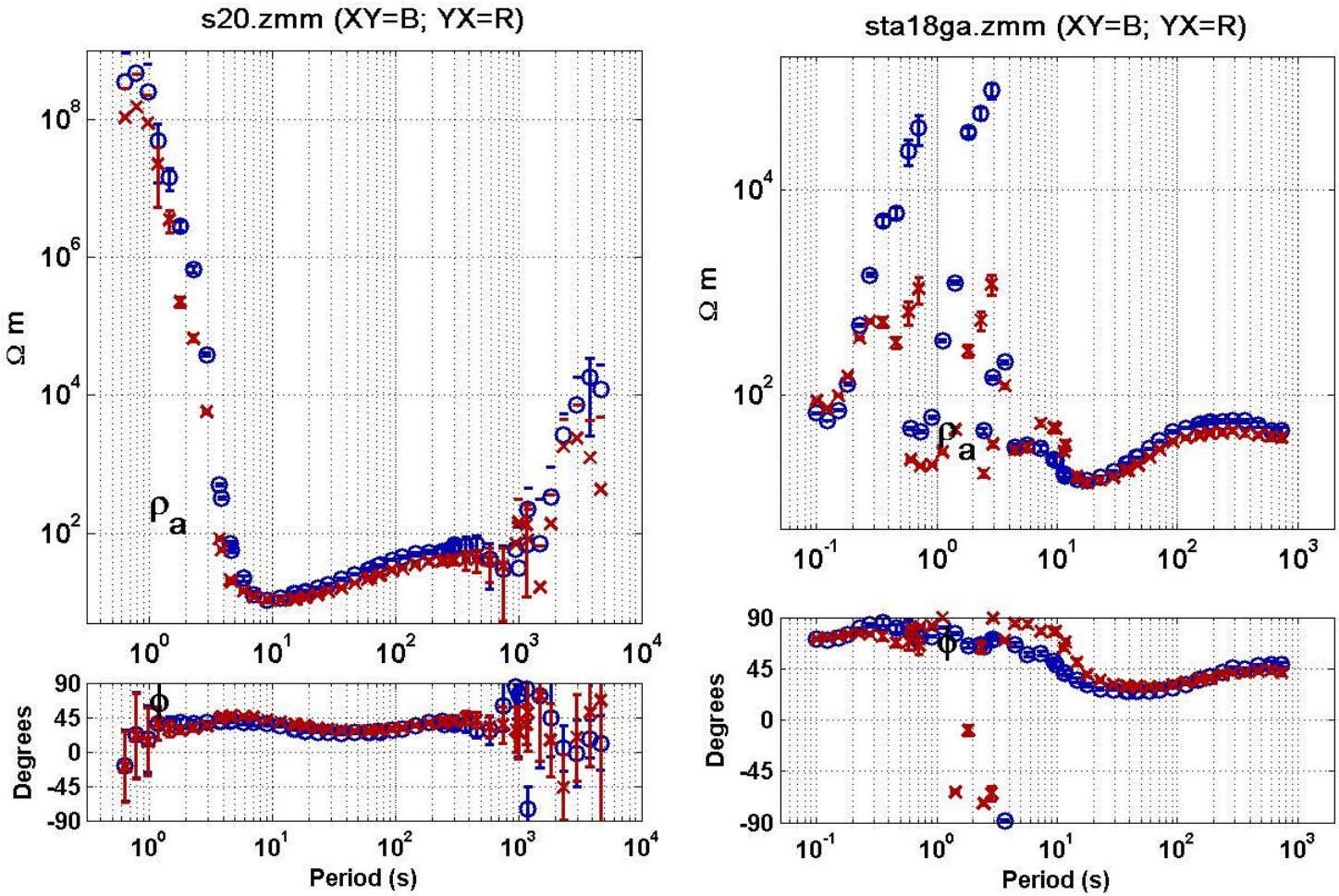

Figure 11 2003 ‘s20’ apparent resistivity and phase from the RMEV method are on left. Apparent resistivity and phase from the RMEV method from collocated 2012 station 18 are on the right.

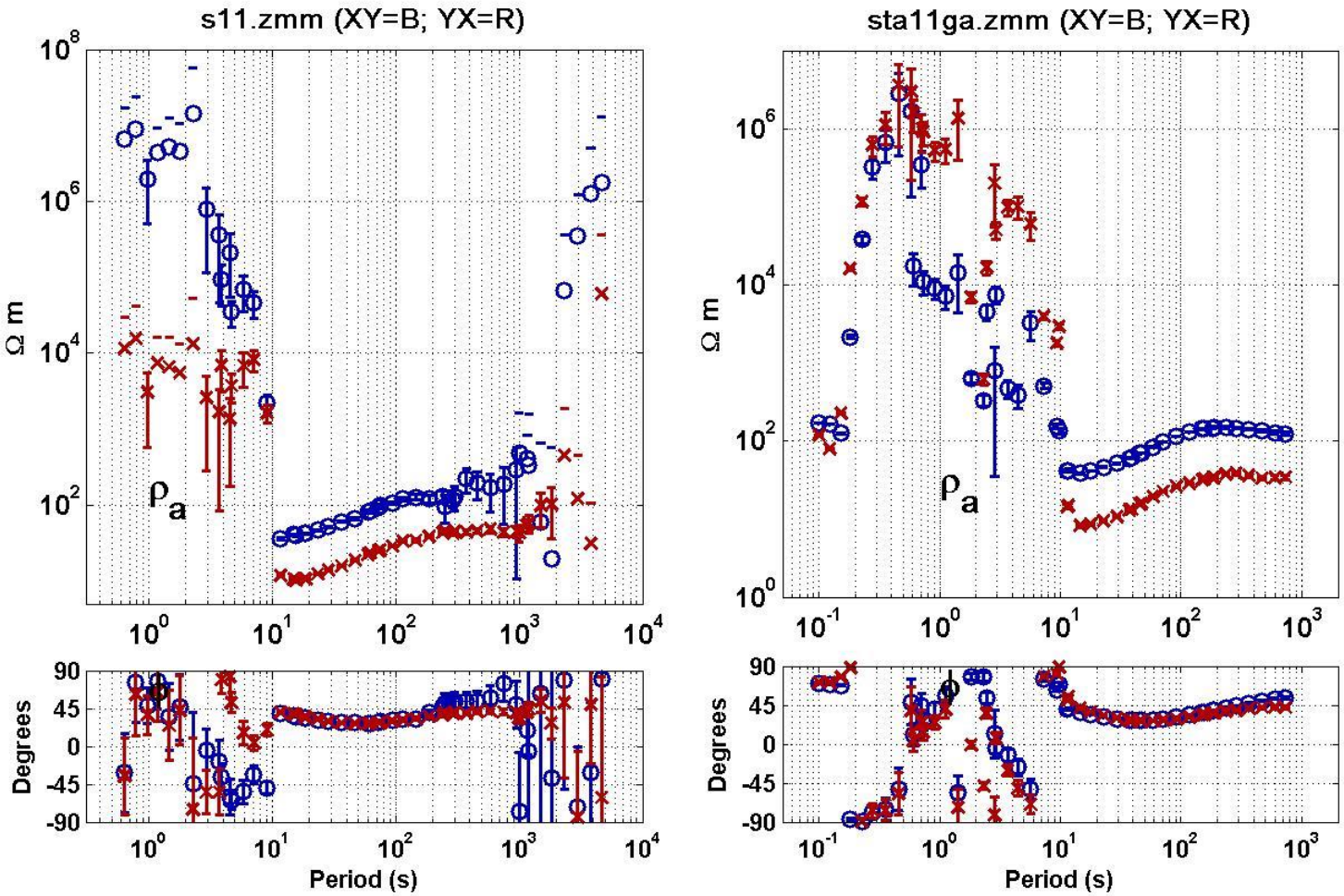

Figure 12 2003's 's11' RMEV method apparent resistivity and phase are plotted in the left panel. Apparent resistivity and phase from the RMEV method from collocated 2012 station 11 are on the right.

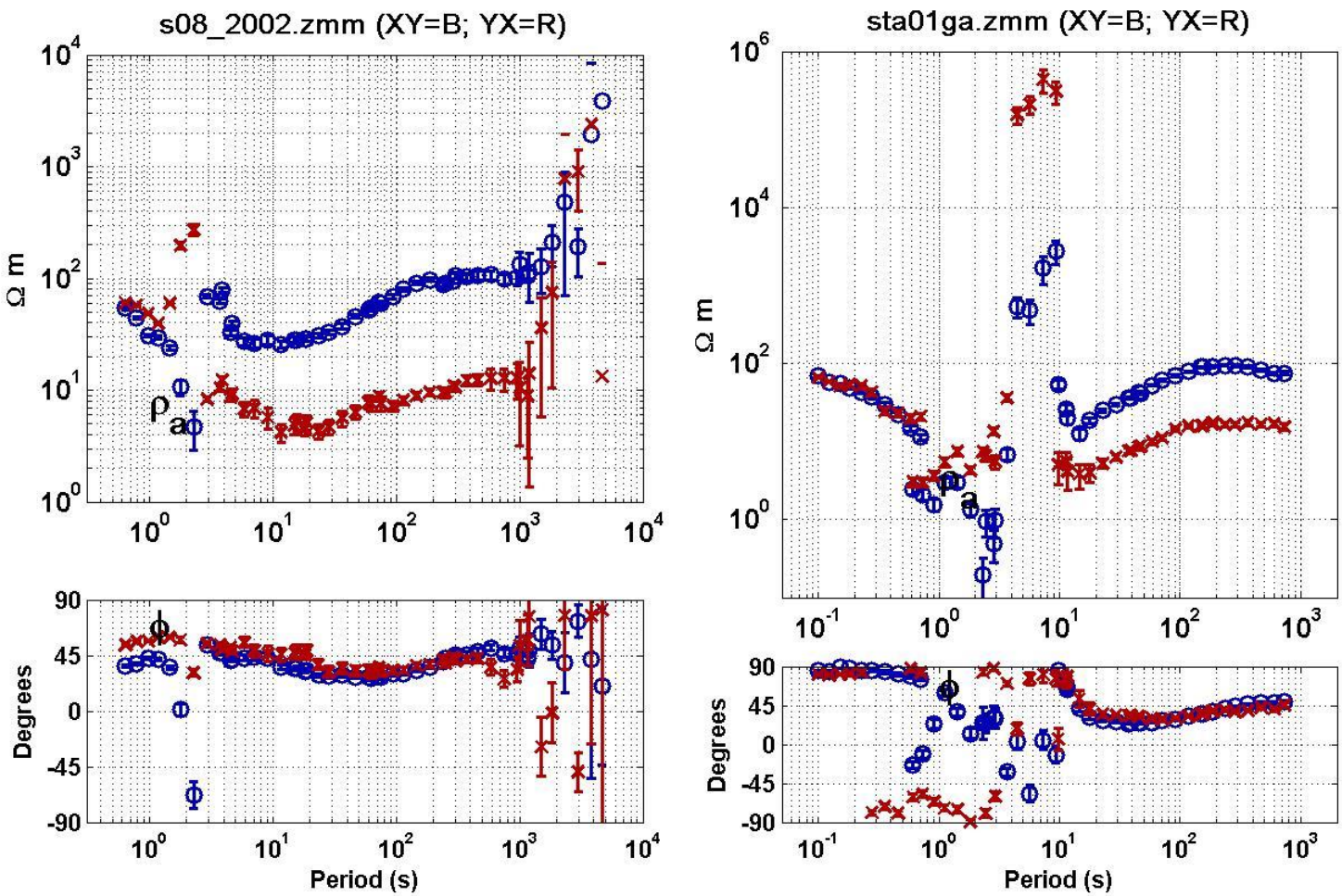

Figure 13 2002's 's08_2002 RMEV method apparent resistivity and phase are plotted in the left panel. Apparent resistivity and phase from the RMEV method from collocated 2012 station 1 are on the right.

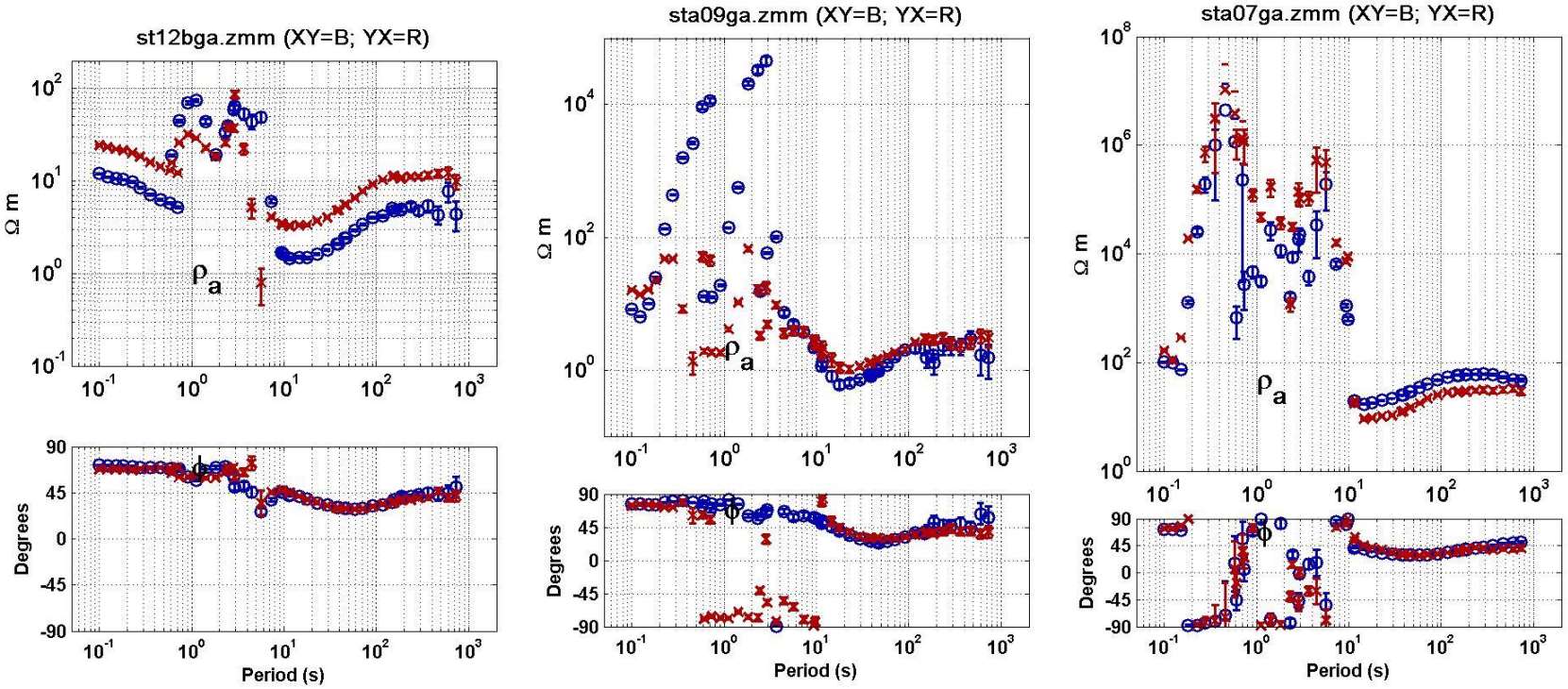

Figure 14 Apparent resistivity and phase from station 12b, 9, and 7 acquired in 2012-2013 processed with the RMEV method.

APPENDIX B

Dominant SDM eigenvalues and canonical coherence for 6 hour data segments

First four dominant SDM eigenvalues and associated canonical correlation for 6 hour data segments. Plots are displayed by group (1-6). The station number and eigenvalues or canonical coherency is indicated in the plots title.

Group 1

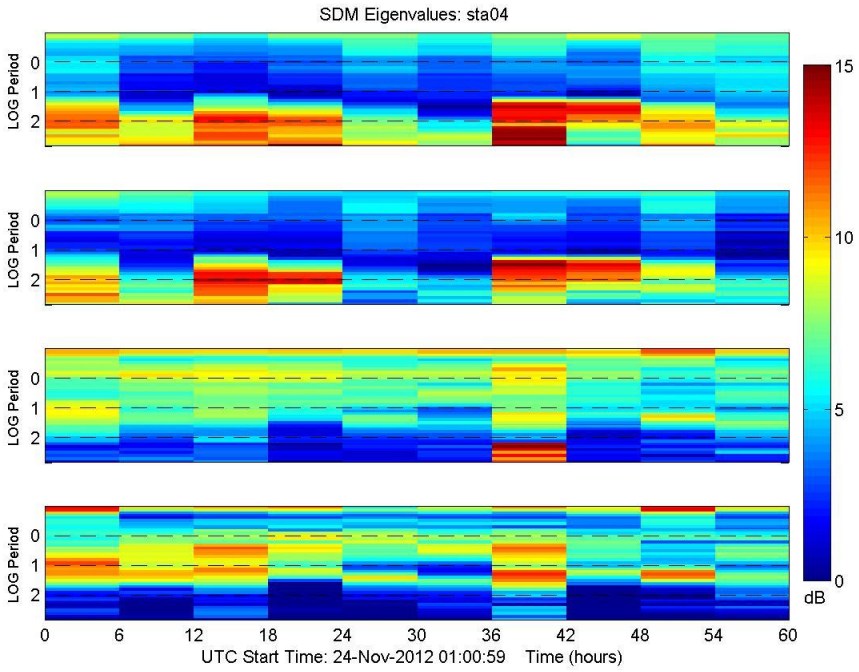

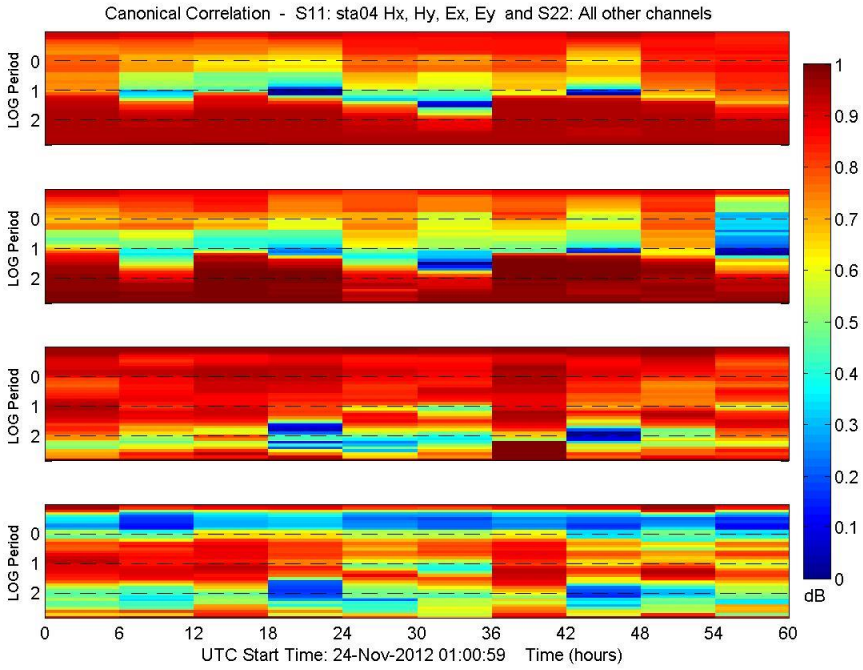
Canonical Correlation - S11: sta04 Hx, Hy, Ex, Ey and S22: All other channels
LOG Period
0
1
2
1
0.9
0.8
0.7
0.6
0.5
0.4
0.3
0.2
0.1
0
dB
0
6
12
18
24
30
36
42
48
54
60
UTC Start Time: 24-Nov-2012 01:00:59 Time (hours)

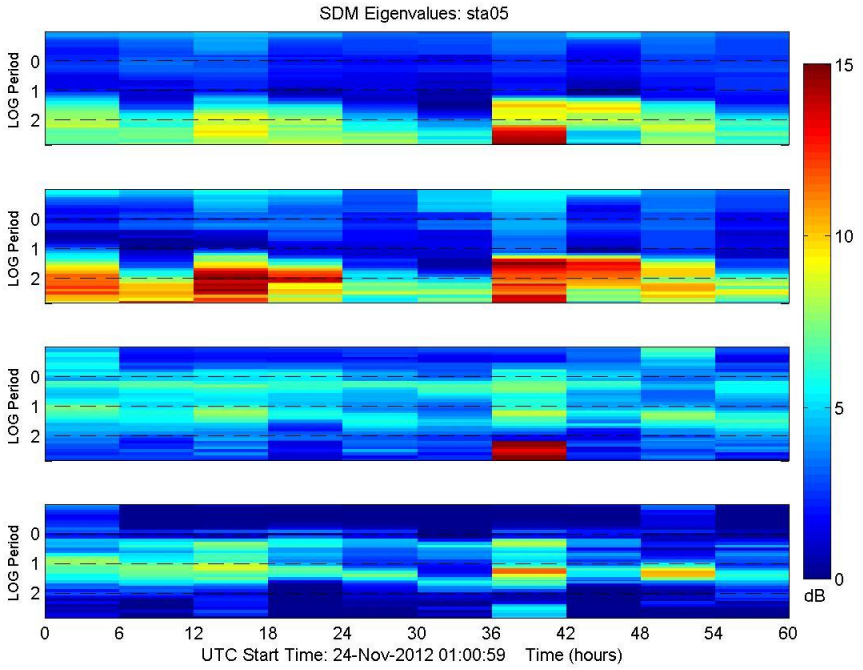
SDM Eigenvalues: sta05
LOG Period
0
1
2
15
10
5
0
dB
0
6
12
18
24
30
36
42
48
54
60
UTC Start Time: 24-Nov-2012 01:00:59 Time (hours)

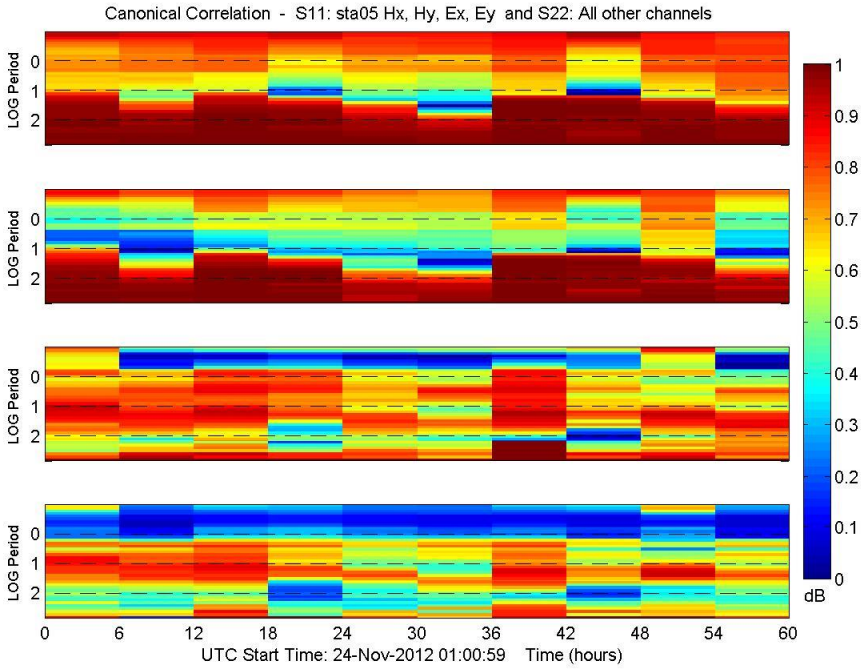
Canonical Correlation - S11: sta05 Hx, Hy, Ex, Ey and S22: All other channels
LOG Period
0
1
2
1
0.9
0.8
0.7
0.6
0.5
0.4
0.3
0.2
0.1
0
dB
0
6
12
18
24
30
36
42
48
54
60
UTC Start Time: 24-Nov-2012 01:00:59 Time (hours)

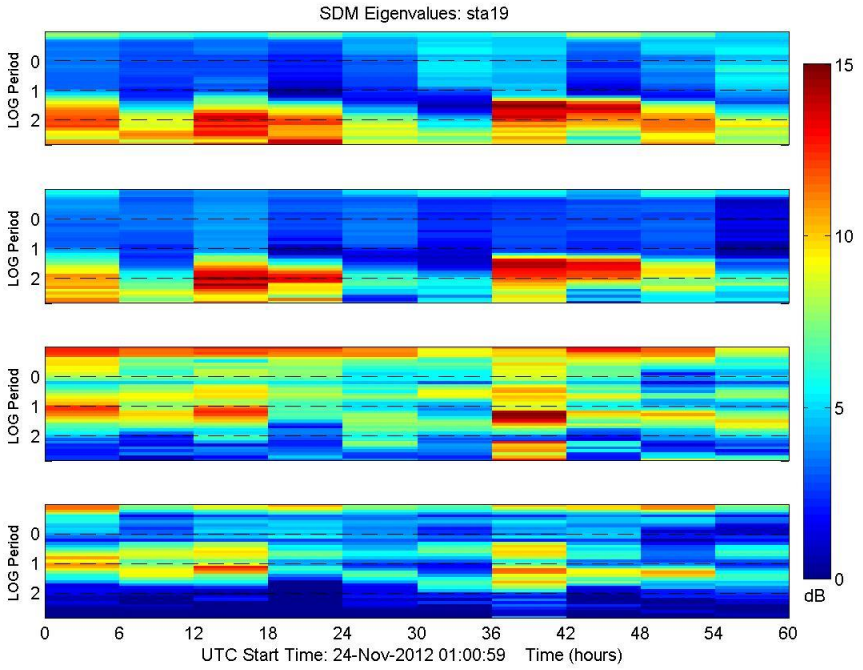
SDM Eigenvalues: sta19
LOG Period
0
1
2
15
10
5
0
dB
0
6
12
18
24
30
36
42
48
54
60
UTC Start Time: 24-Nov-2012 01:00:59 Time (hours)

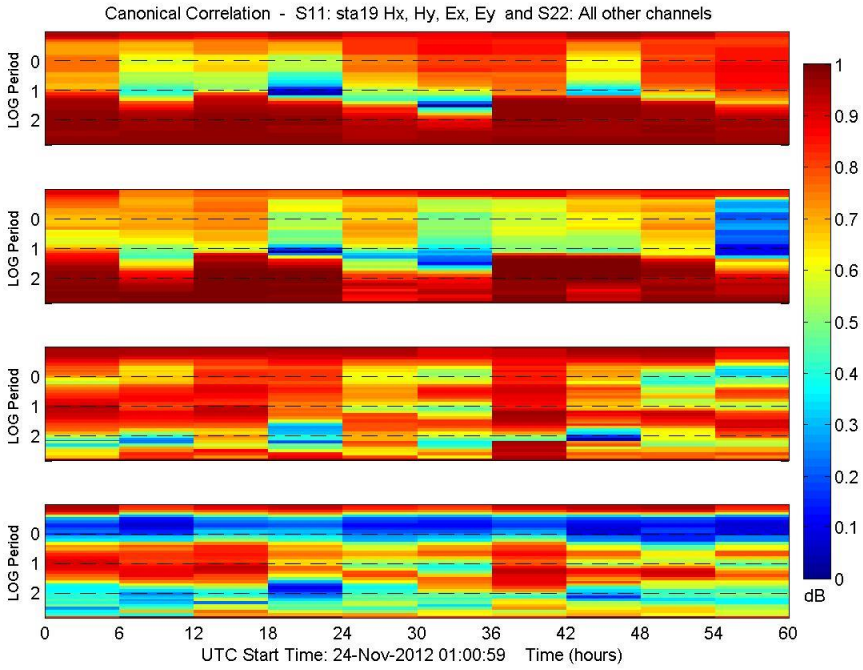
Canonical Correlation - S11: sta19 Hx, Hy, Ex, Ey and S22: All other channels
LOG Period
0
1
2
1
0.9
0.8
0.7
0.6
0.5
0.4
0.3
0.2
0.1
0
dB
0
6
12
18
24
30
36
42
48
54
60
UTC Start Time: 24-Nov-2012 01:00:59 Time (hours)

Group 2

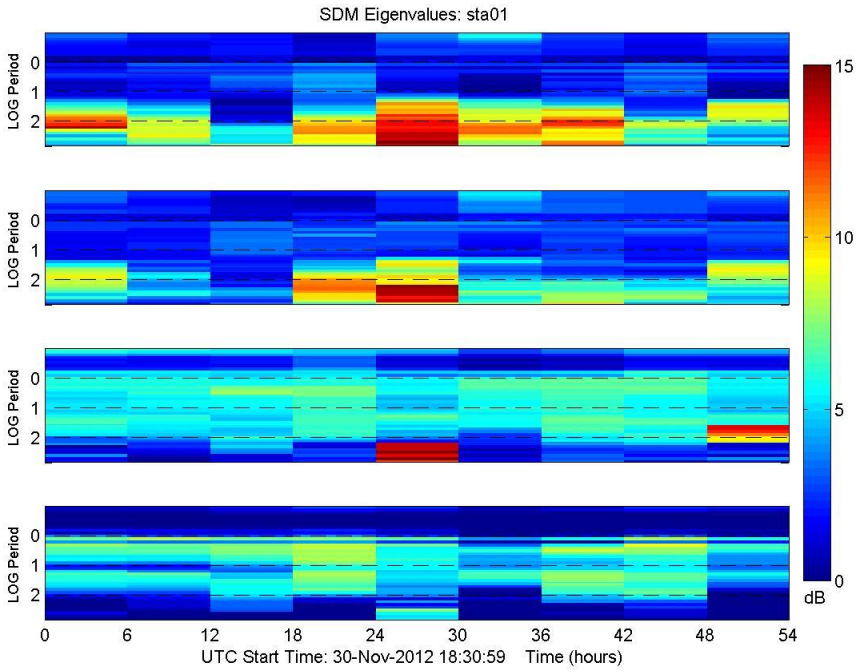
SDM Eigenvalues: sta01
LOG Period
0
1
2
15
10
5
0
dB
0
6
12
18
24
30
36
42
48
54
UTC Start Time: 30-Nov-2012 18:30:59 Time (hours)

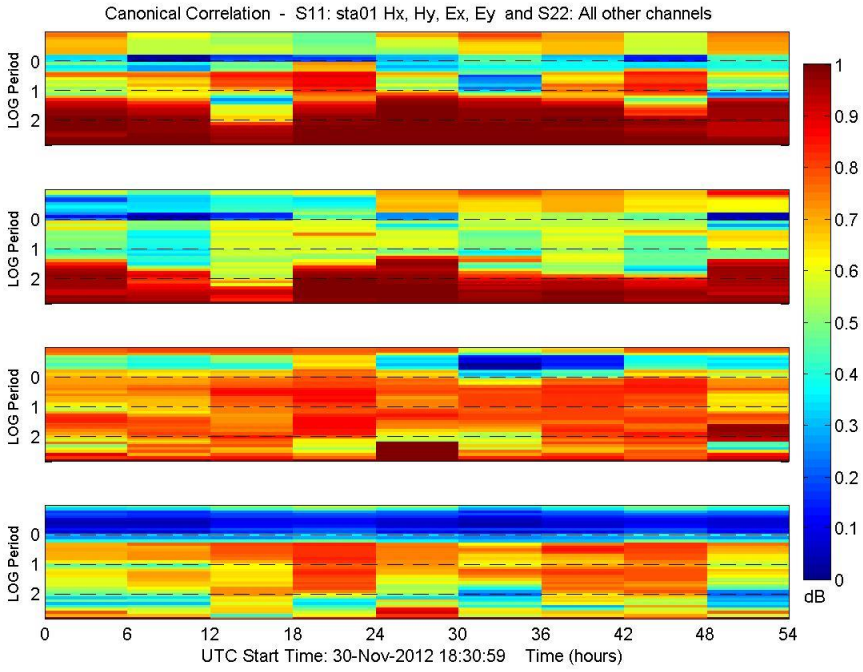
Canonical Correlation - S11: sta01 Hx, Hy, Ex, Ey and S22: All other channels
LOG Period
0
1
2
1
0.9
0.8
0.7
0.6
0.5
0.4
0.3
0.2
0.1
0
dB
0
6
12
18
24
30
36
42
48
54
UTC Start Time: 30-Nov-2012 18:30:59 Time (hours)

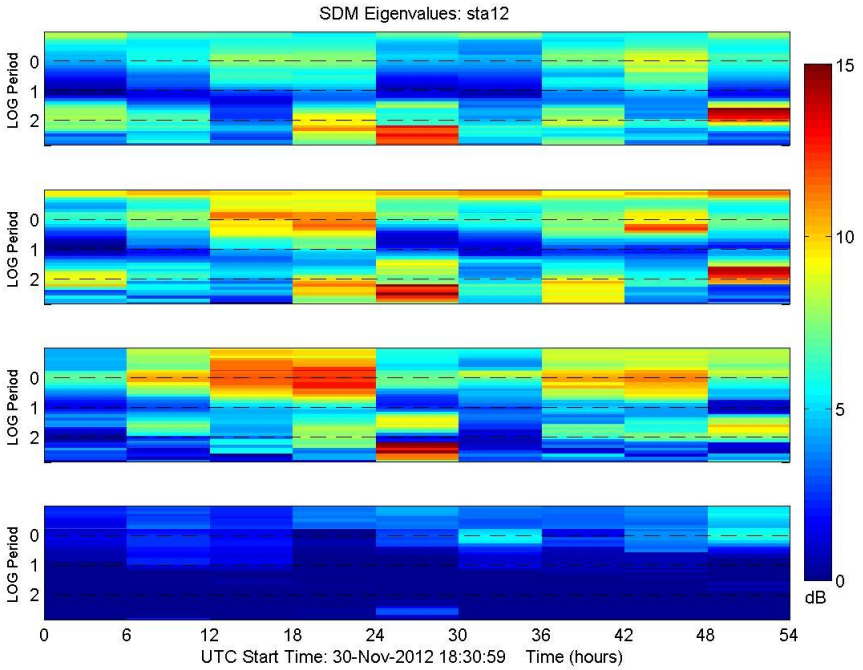
SDM Eigenvalues: sta12
LOG Period
0
1
2
15
10
5
0
dB
0
6
12
18
24
30
36
42
48
54
UTC Start Time: 30-Nov-2012 18:30:59 Time (hours)

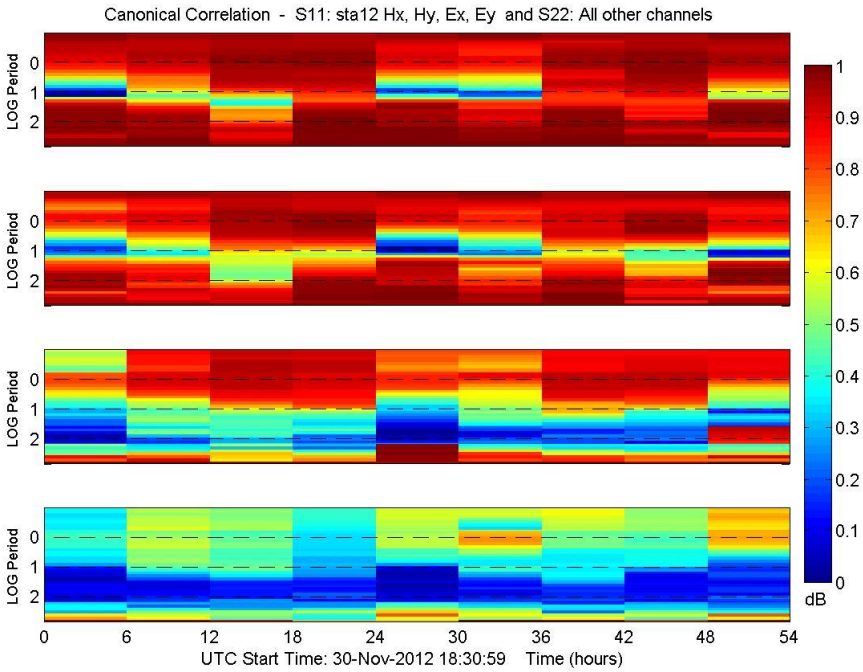
Canonical Correlation - S11: sta12 Hx, Hy, Ex, Ey and S22: All other channels
LOG Period
0
1
2
1
0.9
0.8
0.7
0.6
0.5
0.4
0.3
0.2
0.1
0
dB
0
6
12
18
24
30
36
42
48
54
UTC Start Time: 30-Nov-2012 18:30:59 Time (hours)

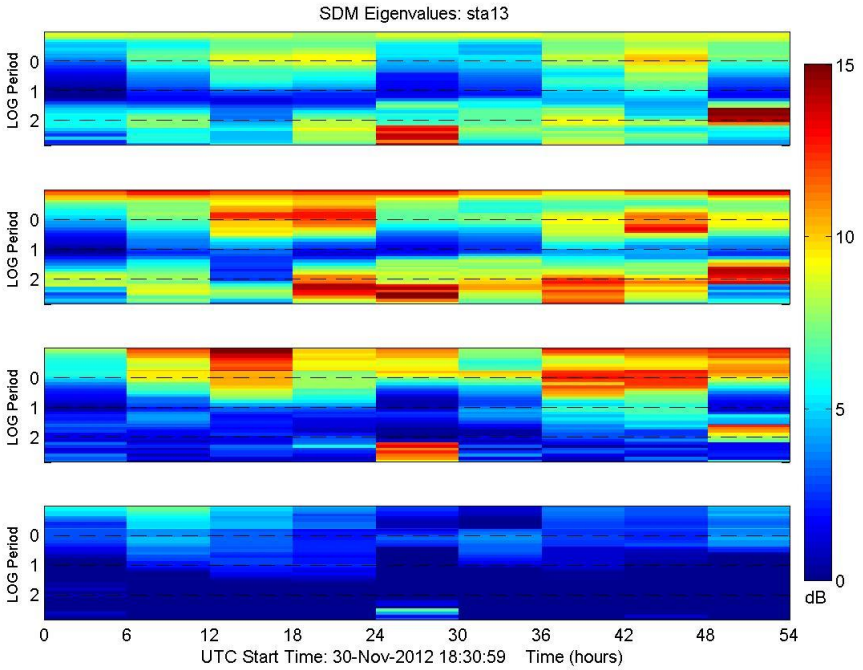
SDM Eigenvalues: sta13
LOG Period
0
1
2
15
10
5
0
dB
0
6
12
18
24
30
36
42
48
54
UTC Start Time: 30-Nov-2012 18:30:59 Time (hours)

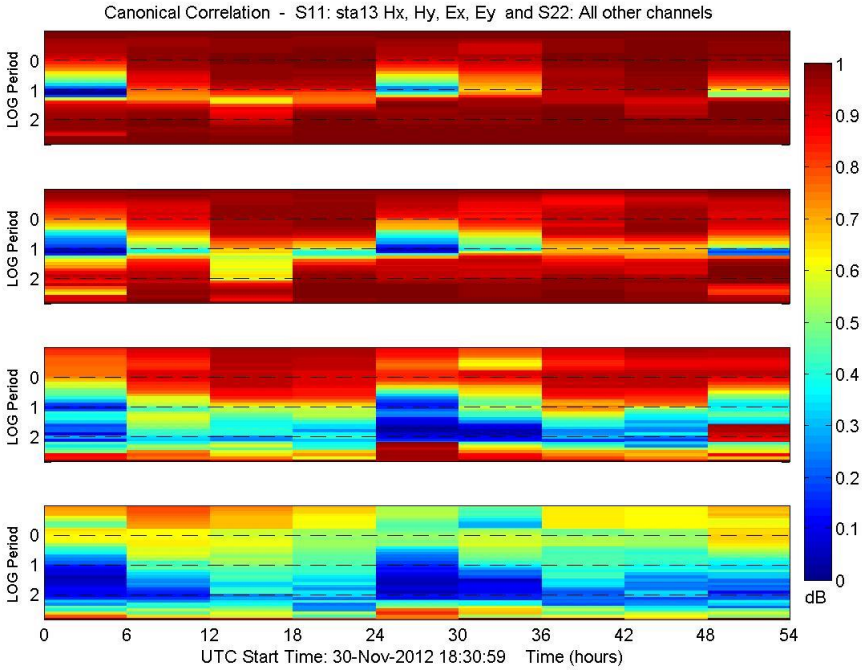
Canonical Correlation - S11: sta13 Hx, Hy, Ex, Ey and S22: All other channels
LOG Period
0
1
2
1
0.9
0.8
0.7
0.6
0.5
0.4
0.3
0.2
0.1
0
dB
0
6
12
18
24
30
36
42
48
54
UTC Start Time: 30-Nov-2012 18:30:59 Time (hours)

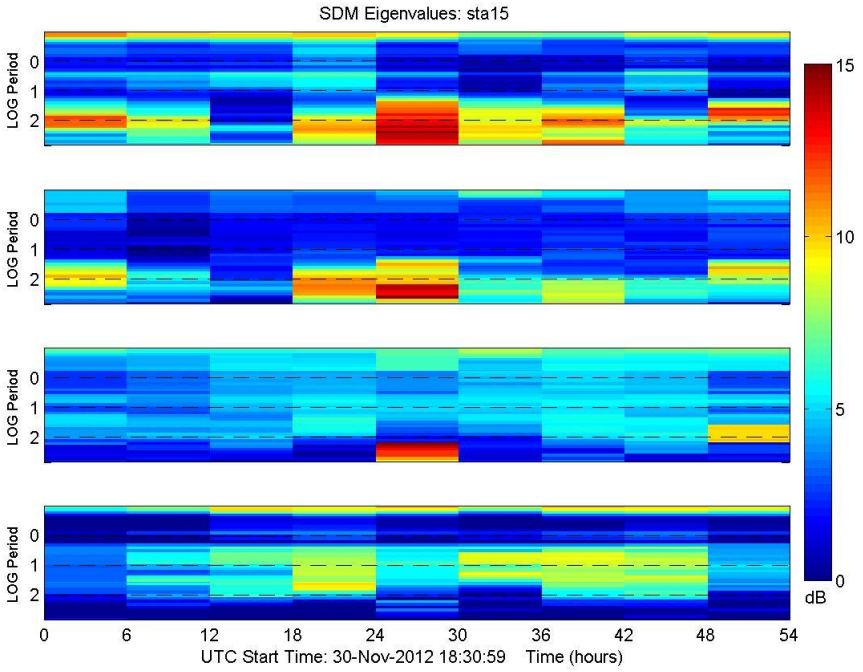
SDM Eigenvalues: sta15
LOG Period
0
1
2
15
10
5
0
dB
0
6
12
18
24
30
36
42
48
54
UTC Start Time: 30-Nov-2012 18:30:59 Time (hours)

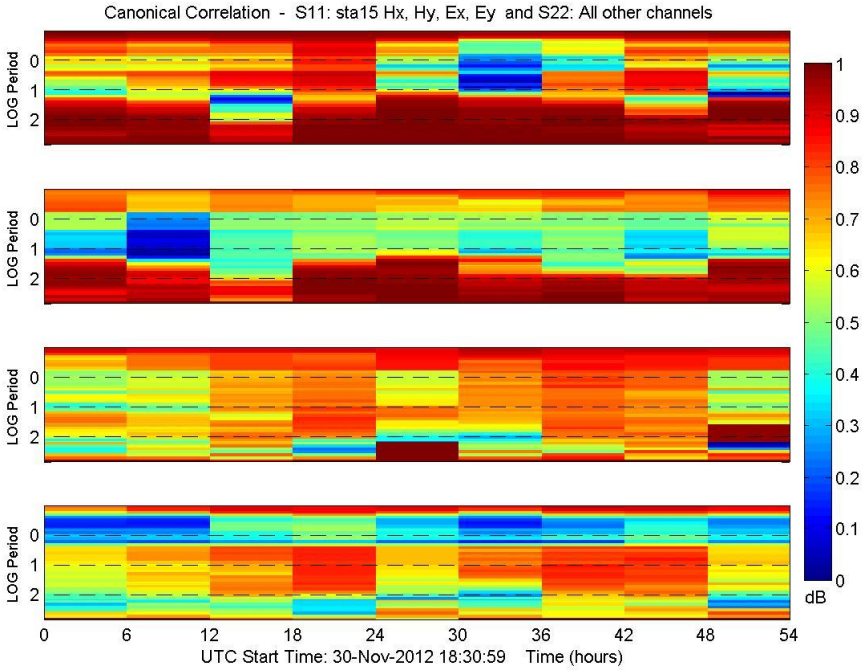
Canonical Correlation - S11: sta15 Hx, Hy, Ex, Ey and S22: All other channels
LOG Period
0
1
2
1
0.9
0.8
0.7
0.6
0.5
0.4
0.3
0.2
0.1
0
dB
0
6
12
18
24
30
36
42
48
54
UTC Start Time: 30-Nov-2012 18:30:59 Time (hours)

Group 3

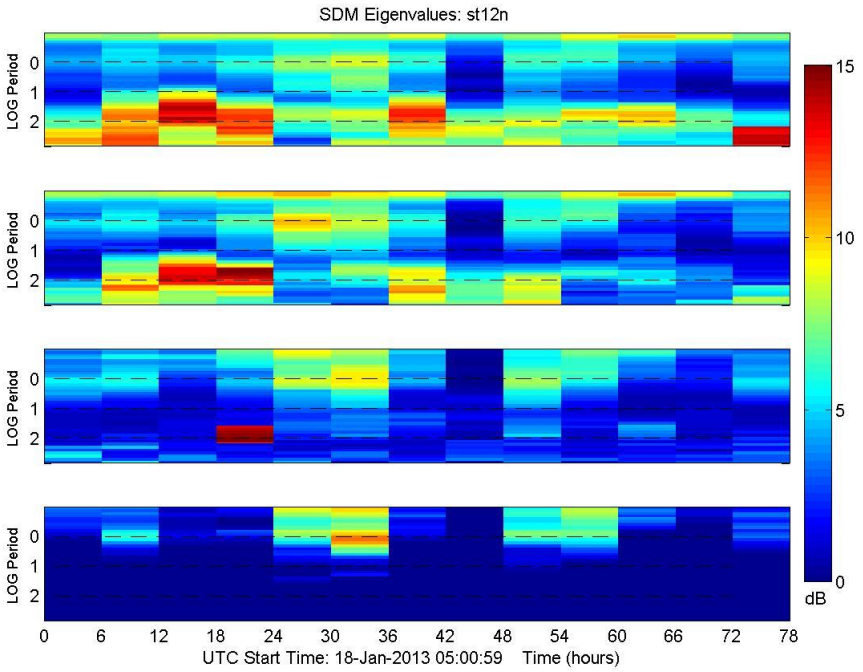
SDM Eigenvalues: st12n
LOG Period
0
1
2
15
10
5
0
dB
0 6 12 18 24 30 36 42 48 54 60 66 72 78
UTC Start Time: 18-Jan-2013 05:00:59 Time (hours)

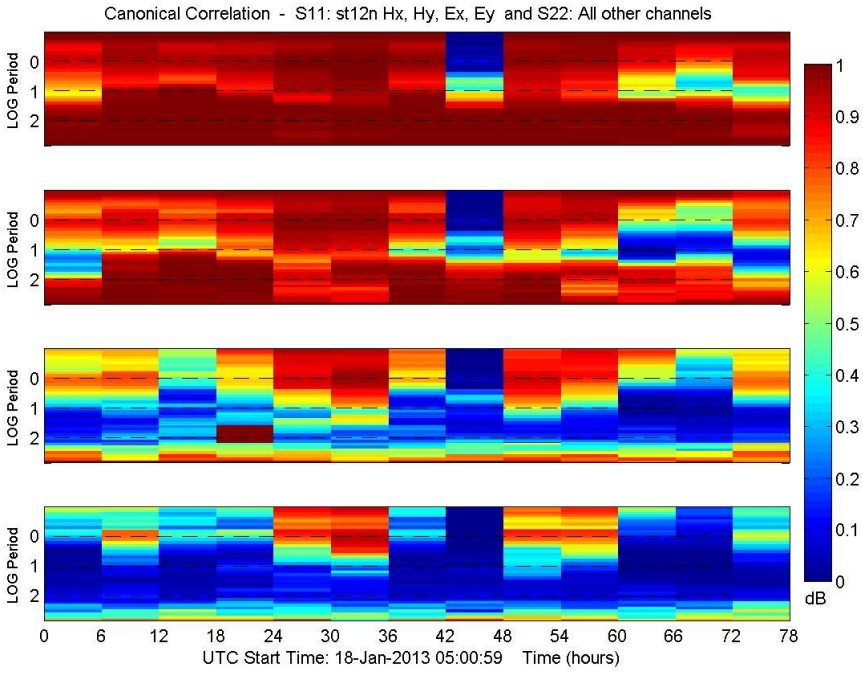
Canonical Correlation - S11: st12n Hx, Hy, Ex, Ey and S22: All other channels
LOG Period
0
1
2
1
0.9
0.8
0.7
0.6
0.5
0.4
0.3
0.2
0.1
0
dB
0 6 12 18 24 30 36 42 48 54 60 66 72 78
UTC Start Time: 18-Jan-2013 05:00:59 Time (hours)

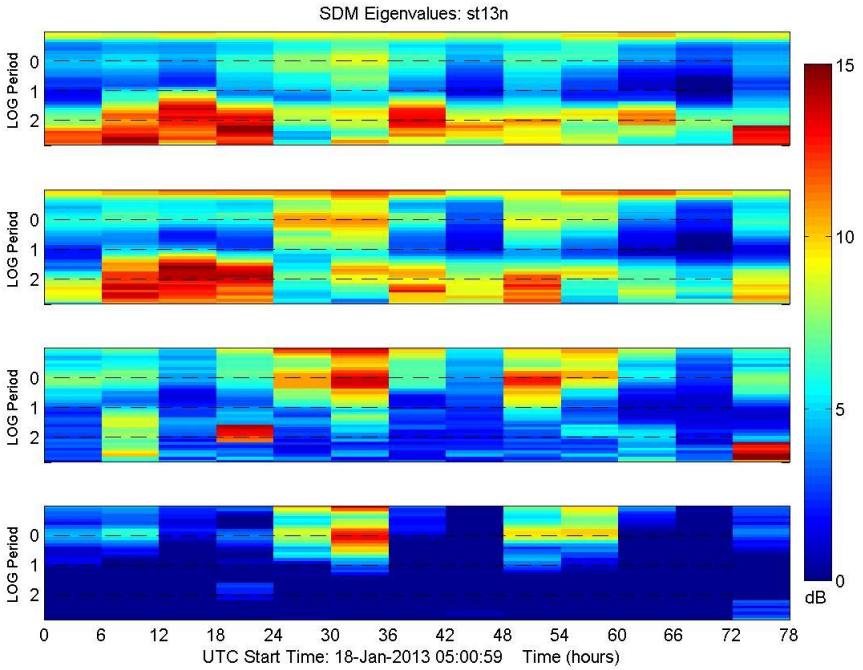
SDM Eigenvalues: st13n
LOG Period
0
1
2
15
10
5
0
dB
0 6 12 18 24 30 36 42 48 54 60 66 72 78
UTC Start Time: 18-Jan-2013 05:00:59 Time (hours)

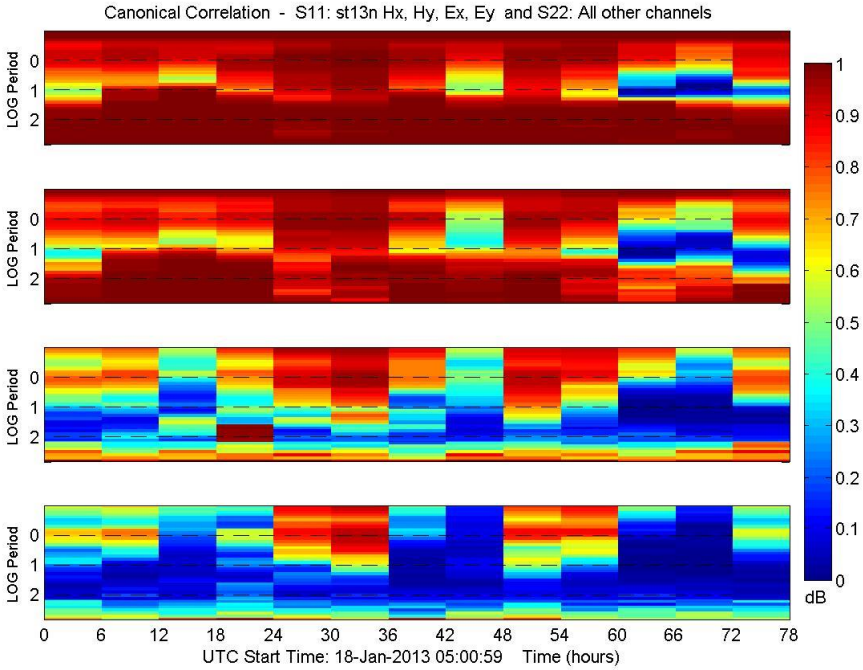
Canonical Correlation - S11: st13n Hx, Hy, Ex, Ey and S22: All other channels
LOG Period
0
1
2
1
0.9
0.8
0.7
0.6
0.5
0.4
0.3
0.2
0.1
0
dB
0 6 12 18 24 30 36 42 48 54 60 66 72 78
UTC Start Time: 18-Jan-2013 05:00:59 Time (hours)

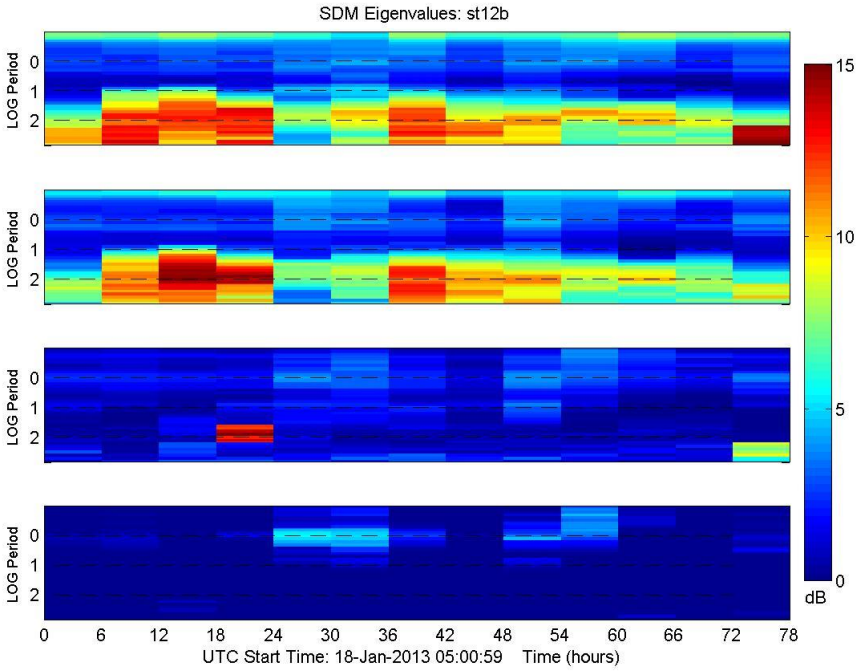
SDM Eigenvalues: st12b
LOG Period
0
1
2
0 6 12 18 24 30 36 42 48 54 60 66 72 78
UTC Start Time: 18-Jan-2013 05:00:59 Time (hours)
15
10
5
0
dB

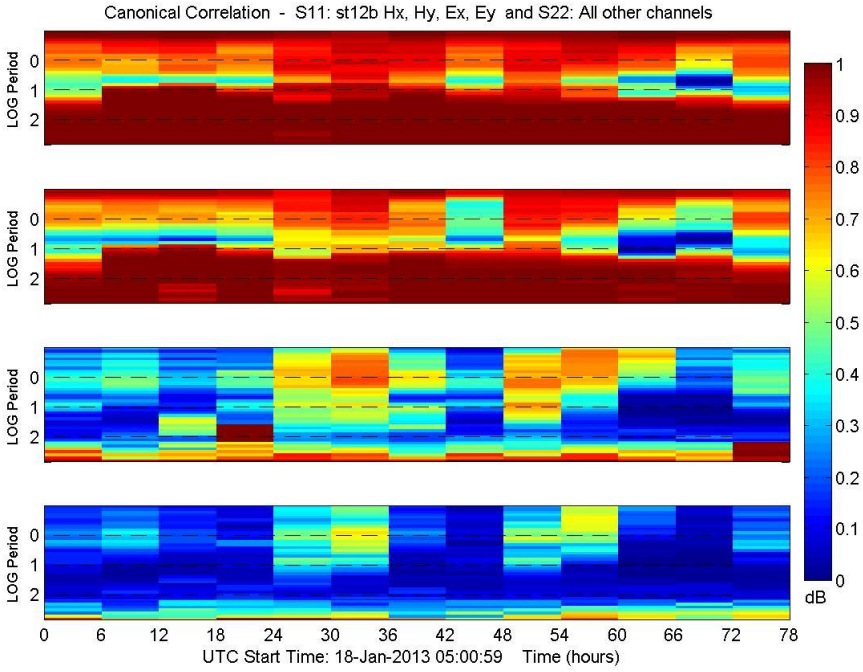
Canonical Correlation - S11: st12b Hx, Hy, Ex, Ey and S22: All other channels
LOG Period
0
1
2
0 6 12 18 24 30 36 42 48 54 60 66 72 78
UTC Start Time: 18-Jan-2013 05:00:59 Time (hours)
1
0.9
0.8
0.7
0.6
0.5
0.4
0.3
0.2
0.1
0
dB

Group 4

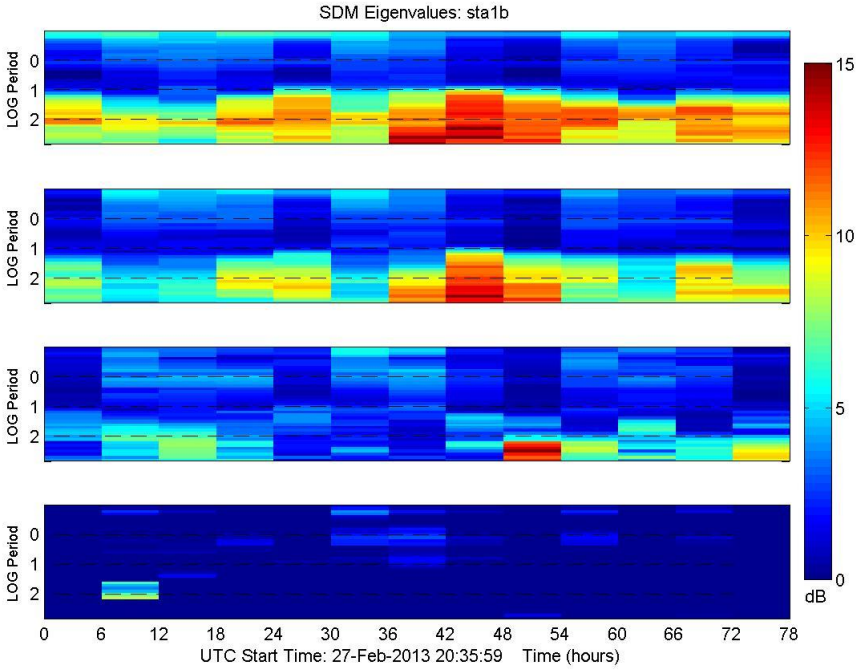
SDM Eigenvalues: sta1b
LOG Period
0
1
2
15
10
5
0
dB
0 6 12 18 24 30 36 42 48 54 60 66 72 78
UTC Start Time: 27-Feb-2013 20:35:59 Time (hours)

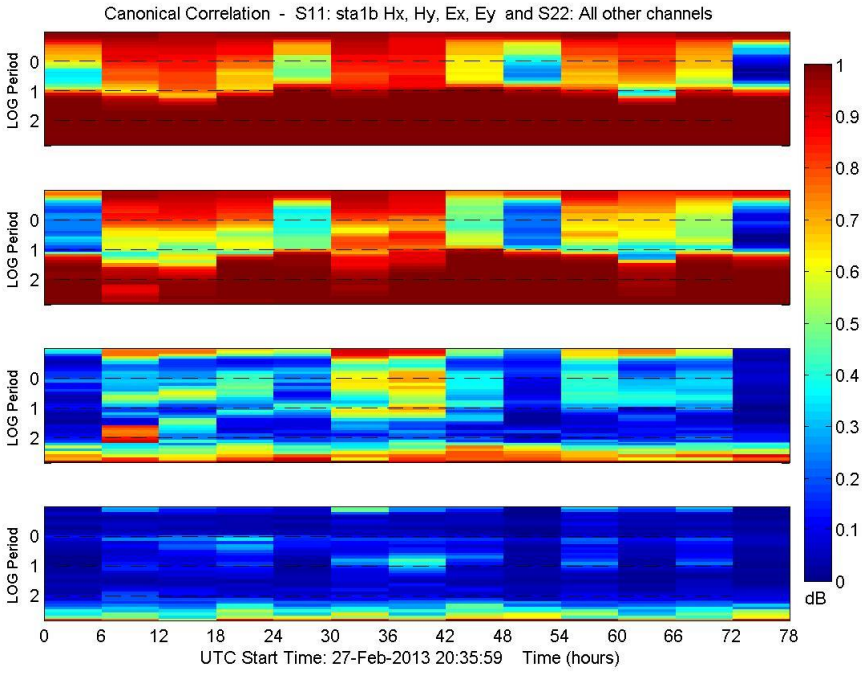
Canonical Correlation - S11: sta1b Hx, Hy, Ex, Ey and S22: All other channels
LOG Period
0
1
2
1
0.9
0.8
0.7
0.6
0.5
0.4
0.3
0.2
0.1
0
dB
0 6 12 18 24 30 36 42 48 54 60 66 72 78
UTC Start Time: 27-Feb-2013 20:35:59 Time (hours)

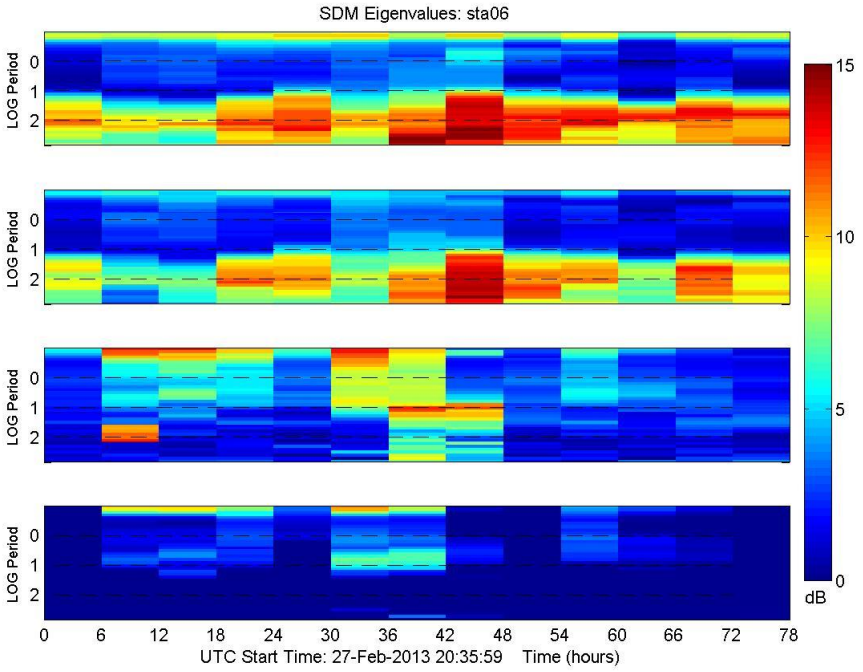
SDM Eigenvalues: sta06
LOG Period
0
1
2
15
10
5
0
dB
0 6 12 18 24 30 36 42 48 54 60 66 72 78
UTC Start Time: 27-Feb-2013 20:35:59 Time (hours)

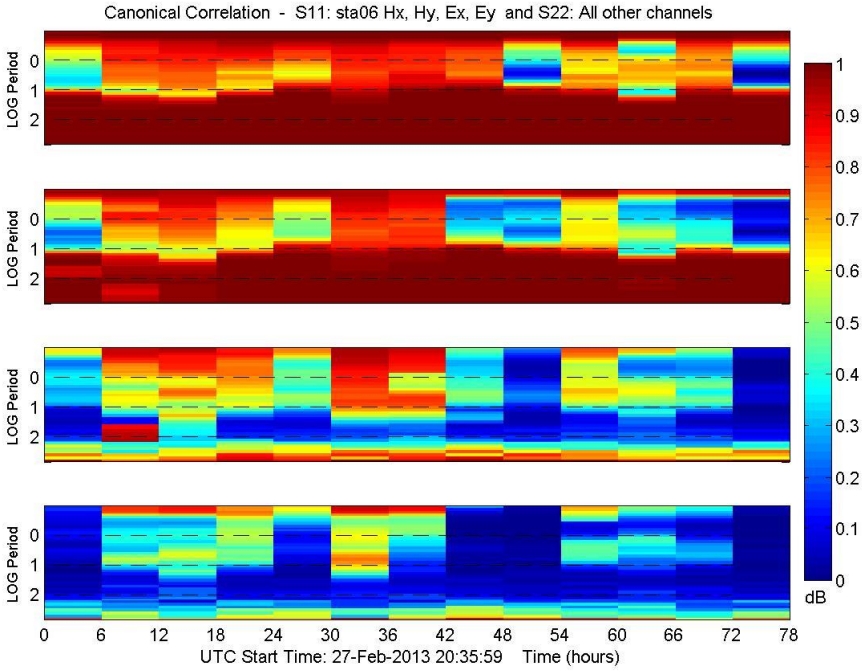
Canonical Correlation - S11: sta06 Hx, Hy, Ex, Ey and S22: All other channels
LOG Period
0
1
2
1
0.9
0.8
0.7
0.6
0.5
0.4
0.3
0.2
0.1
0
dB
0 6 12 18 24 30 36 42 48 54 60 66 72 78
UTC Start Time: 27-Feb-2013 20:35:59 Time (hours)

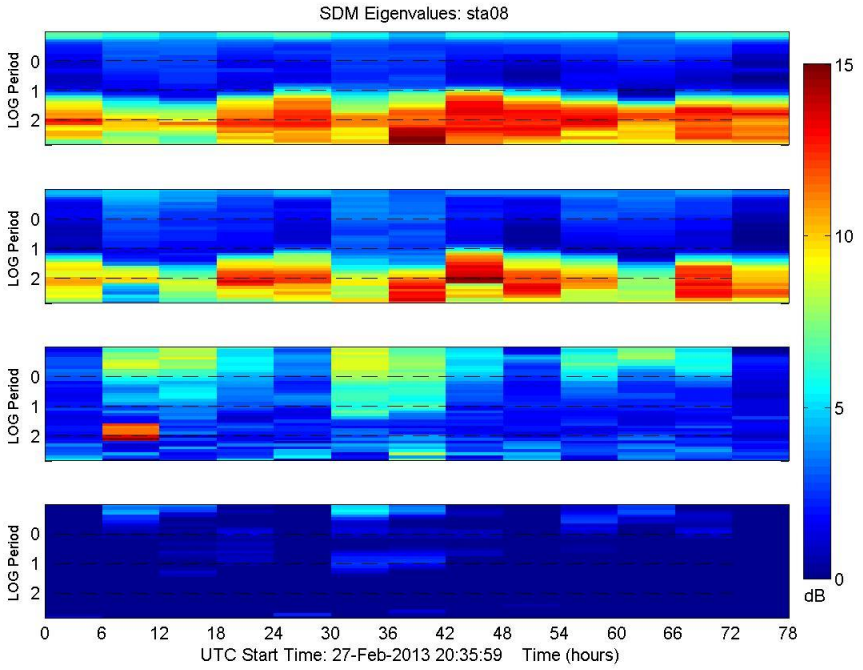
SDM Eigenvalues: sta08
LOG Period
0
1
2
15
10
5
0
dB
0 6 12 18 24 30 36 42 48 54 60 66 72 78
UTC Start Time: 27-Feb-2013 20:35:59 Time (hours)

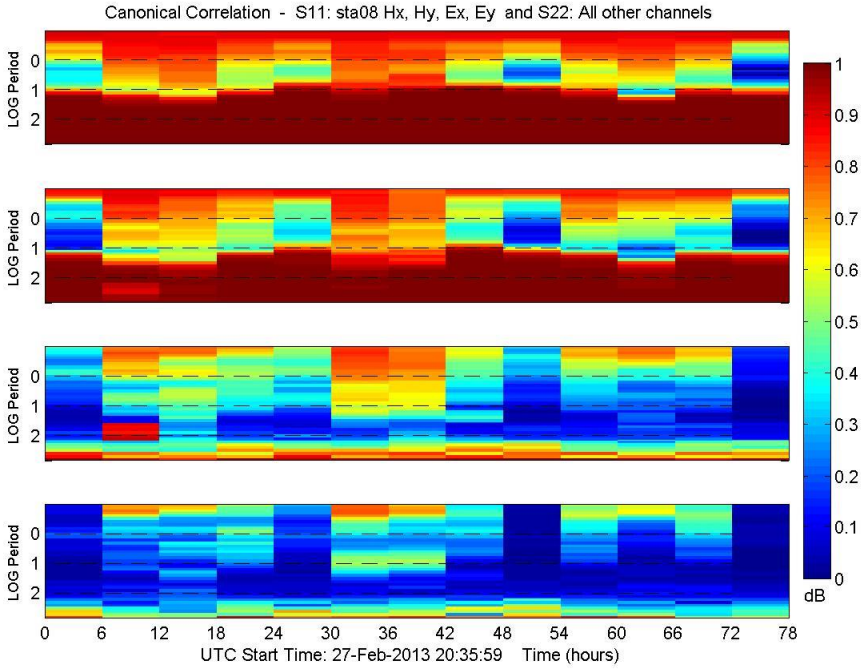
Canonical Correlation - S11: sta08 Hx, Hy, Ex, Ey and S22: All other channels
LOG Period
0
1
2
1
0.9
0.8
0.7
0.6
0.5
0.4
0.3
0.2
0.1
0
dB
0 6 12 18 24 30 36 42 48 54 60 66 72 78
UTC Start Time: 27-Feb-2013 20:35:59 Time (hours)

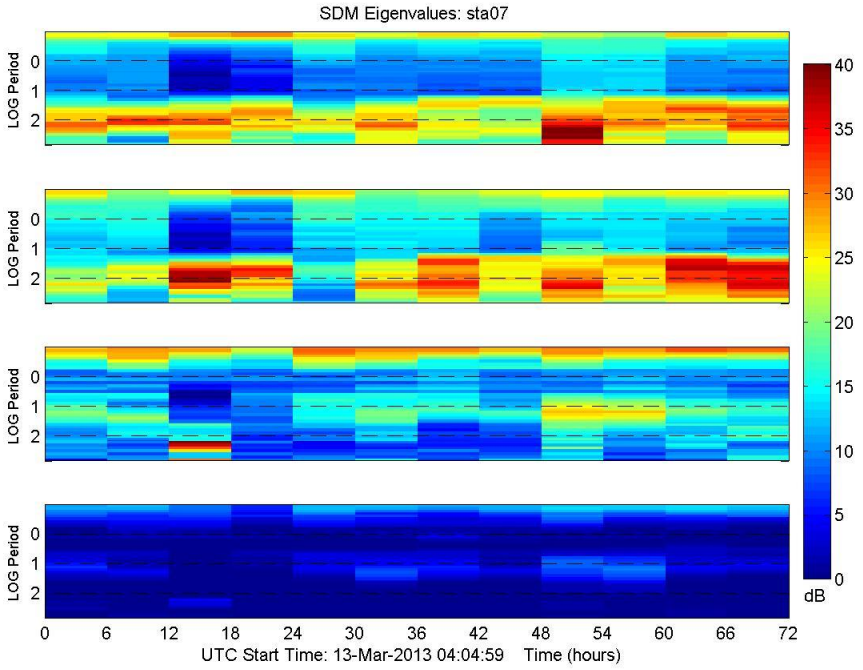
SDM Eigenvalues: sta07
LOG Period
0
1
2
40
35
30
25
20
15
10
5
0
dB
0 6 12 18 24 30 36 42 48 54 60 66 72
UTC Start Time: 13-Mar-2013 04:04:59 Time (hours)

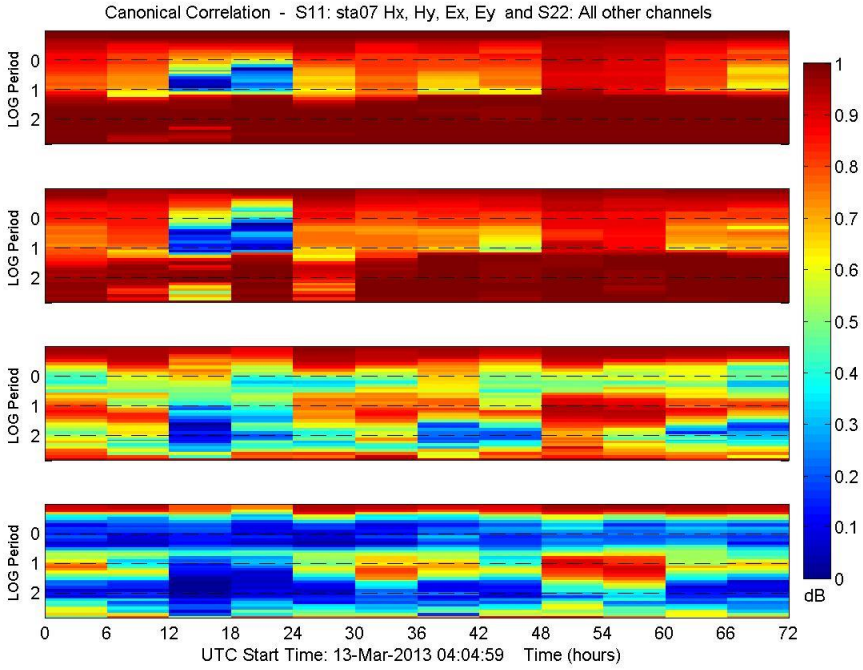
Canonical Correlation - S11: sta07 Hx, Hy, Ex, Ey and S22: All other channels
LOG Period
0
1
2
1
0.9
0.8
0.7
0.6
0.5
0.4
0.3
0.2
0.1
0
dB
0 6 12 18 24 30 36 42 48 54 60 66 72
UTC Start Time: 13-Mar-2013 04:04:59 Time (hours)

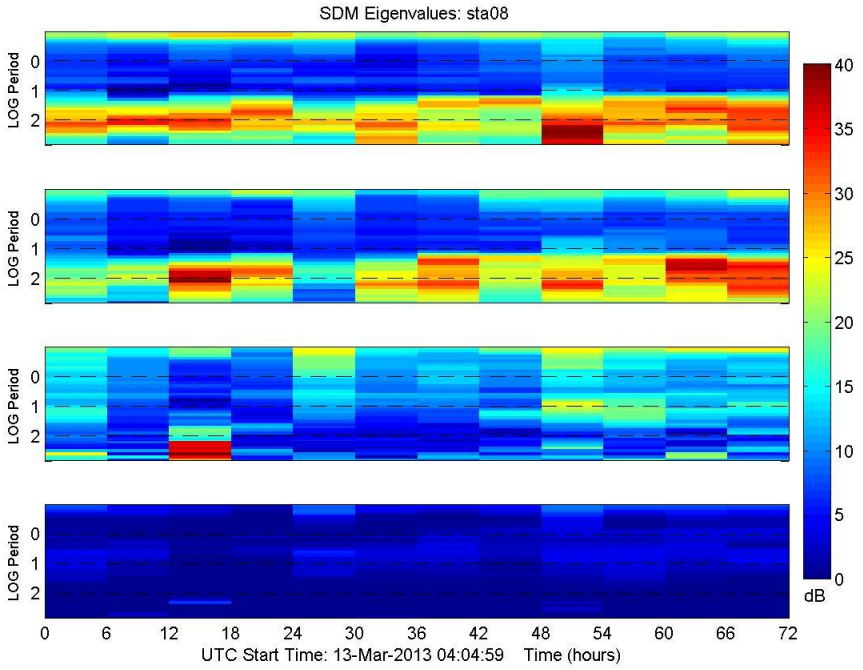
SDM Eigenvalues: sta08
LOG Period
0
1
2
40
35
30
25
20
15
10
5
0
dB
0 6 12 18 24 30 36 42 48 54 60 66 72
UTC Start Time: 13-Mar-2013 04:04:59 Time (hours)

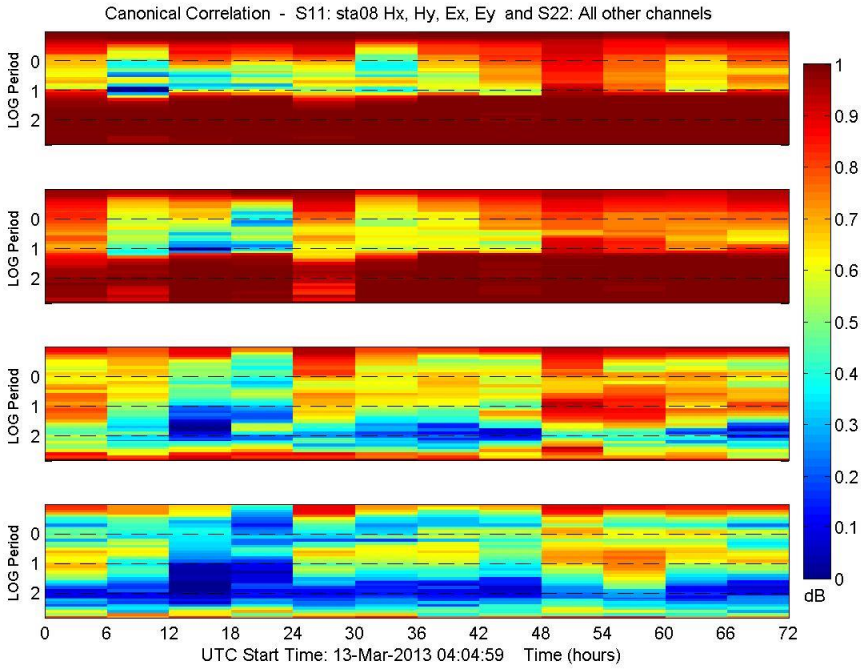
Canonical Correlation - S11: sta08 Hx, Hy, Ex, Ey and S22: All other channels
LOG Period
0
1
2
1
0.9
0.8
0.7
0.6
0.5
0.4
0.3
0.2
0.1
0
dB
0 6 12 18 24 30 36 42 48 54 60 66 72
UTC Start Time: 13-Mar-2013 04:04:59 Time (hours)

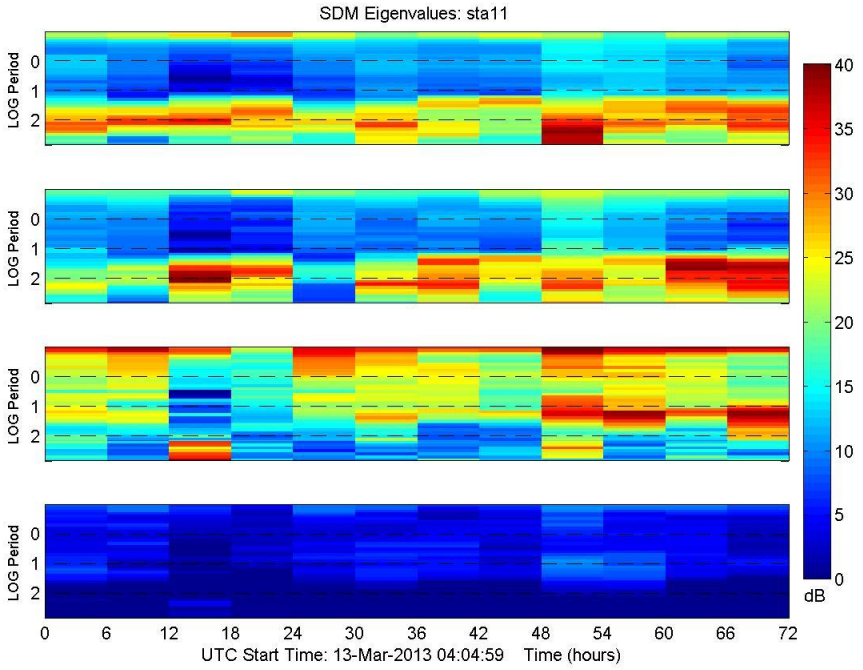
SDM Eigenvalues: sta11
LOG Period
0
1
2
40
35
30
25
20
15
10
5
0
dB
0 6 12 18 24 30 36 42 48 54 60 66 72
UTC Start Time: 13-Mar-2013 04:04:59 Time (hours)

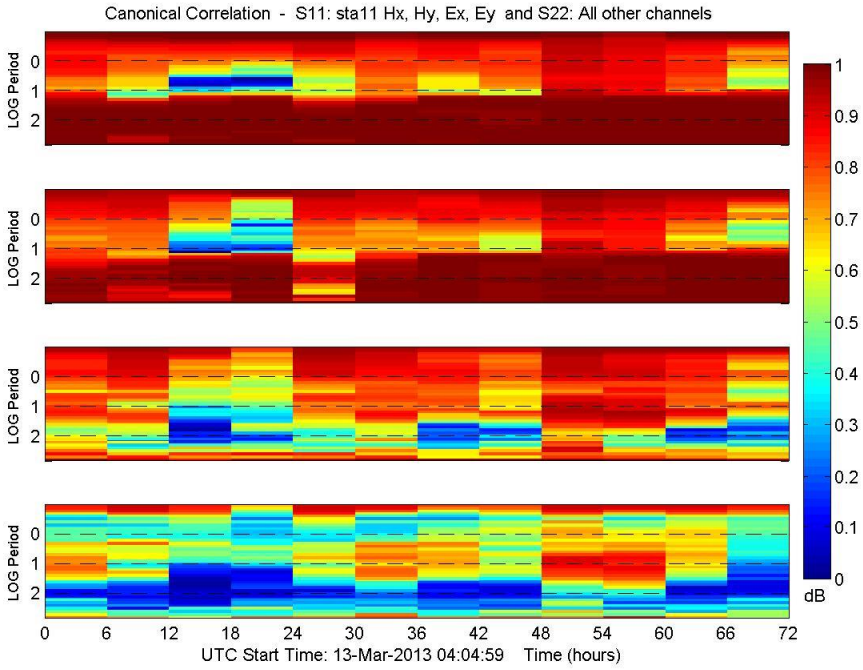
Canonical Correlation - S11: sta11 Hx, Hy, Ex, Ey and S22: All other channels
LOG Period
0
1
2
1
0.9
0.8
0.7
0.6
0.5
0.4
0.3
0.2
0.1
0
dB
0 6 12 18 24 30 36 42 48 54 60 66 72
UTC Start Time: 13-Mar-2013 04:04:59 Time (hours)

Group 6

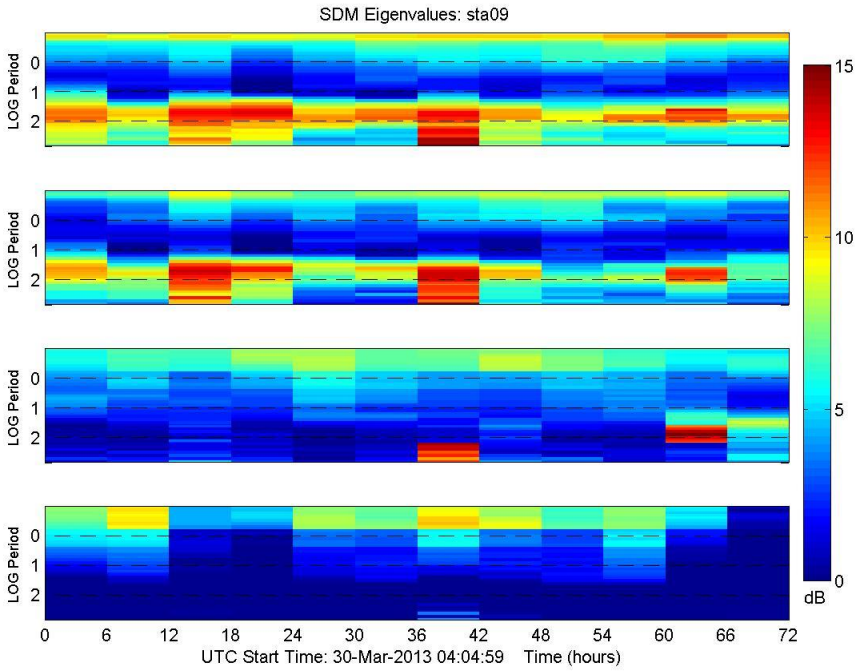
SDM Eigenvalues: sta09
LOG Period
0
1
2
15
10
5
0
dB
0 6 12 18 24 30 36 42 48 54 60 66 72
UTC Start Time: 30-Mar-2013 04:04:59 Time (hours)

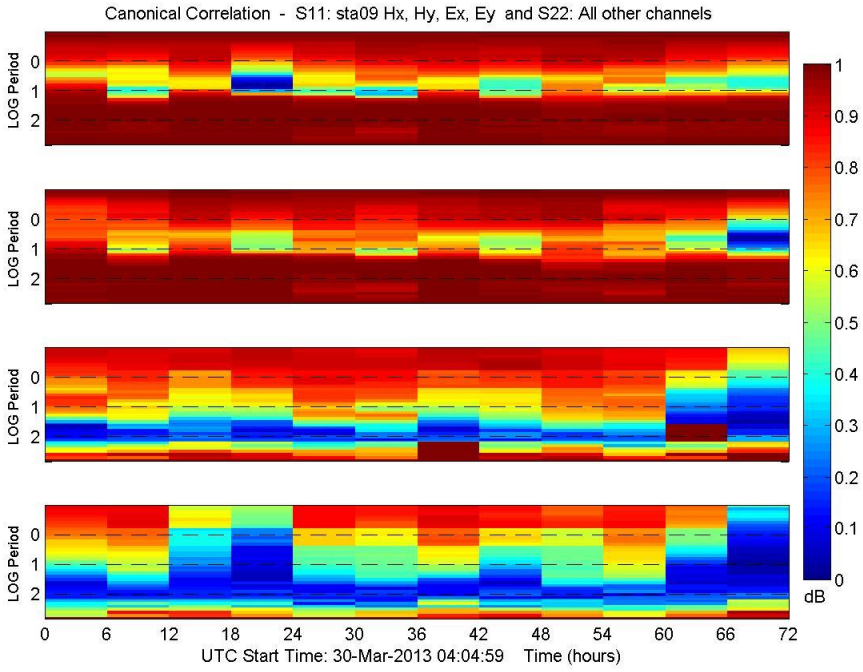
Canonical Correlation - S11: sta09 Hx, Hy, Ex, Ey and S22: All other channels
LOG Period
0
1
2
1
0.9
0.8
0.7
0.6
0.5
0.4
0.3
0.2
0.1
0
dB
0 6 12 18 24 30 36 42 48 54 60 66 72
UTC Start Time: 30-Mar-2013 04:04:59 Time (hours)

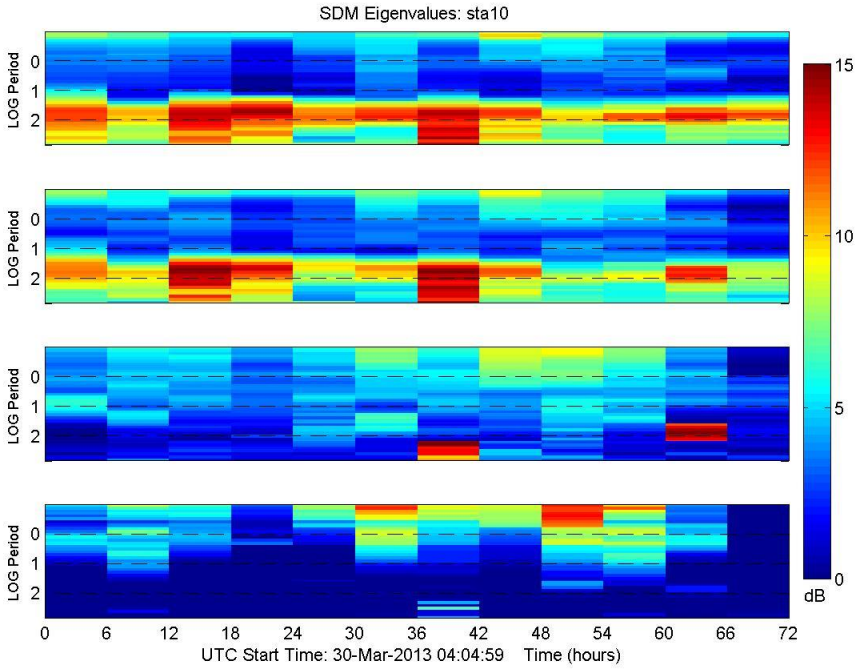
SDM Eigenvalues: sta10
LOG Period
0
1
2
15
10
5
0
dB
0 6 12 18 24 30 36 42 48 54 60 66 72
UTC Start Time: 30-Mar-2013 04:04:59 Time (hours)

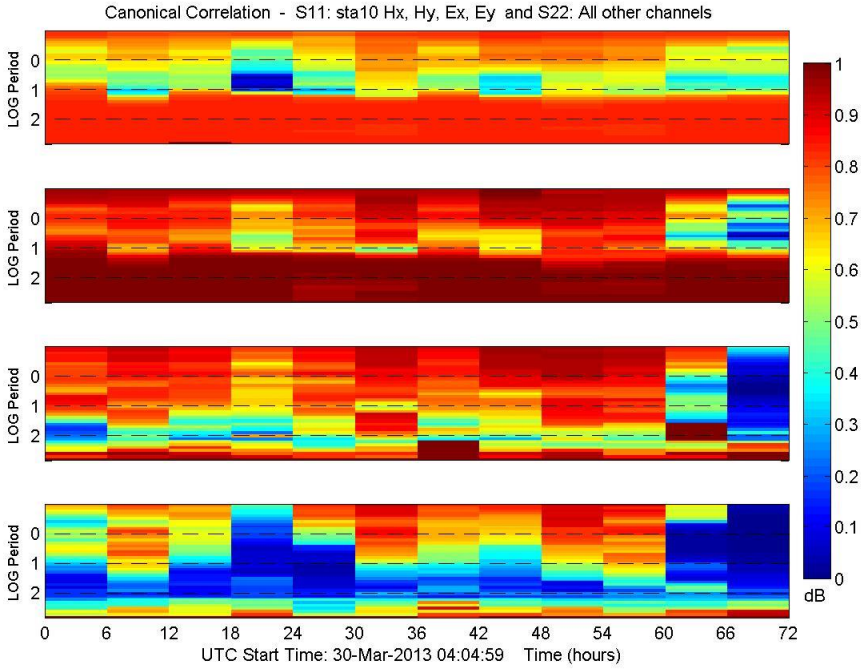
Canonical Correlation - S11: sta10 Hx, Hy, Ex, Ey and S22: All other channels
LOG Period
0
1
2
1
0.9
0.8
0.7
0.6
0.5
0.4
0.3
0.2
0.1
0
dB
0 6 12 18 24 30 36 42 48 54 60 66 72
UTC Start Time: 30-Mar-2013 04:04:59 Time (hours)

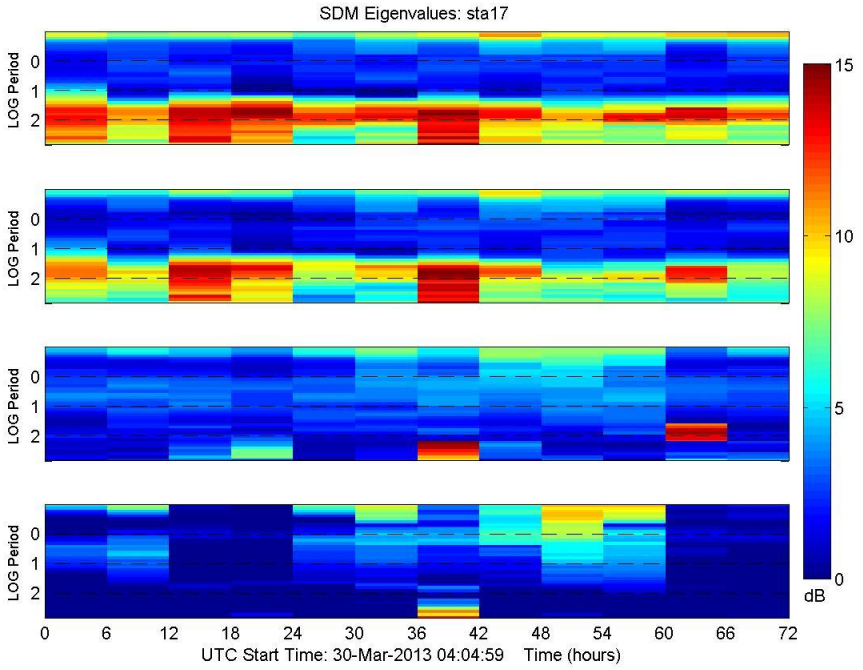
SDM Eigenvalues: sta17
LOG Period
0
1
2
15
10
5
0
dB
0 6 12 18 24 30 36 42 48 54 60 66 72
UTC Start Time: 30-Mar-2013 04:04:59 Time (hours)

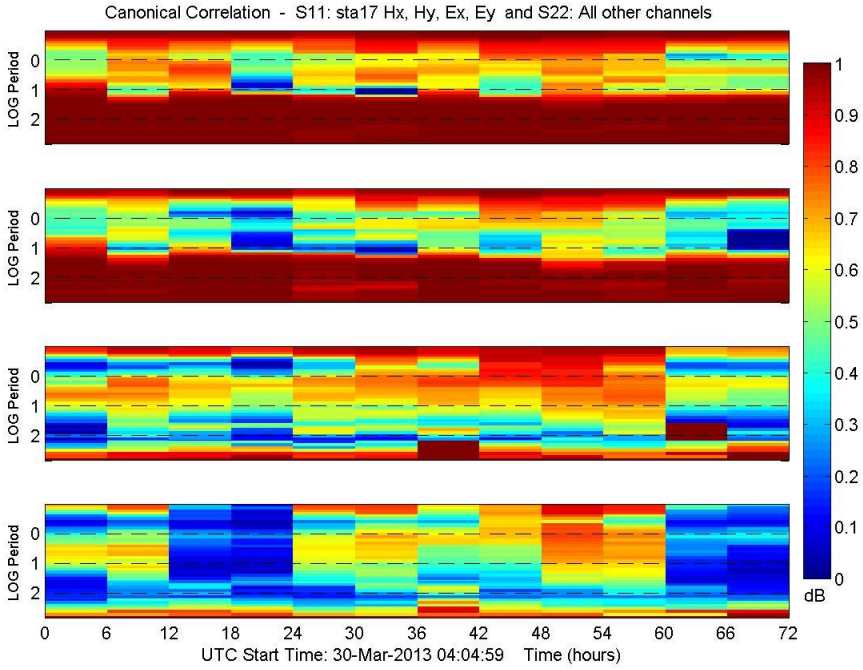
Canonical Correlation - S11: sta17 Hx, Hy, Ex, Ey and S22: All other channels
LOG Period
0
1
2
1
0.9
0.8
0.7
0.6
0.5
0.4
0.3
0.2
0.1
0
dB
0 6 12 18 24 30 36 42 48 54 60 66 72
UTC Start Time: 30-Mar-2013 04:04:59 Time (hours)

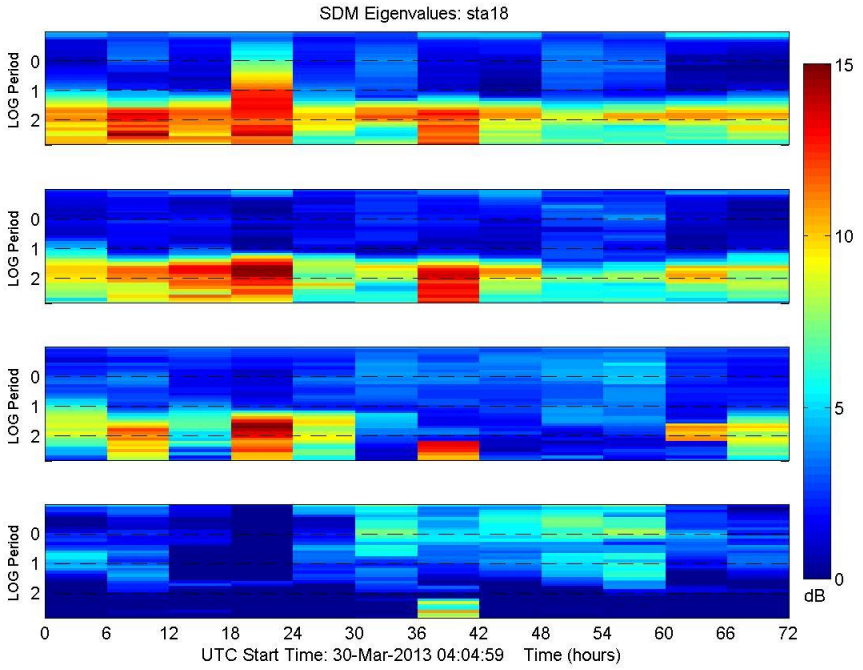
SDM Eigenvalues: sta18
LOG Period
0
1
2
15
10
5
0
dB
0 6 12 18 24 30 36 42 48 54 60 66 72
UTC Start Time: 30-Mar-2013 04:04:59 Time (hours)

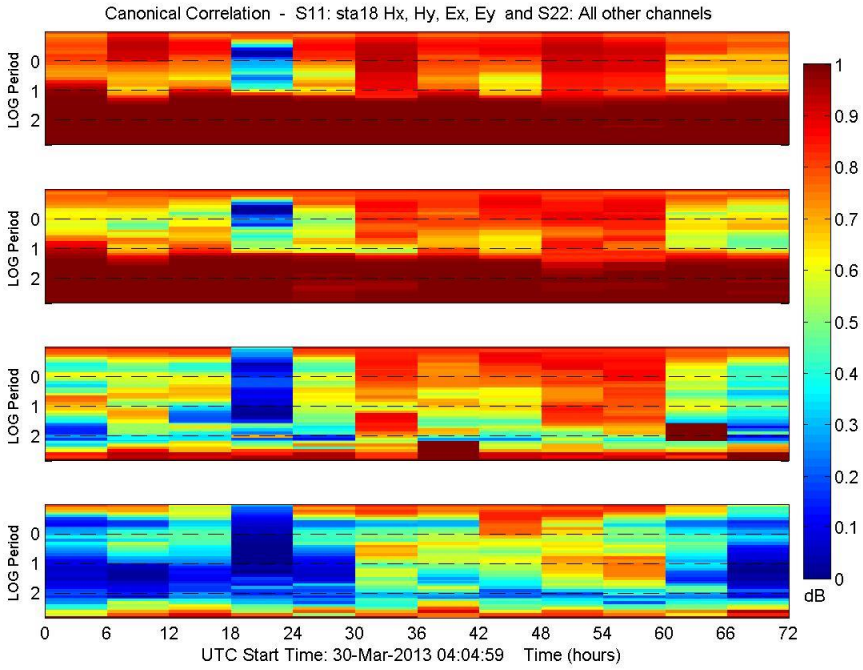
Canonical Correlation - S11: sta18 Hx, Hy, Ex, Ey and S22: All other channels
LOG Period
0
1
2
1
0.9
0.8
0.7
0.6
0.5
0.4
0.3
0.2
0.1
0
dB
0 6 12 18 24 30 36 42 48 54 60 66 72
UTC Start Time: 30-Mar-2013 04:04:59 Time (hours)

APPENDIX C

Difference between normalized third eigenvalue and canonical correlation for Kilauea data 2012-2013

Difference between the normalized third eigenvalue of each station (Hx, Hy, Ex and Ey channels) included in S_{AA} with other channels from the group included in S_{BB} , where S_{AA} and S_{BB} are submatrices of the SDM. S_{BB} includes either all other E field channels.High values as indicated by yellow and red colors, imply large inverse correlations between S_{AA} and S_{BB}, and are an indication of spectral self-potential signals that may be related to fluid flow.

C.1 Group 1: Stations 3, 4, 5, 19

These results come from the differencing of the normalized third dominant eigenvalue and the canonical correlation. These are from the 6 hour segmented Kilauea data. Figures C.1.1 – C.1.4 are the diagnostic difference of the third eigenvalue of each station (Hx, Hy, Ex and Ey channels) included in S_{AA}, with all other Electric field channels in the group placed into S_{BB}. The higher the value, the less correlation between S_{AA} and S_{BB}. The line plots below each colored plot are the normalized signal and the canonical correlation at each time band.

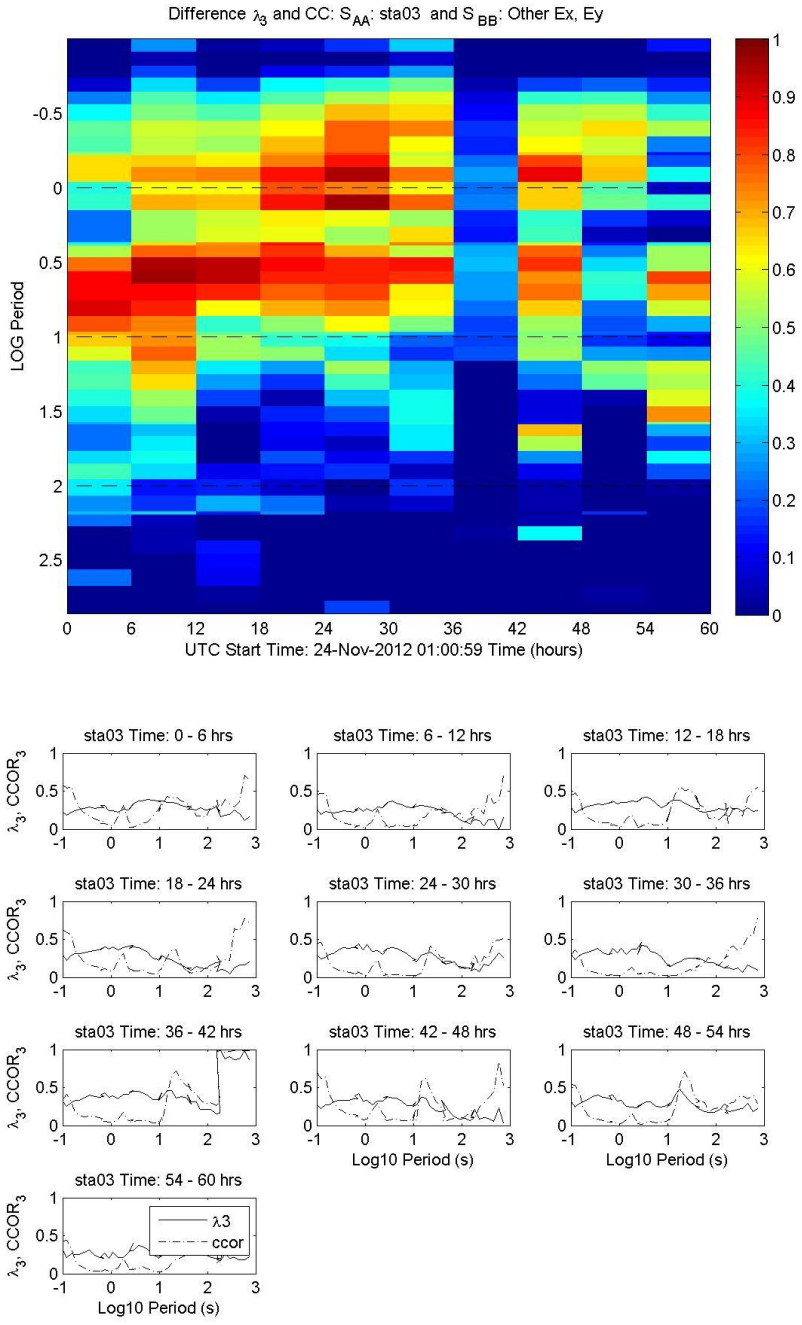
Difference λ3 and CC: SAA: sta03 and SBB: Other Ex, Ey
LOG Period
UTC Start Time: 24-Nov-2012 01:00:59 Time (hours)
sta03 Time: 0 - 6 hrs
sta03 Time: 6 - 12 hrs
sta03 Time: 12 - 18 hrs
sta03 Time: 18 - 24 hrs
sta03 Time: 24 - 30 hrs
sta03 Time: 30 - 36 hrs
sta03 Time: 36 - 42 hrs
sta03 Time: 42 - 48 hrs
sta03 Time: 48 - 54 hrs
sta03 Time: 54 - 60 hrs
λ3, CCOR3
Log10 Period (s)
λ3
ccor

Figure C.1.1

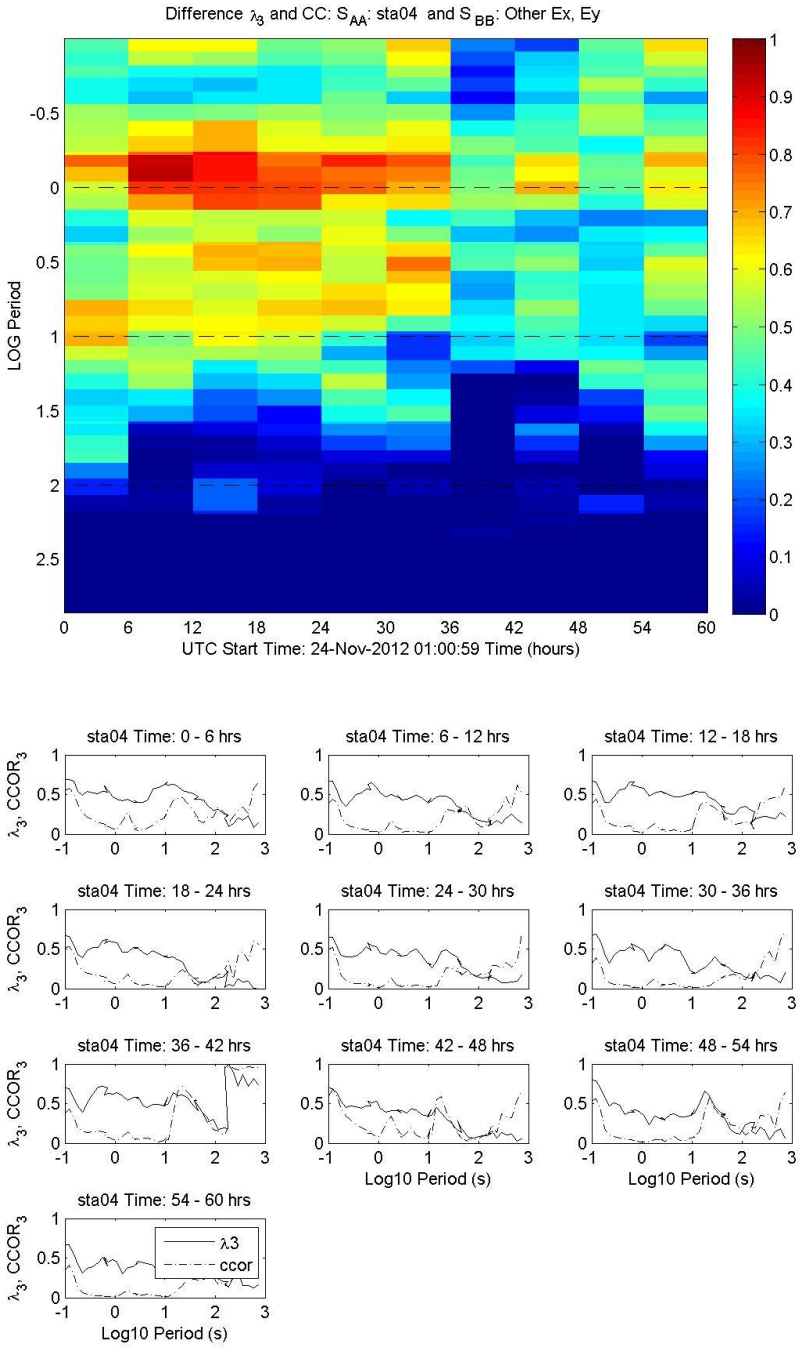
Difference λ3 and CC: SAA: sta04 and SBB: Other Ex, Ey
LOG Period
UTC Start Time: 24-Nov-2012 01:00:59 Time (hours)
sta04 Time: 0 - 6 hrs
sta04 Time: 6 - 12 hrs
sta04 Time: 12 - 18 hrs
sta04 Time: 18 - 24 hrs
sta04 Time: 24 - 30 hrs
sta04 Time: 30 - 36 hrs
sta04 Time: 36 - 42 hrs
sta04 Time: 42 - 48 hrs
sta04 Time: 48 - 54 hrs
sta04 Time: 54 - 60 hrs
λ3, CCOR3
Log10 Period (s)
λ3
ccor

Figure C.1.2

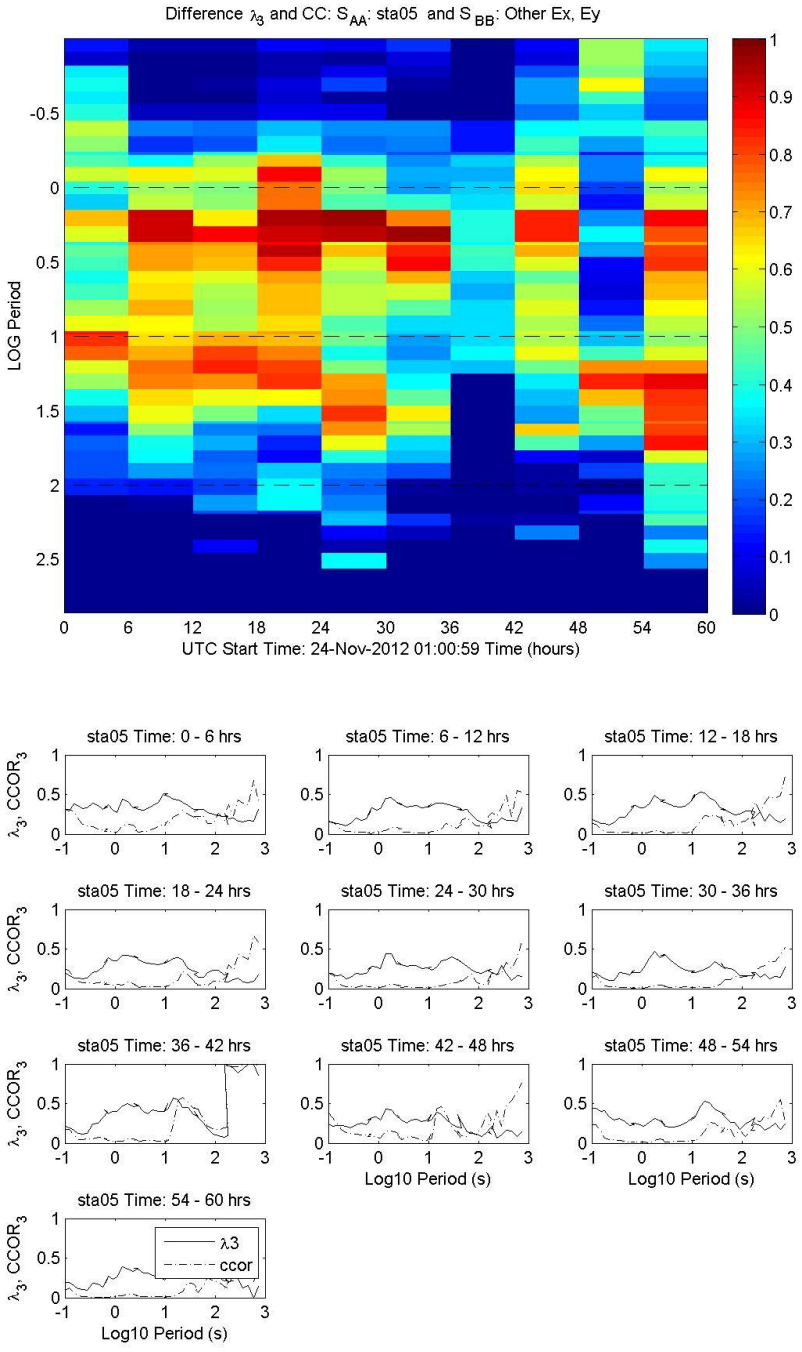
Difference λ3 and CC: S AA: sta05 and S BB: Other Ex, Ey
LOG Period
UTC Start Time: 24-Nov-2012 01:00:59 Time (hours)
sta05 Time: 0 - 6 hrs
sta05 Time: 6 - 12 hrs
sta05 Time: 12 - 18 hrs
sta05 Time: 18 - 24 hrs
sta05 Time: 24 - 30 hrs
sta05 Time: 30 - 36 hrs
sta05 Time: 36 - 42 hrs
sta05 Time: 42 - 48 hrs
sta05 Time: 48 - 54 hrs
sta05 Time: 54 - 60 hrs
λ3, CCOR3
Log10 Period (s)
λ3
ccor

Figure C.1.3

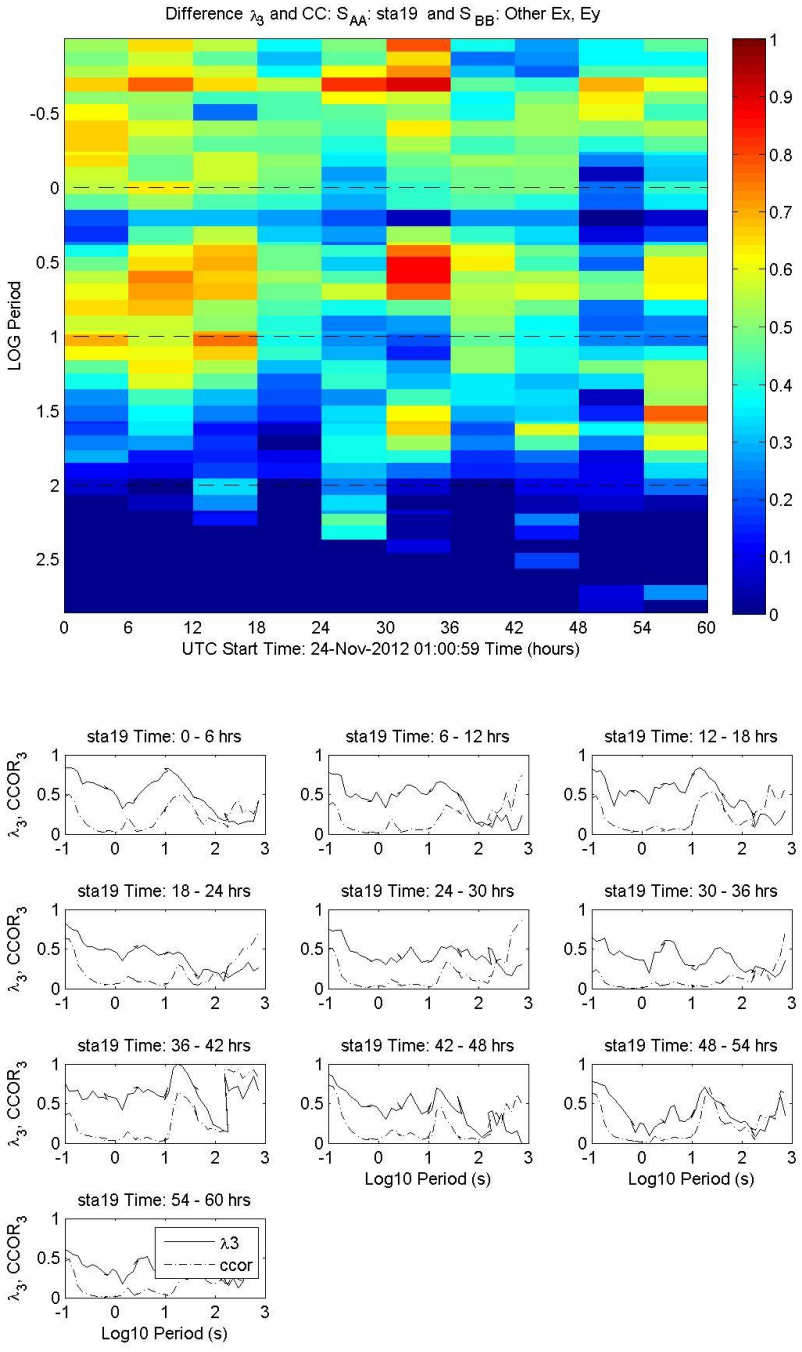
Difference λ3 and CC: SAA: sta19 and SBB: Other Ex, Ey
LOG Period
UTC Start Time: 24-Nov-2012 01:00:59 Time (hours)
sta19 Time: 0 - 6 hrs
sta19 Time: 6 - 12 hrs
sta19 Time: 12 - 18 hrs
sta19 Time: 18 - 24 hrs
sta19 Time: 24 - 30 hrs
sta19 Time: 30 - 36 hrs
sta19 Time: 36 - 42 hrs
sta19 Time: 42 - 48 hrs
sta19 Time: 48 - 54 hrs
sta19 Time: 54 - 60 hrs
λ3, CCOR3
Log10 Period (s)
λ3
ccor

Figure C.1.4

C.2 Group 2: Stations 1, 12, 13, 15

These results come from the differencing of the normalized third dominant eigenvalue and the canonical correlation. These are from the 6 hour segmented Kilauea data. Figures C.2.1 – C.2.4 are the diagnostic difference of the third eigenvalue of each station (Hx, Hy, Ex and Ey channels) included in S_{AA}, with all other Electric field channels in the group placed into S_{BB}. The higher the value, the less correlation between S_{AA} and S_{BB}. The line plots below each colored plot are the normalized signal and the canonical correlation at each time band.

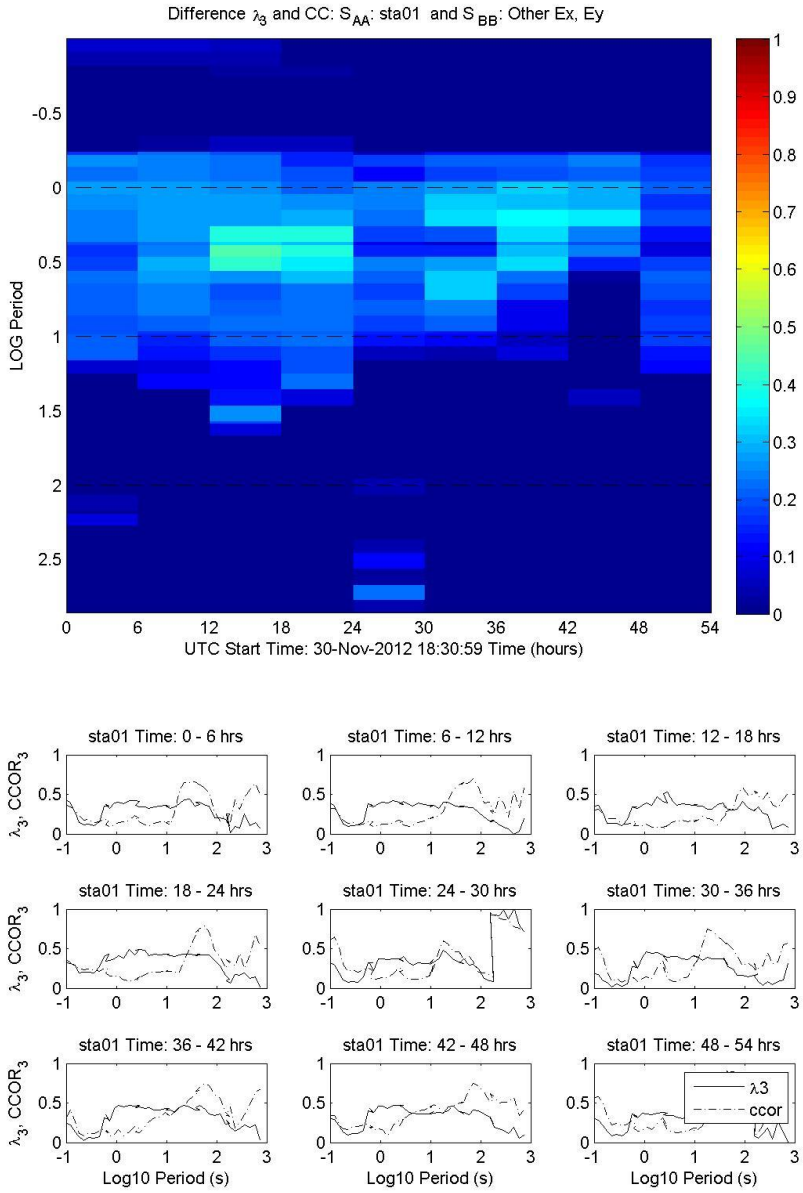
Difference λ3 and CC: S AA: sta01 and S BB: Other Ex, Ey
LOG Period
UTC Start Time: 30-Nov-2012 18:30:59 Time (hours)
sta01 Time: 0 - 6 hrs
sta01 Time: 6 - 12 hrs
sta01 Time: 12 - 18 hrs
sta01 Time: 18 - 24 hrs
sta01 Time: 24 - 30 hrs
sta01 Time: 30 - 36 hrs
sta01 Time: 36 - 42 hrs
sta01 Time: 42 - 48 hrs
sta01 Time: 48 - 54 hrs
λ3, CCOR3
Log10 Period (s)
λ3
ccor

Figure C.2.1

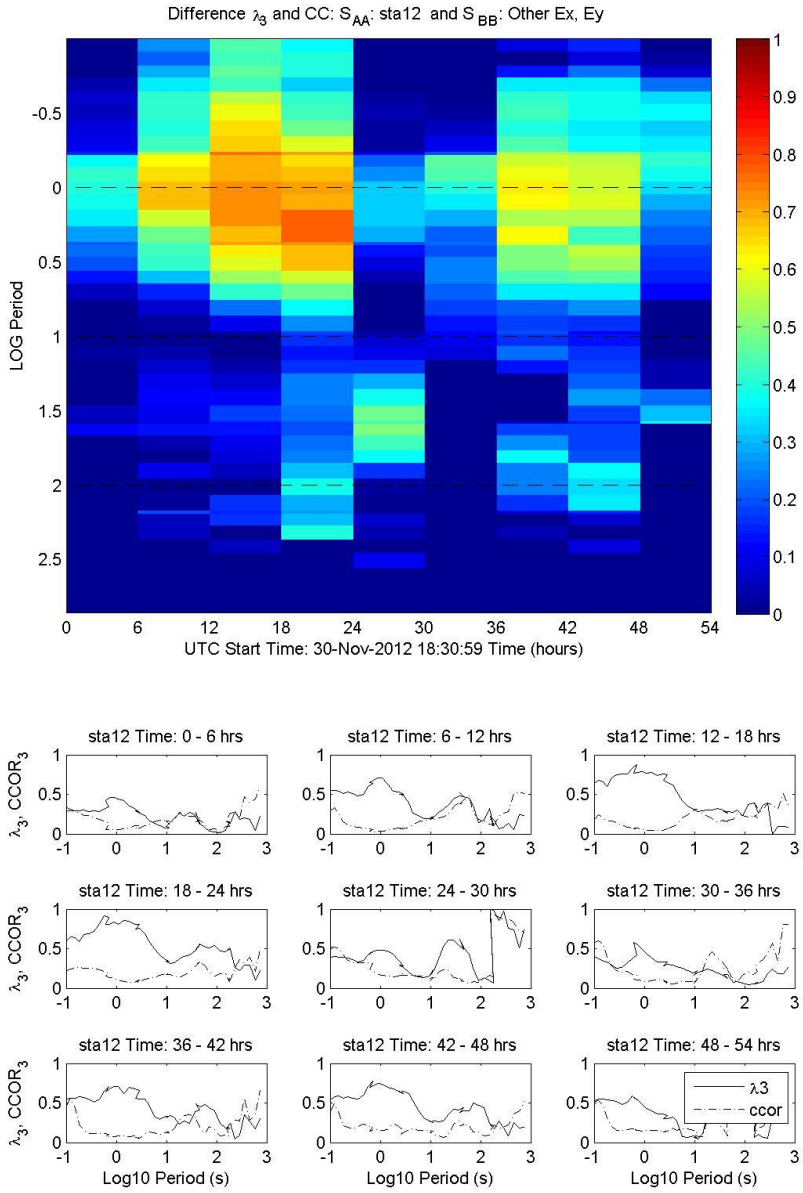
Difference λ3 and CC: S AA: sta12 and S BB: Other Ex, Ey
LOG Period
UTC Start Time: 30-Nov-2012 18:30:59 Time (hours)
sta12 Time: 0 - 6 hrs
sta12 Time: 6 - 12 hrs
sta12 Time: 12 - 18 hrs
sta12 Time: 18 - 24 hrs
sta12 Time: 24 - 30 hrs
sta12 Time: 30 - 36 hrs
sta12 Time: 36 - 42 hrs
sta12 Time: 42 - 48 hrs
sta12 Time: 48 - 54 hrs
λ3, CCOR3
Log10 Period (s)
λ3
ccor

Figure C.2.2

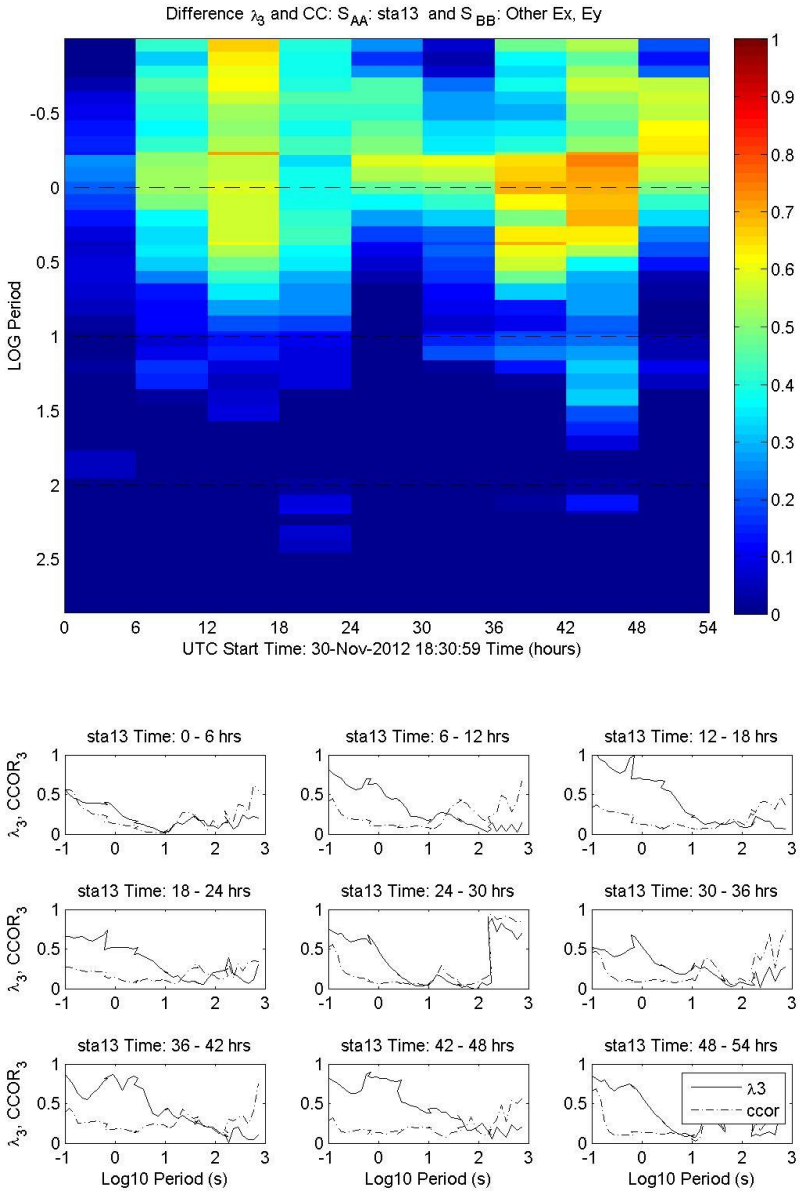
Difference λ3 and CC: S AA: sta13 and S BB: Other Ex, Ey
LOG Period
UTC Start Time: 30-Nov-2012 18:30:59 Time (hours)
sta13 Time: 0 - 6 hrs
sta13 Time: 6 - 12 hrs
sta13 Time: 12 - 18 hrs
sta13 Time: 18 - 24 hrs
sta13 Time: 24 - 30 hrs
sta13 Time: 30 - 36 hrs
sta13 Time: 36 - 42 hrs
sta13 Time: 42 - 48 hrs
sta13 Time: 48 - 54 hrs
λ3, CCOR3
Log10 Period (s)
λ3
ccor

Figure C.2.3

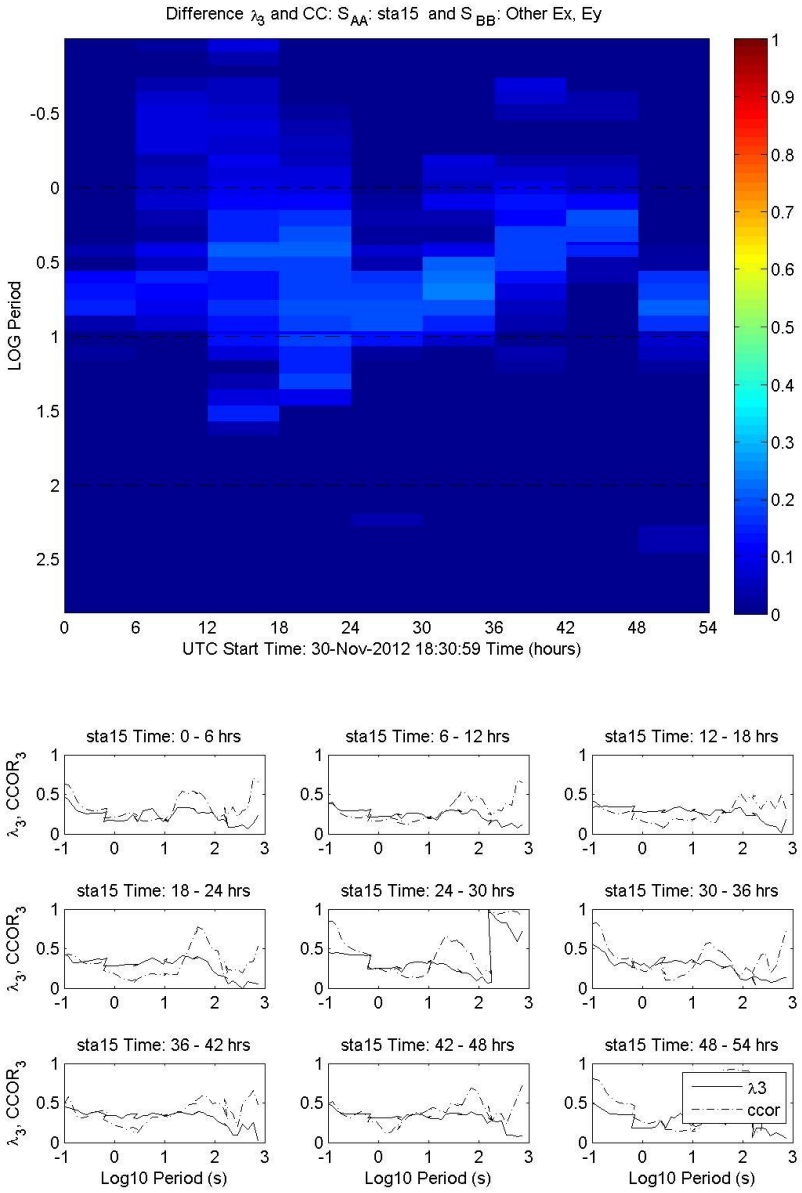
Difference λ3 and CC: SAA: sta15 and SBB: Other Ex, Ey
LOG Period
UTC Start Time: 30-Nov-2012 18:30:59 Time (hours)
sta15 Time: 0 - 6 hrs
sta15 Time: 6 - 12 hrs
sta15 Time: 12 - 18 hrs
sta15 Time: 18 - 24 hrs
sta15 Time: 24 - 30 hrs
sta15 Time: 30 - 36 hrs
sta15 Time: 36 - 42 hrs
sta15 Time: 42 - 48 hrs
sta15 Time: 48 - 54 hrs
λ3, CCOR3
Log10 Period (s)
λ3
ccor

Figure C.2.4

C.3 Group 3: Stations 12, 13, 12b

These results come from the differencing of the normalized third dominant eigenvalue and the canonical correlation. These are from the 6 hour segmented Kilauea data. Figures C.3.1 – C.3.3 are the diagnostic difference of the third eigenvalue of each station (Hx, Hy, Ex and Ey channels) included in S_{AA}, with all other Electric field channels in the group placed into S_{BB}. The higher the value, the less correlation between S_{AA} and S_{BB}. The line plots below each colored plot are the normalized signal and the canonical correlation at each time band.

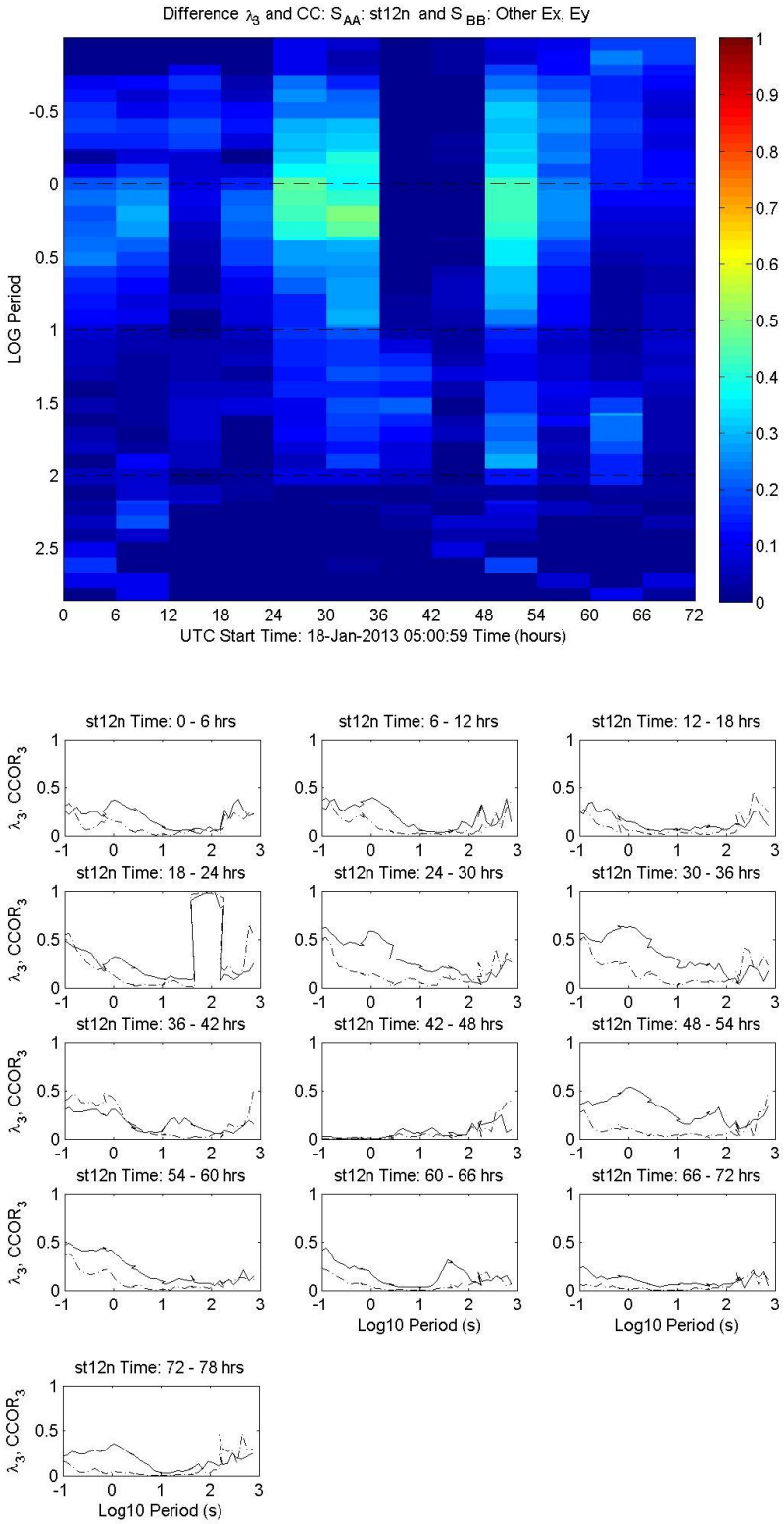
Difference λ3 and CC: SAA: st12n and SBB: Other Ex, Ey
LOG Period
UTC Start Time: 18-Jan-2013 05:00:59 Time (hours)
st12n Time: 0 - 6 hrs
st12n Time: 6 - 12 hrs
st12n Time: 12 - 18 hrs
st12n Time: 18 - 24 hrs
st12n Time: 24 - 30 hrs
st12n Time: 30 - 36 hrs
st12n Time: 36 - 42 hrs
st12n Time: 42 - 48 hrs
st12n Time: 48 - 54 hrs
st12n Time: 54 - 60 hrs
st12n Time: 60 - 66 hrs
st12n Time: 66 - 72 hrs
st12n Time: 72 - 78 hrs
λ3, CCOR3
Log10 Period (s)

Figure C.3.1

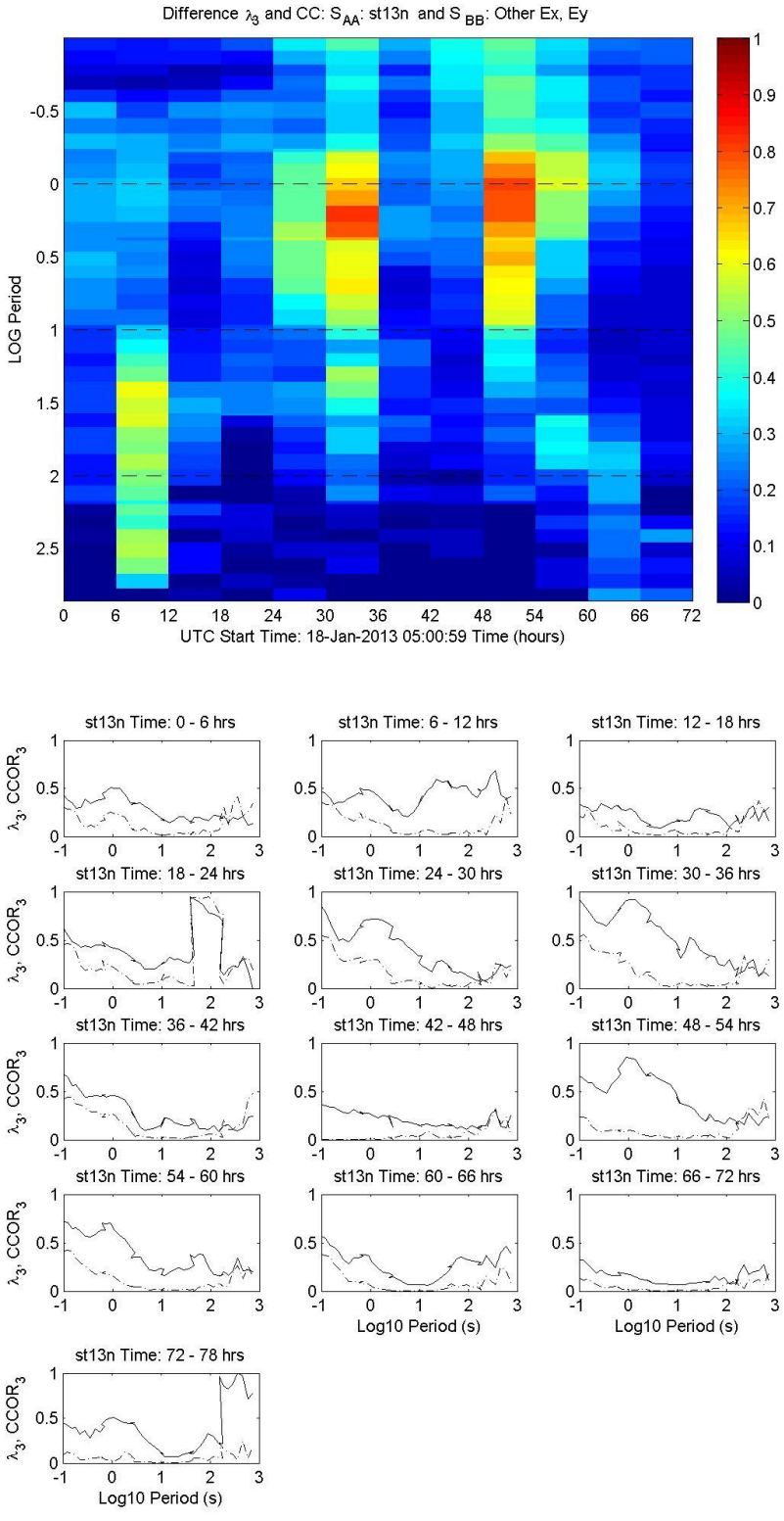
Difference λ3 and CC: SAA: st13n and SBB: Other Ex, Ey
LOG Period
UTC Start Time: 18-Jan-2013 05:00:59 Time (hours)
st13n Time: 0 - 6 hrs
st13n Time: 6 - 12 hrs
st13n Time: 12 - 18 hrs
st13n Time: 18 - 24 hrs
st13n Time: 24 - 30 hrs
st13n Time: 30 - 36 hrs
st13n Time: 36 - 42 hrs
st13n Time: 42 - 48 hrs
st13n Time: 48 - 54 hrs
st13n Time: 54 - 60 hrs
st13n Time: 60 - 66 hrs
st13n Time: 66 - 72 hrs
st13n Time: 72 - 78 hrs
λ3, CCOR3
Log10 Period (s)

Figure 1

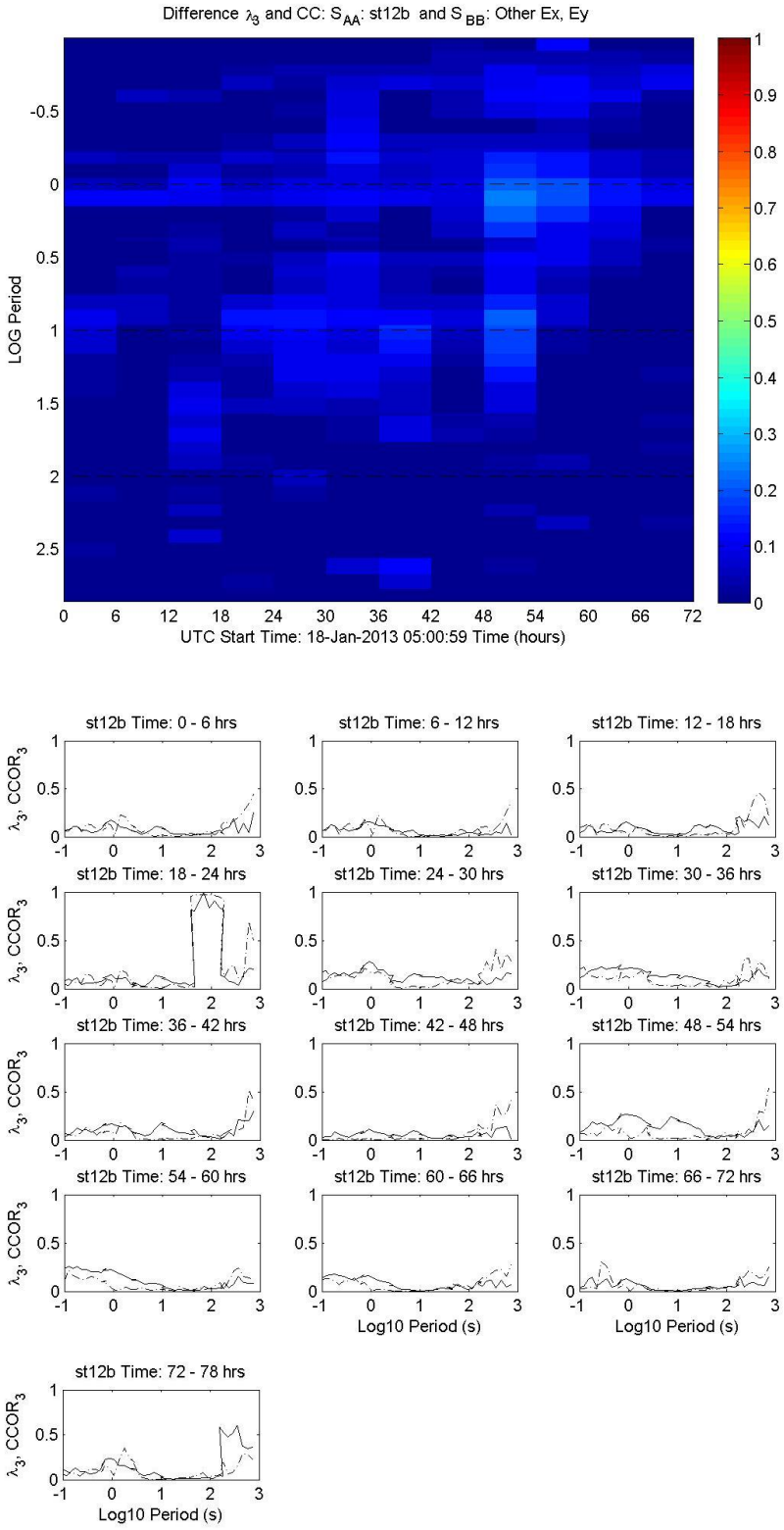
Difference λ_3 and CC: S_{AA}: st12b and S_{BB}: Other Ex, Ey
LOG Period
UTC Start Time: 18-Jan-2013 05:00:59 Time (hours)
st12b Time: 0 - 6 hrs
st12b Time: 6 - 12 hrs
st12b Time: 12 - 18 hrs
st12b Time: 18 - 24 hrs
st12b Time: 24 - 30 hrs
st12b Time: 30 - 36 hrs
st12b Time: 36 - 42 hrs
st12b Time: 42 - 48 hrs
st12b Time: 48 - 54 hrs
st12b Time: 54 - 60 hrs
st12b Time: 60 - 66 hrs
st12b Time: 66 - 72 hrs
st12b Time: 72 - 78 hrs
λ_3, CCOR$_3$
Log10 Period (s)

Figure C.3.3

C.4 Group 4: Stations 1, 6, 8

These results come from the differencing of the normalized third dominant eigenvalue and the canonical correlation. These are from the 6 hour segmented Kilauea data. Figures C.4.1 – C.4.3 are the diagnostic difference of the third eigenvalue of each station (Hx, Hy, Ex and Ey channels) included in S_{AA}, with all other Electric field channels in the group placed into S_{BB}. The higher the value, the less correlation between S_{AA} and S_{BB}. The line plots below each colored plot are the normalized signal and the canonical correlation at each time band.

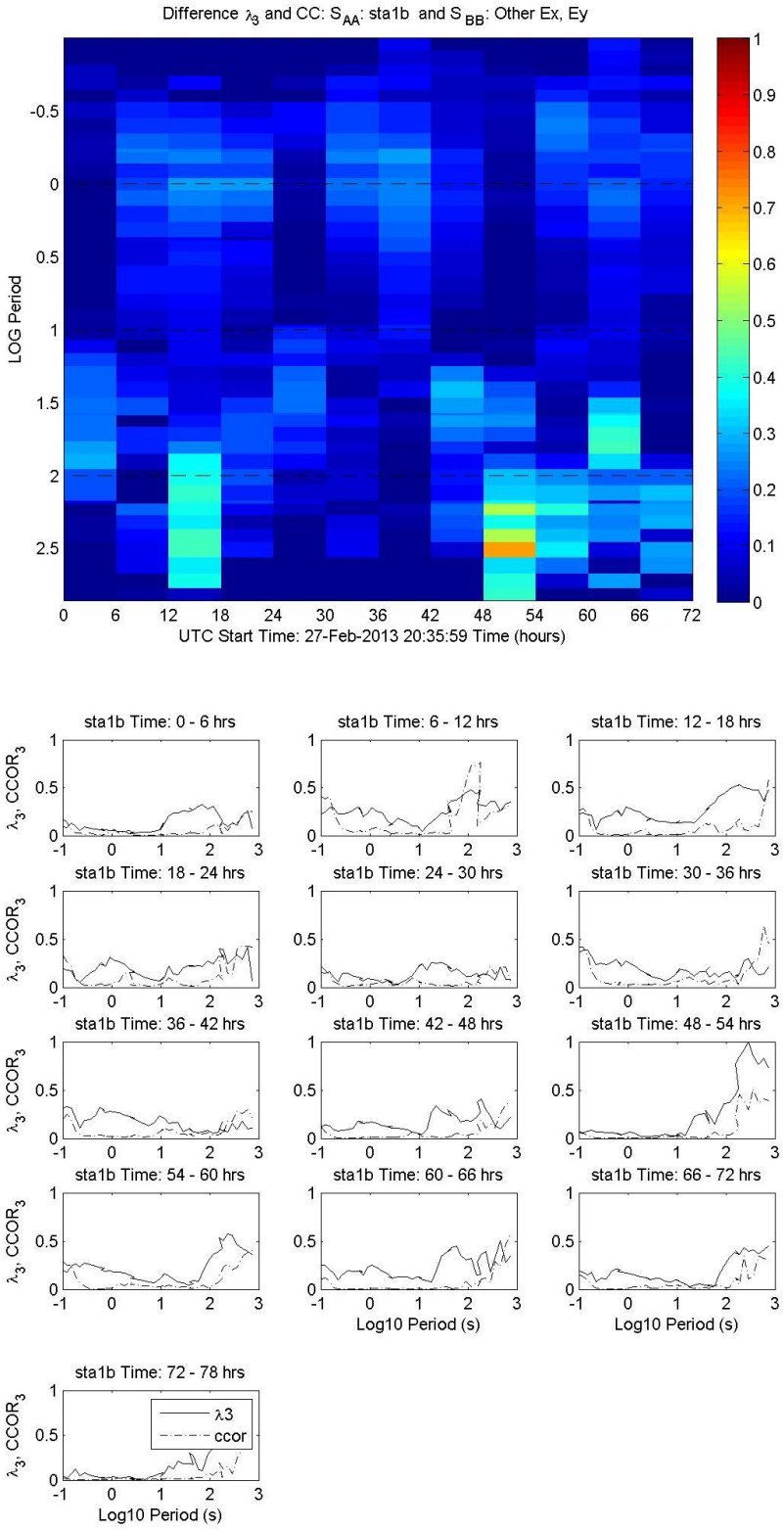
Difference λ3 and CC: SAA: sta1b and SBB: Other Ex, Ey
LOG Period
UTC Start Time: 27-Feb-2013 20:35:59 Time (hours)
sta1b Time: 0 - 6 hrs
sta1b Time: 6 - 12 hrs
sta1b Time: 12 - 18 hrs
sta1b Time: 18 - 24 hrs
sta1b Time: 24 - 30 hrs
sta1b Time: 30 - 36 hrs
sta1b Time: 36 - 42 hrs
sta1b Time: 42 - 48 hrs
sta1b Time: 48 - 54 hrs
sta1b Time: 54 - 60 hrs
sta1b Time: 60 - 66 hrs
sta1b Time: 66 - 72 hrs
sta1b Time: 72 - 78 hrs
λ3, CCOR3
λ3
ccor
Log10 Period (s)

Figure C.4.1.1

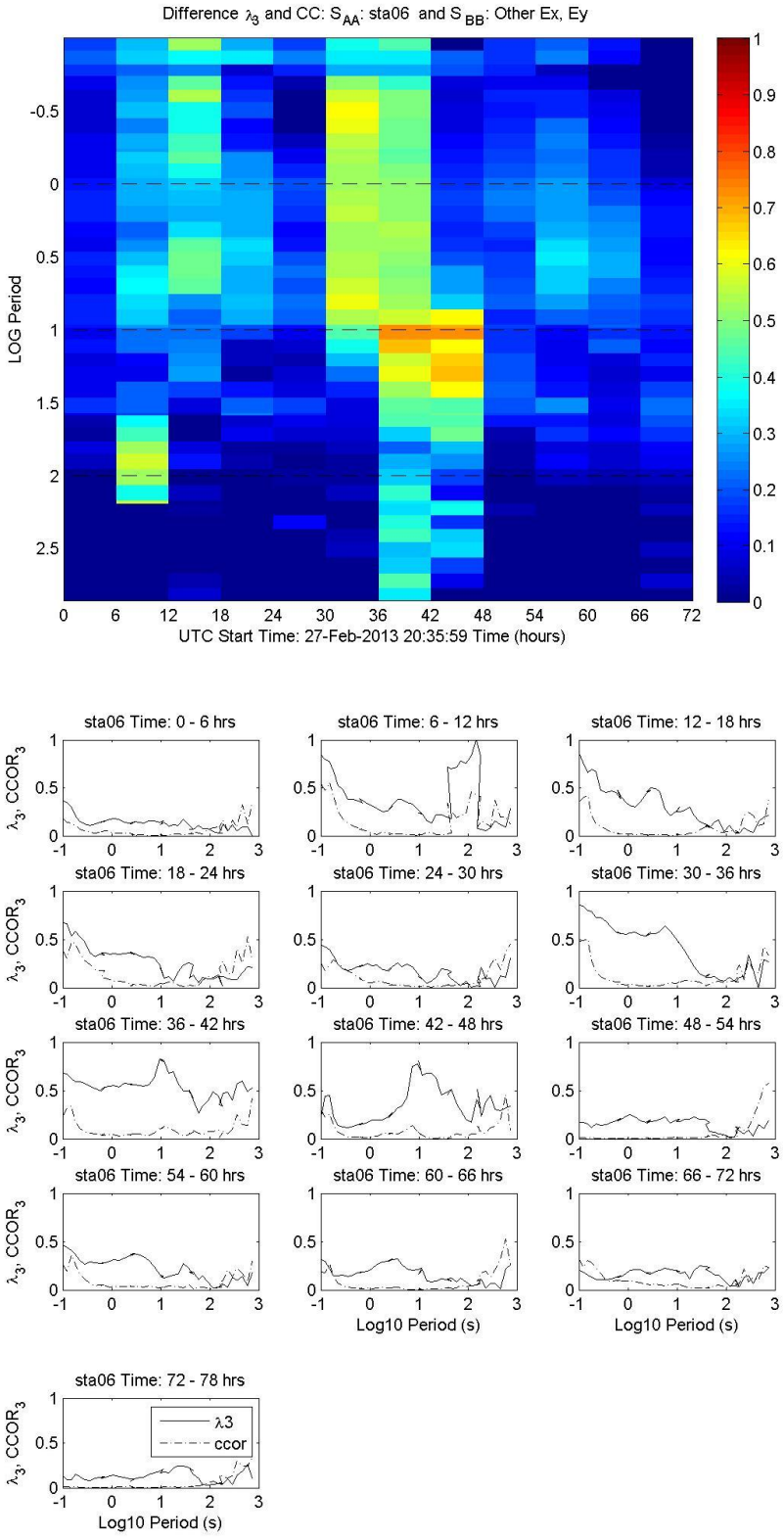
Difference λ3 and CC: S AA: sta06 and S BB: Other Ex, Ey
LOG Period
UTC Start Time: 27-Feb-2013 20:35:59 Time (hours)
sta06 Time: 0 - 6 hrs
sta06 Time: 6 - 12 hrs
sta06 Time: 12 - 18 hrs
sta06 Time: 18 - 24 hrs
sta06 Time: 24 - 30 hrs
sta06 Time: 30 - 36 hrs
sta06 Time: 36 - 42 hrs
sta06 Time: 42 - 48 hrs
sta06 Time: 48 - 54 hrs
sta06 Time: 54 - 60 hrs
sta06 Time: 60 - 66 hrs
sta06 Time: 66 - 72 hrs
sta06 Time: 72 - 78 hrs
λ3, CCOR3
λ3
ccor
Log10 Period (s)

Figure C.4.2

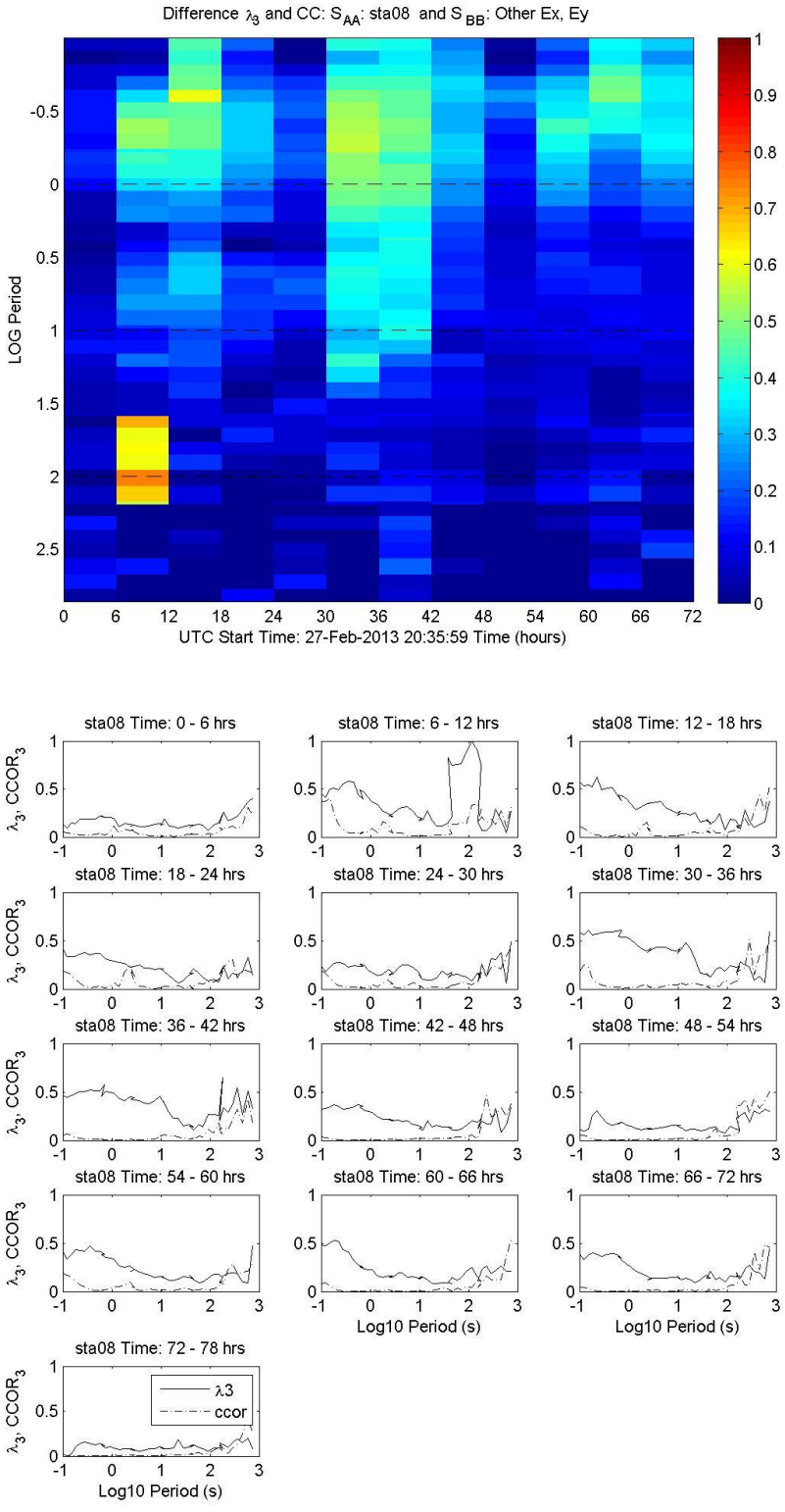
Difference λ3 and CC: SAA: sta08 and SBB: Other Ex, Ey
LOG Period
UTC Start Time: 27-Feb-2013 20:35:59 Time (hours)
sta08 Time: 0 - 6 hrs
sta08 Time: 6 - 12 hrs
sta08 Time: 12 - 18 hrs
sta08 Time: 18 - 24 hrs
sta08 Time: 24 - 30 hrs
sta08 Time: 30 - 36 hrs
sta08 Time: 36 - 42 hrs
sta08 Time: 42 - 48 hrs
sta08 Time: 48 - 54 hrs
sta08 Time: 54 - 60 hrs
sta08 Time: 60 - 66 hrs
sta08 Time: 66 - 72 hrs
sta08 Time: 72 - 78 hrs
λ3, CCOR3
Log10 Period (s)
λ3
ccor

Figure C.4.3

C.5 Group 5: Stations 7, 8, 11

These results come from the differencing of the normalized third dominant eigenvalue and the canonical correlation. These are from the 6 hour segmented Kilauea data. Figures C.5.1 – C.5.3 are the diagnostic difference of the third eigenvalue of each station (Hx, Hy, Ex and Ey channels) included in S_{AA}, with all other Electric field channels in the group placed into S_{BB}. The higher the value, the less correlation between S_{AA} and S_{BB}. The line plots below each colored plot are the normalized signal and the canonical correlation at each time band.

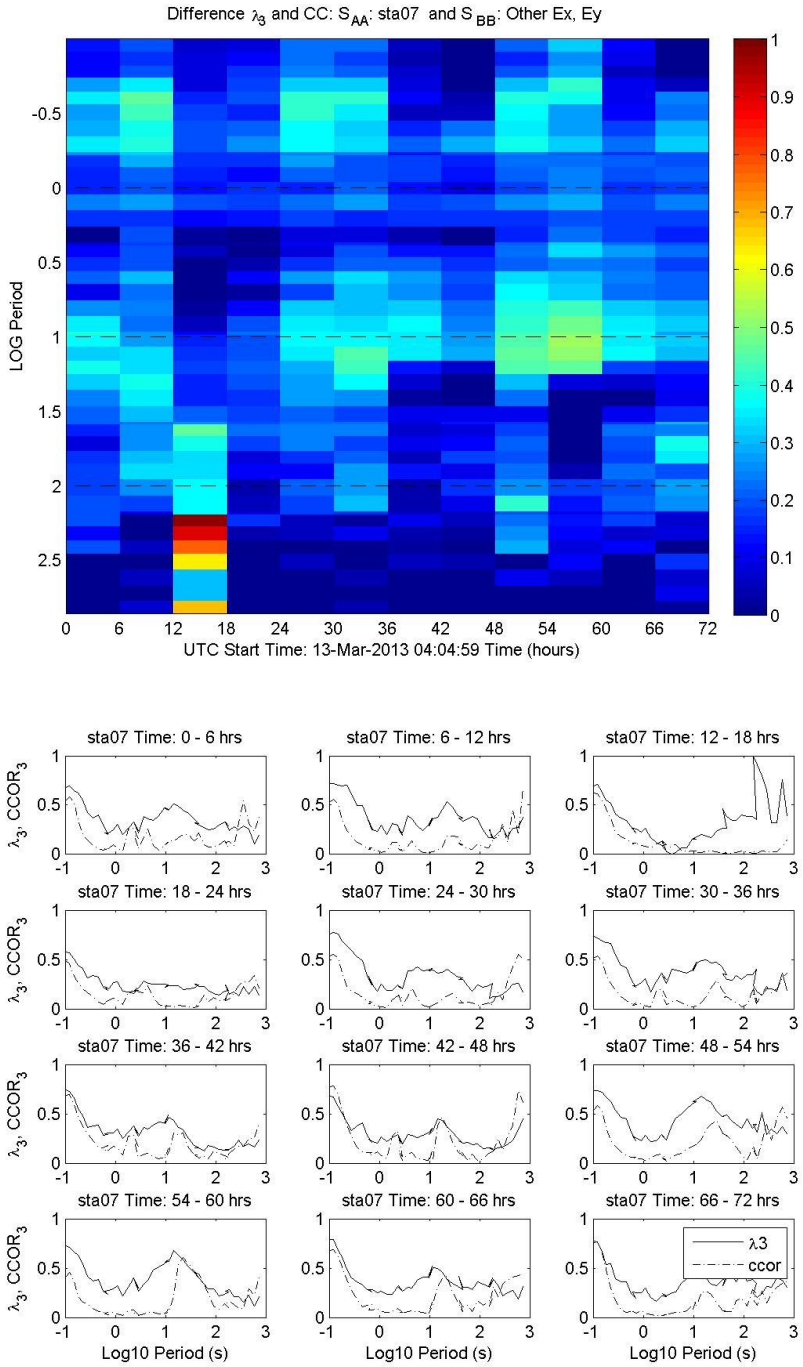
Difference λ3 and CC: SAA: sta07 and SBB: Other Ex, Ey
LOG Period
UTC Start Time: 13-Mar-2013 04:04:59 Time (hours)
sta07 Time: 0 - 6 hrs
sta07 Time: 6 - 12 hrs
sta07 Time: 12 - 18 hrs
sta07 Time: 18 - 24 hrs
sta07 Time: 24 - 30 hrs
sta07 Time: 30 - 36 hrs
sta07 Time: 36 - 42 hrs
sta07 Time: 42 - 48 hrs
sta07 Time: 48 - 54 hrs
sta07 Time: 54 - 60 hrs
sta07 Time: 60 - 66 hrs
sta07 Time: 66 - 72 hrs
λ3, CCOR3
Log10 Period (s)
λ3
ccor

Figure C.5.1

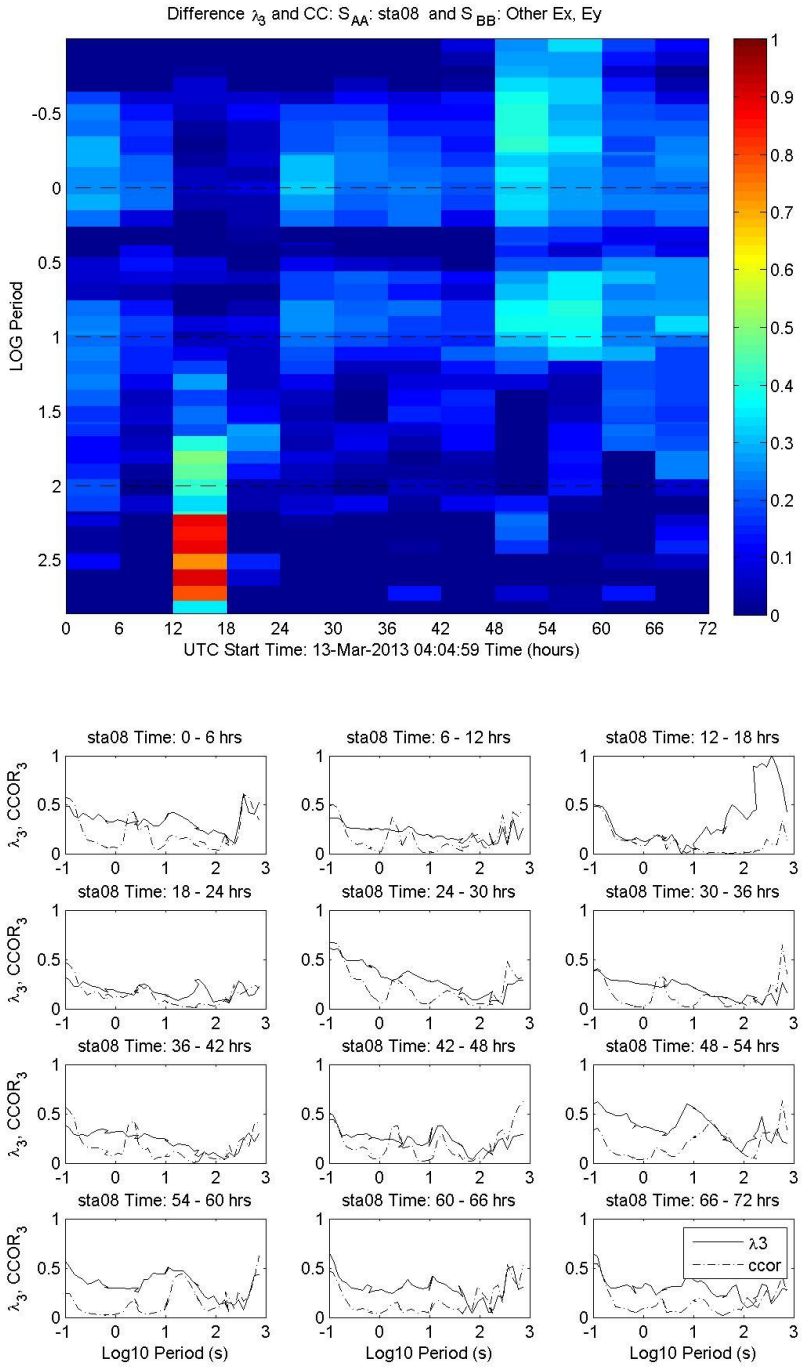
Difference λ3 and CC: SAA: sta08 and SBB: Other Ex, Ey
LOG Period
UTC Start Time: 13-Mar-2013 04:04:59 Time (hours)
sta08 Time: 0 - 6 hrs
sta08 Time: 6 - 12 hrs
sta08 Time: 12 - 18 hrs
sta08 Time: 18 - 24 hrs
sta08 Time: 24 - 30 hrs
sta08 Time: 30 - 36 hrs
sta08 Time: 36 - 42 hrs
sta08 Time: 42 - 48 hrs
sta08 Time: 48 - 54 hrs
sta08 Time: 54 - 60 hrs
sta08 Time: 60 - 66 hrs
sta08 Time: 66 - 72 hrs
λ3, CCOR3
Log10 Period (s)
λ3
ccor

Figure C.5.2

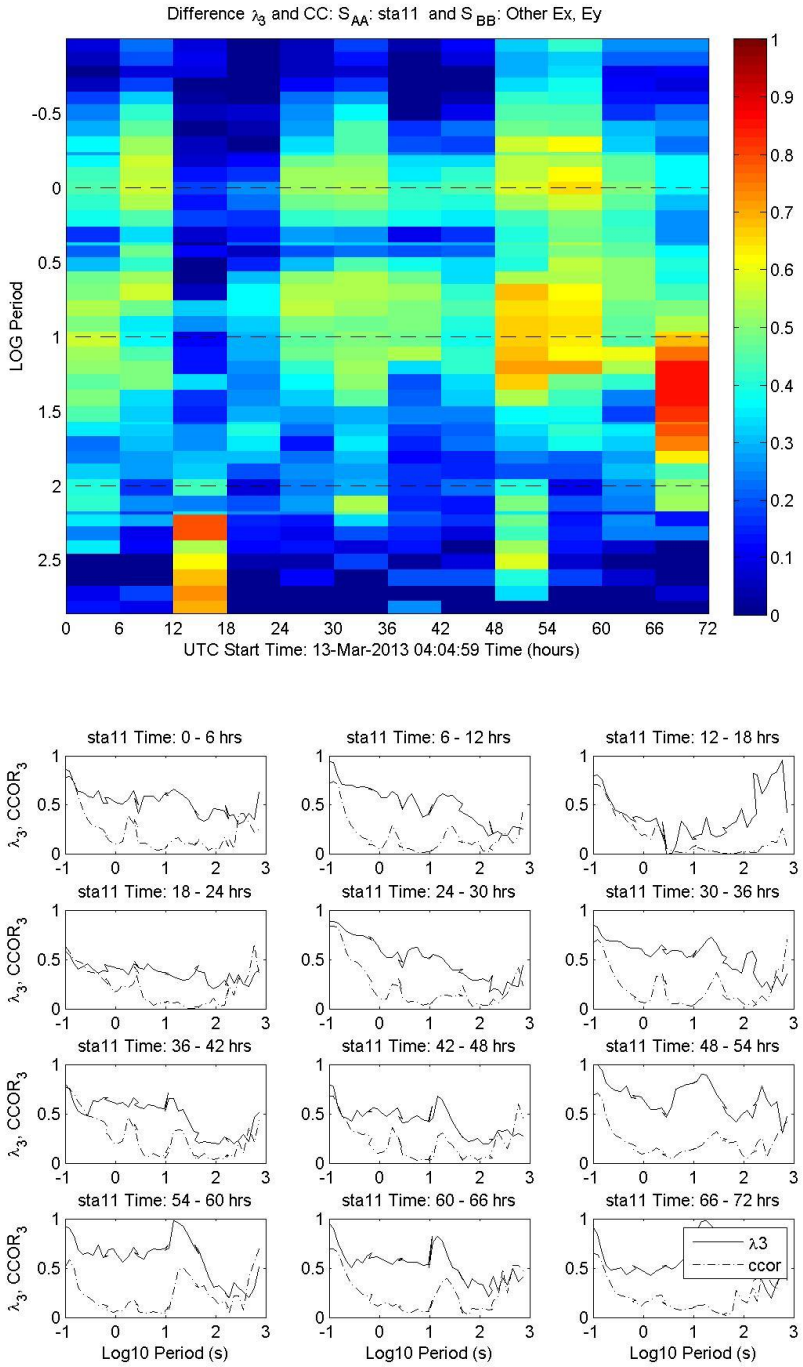
Difference λ3 and CC: SAA: sta11 and SBB: Other Ex, Ey
LOG Period
UTC Start Time: 13-Mar-2013 04:04:59 Time (hours)
sta11 Time: 0 - 6 hrs
sta11 Time: 6 - 12 hrs
sta11 Time: 12 - 18 hrs
sta11 Time: 18 - 24 hrs
sta11 Time: 24 - 30 hrs
sta11 Time: 30 - 36 hrs
sta11 Time: 36 - 42 hrs
sta11 Time: 42 - 48 hrs
sta11 Time: 48 - 54 hrs
sta11 Time: 54 - 60 hrs
sta11 Time: 60 - 66 hrs
sta11 Time: 66 - 72 hrs
λ3, CCOR3
Log10 Period (s)
λ3
ccor

Figure C.5.3

C.6 Group 6: Stations 9, 10, 17 18

These results come from the differencing of the normalized third dominant eigenvalue and the canonical correlation. These are from the 6 hour segmented Kilauea data. Figures C.6.1 – C.6.4 are the diagnostic difference of the third eigenvalue of each station (Hx, Hy, Ex and Ey channels) included in S_{AA}, with all other Electric field channels in the group placed into S_{BB}. The higher the value, the less correlation between S_{AA} and S_{BB}. The line plots below each colored plot are the normalized signal and the canonical correlation at each time band.

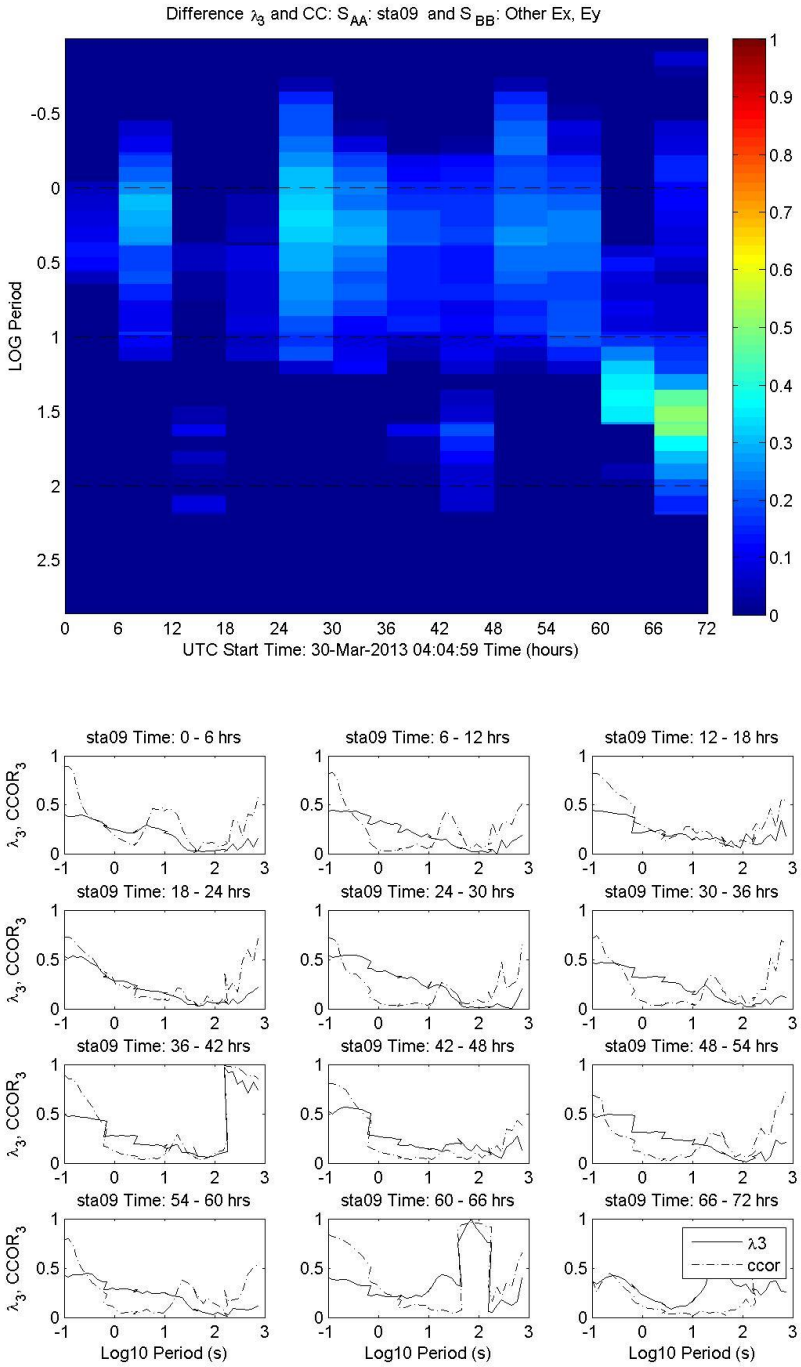
Difference λ3 and CC: S AA: sta09 and S BB: Other Ex, Ey
LOG Period
UTC Start Time: 30-Mar-2013 04:04:59 Time (hours)
sta09 Time: 0 - 6 hrs
sta09 Time: 6 - 12 hrs
sta09 Time: 12 - 18 hrs
sta09 Time: 18 - 24 hrs
sta09 Time: 24 - 30 hrs
sta09 Time: 30 - 36 hrs
sta09 Time: 36 - 42 hrs
sta09 Time: 42 - 48 hrs
sta09 Time: 48 - 54 hrs
sta09 Time: 54 - 60 hrs
sta09 Time: 60 - 66 hrs
sta09 Time: 66 - 72 hrs
λ3, CCOR3
Log10 Period (s)
λ3
ccor

Figure C.6.1

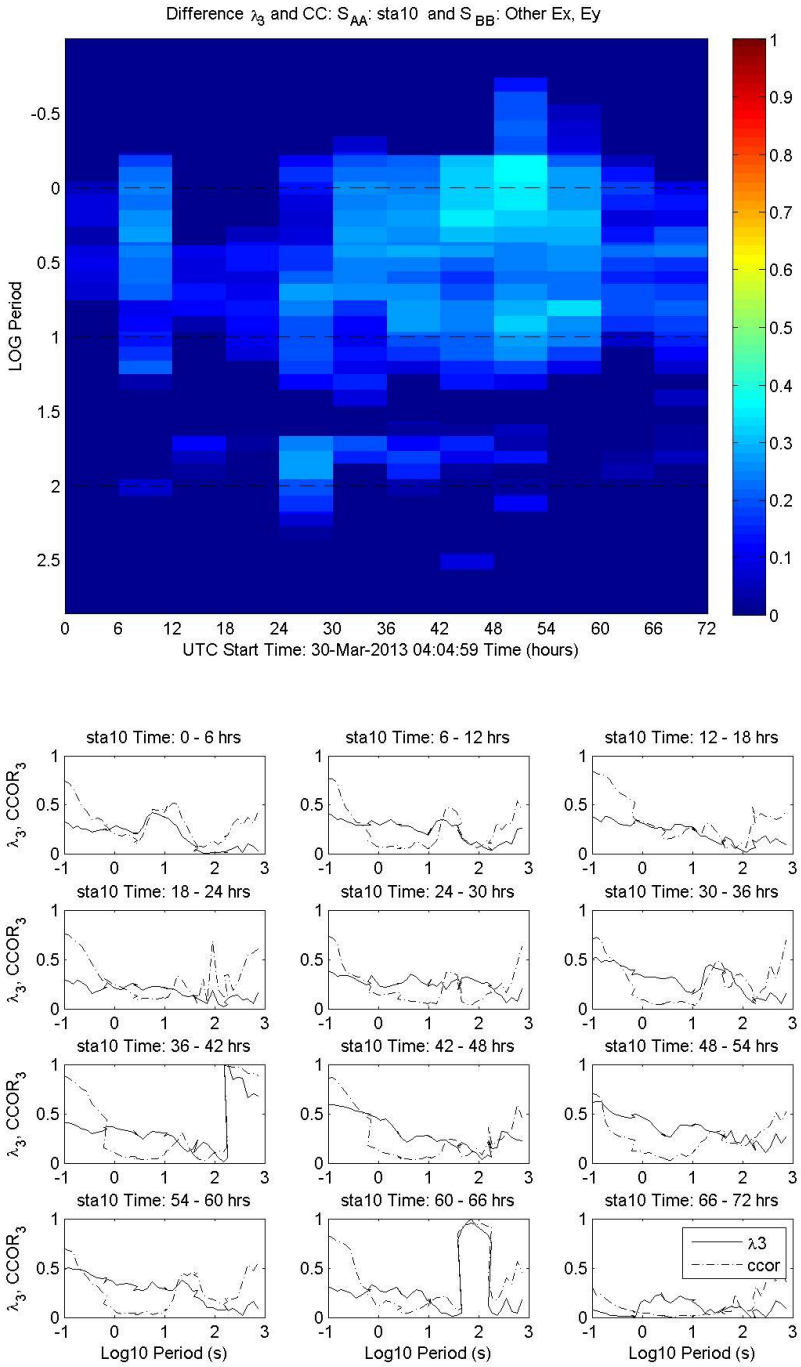
Difference λ3 and CC: S AA: sta10 and S BB: Other Ex, Ey
LOG Period
UTC Start Time: 30-Mar-2013 04:04:59 Time (hours)
sta10 Time: 0 - 6 hrs
sta10 Time: 6 - 12 hrs
sta10 Time: 12 - 18 hrs
sta10 Time: 18 - 24 hrs
sta10 Time: 24 - 30 hrs
sta10 Time: 30 - 36 hrs
sta10 Time: 36 - 42 hrs
sta10 Time: 42 - 48 hrs
sta10 Time: 48 - 54 hrs
sta10 Time: 54 - 60 hrs
sta10 Time: 60 - 66 hrs
sta10 Time: 66 - 72 hrs
λ3, CCOR3
Log10 Period (s)
λ3
ccor

Figure C.6.2

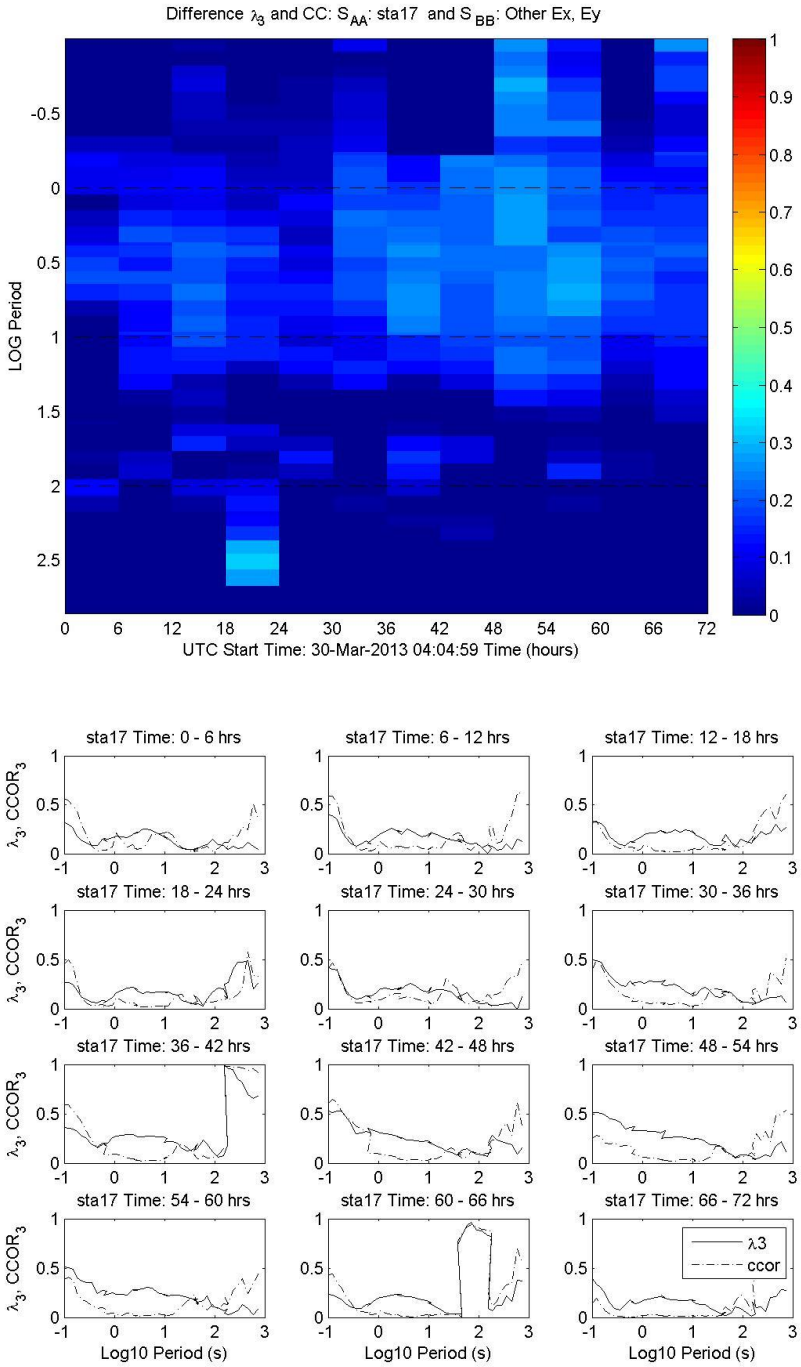
Difference λ3 and CC: SAA: sta17 and SBB: Other Ex, Ey
LOG Period
UTC Start Time: 30-Mar-2013 04:04:59 Time (hours)
sta17 Time: 0 - 6 hrs
sta17 Time: 6 - 12 hrs
sta17 Time: 12 - 18 hrs
sta17 Time: 18 - 24 hrs
sta17 Time: 24 - 30 hrs
sta17 Time: 30 - 36 hrs
sta17 Time: 36 - 42 hrs
sta17 Time: 42 - 48 hrs
sta17 Time: 48 - 54 hrs
sta17 Time: 54 - 60 hrs
sta17 Time: 60 - 66 hrs
sta17 Time: 66 - 72 hrs
λ3, CCOR3
λ3
ccor
Log10 Period (s)

Figure C.6.3

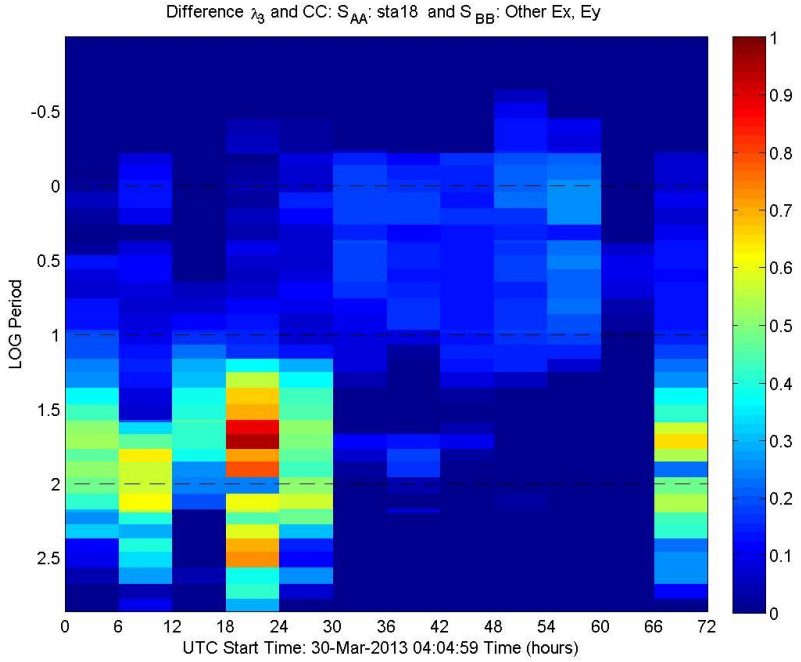
Difference λ3 and CC: S AA: sta18 and S BB: Other Ex, Ey
LOG Period
-0.5
0
0.5
1
1.5
2
2.5
0 6 12 18 24 30 36 42 48 54 60 66 72
UTC Start Time: 30-Mar-2013 04:04:59 Time (hours)
1 0.9 0.8 0.7 0.6 0.5 0.4 0.3 0.2 0.1 0

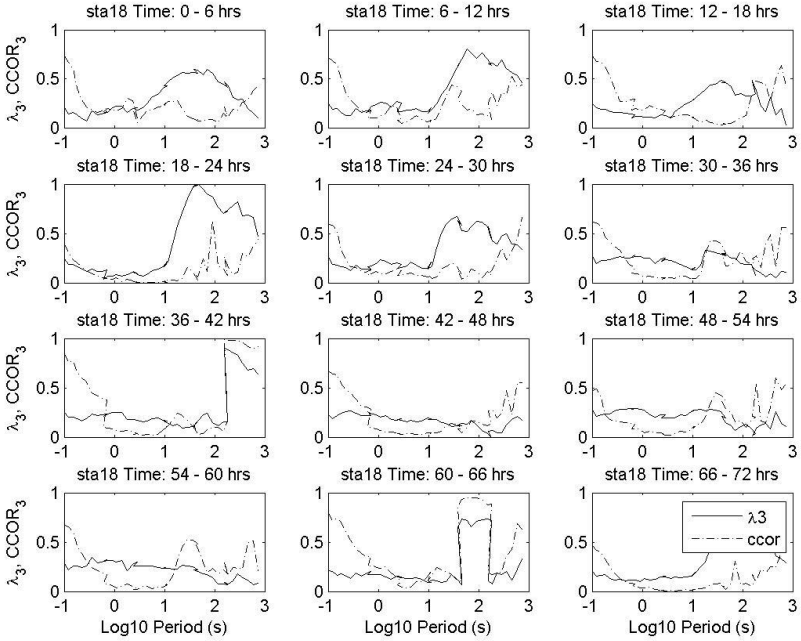
sta18 Time: 0 - 6 hrs
sta18 Time: 6 - 12 hrs
sta18 Time: 12 - 18 hrs
sta18 Time: 18 - 24 hrs
sta18 Time: 24 - 30 hrs
sta18 Time: 30 - 36 hrs
sta18 Time: 36 - 42 hrs
sta18 Time: 42 - 48 hrs
sta18 Time: 48 - 54 hrs
sta18 Time: 54 - 60 hrs
sta18 Time: 60 - 66 hrs
sta18 Time: 66 - 72 hrs
λ3, CCOR3
Log10 Period (s)
λ3
ccor

Figure C.6.4

APPENDIX D

Phase Tensor comparison 2003 data and 2012 data

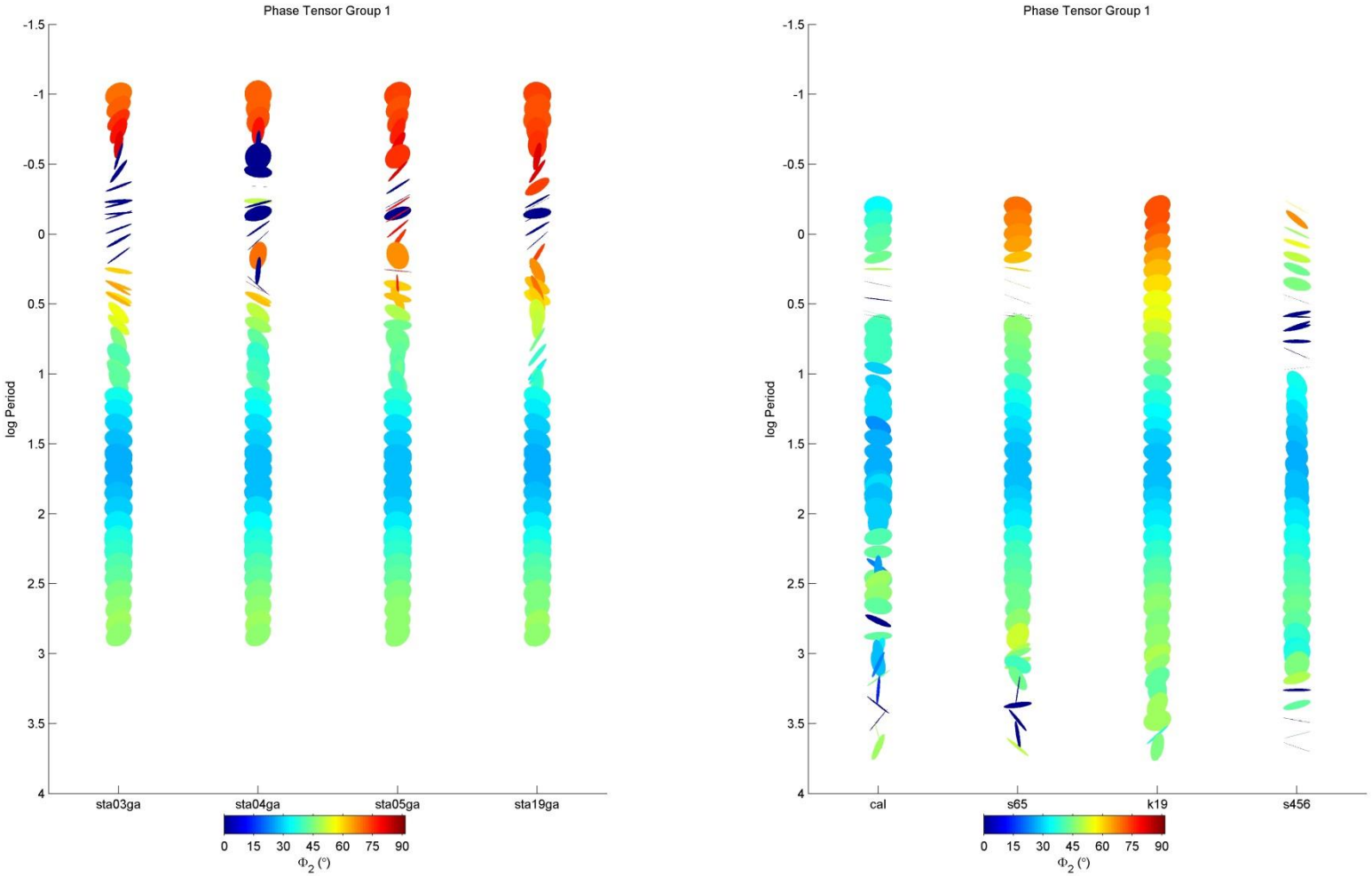

Figure 1. 2003 phase tensors are shown in the right hand panel. 2012 results are in the left panel. 2003 cal, s65, k19 and s456 correspond to 2012's sta03g1, sta04g1, sta05g1 and sta19g1, respectively. While we collected higher frequency (shorter period) data in 2012, there is significant noise in the 2012 phase tensor as evidenced by the needle shapes that occupy more than one decade of frequency around 1 second. This could be due to excessive deadband noise, hydrothermal activity, local noise attributed to electromagnetic interference or caldera activity. As might be expected long period phase tensor values are approximately the same in 2012 as they were in 2003.

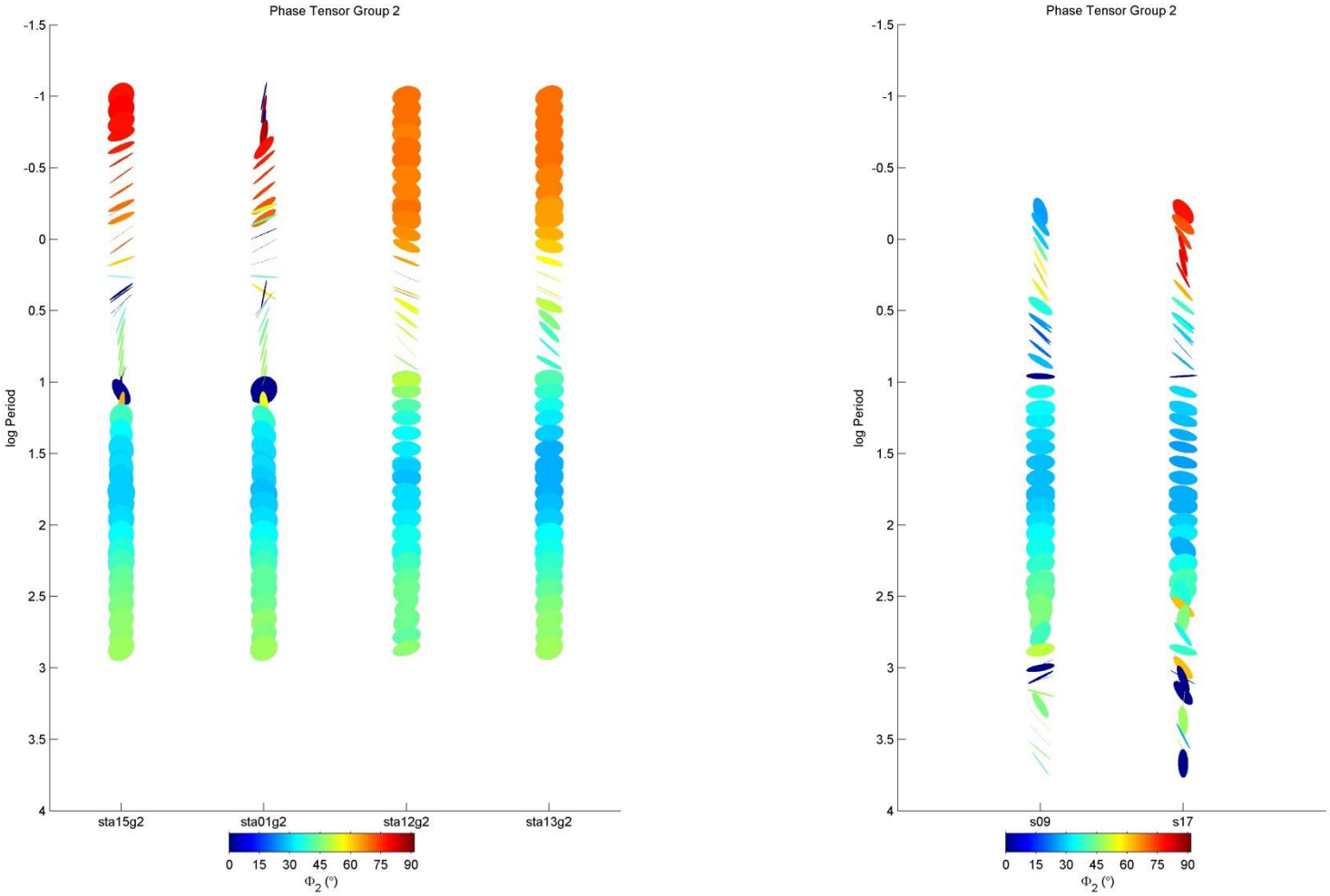

Figure 2 2003 phase tensor is in the right panel, 2012 in the left. 2003's s09 and s17 are in the same location as 2012's sta12g2 and sta13g2 in groups 2 and 3. In group 2 2012 stations 12 and 13 have nearly identical Φ_2 at short period. The Φ_2 values greater than 45 are consistent with increasing conductivity in the shallow zone associated with the caldera. We did not have data from 2003 for sta15 or sta01.

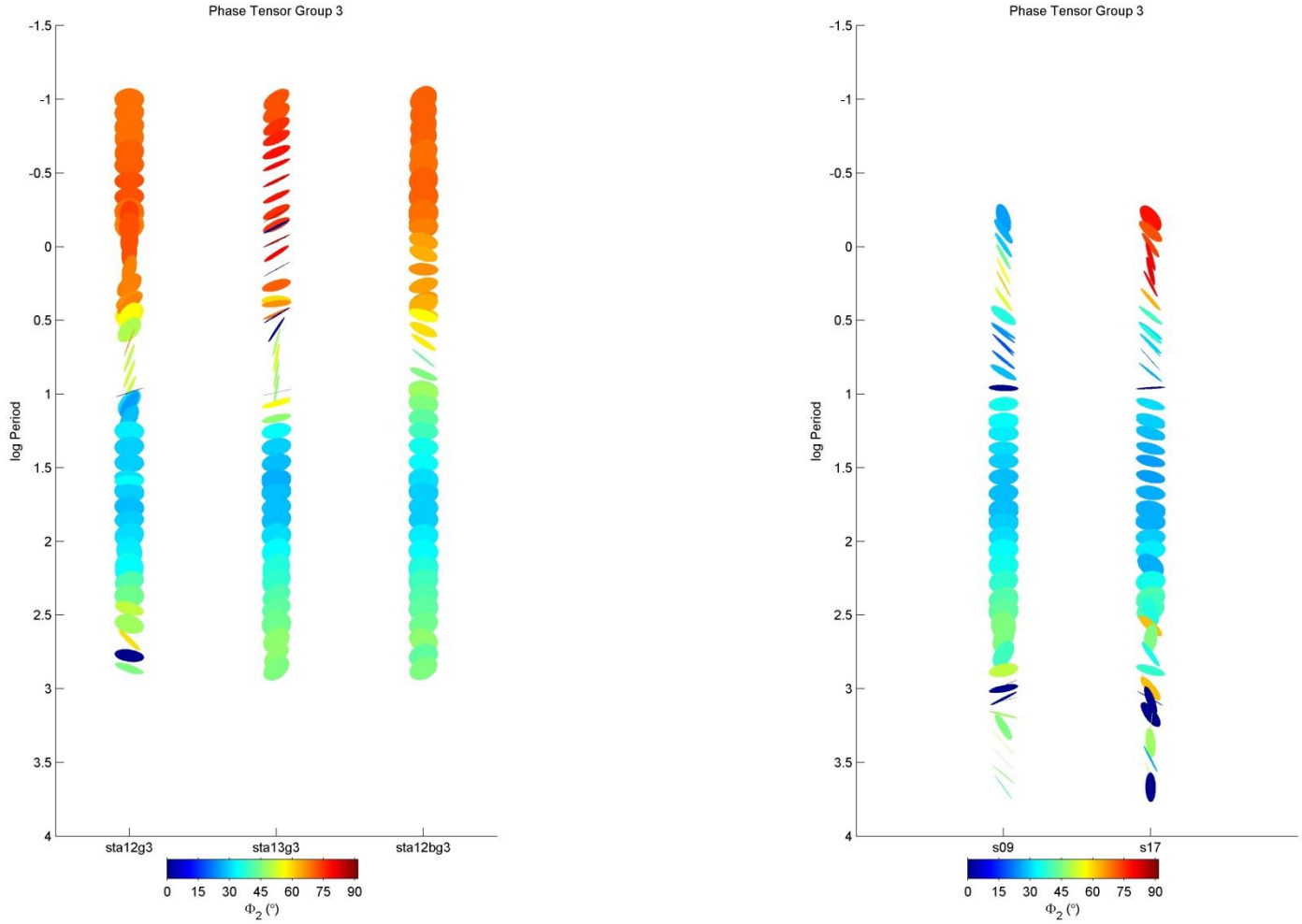

Figure 3. 2003 phase tensor is in the right panel, 2012 is in the left. 2003's s09 and s17 are in the same location as 2012's sta12g3 and sta13g3 in groups 2 and 3. In group 3 2012 stations 12 and 13 no longer have nearly identical Φ_2 at short period. 2012's 12b is similar in appearance now to station 12. The Φ_2 values greater than 45 are consistent with increasing conductivity in the shallow zone associated with the caldera.

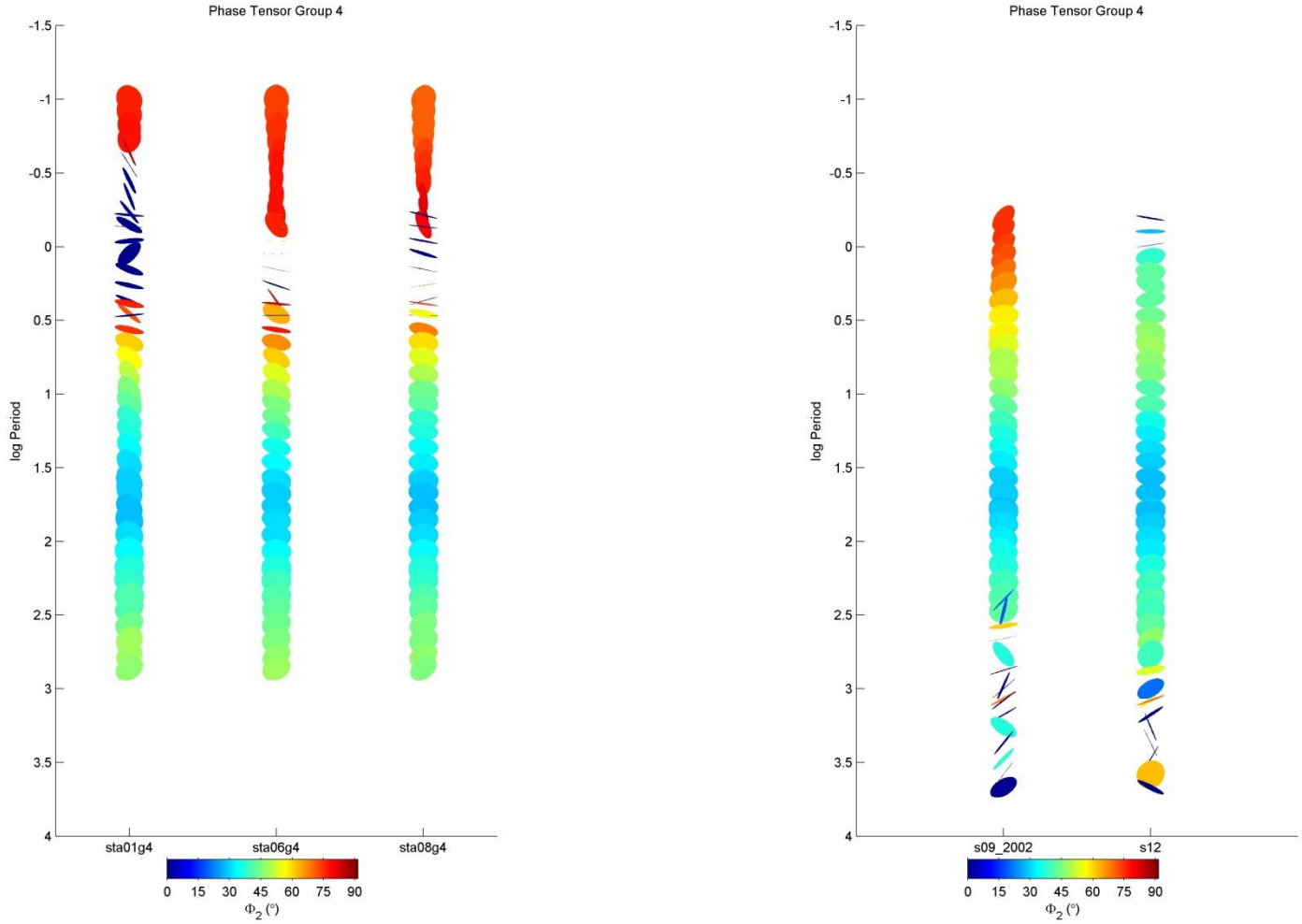

Figure 4. Right panel is 2002 and 2003 data. Left panel shows 2012 data. 2002's s09_2002 corresponds to sta06g4. 2003's s12 is the same as sta08g4. 2002's s09_2002 and 2012's sta06g4 show some different orientations of the phase tensor. We believe that the orientations of the station installations were identical. At this point the nature of this variability in orientation of the major and minor axis is not fully resolved, but could be due to ambiguity in the phase tensor axis. That there is little variability in the angle of Φ_2 at long period is indicative of correctly applying the phase tensor operations to both data sets, and evidence of correctly orienting the instruments.

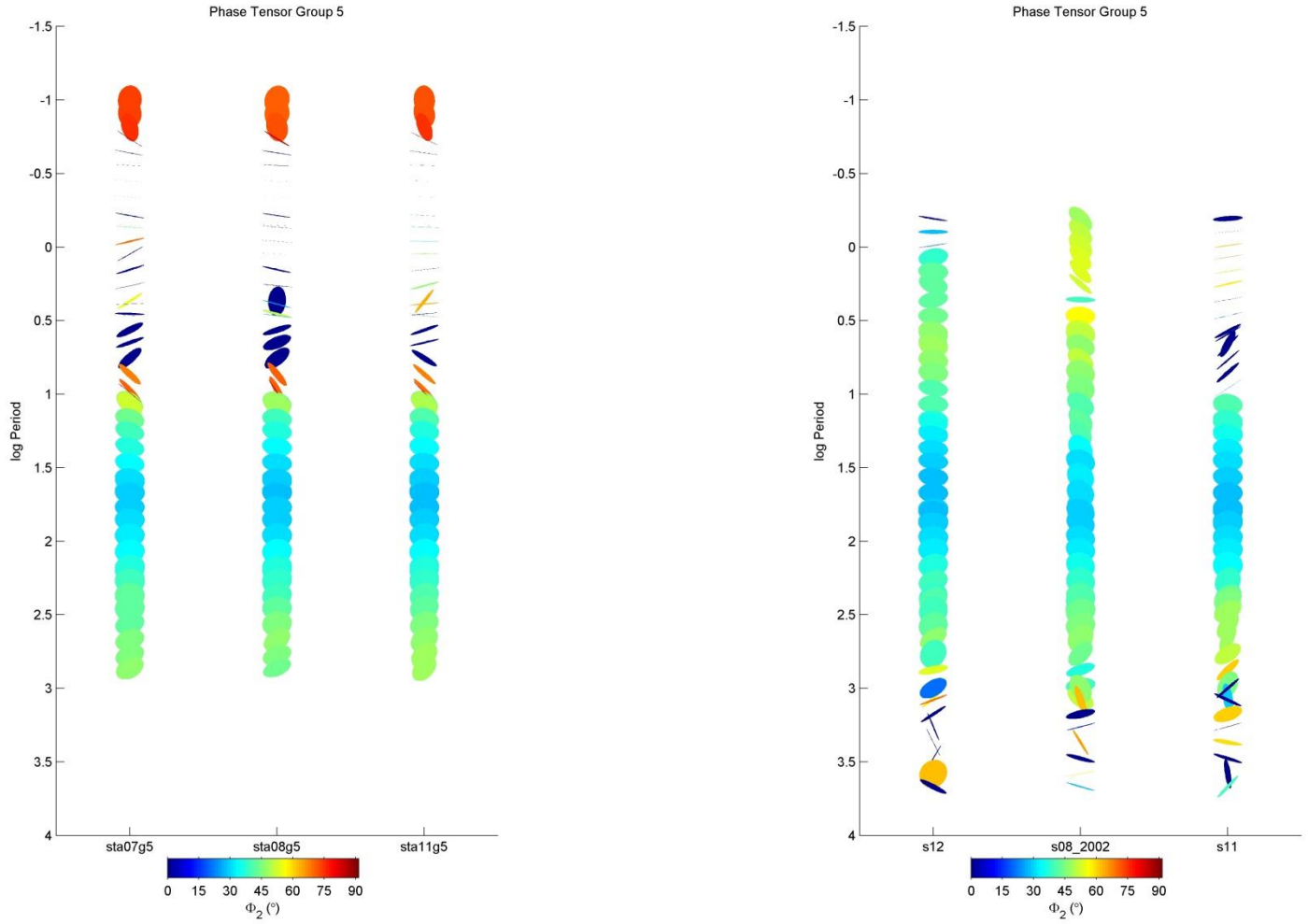

Figure 5. S08_2002, is the same location as 2012's sta11g5, likewise 2003 s11 is also the same location as 2012 sta11g5. Sta08g5 is the same location as 2003 s12. The 2012 phase tensor (left panel) displays over a decade of noisy values (needle shapes). Similarly s11 from 2003 has a comparable band of noisy values similar to the sta11g5 2012 data. S11 has a marked difference between data collected at s08_2002 which was at the same location. Sta07g5 does not have a corresponding station in this grouping.

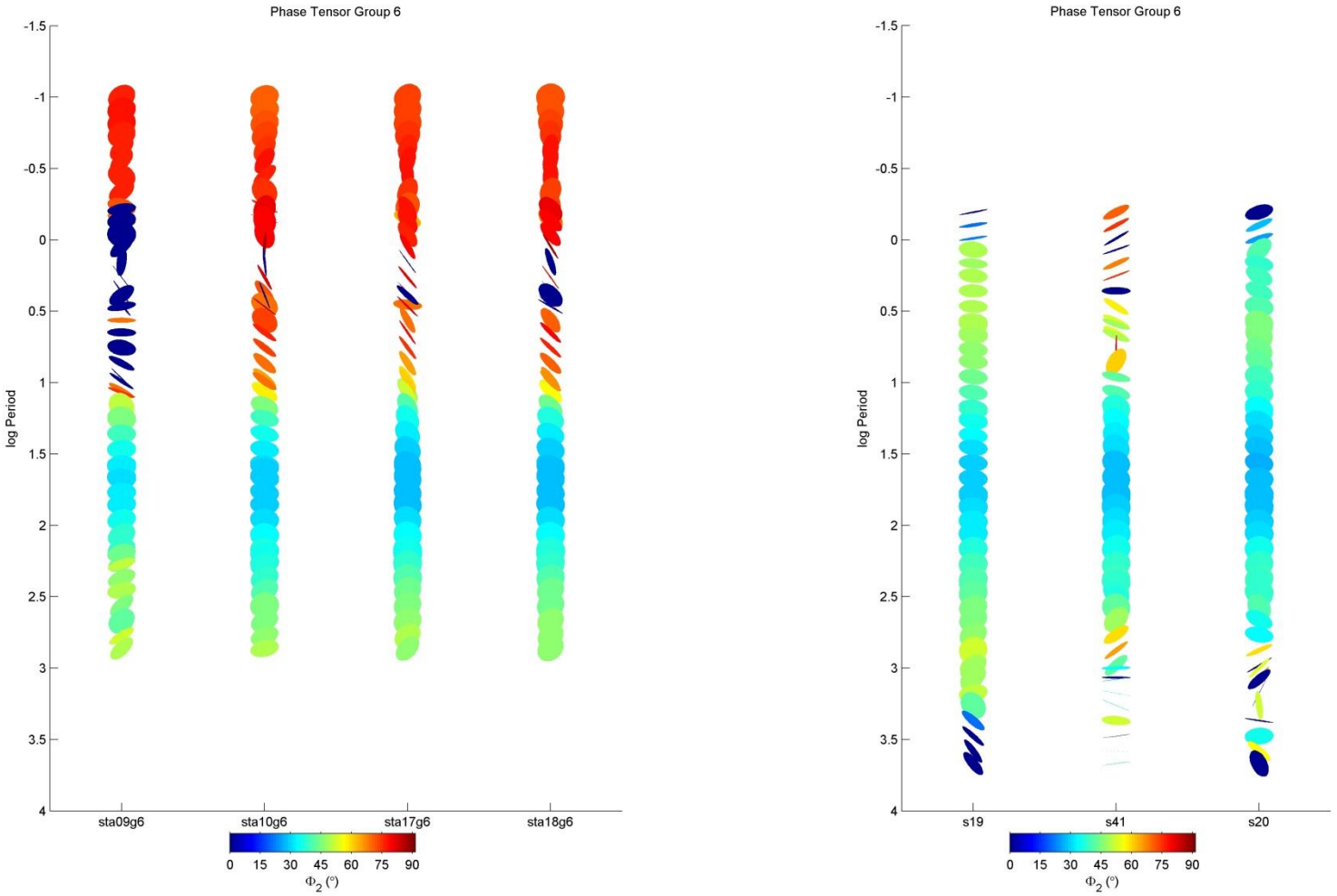

Figure 6 2003's s19, s41 and s20 (right panel) correspond to 2012's sta10g6, sta17g6 and sta18g6 (left panel). The elevated Φ_2 in the 2012 is a significant change over 2003. Could this high Φ_2 be indicative of magma in the conduit that was less prevalent in 2003. Sta09g6 is proximal to the Puhimau Steam Vent area. Is it possible that the small Φ_2 values are associated with the relatively recent intrusion responsible for the steam vent activity. There is no data from 2002 or 2003 to compare with 2012 sta09g6

APPENDIX E

Eigenvalue and Canonical Correlation Differences for Kilauea Data

F.1 λ_4- CC_4 Results for Kilauea Summit Groups 1-6

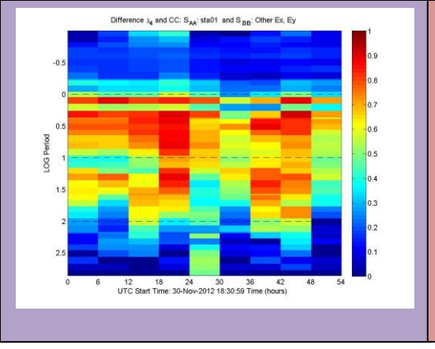

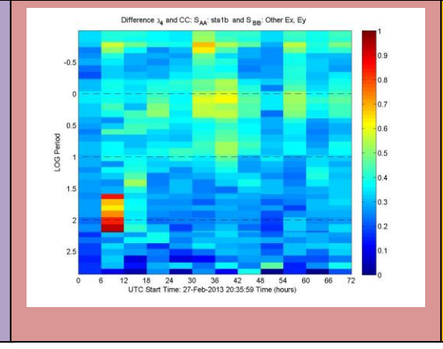

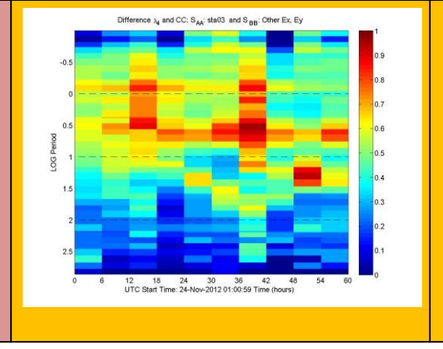

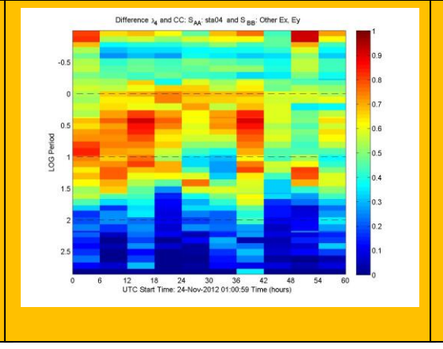

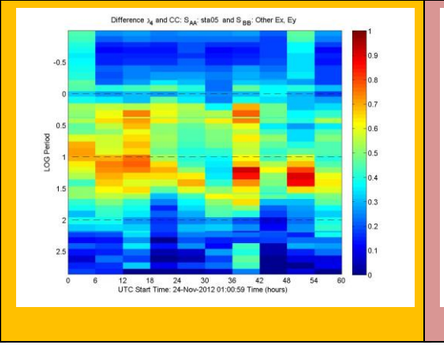

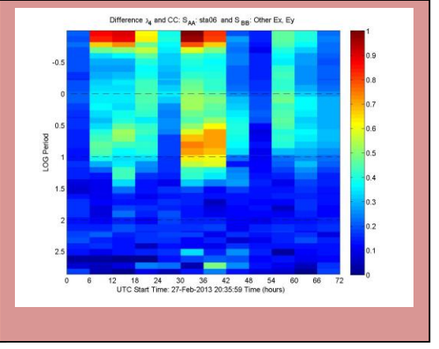

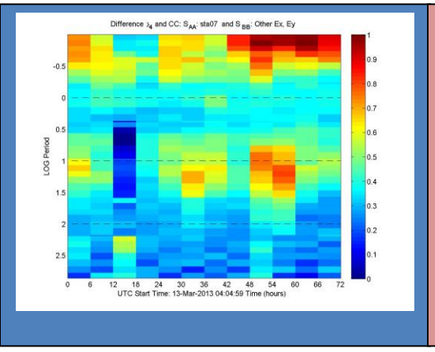

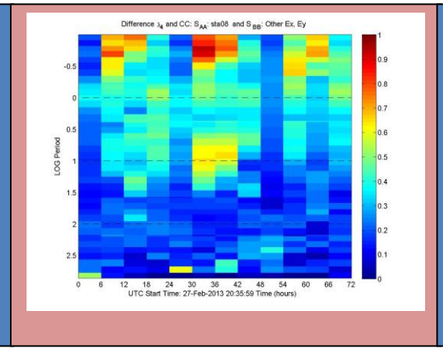

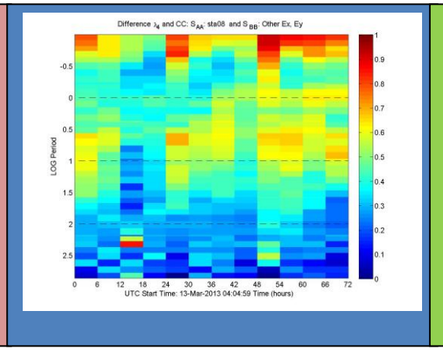

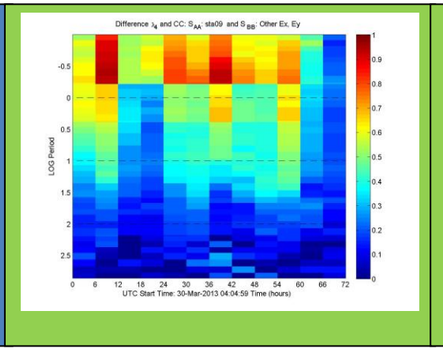

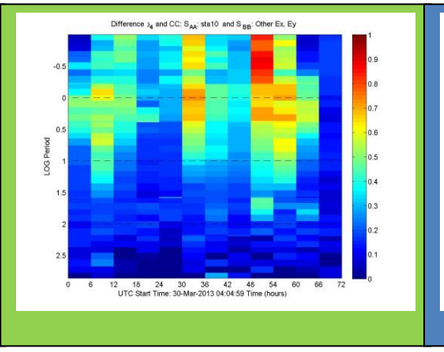

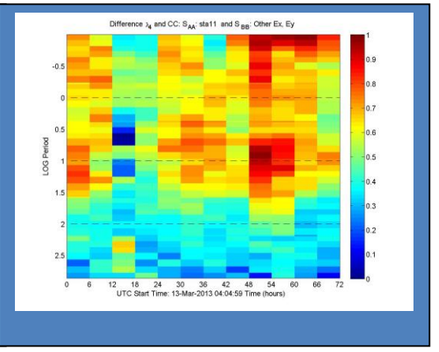

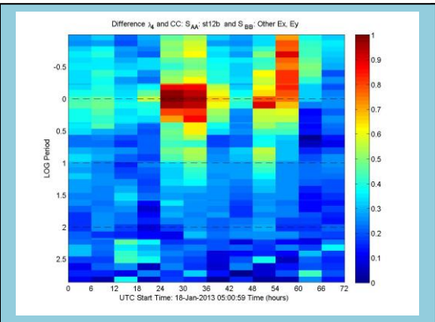

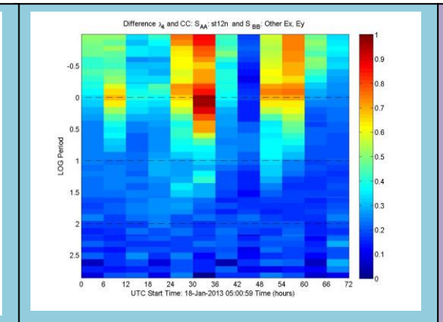

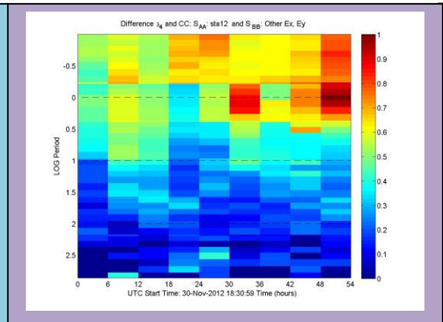

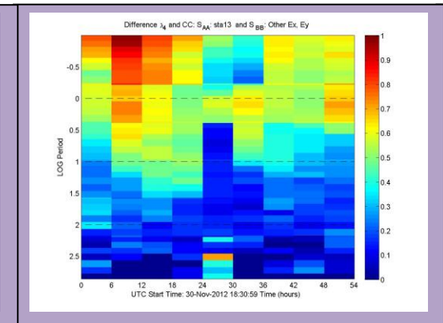

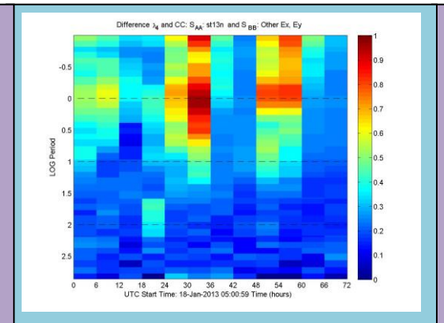

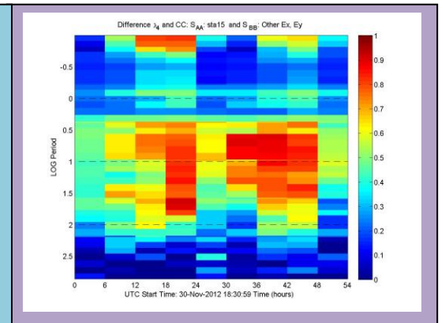

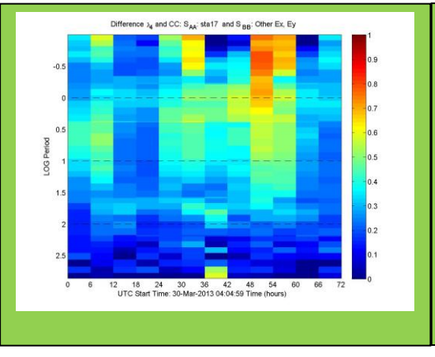

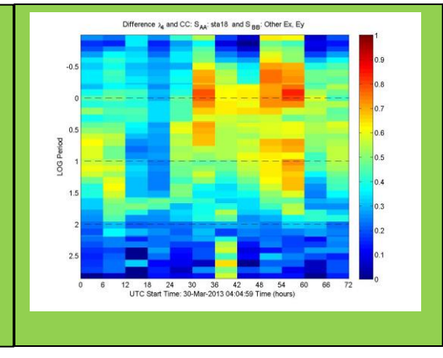

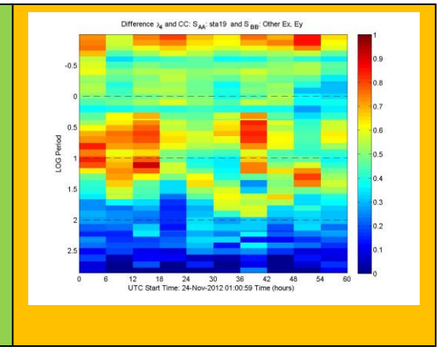

Stations are ordered 1 to 19. Background color indicates stations recorded in the same station grouping. Ignoring the VII deadband, and periods longer than 100 seconds, these stations have $\lambda_4 - CC_4$ differences ~> .7 and spanning at least 18 hours:

Period 10 – 100 seconds: 1, 4, 5, 11, 15, 19

Period .1 to 1 seconds: 7, 8, 9, 13, 19

F.1 λ_3- CC_3 Results for Kilauea Summit Groups 1-6

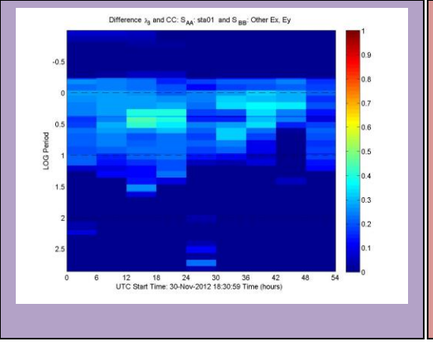

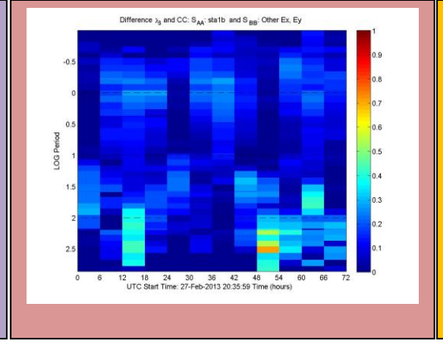

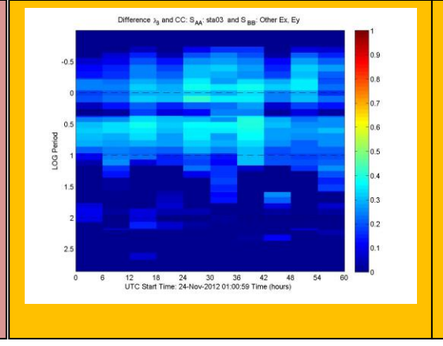

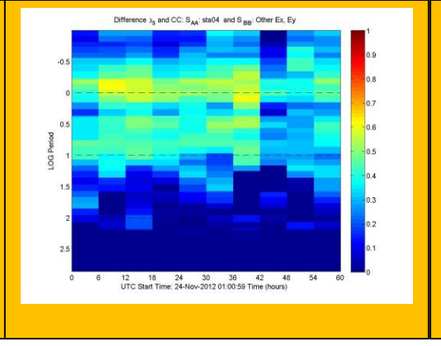

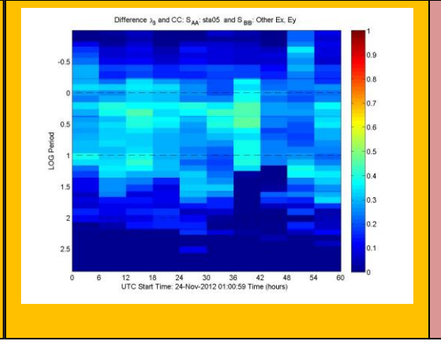

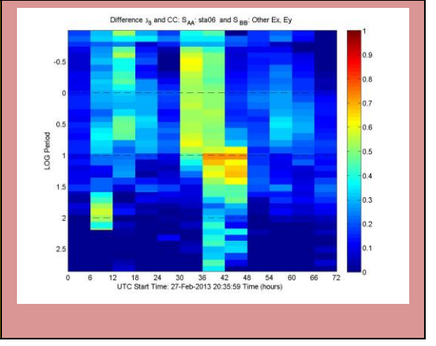

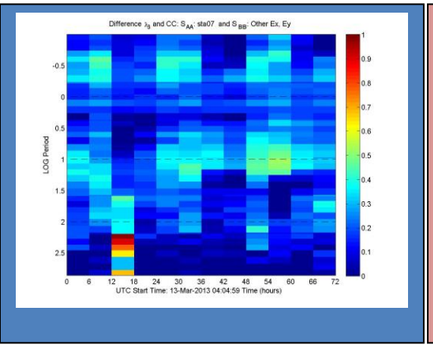

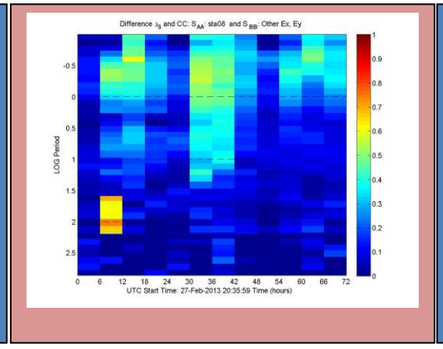

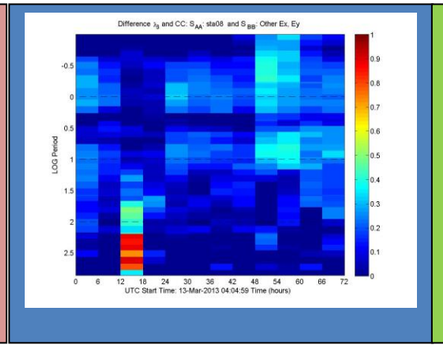

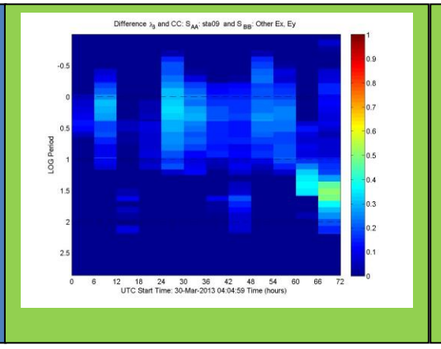

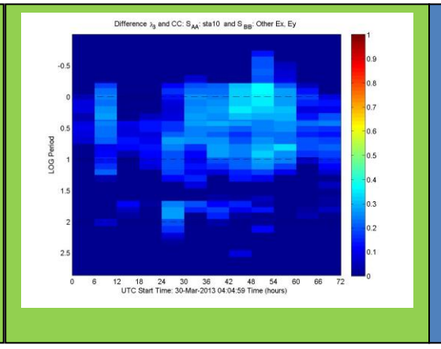

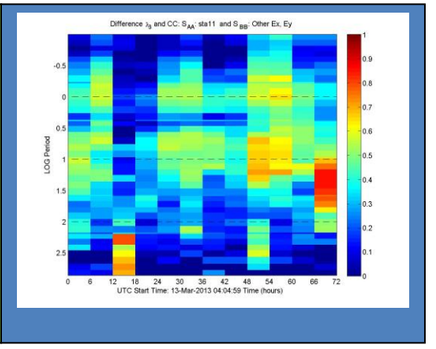

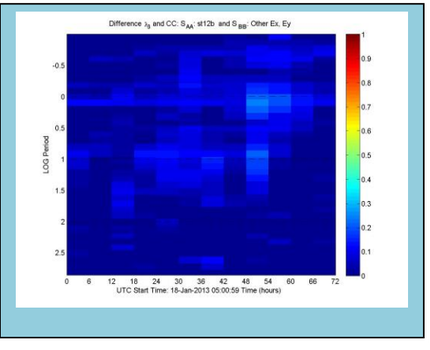

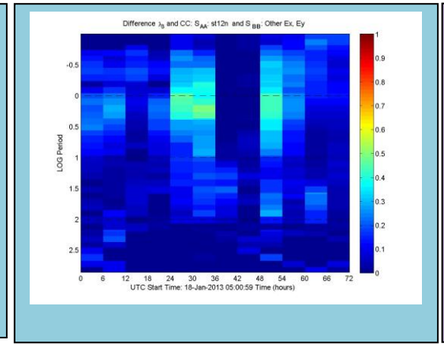

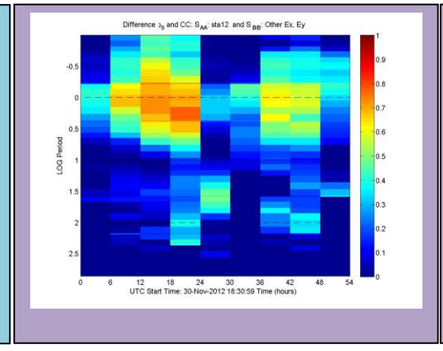

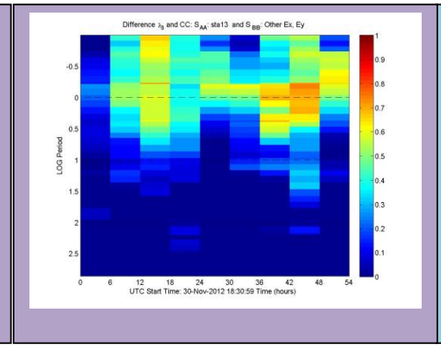

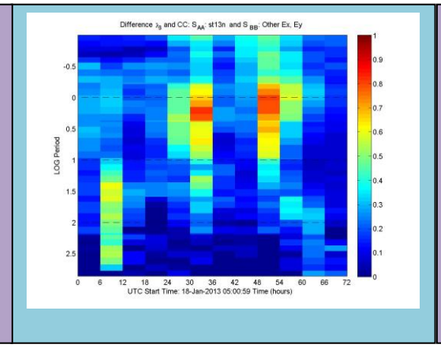

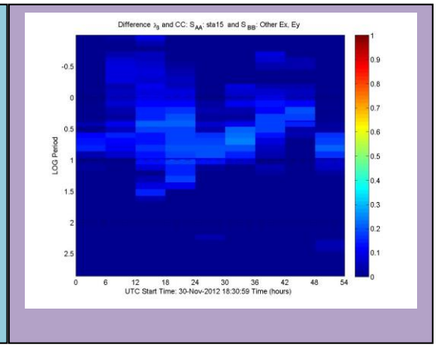

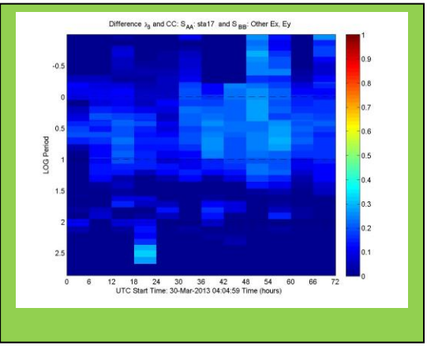

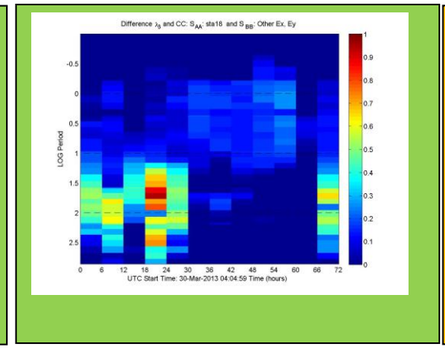

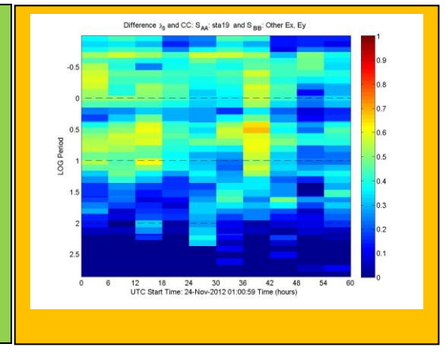

Stations are ordered 1 to 19. Background color indicates stations recorded in the same station grouping. If we ignore the period band related to the MT deadband, and period longer than 100 seconds, there are $\lambda_3 - CC_3$ differences >0.5 at station 3, 4, 6, 7, 8, 11, 12, 13, 18 and 19, and >0.3 at 3, 5, 9, 10 and 17. Maximum of 0.2 at 1, 12b and 15.

APPENDIX F

LBNL Analysis from 2003-2003 and 2012-2013

Analysis of MT data collected from October 2012 until April 2013 for SSP project

and 2003 MT data

at the Hawaiian National Park

Erika Gasperikova

LBNL

April 30, 2014

2012-2013 survey description and site groupings

We collected MT data at 18 sites, from which sta13b is not used since Hx was saturated. Stations sta01, sta12, and sta08 were recorded in two different groups, so we have two sounding curves for these three stations. All station locations are shown in Figure 1a, while the final set is shown in Figure 1b. Each station (except of Parker) consisted of two orthogonal magnetic coils and two orthogonal electric dipoles. The orientations of x and y components were 135 and 225 degrees, respectively. The data were recorded for 72 hours or more, although currently data in group 1 are shorter because of the problems at the beginning of the recording.

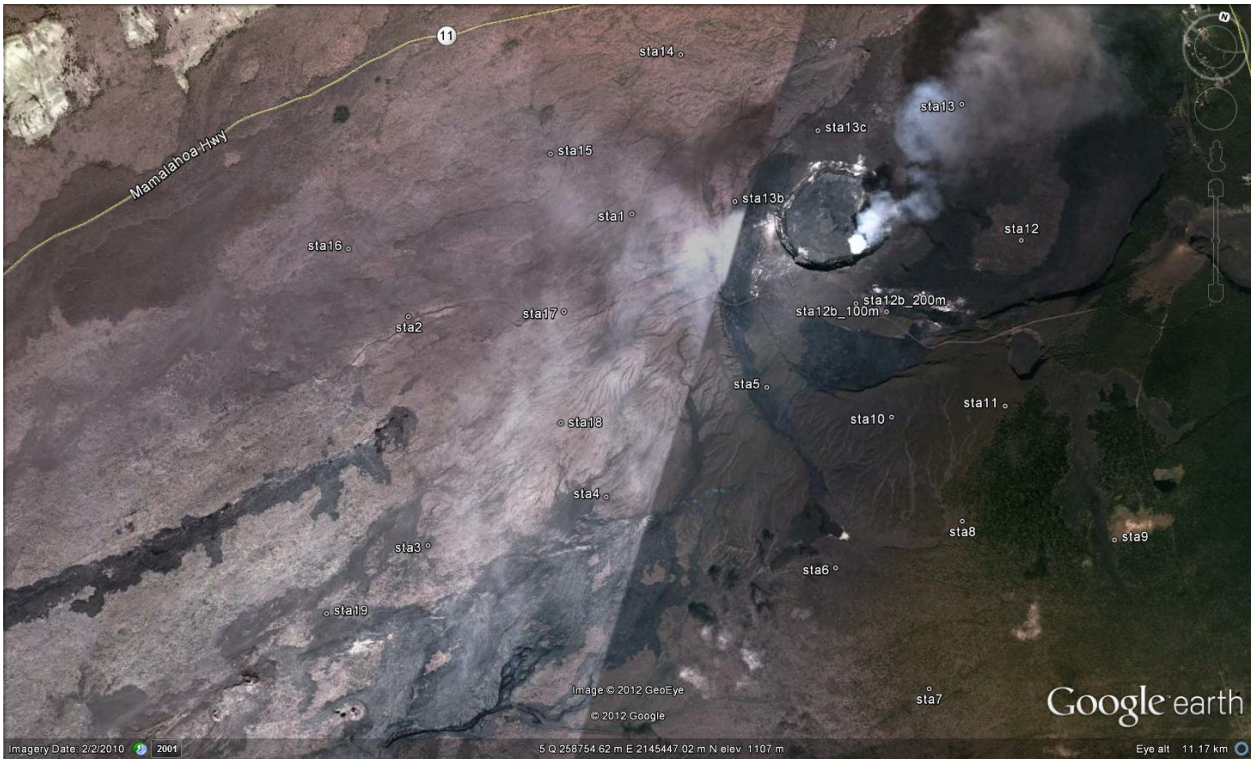

Figure 1a

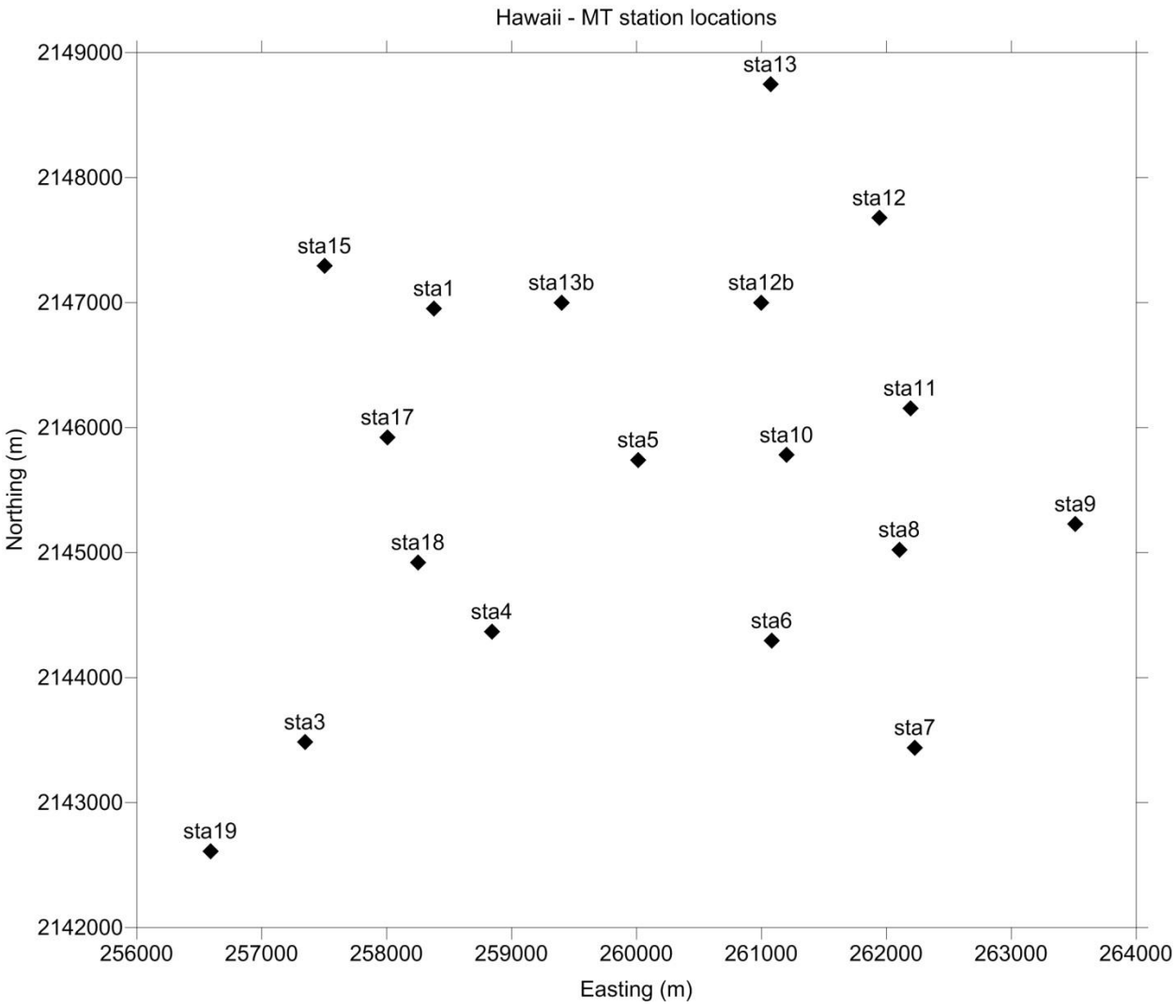

Figure 1b

We have six groups of stations for multi-station robust processing:

Group 1: sta 19, 3, 4, 5 + hkml7

Group 2: sta 15, 1, 12, 13 + hkml8

Group 3: sta 12, 13, 12b, 13b + lau + parker

Group 4: sta 1, 6, 7, 8 (sta07 was noisy and excluded from the processing) + lau + parker

Group 5: sta 7, 8, 9, 11 (sta09 was excluded from processing since it was missing 72 hours data recording) + lau + parker

Group 6: sta 10, 17, 18, 9 + lau + parker

Group1:

For sta05 I am still not sure on orientation of E-dipoles, so the results might not be correct.

E-dipoles need to be flipped, since they were connected backwards (except hkml7)

There was problem with recordings at the beginning, so data needed to be trimmed with the start on 11/24/2012 1:00 AM, which resulted in a record shorter than 72 hours, and results are somewhat noisy

E-fields form hkml7 were not used in multi-station robust processing.

Group2:

E-fields form hkml8 were not used in multi-station robust processing.

All stations (except hkml8) need E-dipole flip

Data used from 11/30/2012 6:30 PM until 12/04/2012 10:30 PM

sta13 Hx flip polarity

Group 3:

E-fields from Lau Lease were not used in multi-station robust processing.

sta13b Hx saturated => not used in the processing

sta12 and sta13 had channels flipped; Ex&Ey are in Ch1&2 and Hx&Hy are in Ch4&5

Group 4:

Lau Lease and Parker had to be trimmed to start the same time as the rest of the stations

E-fields from Lau Lease were not used in multi-station robust processing.

Group 5:

E-fields from Lau Lease WERE used in multi-station robust processing.

Lau Lease Ch6 = -Ex

Group 6:

Use ‘f13’ dataset

E-fields from Lau Lease WERE used in multi-station robust processing.

sta18 was noisy at the end => last hour taken out (71 hours recording)

sta10 has a broad spectral peak at ~ 2 Hz on Ey

Lau Lease Ch6 = -Ex

Initial results of multi-station robust processing of 2012-2013 data set

Group1:

Figures 2a-2d are plots of the transfer function amplitude and phase estimates with respect to the reference hkml7 H-fields and sta19 E-fields. Leaving station sta05 aside for further evaluation (see comments above), estimates of transfer functions are noisy at high frequencies (periods ~ 0.15-15 s), but very stable at lower frequencies (periods > 15 s) for H-fields, and stable at higher frequencies and noisy at lower frequencies for E-fields.

Figures 3a-3d show coherence/correlations between the components of H and E-fields again with respect to the same reference fields. Correlation between Hx and Hy for periods > 15 s is close to 1, at lower periods the correlation decreases much more for Hy than Hx. The correlation between Ex and Ey is relatively high across the frequency (time) range (above 0.8 for Ex and above 0.7 for Ey). Station sta03 has lower coherency and low S/N (Figure 4) at higher frequencies which results in significant departure from 1 and 0 in transfer function estimations of amplitude and phase, respectively (blue curves in Figures 2c and 2d).

Figures 4a-4c show signal, noise, and SNR (S/N) levels respectively. Figure 5 shows eigenvalues of SDM where increased values of 3^{rd} and 4^{th} eigenvalues are present throughout the whole frequency range and increased value of the 5^{th} eigenvalue at the higher frequencies (lower periods).

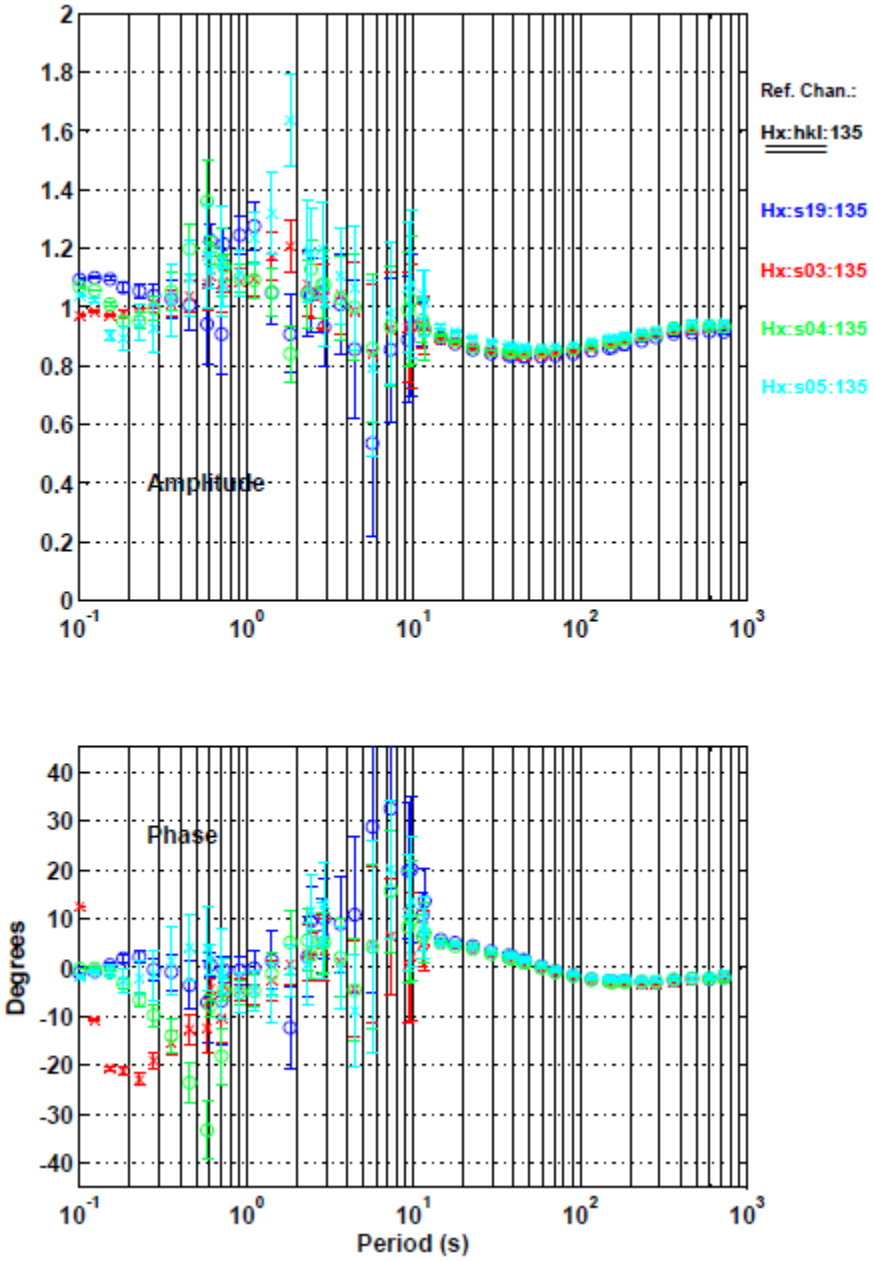
Amplitude
Phase
Degrees
Period (s)
Ref. Chan.:
Hx:hkl:135
Hx:s19:135
Hx:s03:135
Hx:s04:135
Hx:s05:135

Figure 2a

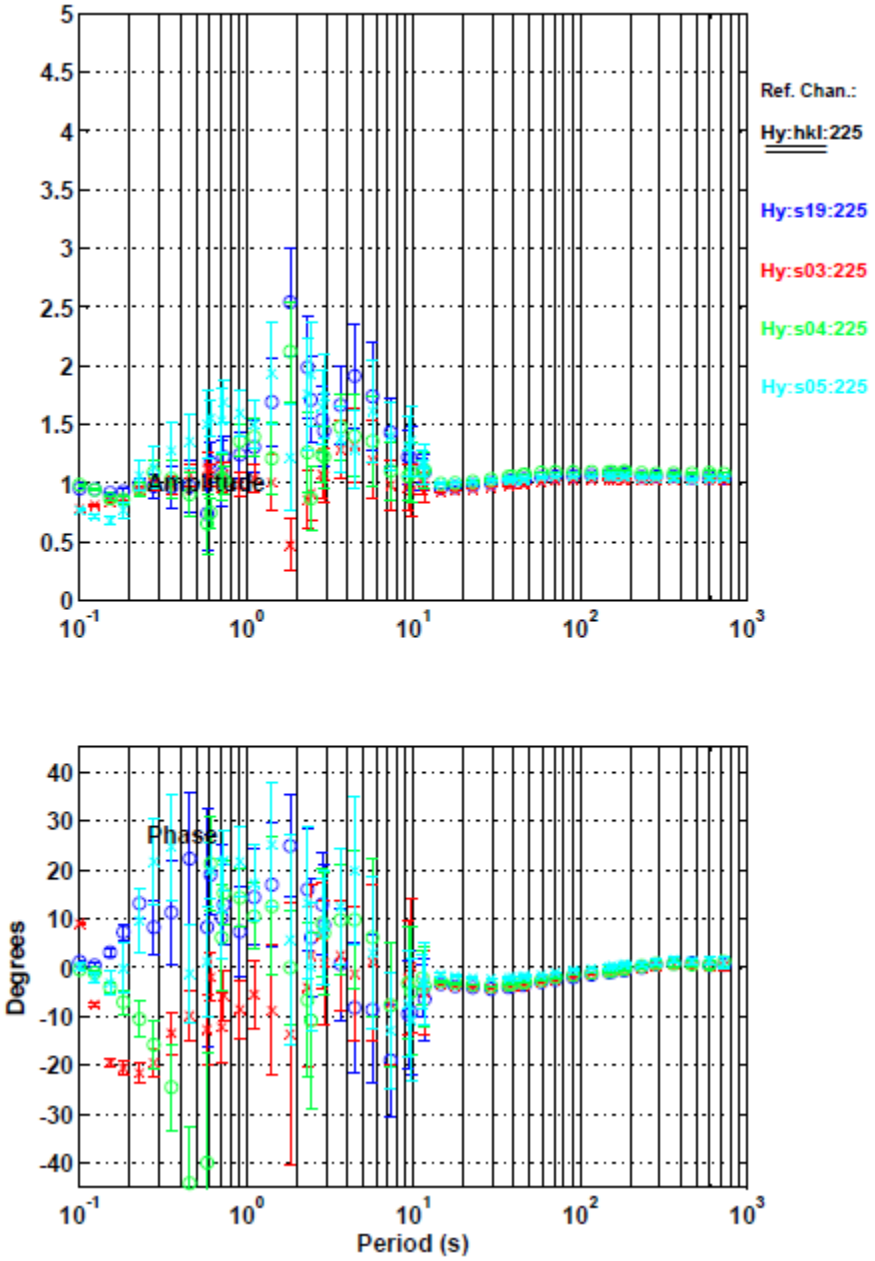
Amplitude
Ref. Chan.:
Hy:hkl:225
Hy:s19:225
Hy:s03:225
Hy:s04:225
Hy:s05:225
Phase
Degrees
Period (s)

Figure 2b

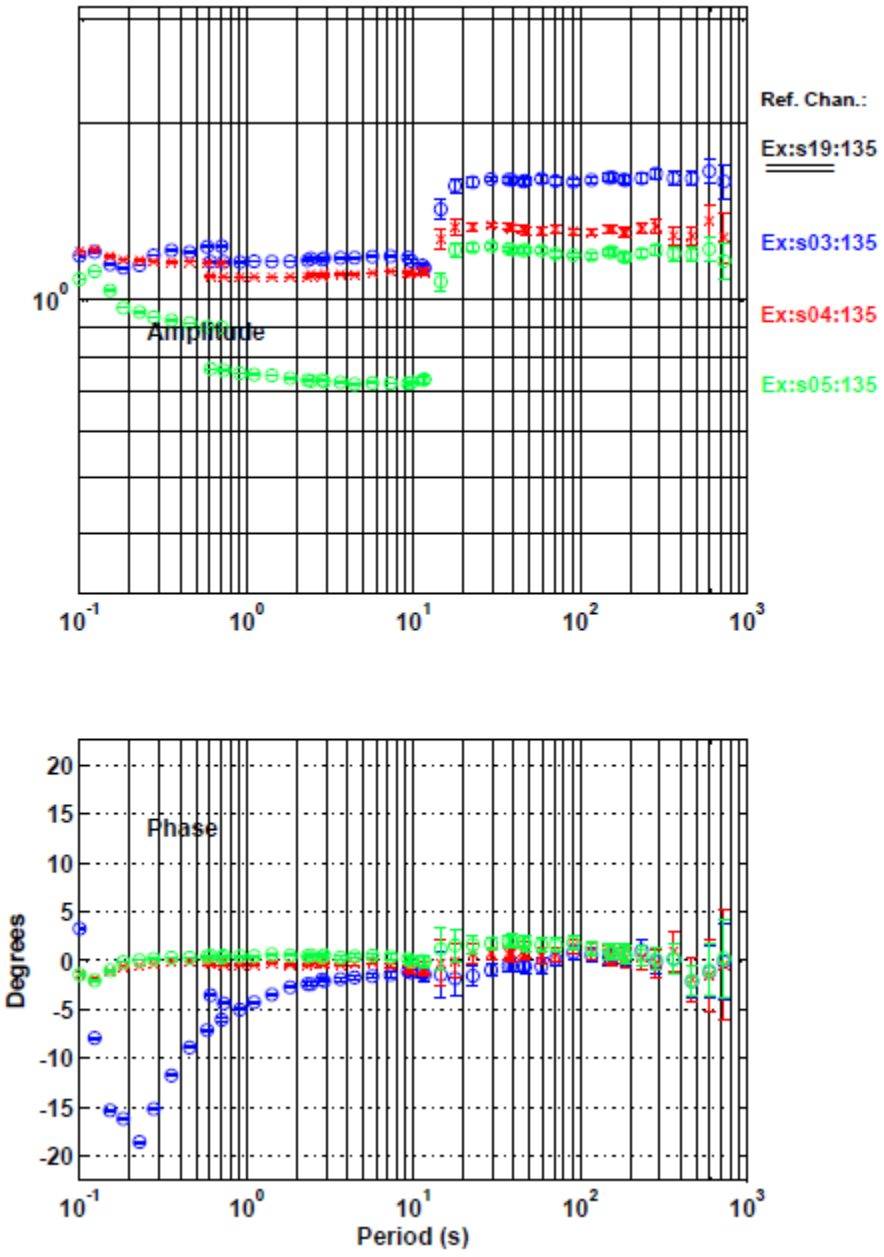
Ref. Chan.:
Ex:s19:135
Ex:s03:135
Ex:s04:135
Ex:s05:135
Amplitude
Phase
Degrees
Period (s)

Figure 2c

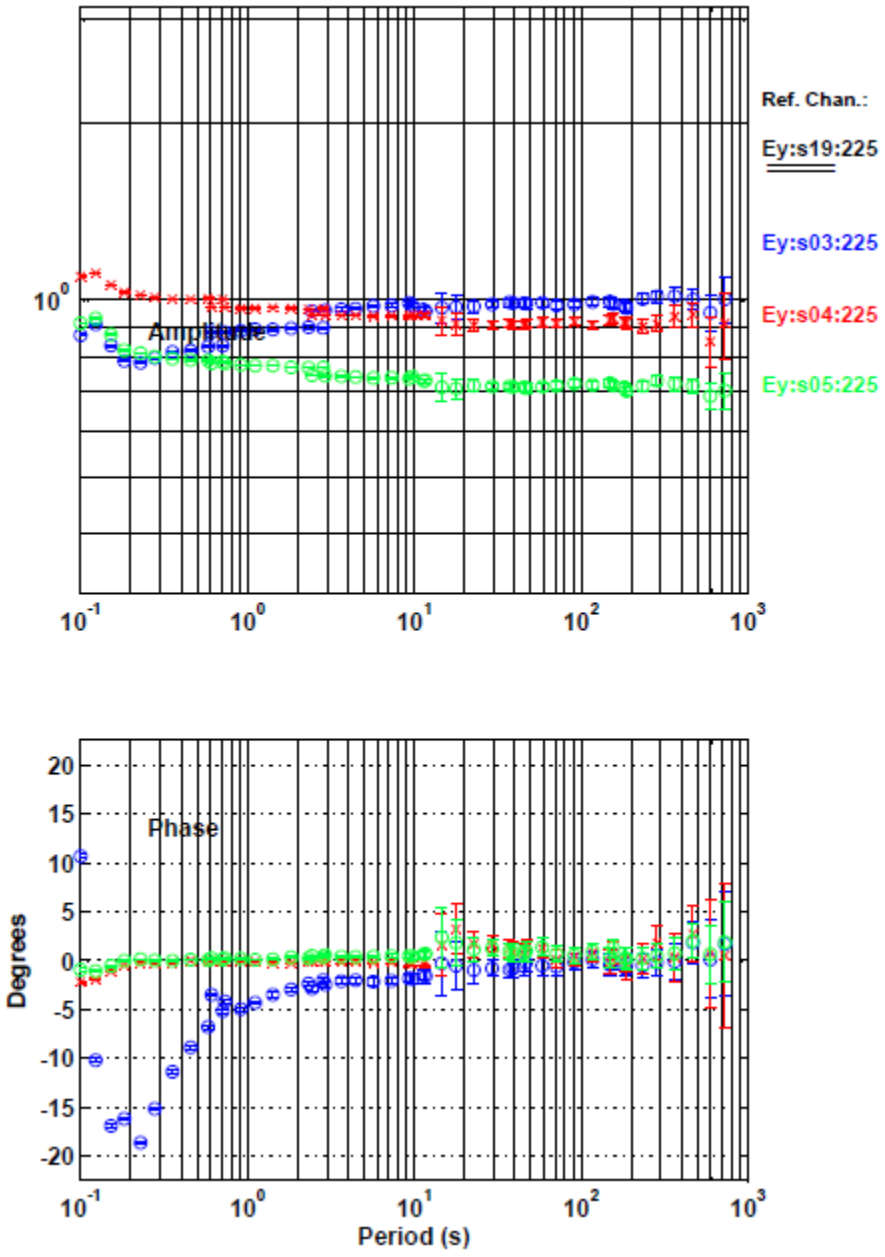
Ref. Chan.:
Ey:s19:225
Ey:s03:225
Ey:s04:225
Ey:s05:225
Amplitude
Phase
Degrees
Period (s)

Figure 2d

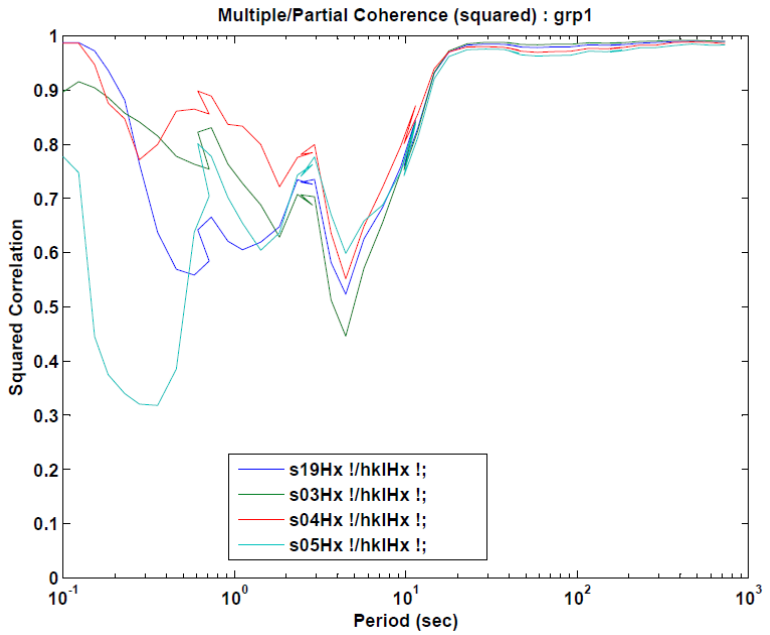

Figure 3a

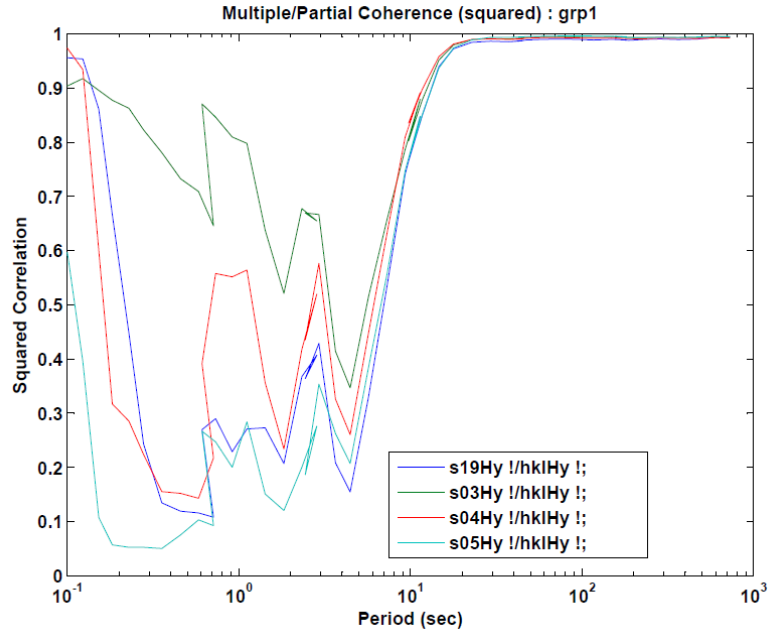

Figure 3b

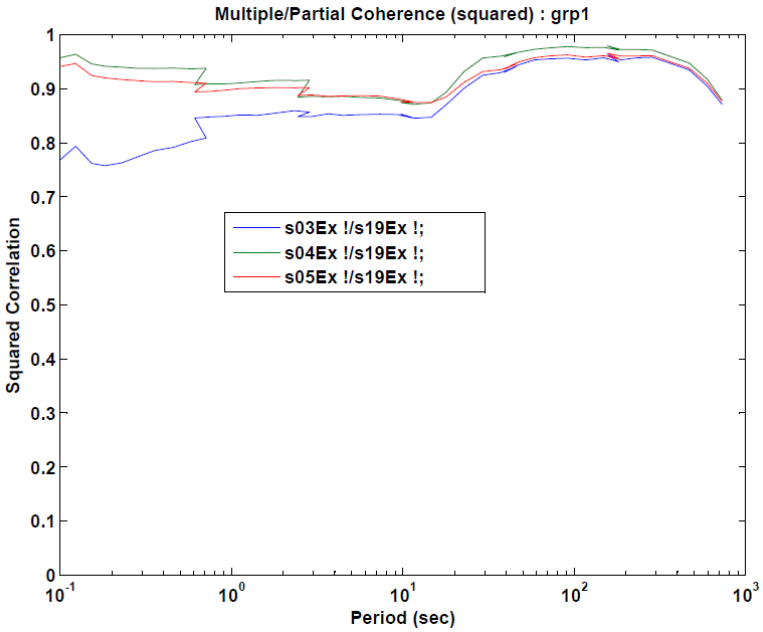

Figure 3c

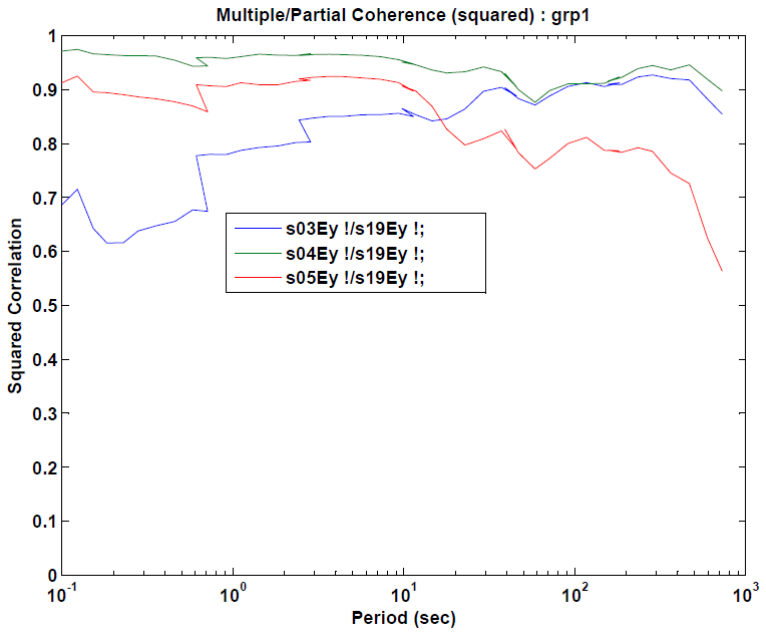

Figure 3d

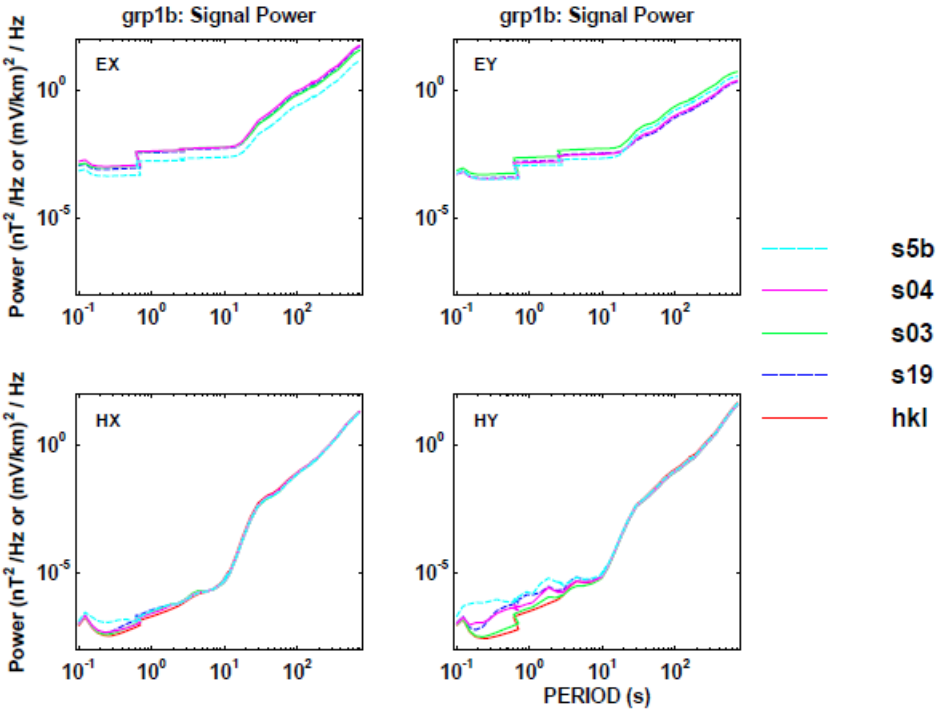

Figure 4a

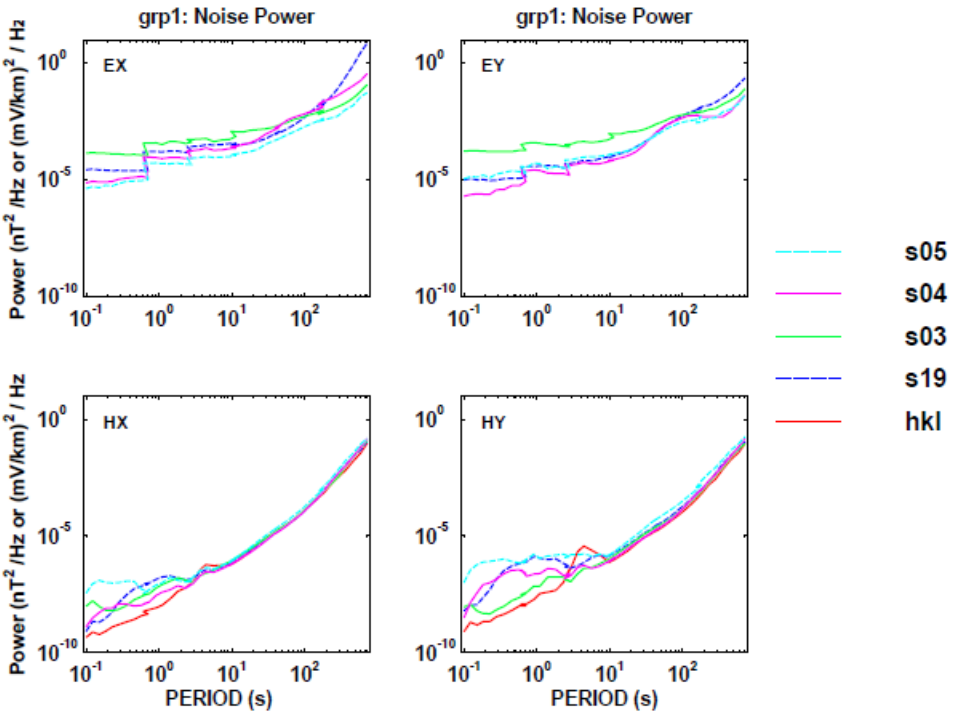

Figure 4b

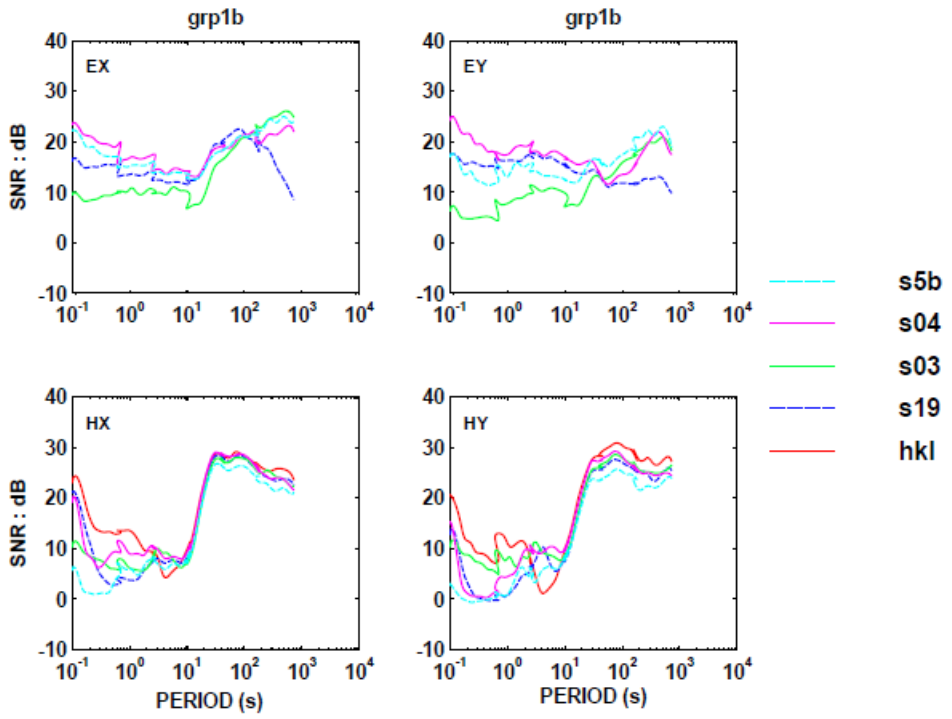

Figure 4c

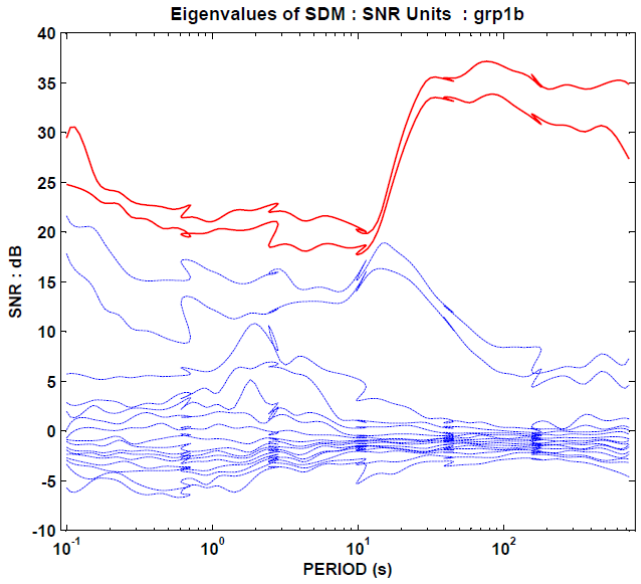

Figure 5

Group 2:

Figures 6a-6d are plots of the transfer function amplitude and phase estimates with respect to the reference hkml8 H-fields and sta01 E-fields. The transfer function estimations of Hx are highly stable except of the dead band (periods ~2-15 s), while the estimates of Hy are more variable and more noisy at the both ends of the frequency range and the dead band. The transfer function estimations of electric field are highly variable and station sta13 appears to have incorrect E-dipoles orientations, which will be corrected in the next processing stage. Only transfer functions between stations sta01 and sta15 are stable. Stations sta12 and sta13 are noisy, and will be evaluated in group 3, as their acquisition was repeated.

Figures 7a-7d are coherence/correlations plots between the components of H and E-fields using hkml magnetics and sta15 electrics as references. While Hy is highly coherent (except sta01) throughout the frequency range, the Hx has almost no coherency at the high frequencies and the dead band. E-fields between sta15 and sta01 are highly coherent, while there is a very low correlation with fields at sta12 and sta13.

Figures 8a-8c show signal, noise, and SNR (S/N) levels respectively. Figure 9 shows eigenvalues of SDM where increased values of 3^{rd} and 4^{th} eigenvalues are present throughout the whole frequency range and increased values of the 5^{th} and 6^{th} eigenvalue at the higher frequencies (lower periods).

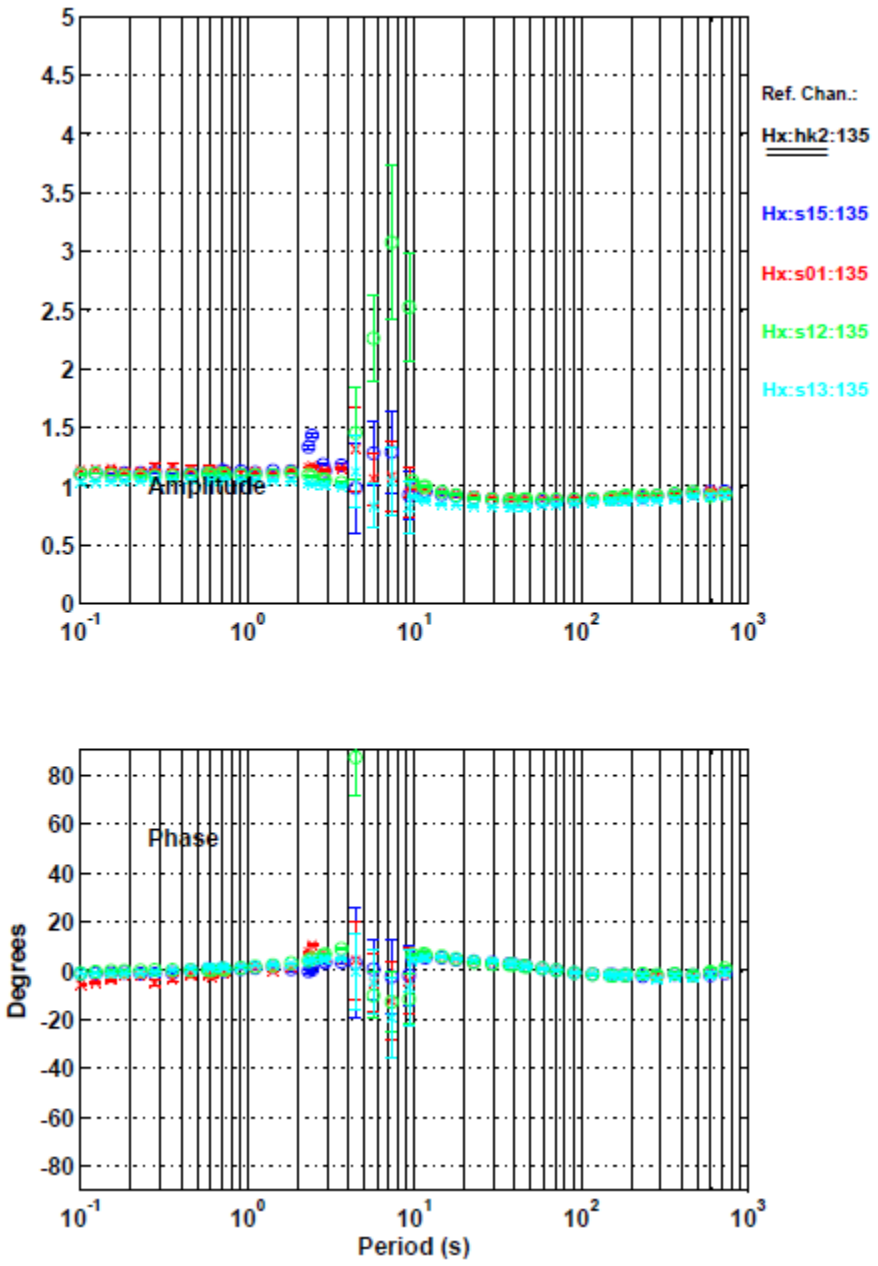
Amplitude
Phase
Degrees
Period (s)
Ref. Chan.:
Hx:hk2:135
Hx:s15:135
Hx:s01:135
Hx:s12:135
Hx:s13:135

Figure 6a

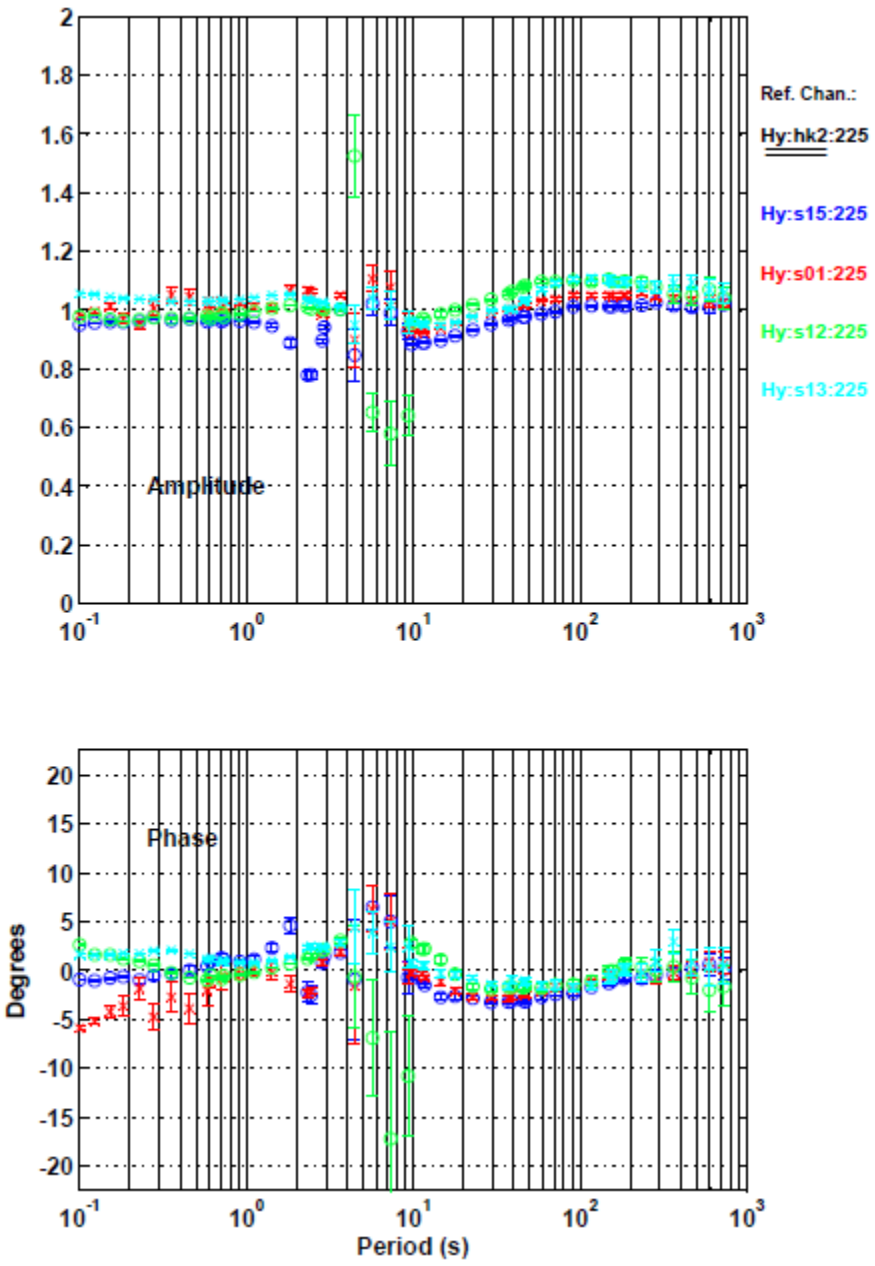
Amplitude
Ref. Chan.:
Hy:hk2:225
Hy:s15:225
Hy:s01:225
Hy:s12:225
Hy:s13:225
Phase
Degrees
Period (s)

Figure 6b

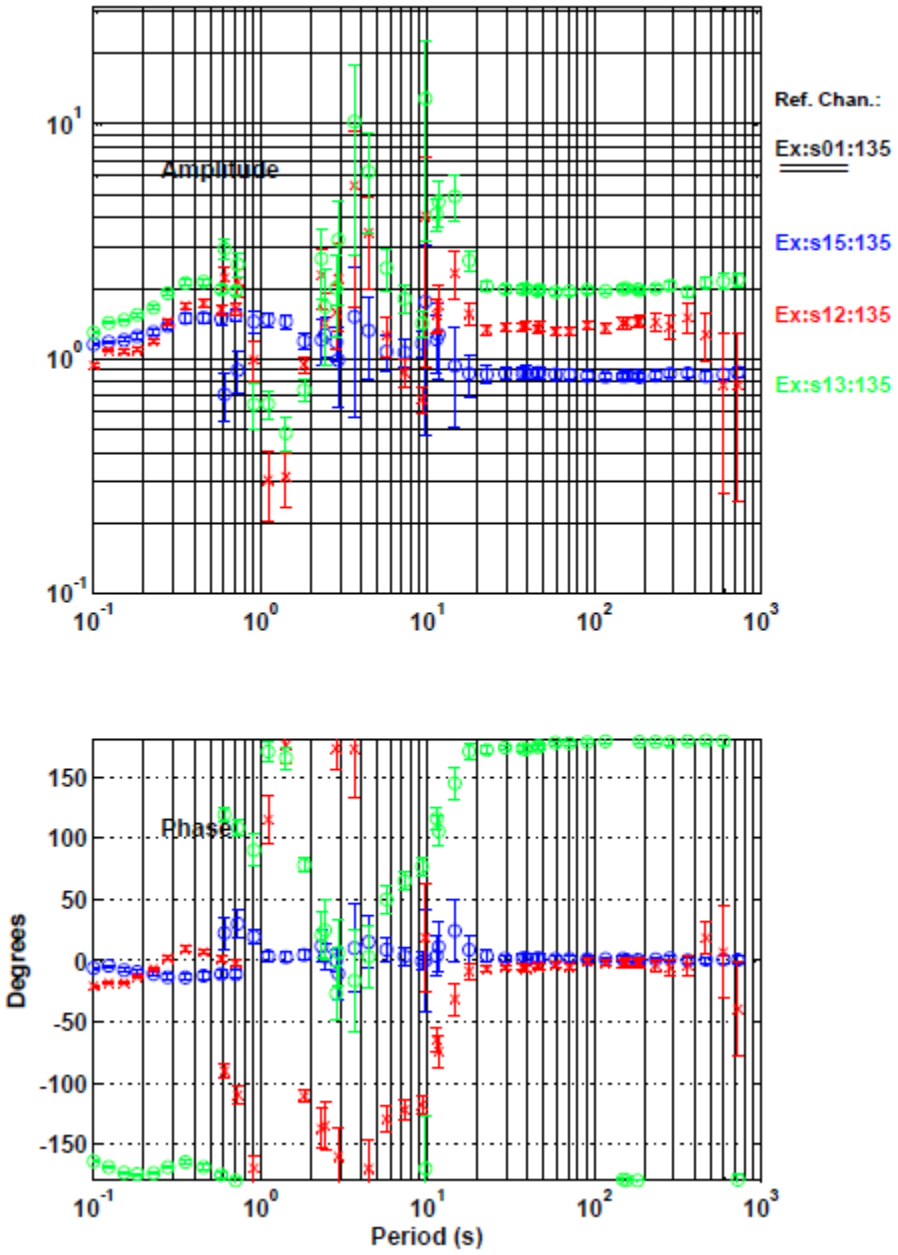
Amplitude
Ref. Chan.:
Ex:s01:135
Ex:s15:135
Ex:s12:135
Ex:s13:135
Phase
Degrees
Period (s)

Figure 6c

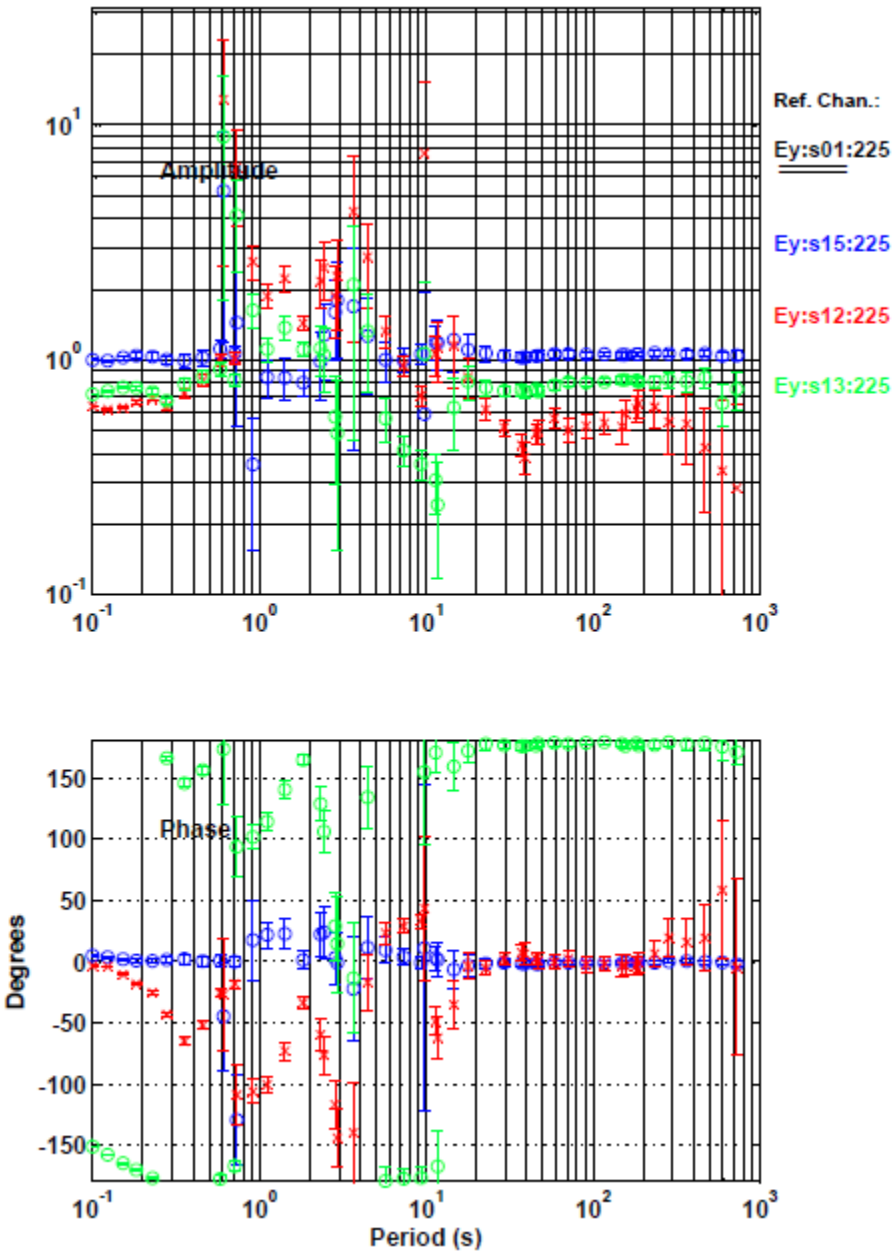
Amplitude
Ref. Chan.:
Ey:s01:225
Ey:s15:225
Ey:s12:225
Ey:s13:225
Phase
Degrees
Period (s)

Figure 6d

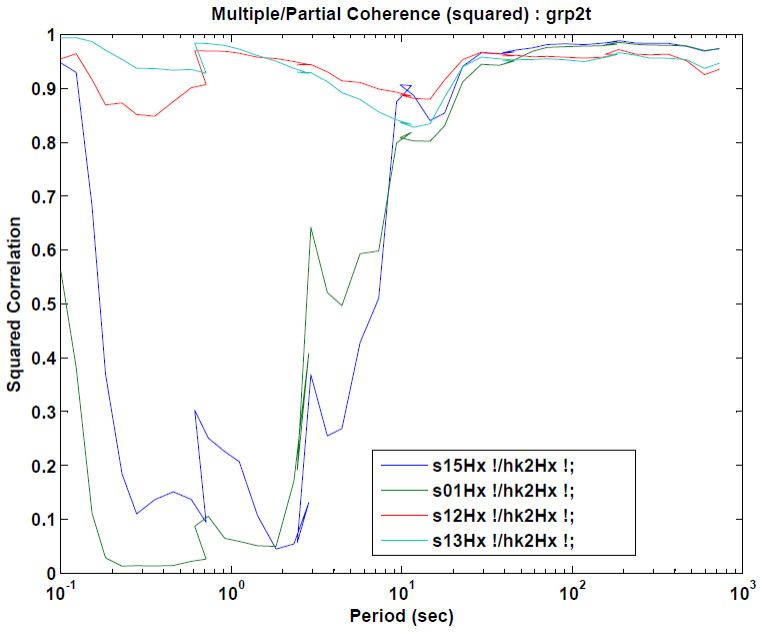

Figure 7a

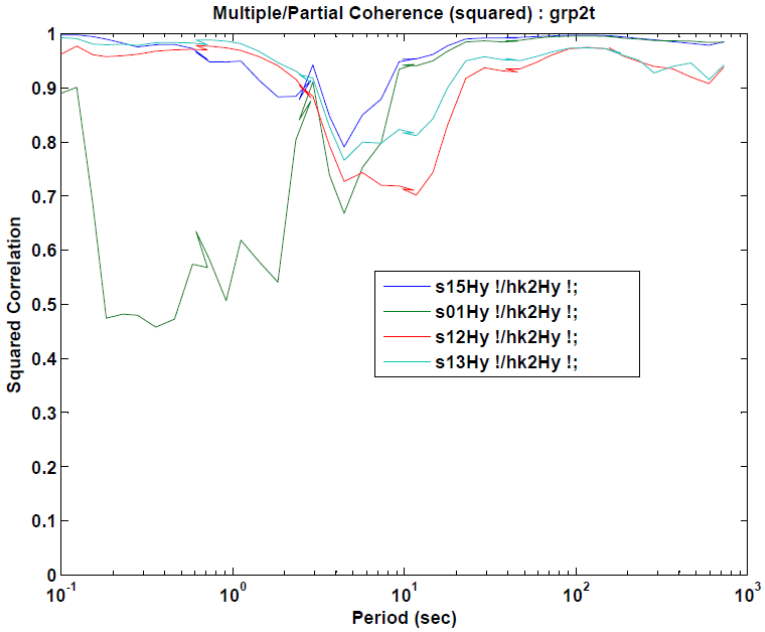

Figure 7b

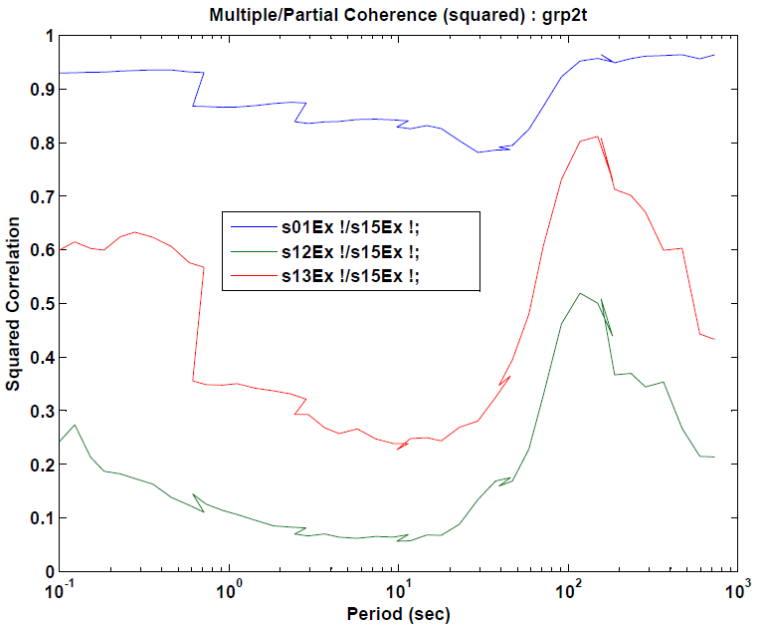

Figure 7c

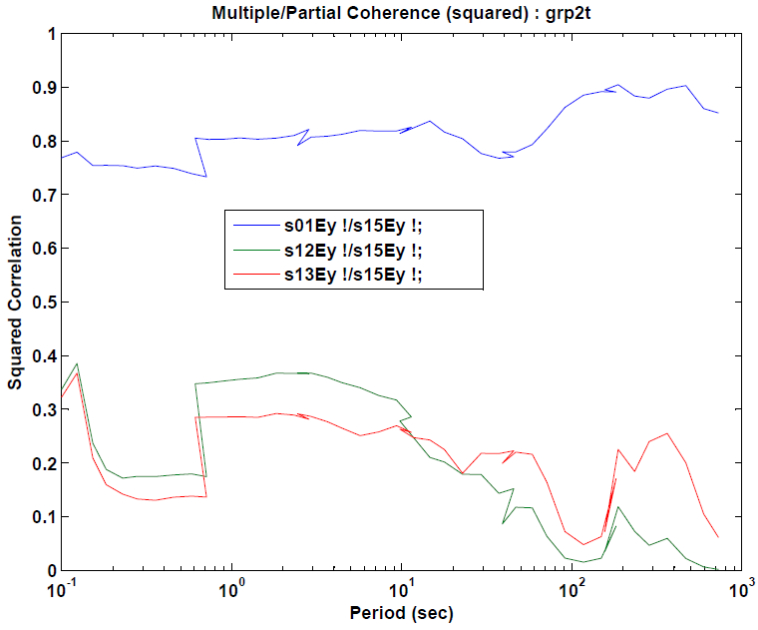

Figure 7d

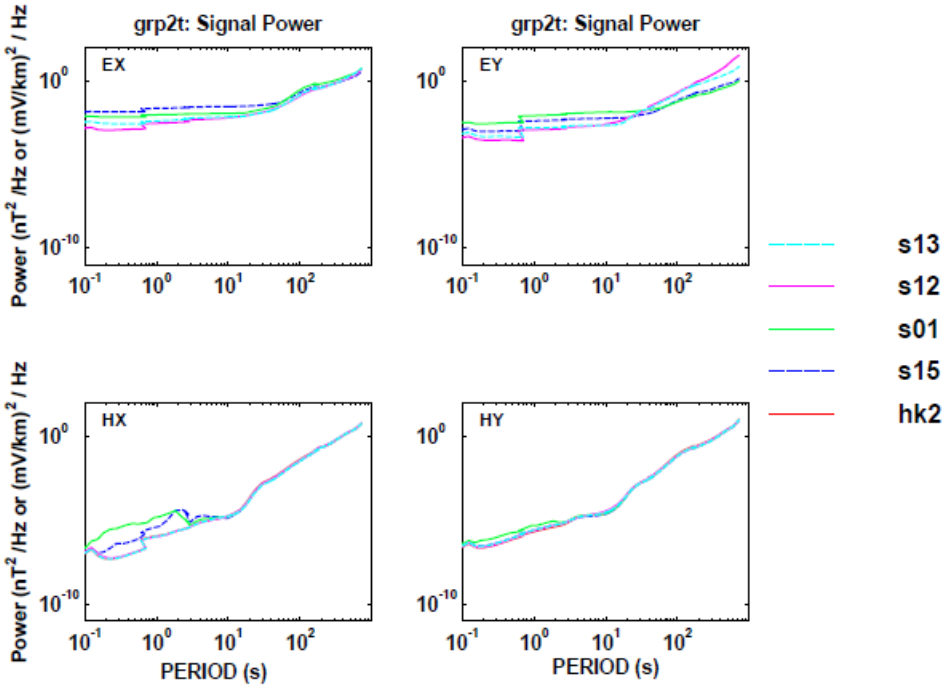

Figure 8a

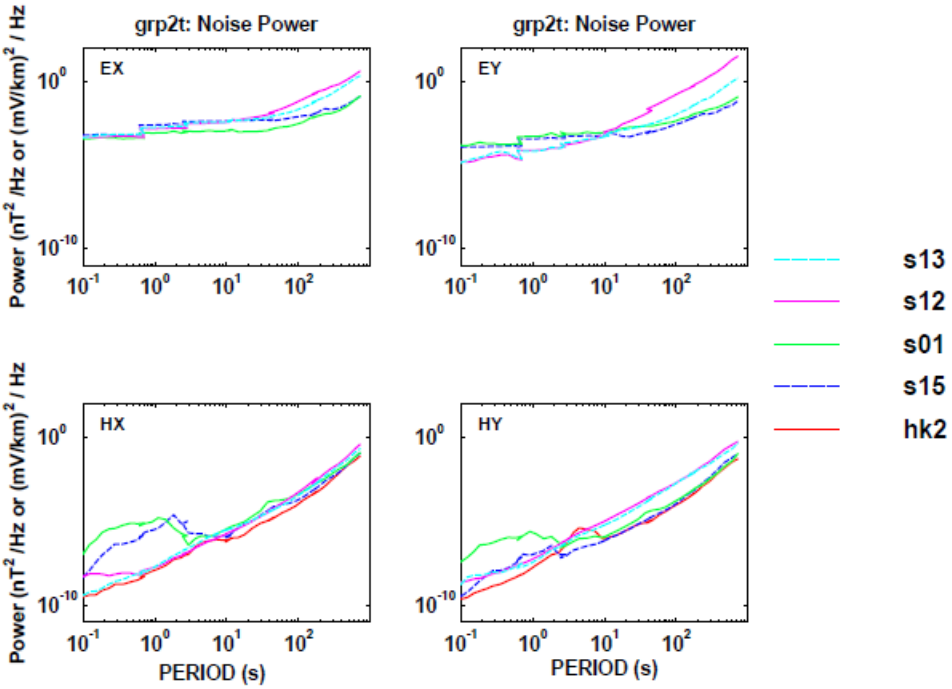

Figure 8b

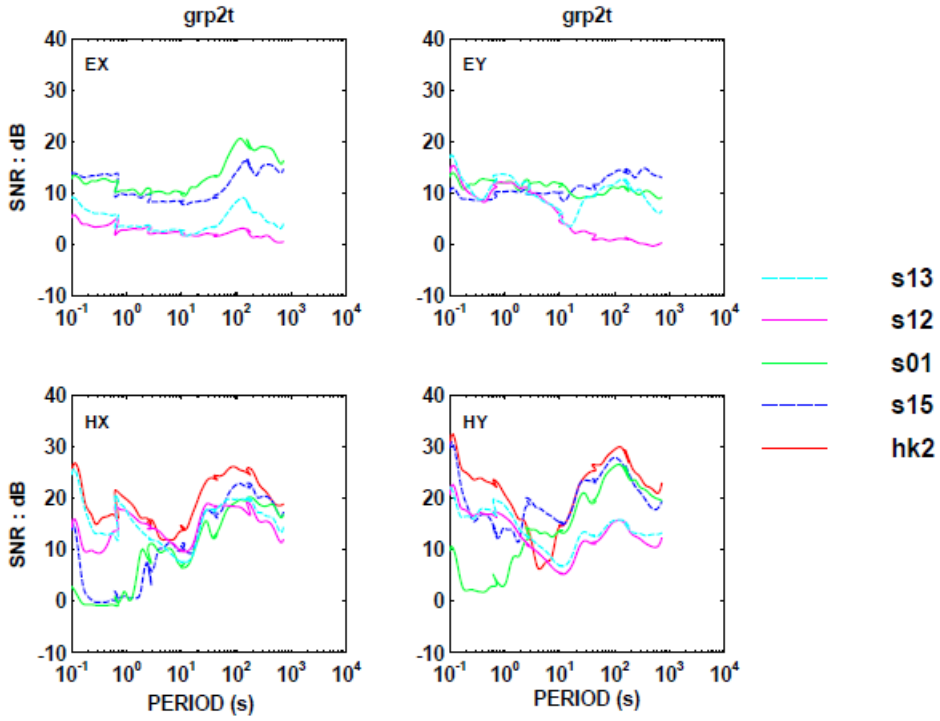

Figure 8c

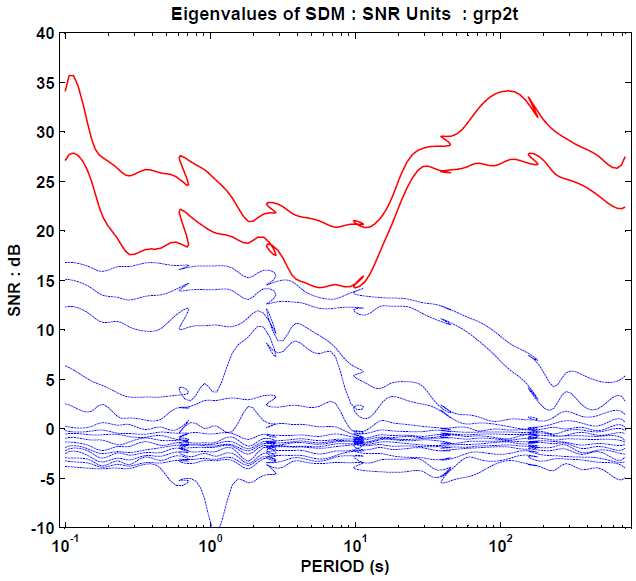

Figure 9

Group 3:

Figures 10a-10d show the transfer function amplitude and phase estimates with respect to the reference Parker H-fields and sta12 E-fields. The transfer function estimations of Hx and Hy are highly stable except of the dead band (periods ~0.5-15 s). Since all E-fields in this group were recorded at or close to the caldera the transfer function estimations are highly variable and noisy in the dead band and low frequencies (periods > 100 s).

Figures 11a-11d are coherence/correlations plots between the components of H and E-fields using Parker magnetics and sta12 electrics as references. Hx-fields are more coherent than Hy-fields for periods 0.1-10 s, and both of them have high coherencies for periods > 10 s. Hy shows extremely low correlations between 1 and 10 s periods. E-fields correlations are highly variable.

Figures 12a-12c show signal, noise, and SNR (S/N) levels respectively. Figure 13 shows eigenvalues of SDM where increased values of 3^{rd} and 4^{th} eigenvalues are present throughout the whole frequency range and slightly increased values of the 5^{th} eigenvalue at the higher frequencies (lower periods).

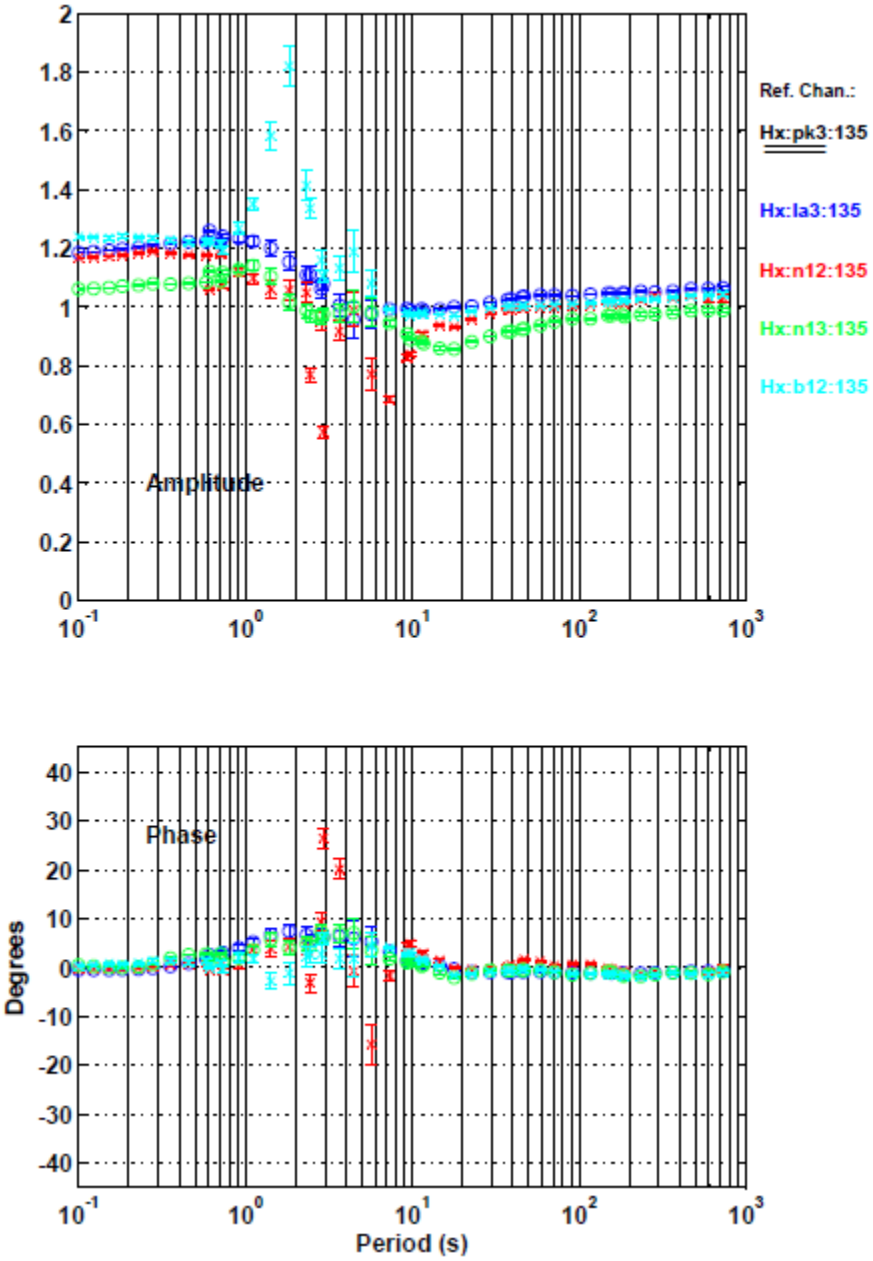
Amplitude
Phase
Degrees
Period (s)
Ref. Chan.:
Hx:pk3:135
Hx:la3:135
Hx:n12:135
Hx:n13:135
Hx:b12:135

Figure 10a

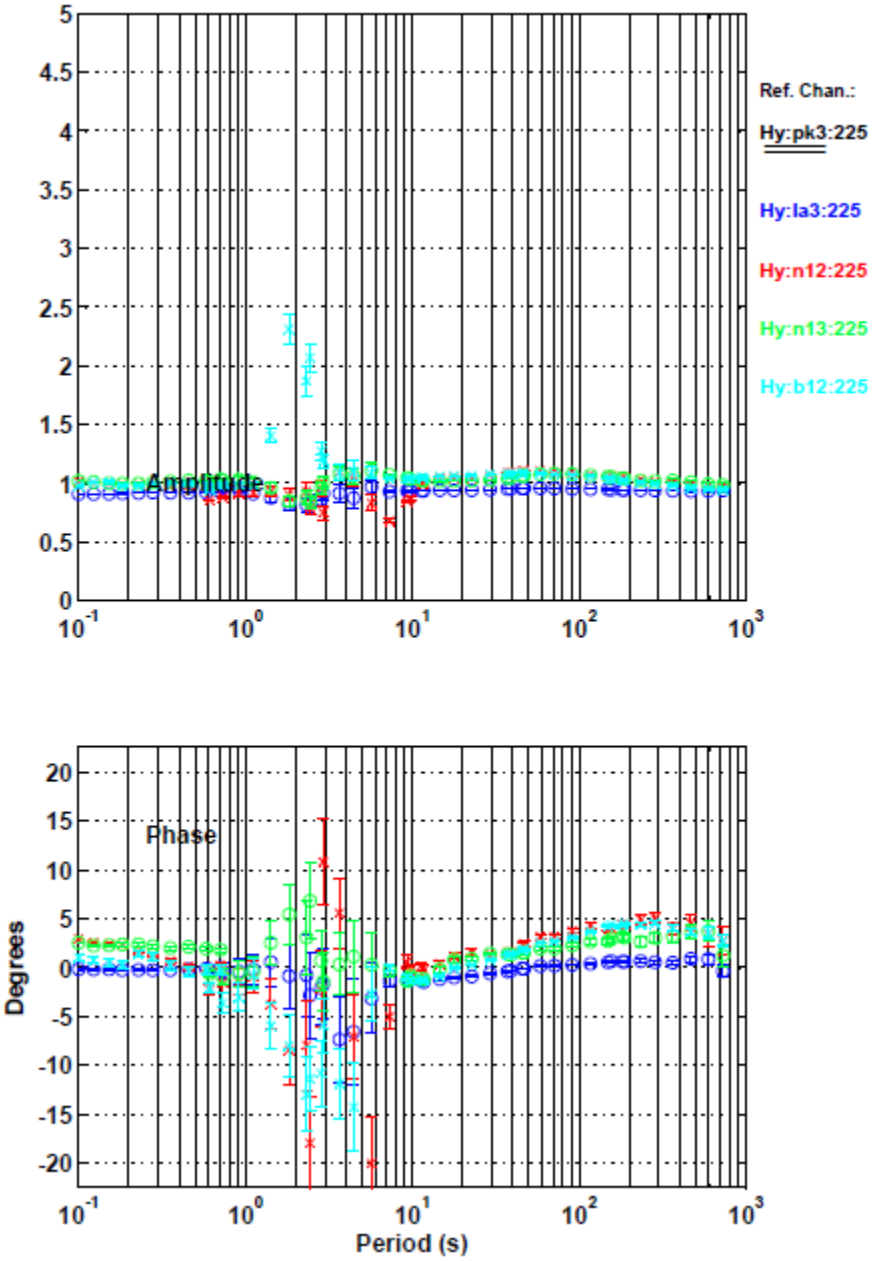
Amplitude
Ref. Chan.:
Hy:pk3:225
Hy:la3:225
Hy:n12:225
Hy:n13:225
Hy:b12:225
Phase
Degrees
Period (s)

Figure 10b

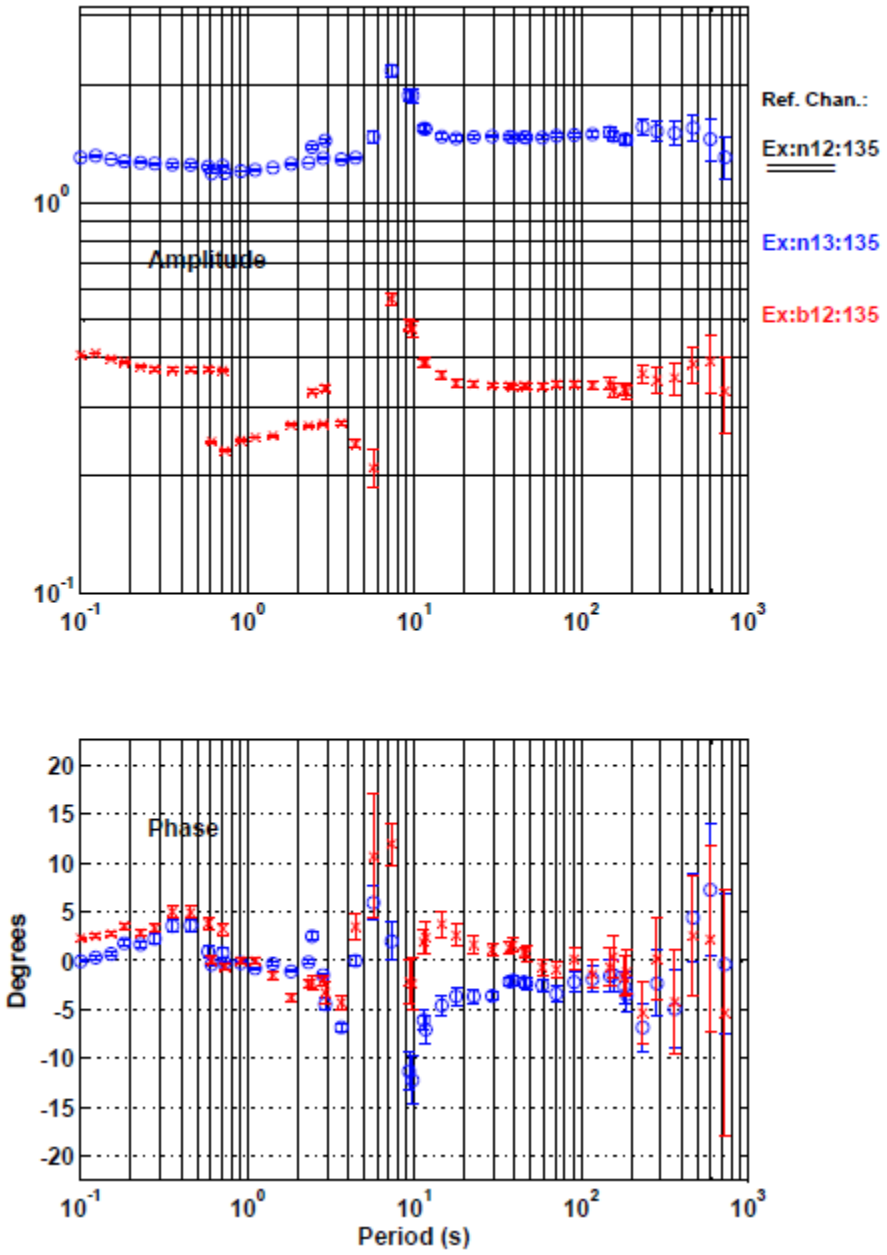
Ref. Chan.:
Ex:n12:135
Ex:n13:135
Ex:b12:135
Amplitude
Phase
Degrees
Period (s)

Figure 10c

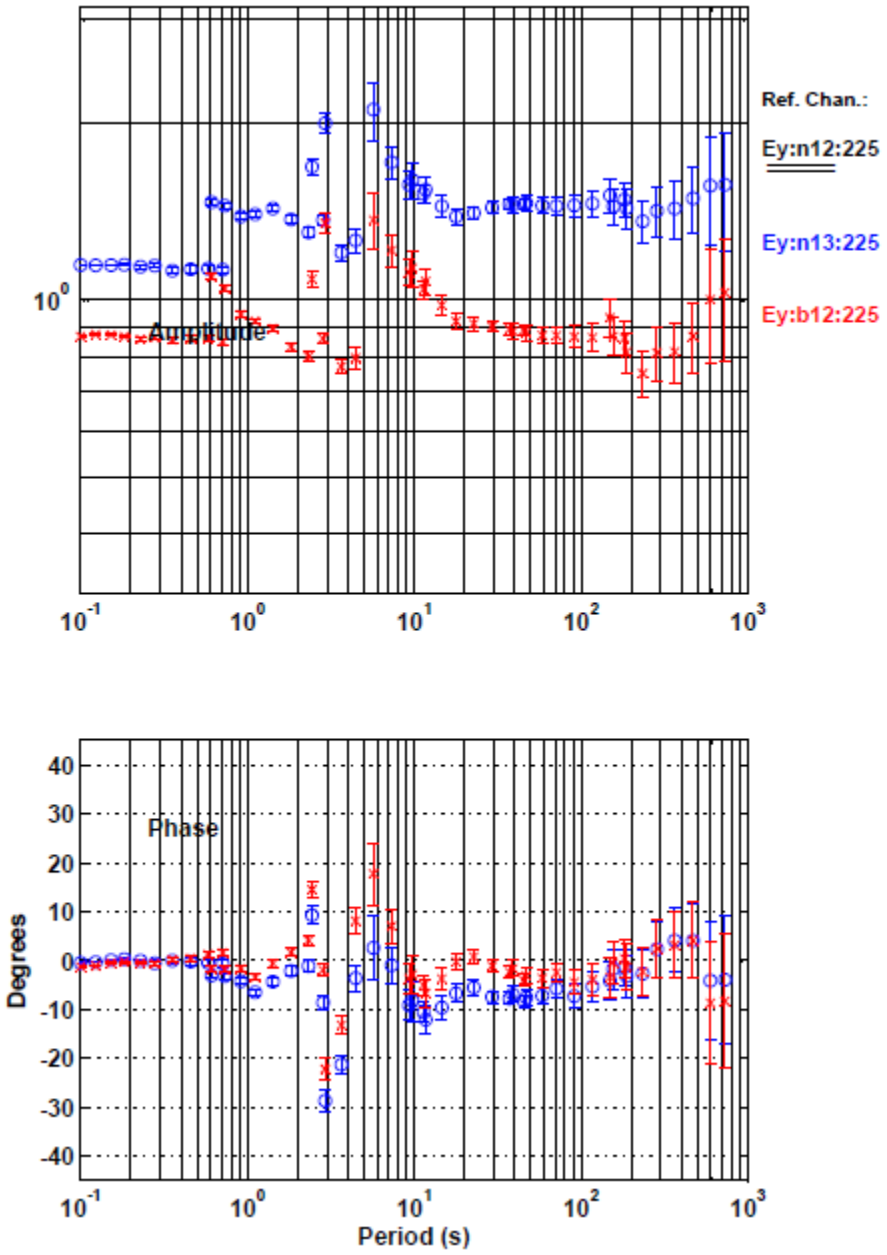
Ref. Chan.:
Ey:n12:225
Ey:n13:225
Ey:b12:225
Amplitude
Phase
Degrees
Period (s)

Figure 10d

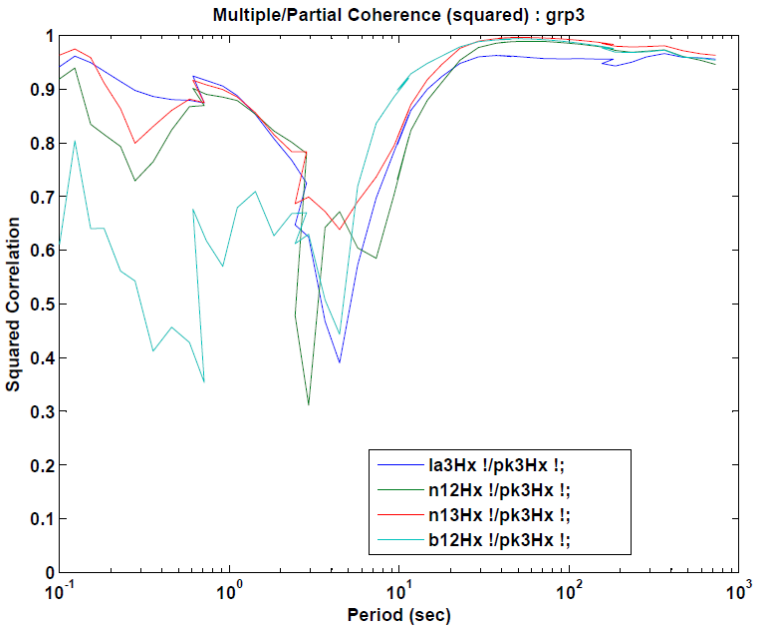

Figure 11a

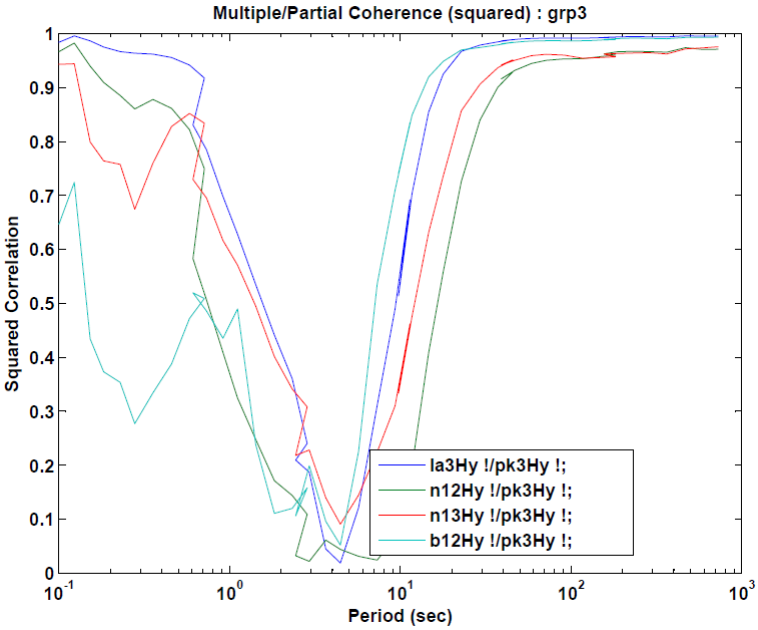

Figure 11b

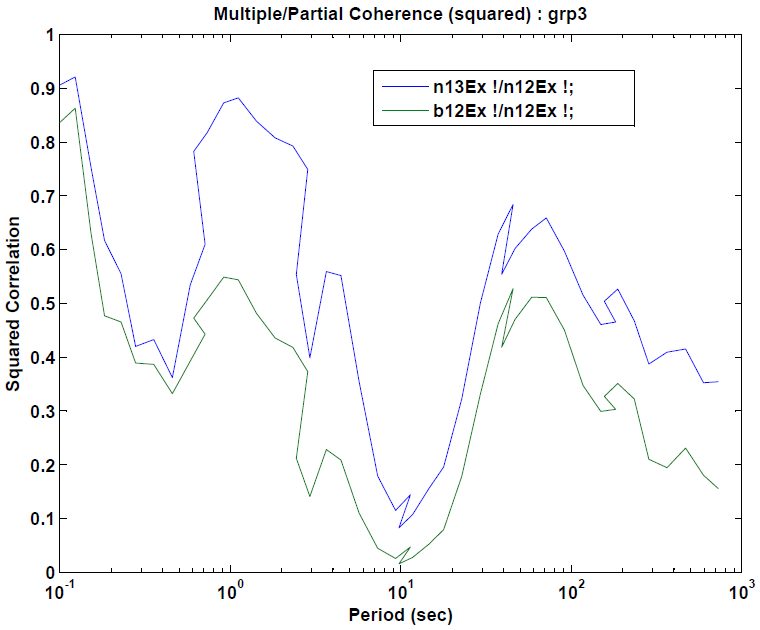

Figure 11c

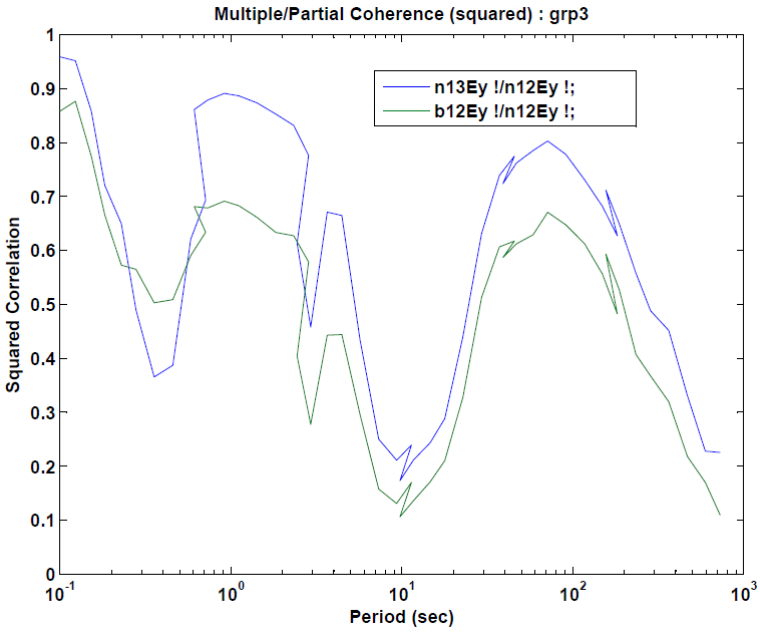

Figure 11d

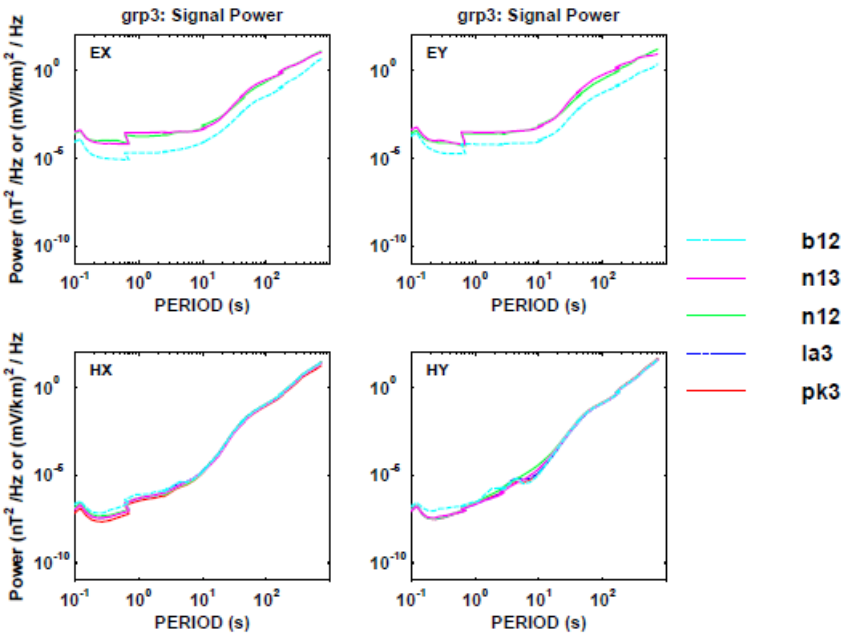

Figure 12a

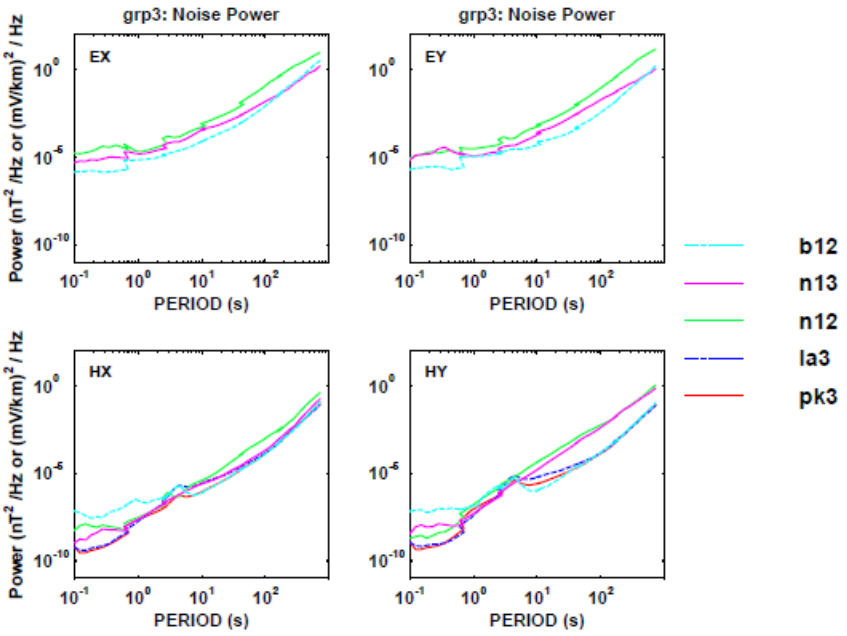

Figure 12b

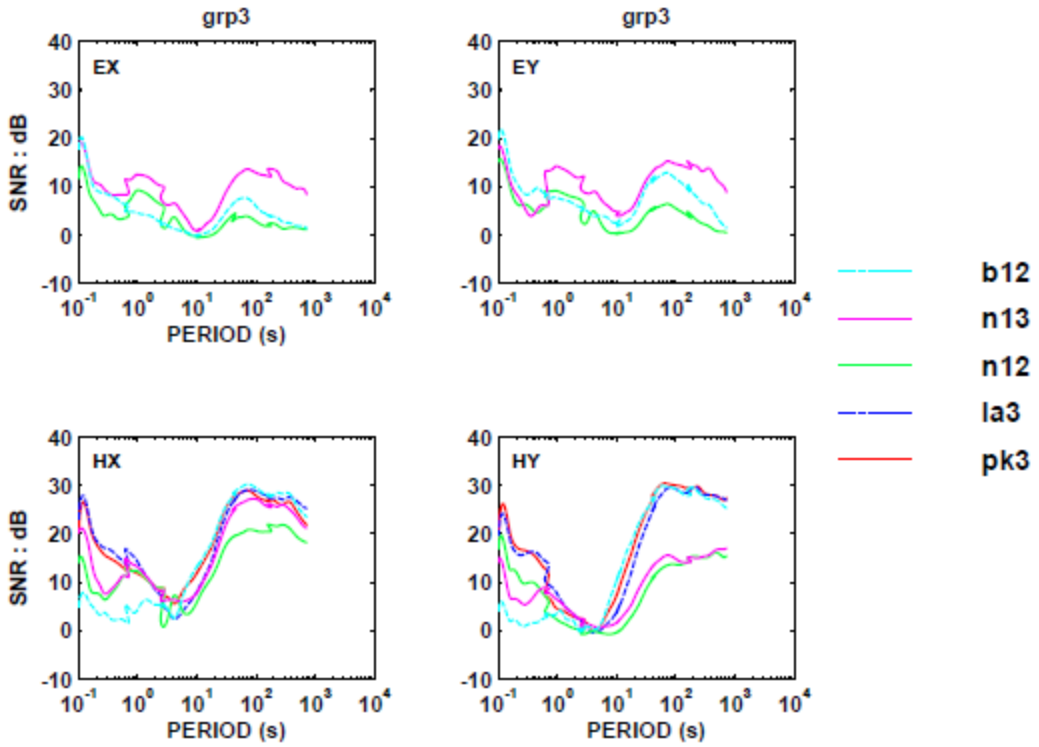

Figure 12c

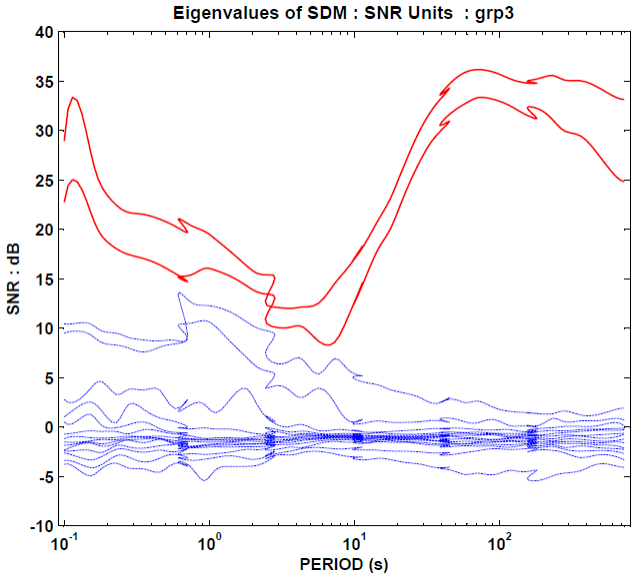

Figure 13

Group 4:

Figures 14a-14d show the transfer function amplitude and phase estimates with respect to the reference Parker H-fields and sta08 E-fields. The transfer function estimations of Hx and Hy are highly stable (except of the dead band (periods ~0.5-15 s)) for all of the stations except sta08. Sta08 variable phase at high frequencies might be due to timing errors in that system (however the mmt should have corrected for that so maybe something else is causing it). The transfer function estimations of Ex-fields and Ey-fields at sta06 and sta08 are highly stable at low frequencies, but variable and noisy at high frequencies and the dead-band. Sta01 Ey-field is very different from the rest of the stations.

Figures 15a-15d are coherence/correlations plots between the components of H and E-fields using Parker magnetics and sta01 electrics as references. Again, Hx-fields are more coherent than Hy-fields for periods 0.1-10 s, and both of them have high coherencies for periods > 10 s. Hy shows extremely low correlations between 0.2 and 5 s periods. Ex-fields and Ey-fields at sta06 and sta08 correlations are relatively high, including the dead band. Ey-fields at sta01 have no correlations at low frequencies (> 10 s), but high at the dead band and higher frequencies.

Figures 16a-16c show signal, noise, and SNR (S/N) levels respectively. Low coherency of magnetic fields at high frequencies and Ey-fields at low frequencies can be attributed to a very low S/N. Figure 17 shows eigenvalues of SDM where increased values of 3^{rd} and 4^{th} eigenvalues are present throughout the whole frequency range and somewhat increased values of the 5^{th} eigenvalue at the higher frequencies (lower periods).

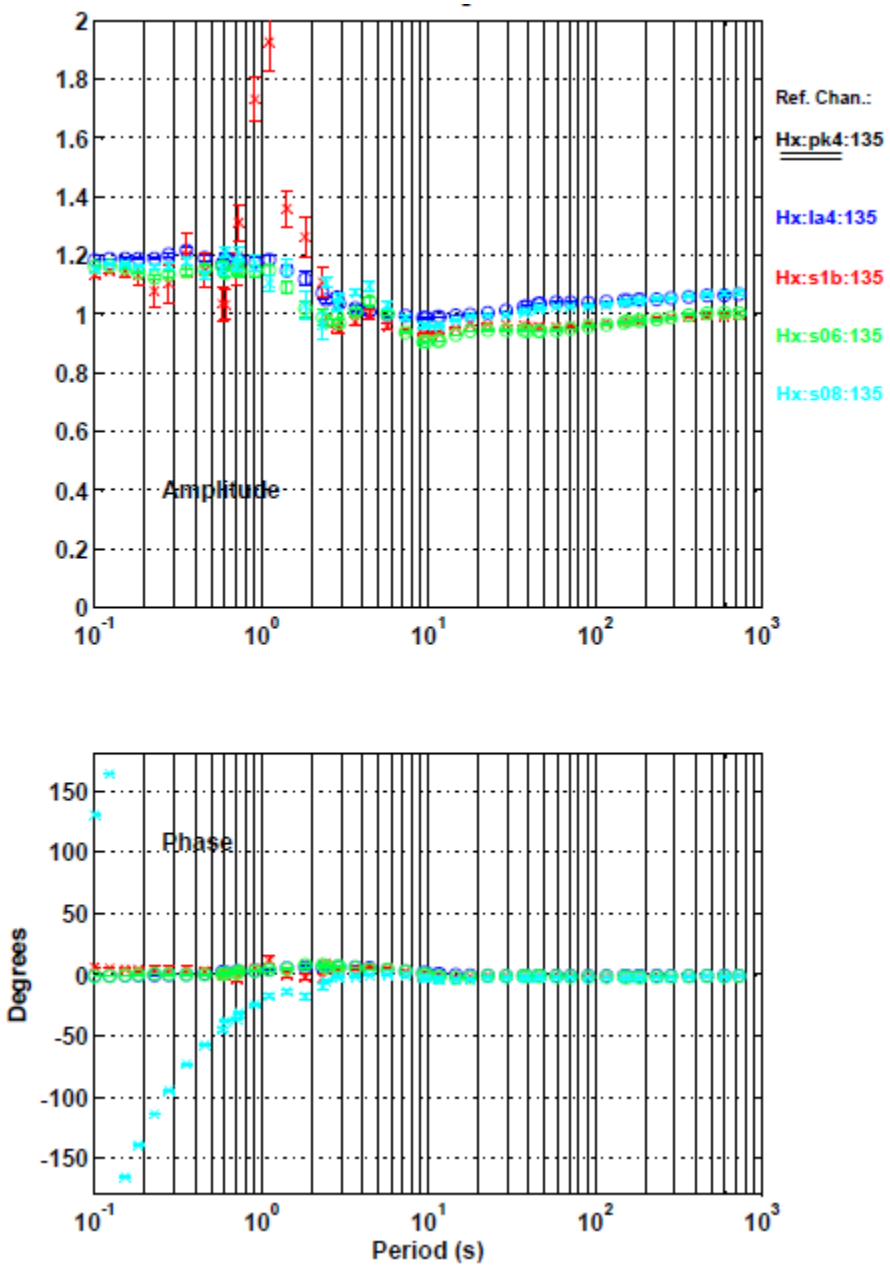
Amplitude
Ref. Chan.:
Hx:pk4:135
Hx:la4:135
Hx:s1b:135
Hx:s06:135
Hx:s08:135
Phase
Degrees
Period (s)

Figure 14a

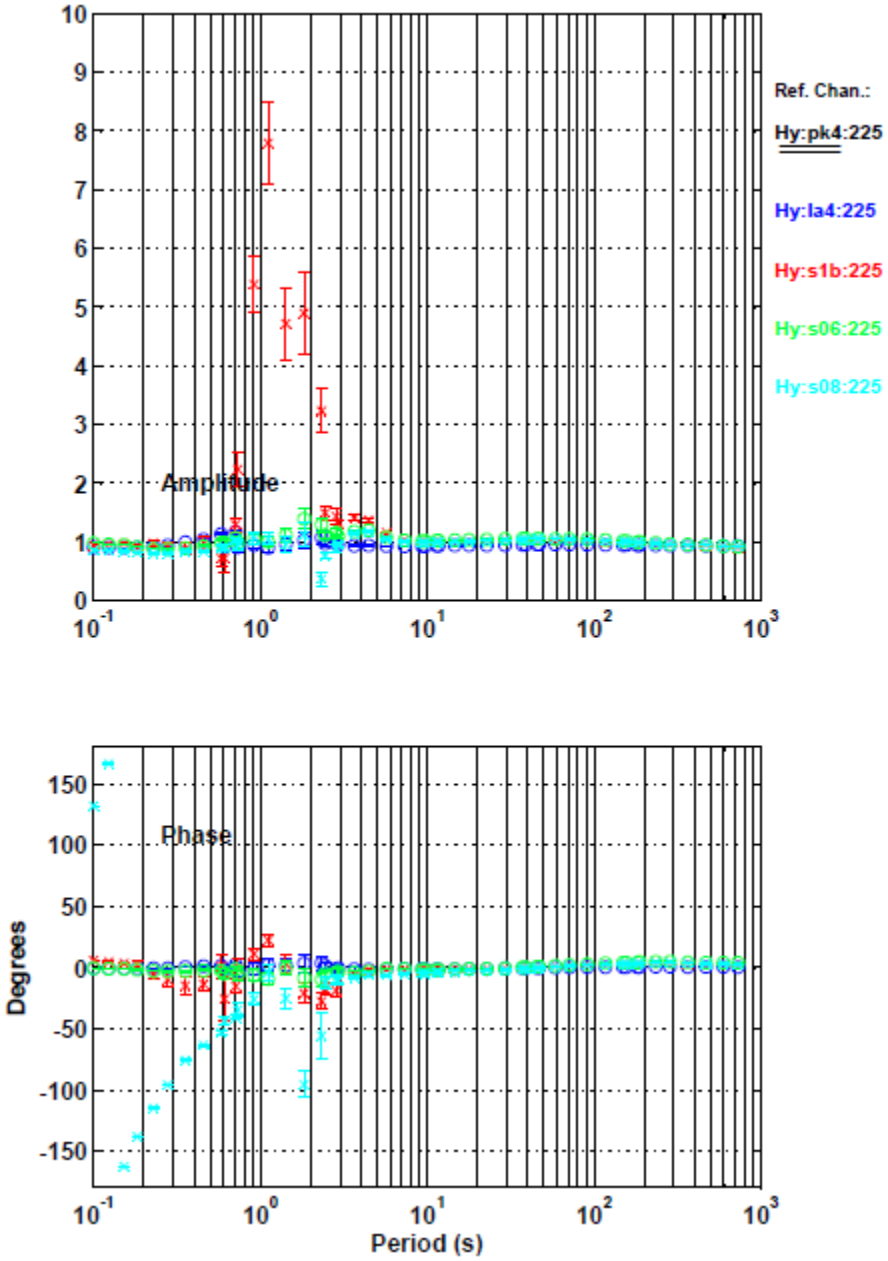
Amplitude
Ref. Chan.:
Hy:pk4:225
Hy:la4:225
Hy:s1b:225
Hy:s06:225
Hy:s08:225
Phase
Degrees
Period (s)

Figure 14b

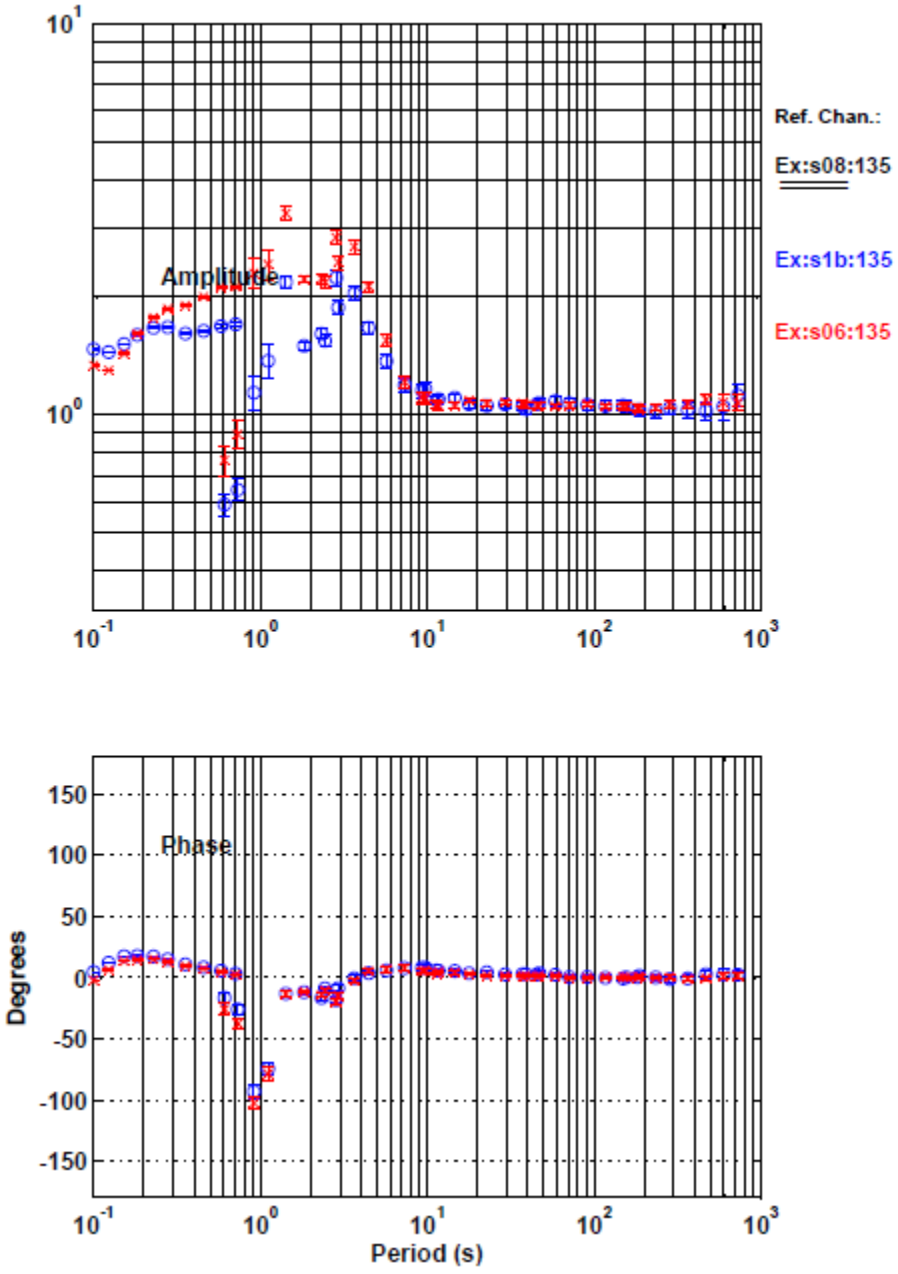
Amplitude
Ref. Chan.:
Ex:s08:135
Ex:s1b:135
Ex:s06:135
Phase
Degrees
Period (s)

Figure 14c

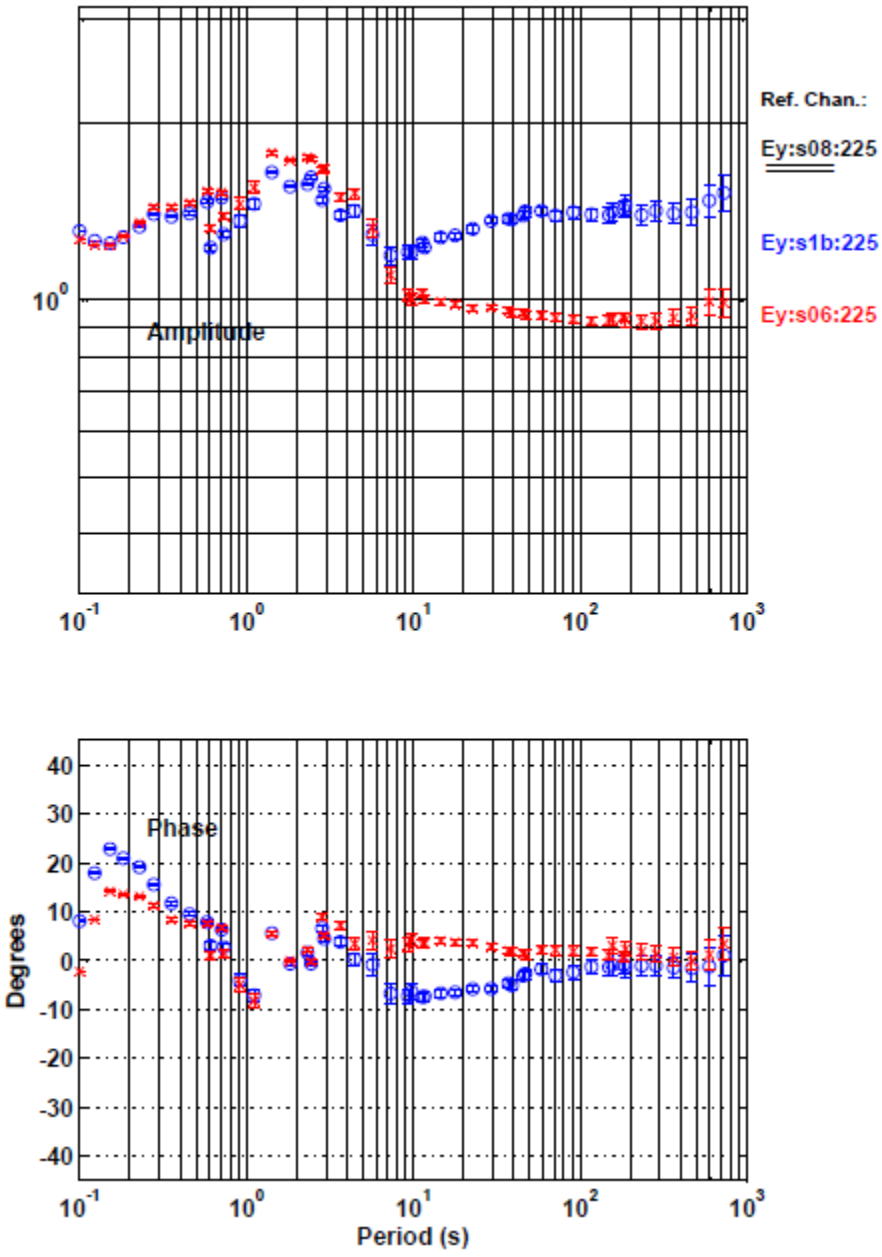
Ref. Chan.:
Ey:s08:225
Ey:s1b:225
Ey:s06:225
Amplitude
Phase
Degrees
Period (s)

Figure 14d

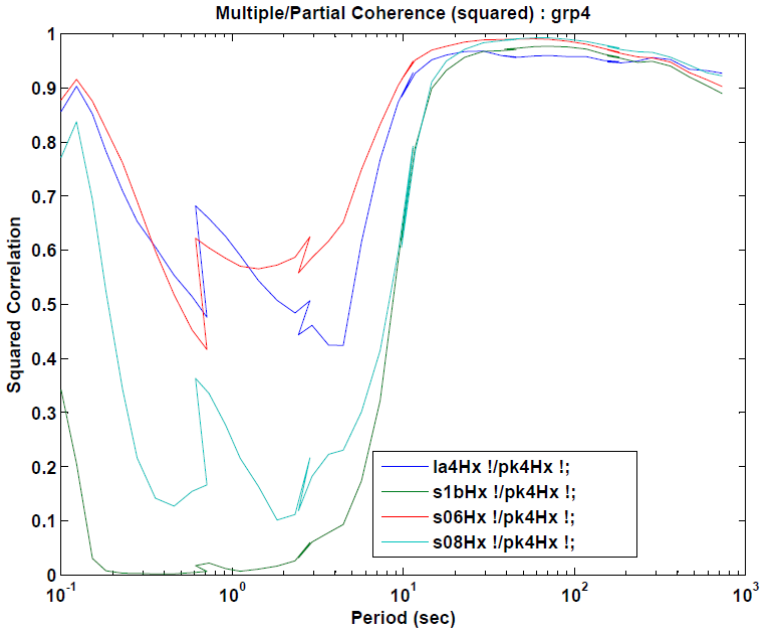

Figure 15a

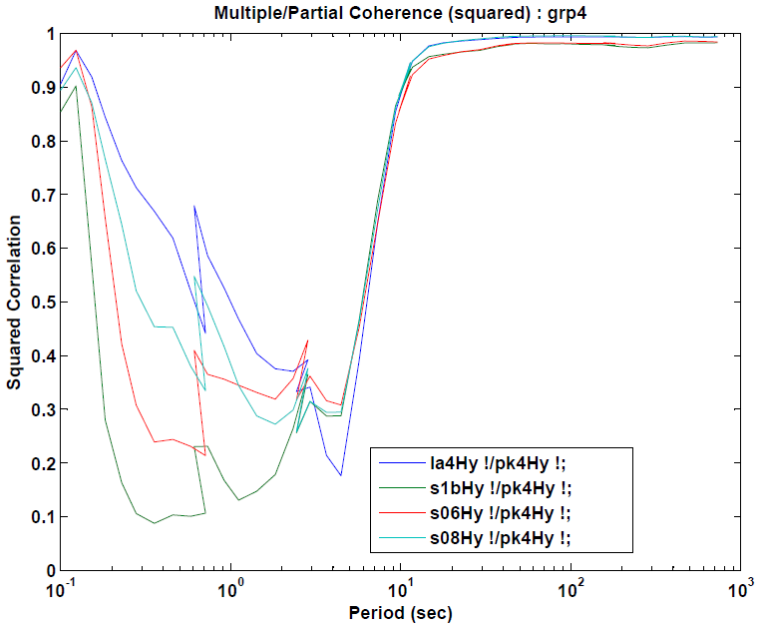

Figure 15b

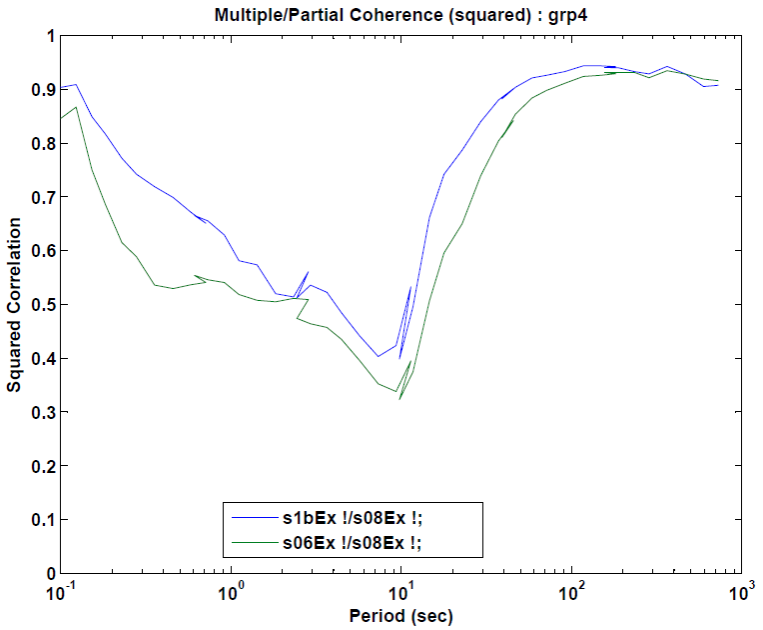

Figure 15c

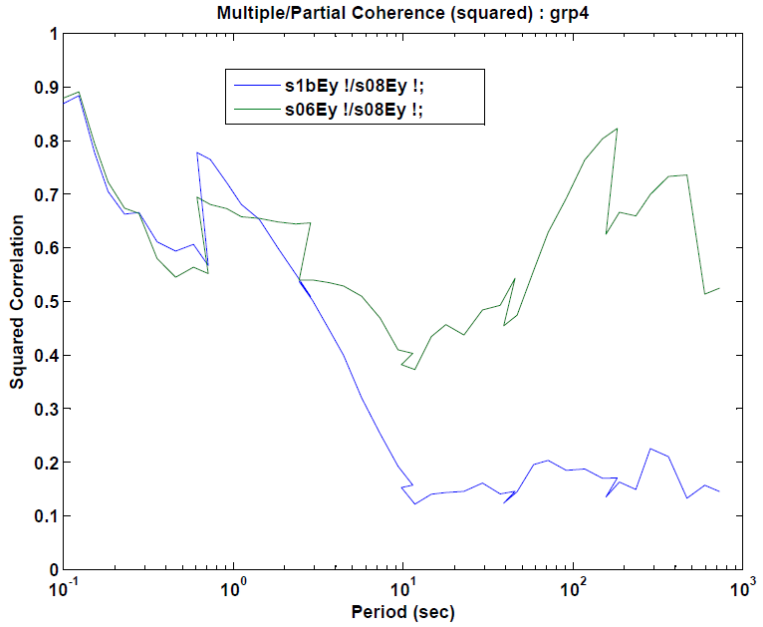

Figure 15d

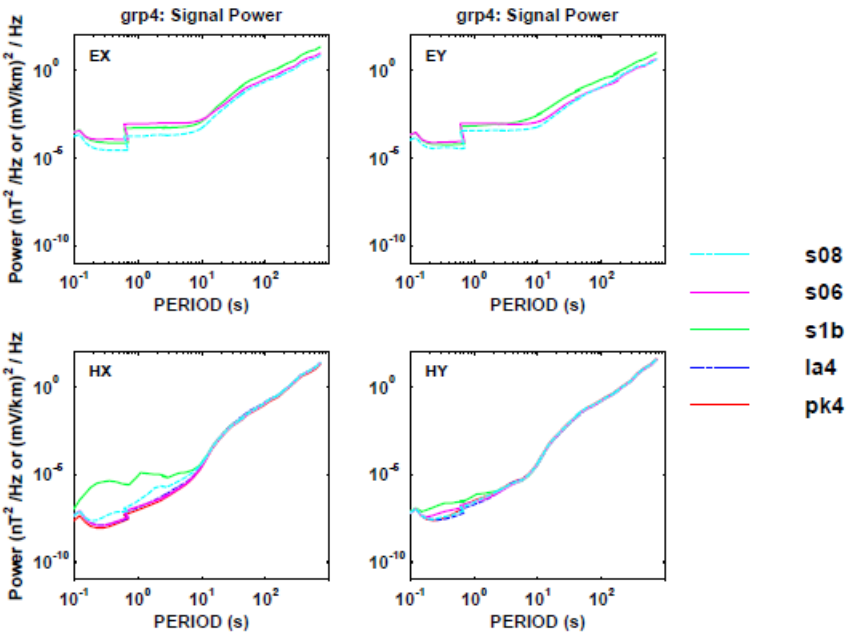

Figure 16a

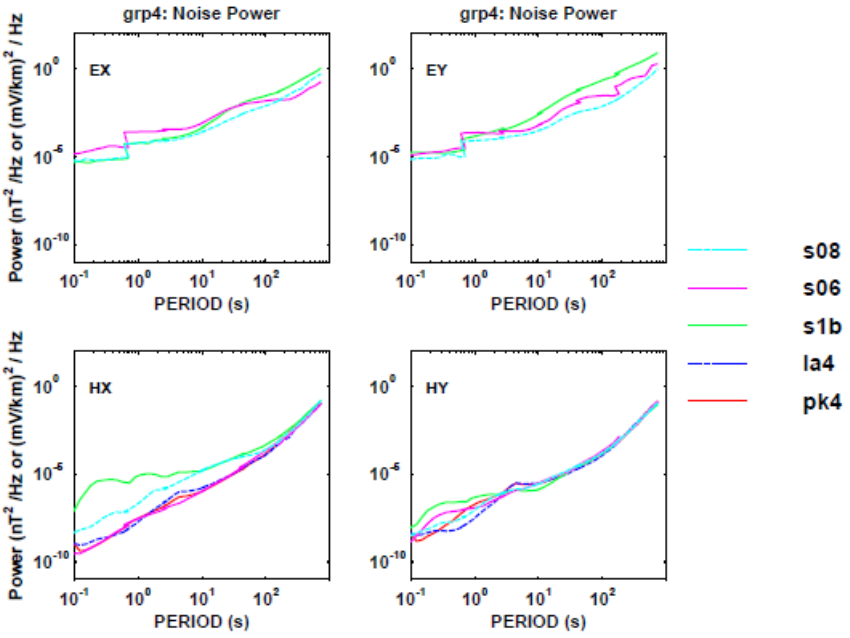

Figure 16b

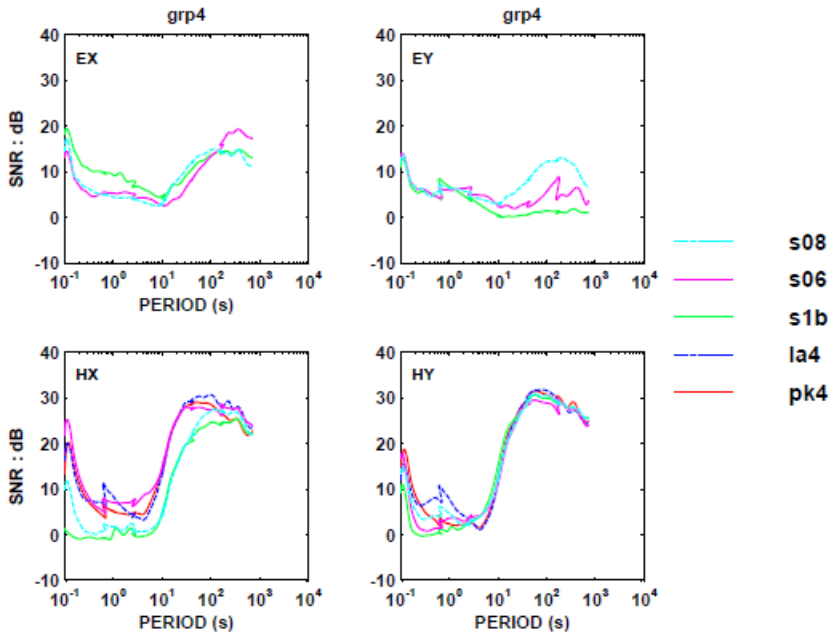

Figure 16c

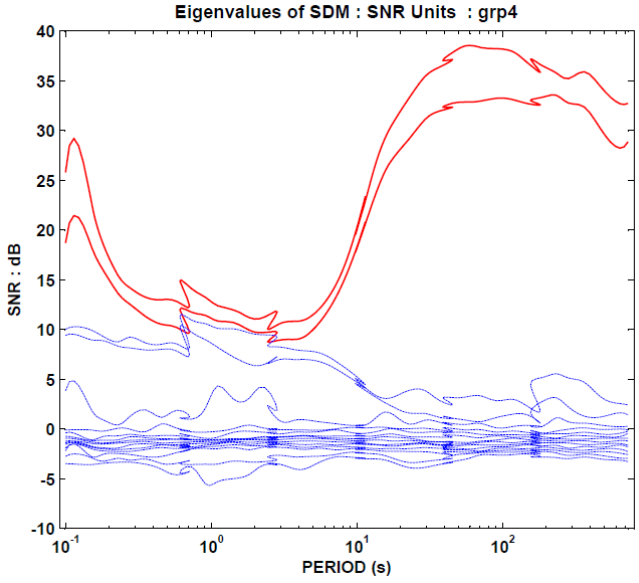

Figure 17

Group 5:

Figures 18a-18d show the transfer function amplitude and phase estimates with respect to the reference Parker H-fields and sta07 E-fields. The transfer function estimations of magnetic fields are stable and excellent except of the dead band (periods ~0.3-7 s). The transfer function estimations of E-fields are stable at periods between 15 and 200 s.

Figures 19a-19d are coherence/correlations plots between the components of H and E-fields using Parker magnetics and sta07 electrics as references. Except of the dead band the magnetic fields are highly correlated. Electric fields at sites sta07, sta08, and sta11 show high coherence. Given a large distance between Lau Lease (one of our remote sites) and the National park, low coherence in E-signals as shown in Figures 19c and 19d is expected.

Figures 20a-20c show signal, noise, and SNR (S/N) levels respectively. The values are low only in the dead band. Figure 21 shows eigenvalues of SDM where increased values of 3^{rd} and 4^{th} eigenvalues are present up to ~500 s and hints of the 5^{th} eigenvalue at the higher frequencies (lower periods).

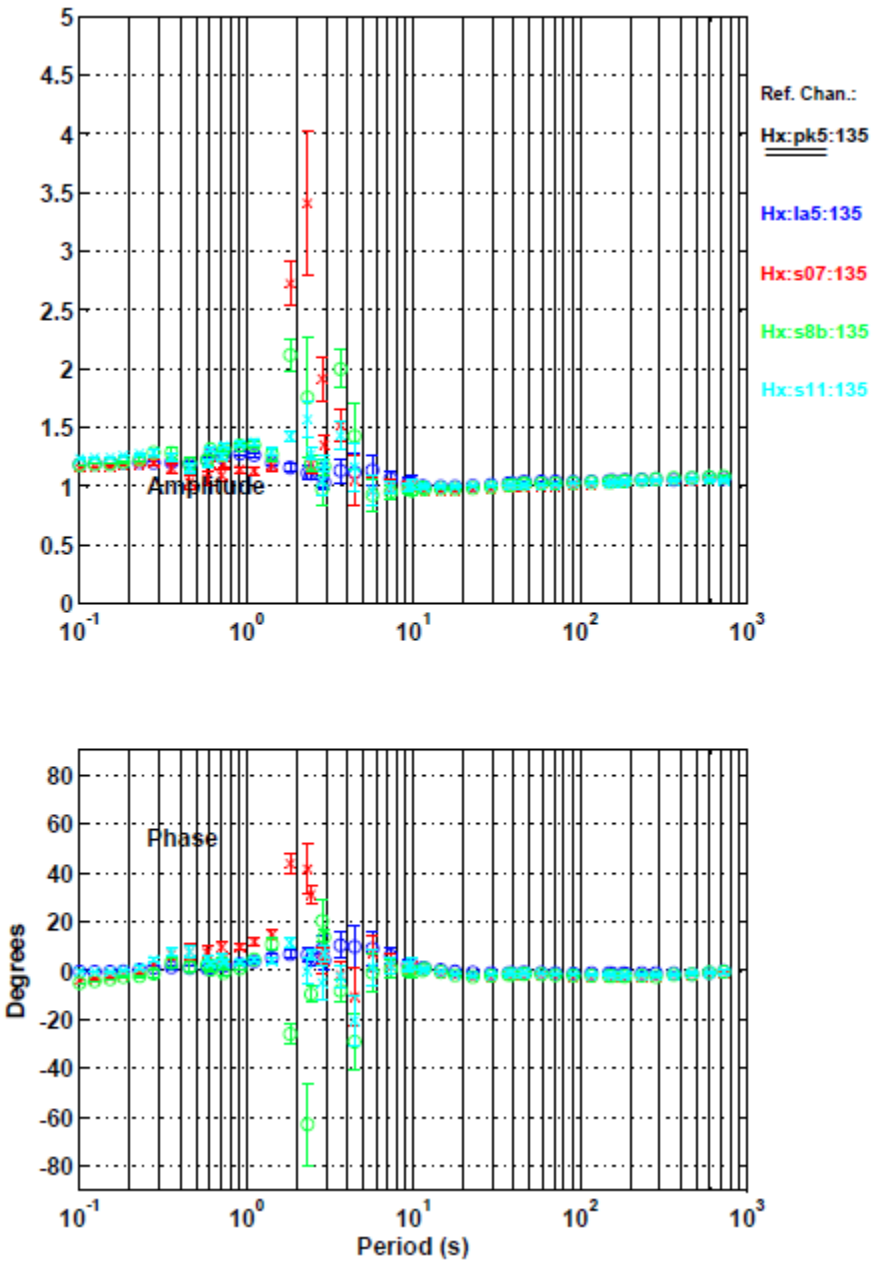
Amplitude
Ref. Chan.:
Hx:pk5:135
Hx:la5:135
Hx:s07:135
Hx:s8b:135
Hx:s11:135
Phase
Degrees
Period (s)

Figure 18a

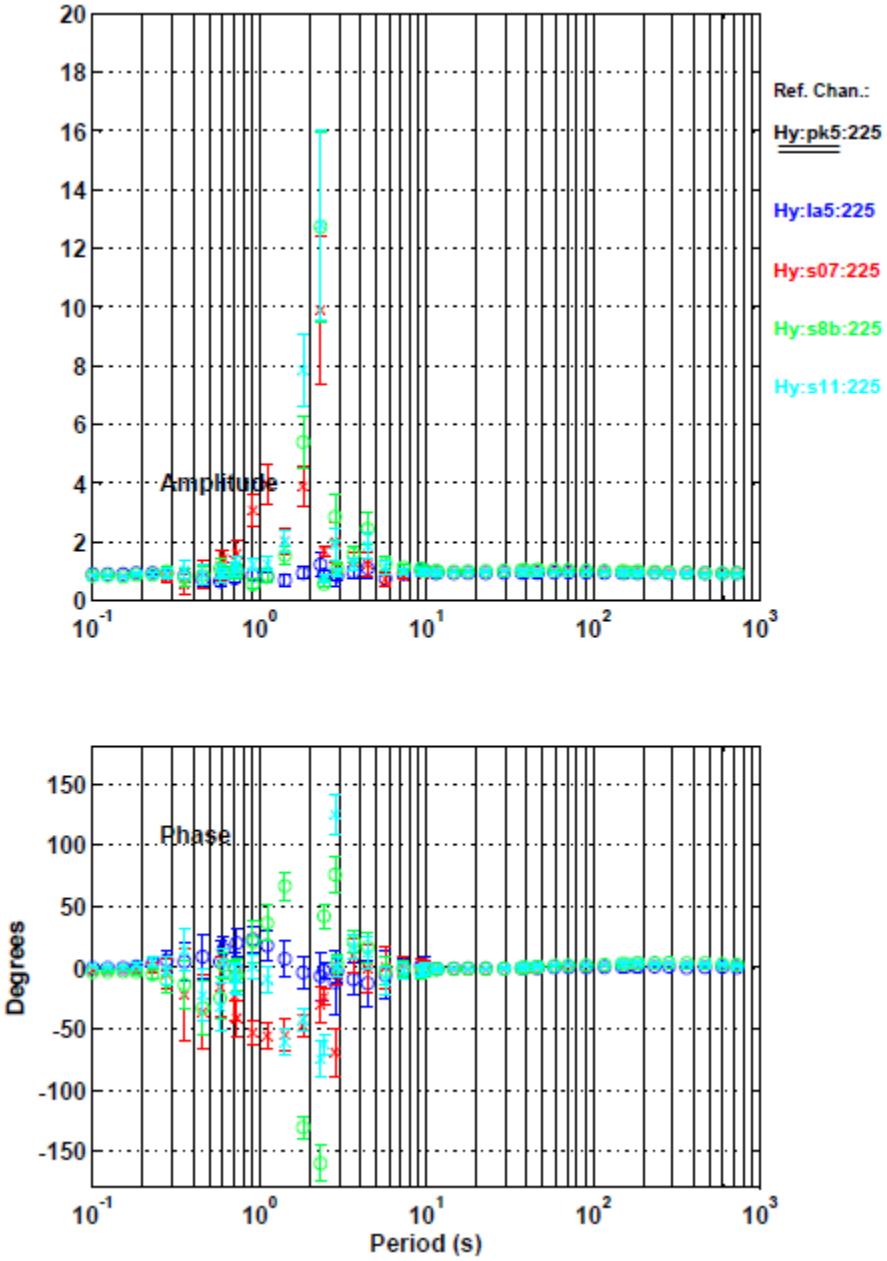
Amplitude
Ref. Chan.:
Hy:pk5:225
Hy:la5:225
Hy:s07:225
Hy:s8b:225
Hy:s11:225
Phase
Degrees
Period (s)

Figure 18b

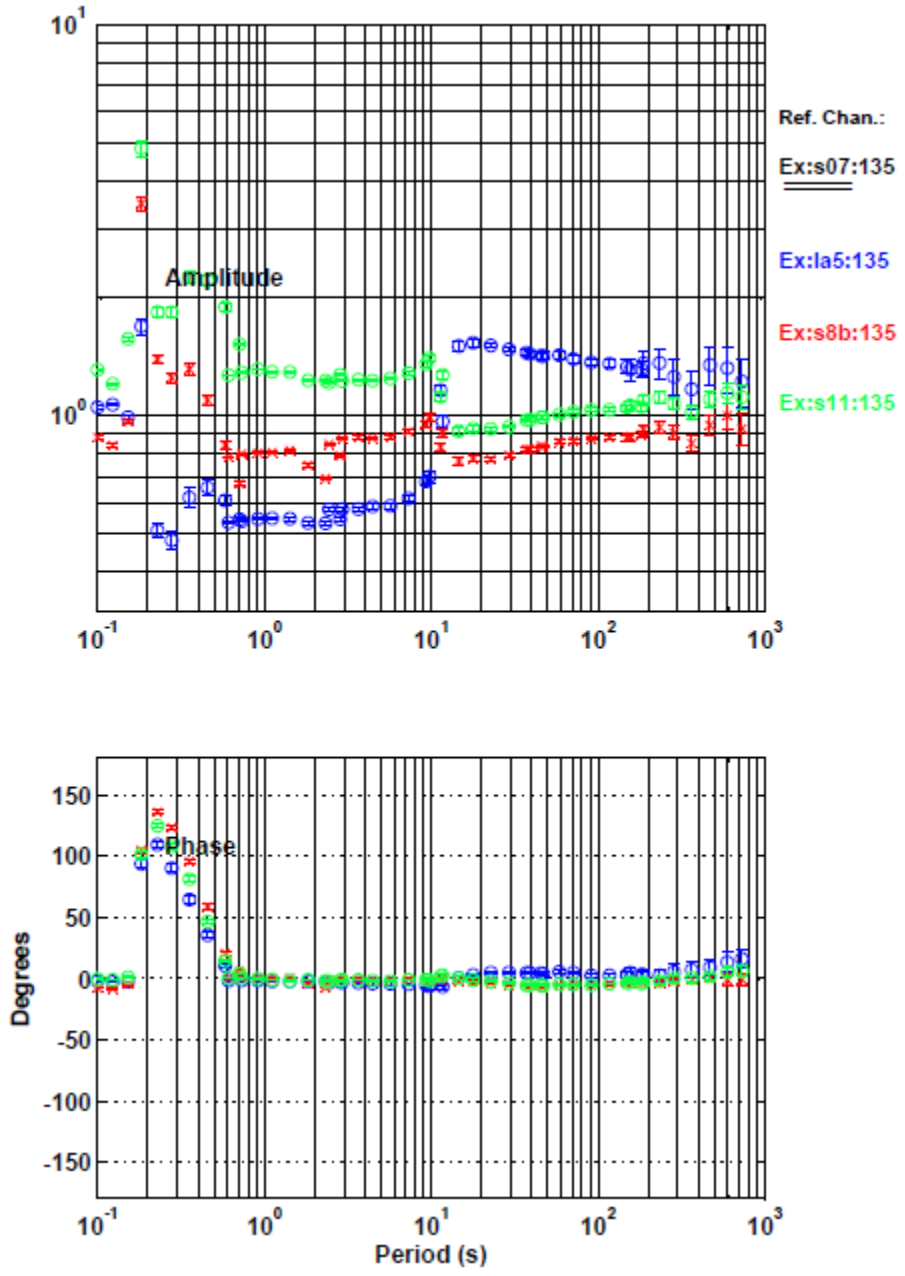
Amplitude
Ref. Chan.:
Ex:s07:135
Ex:la5:135
Ex:s8b:135
Ex:s11:135
Phase
Degrees
Period (s)

Figure 18c

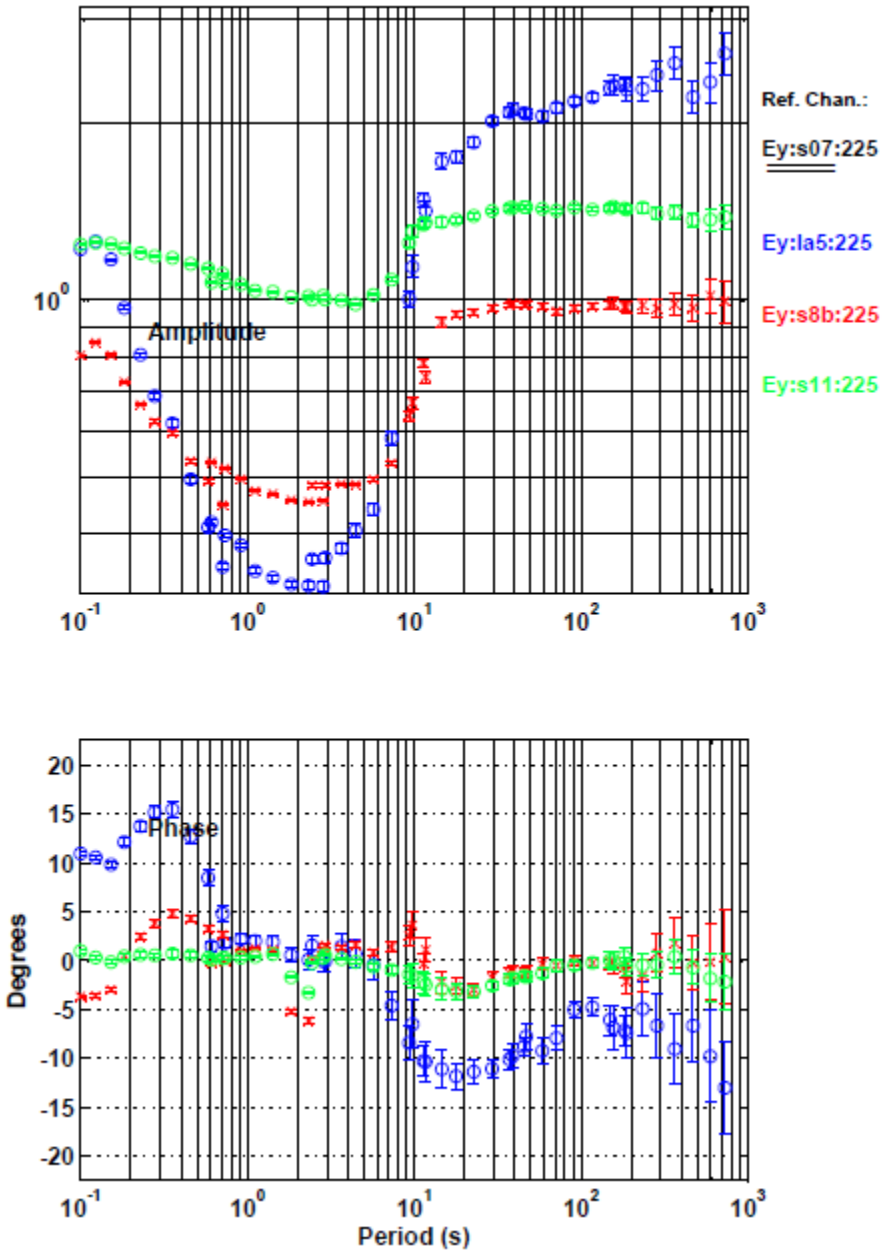
Ref. Chan.:
Ey:s07:225
Ey:la5:225
Ey:s8b:225
Ey:s11:225
Amplitude
Phase
Degrees
Period (s)

Figure 18d

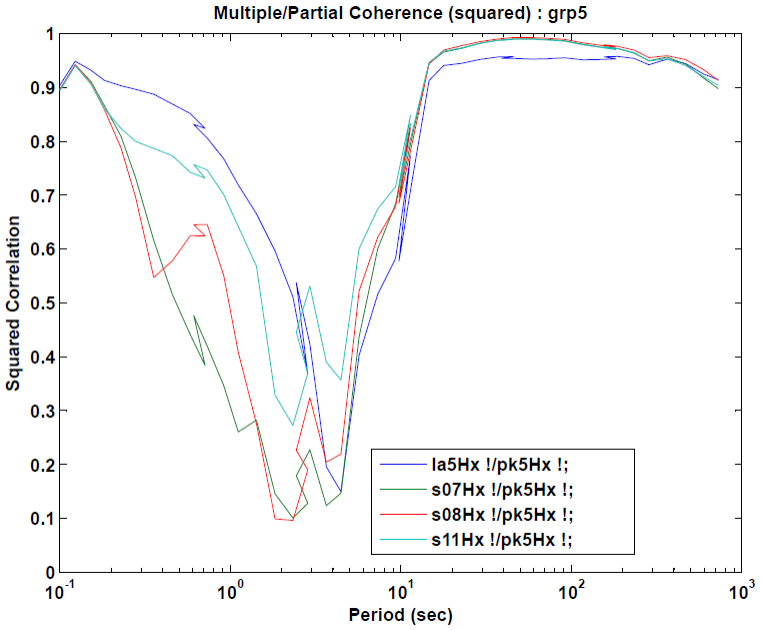

Figure 19a

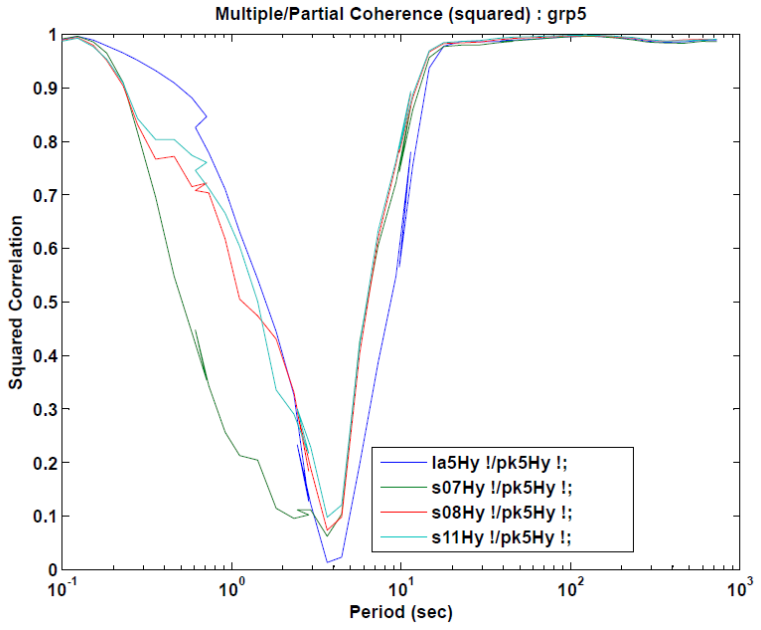

Figure 19b

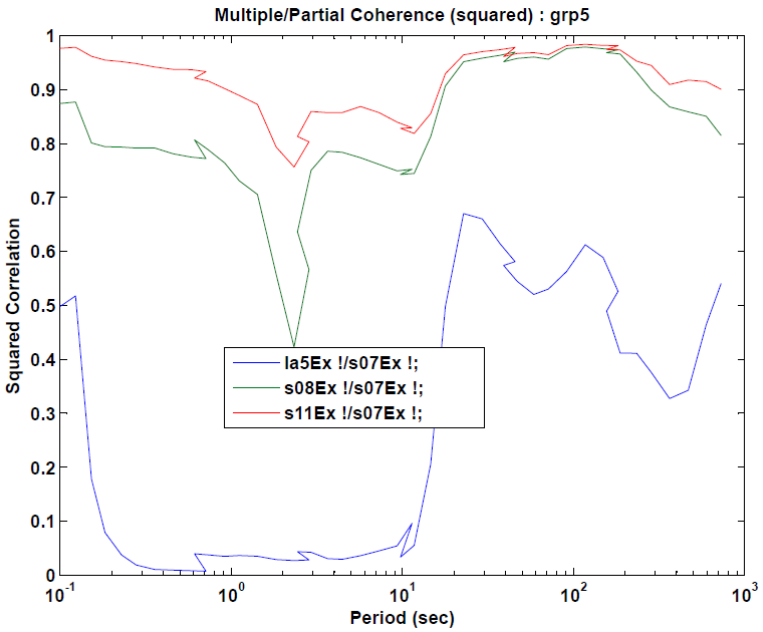

Figure 19c

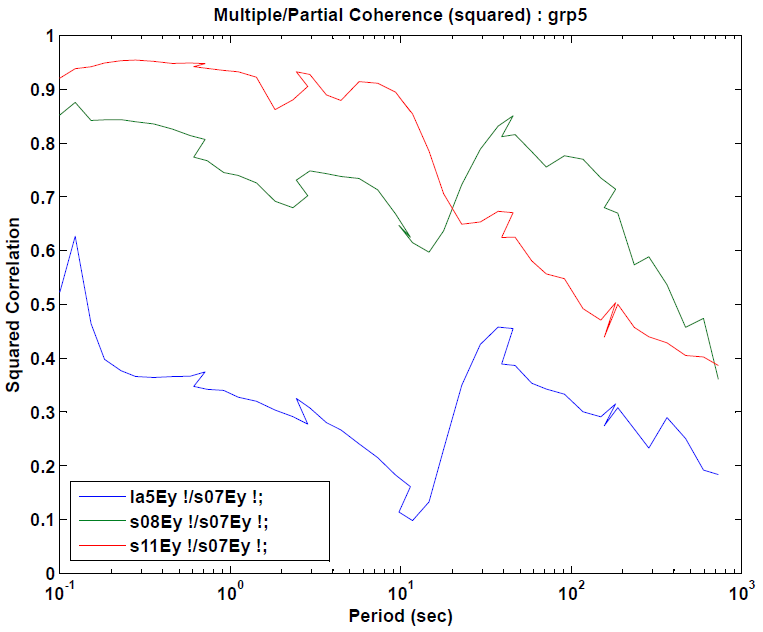

Figure 19d

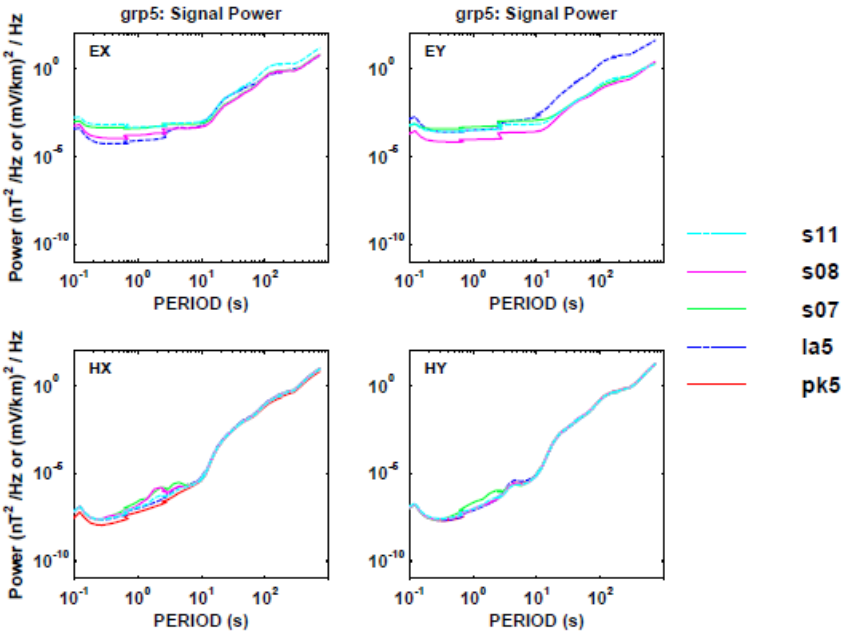

Figure 20a

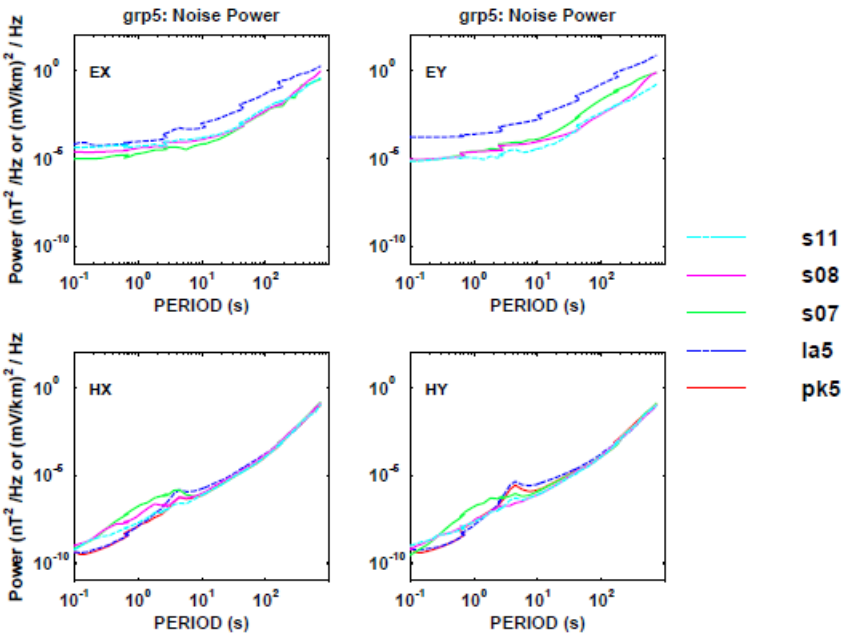

Figure 20b

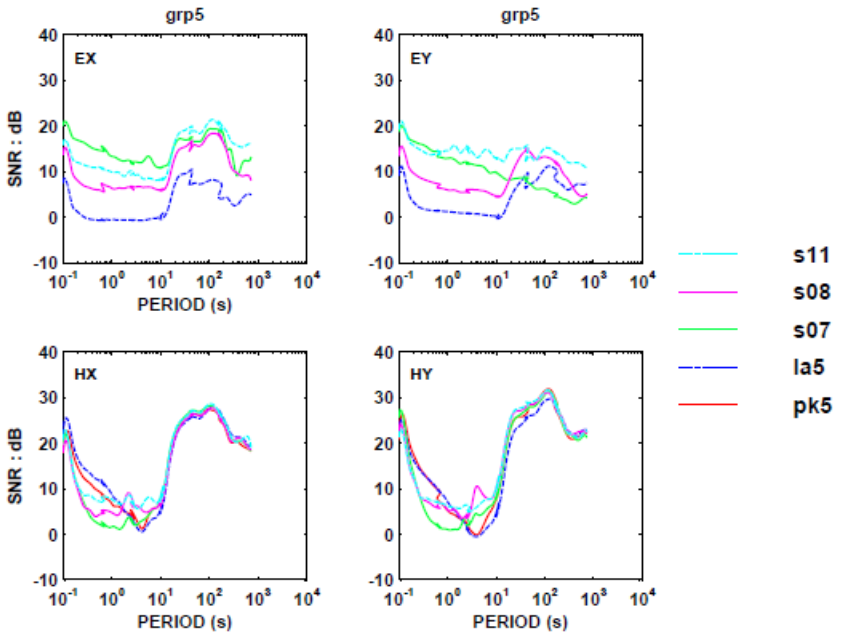

Figure 20c

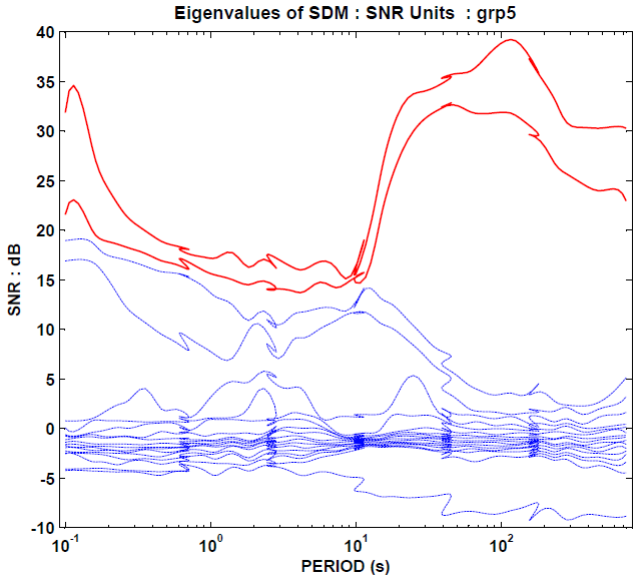

Figure 21

Group 6:

Figures 22a-22d show the transfer function amplitude and phase estimates with respect to the reference Parker H-fields and sta18 E-fields. Estimates of the magnetic fields transfer function are stable for Lau Lease, sta09, and sta10. Estimates of Hx at sta18 and Hy at sta17 and sta18 are noisy at high frequencies and the dead band. Except of the station sta09, the transfer function estimations of E-fields are stable. Station sta09 should be reanalyzed and studied in more details in the next processing round.

Figures 23a-23d are coherence/correlations plots between the components of H and E-fields using Parker magnetics and sta18 electrics as references. Except of the dead band and higher frequencies the magnetic fields are highly correlated. Ex-fields have higher correlations than Ey. Correlations of E-fields at Lau Lease and s09 are low, most likely due to a low S/N as shown in Figure 24.

Figures 24a-24c show signal, noise, and SNR (S/N) levels respectively. Figure 25 shows eigenvalues of SDM where increased values of 3^{rd} and 4^{th} eigenvalues are present up to ~500s.

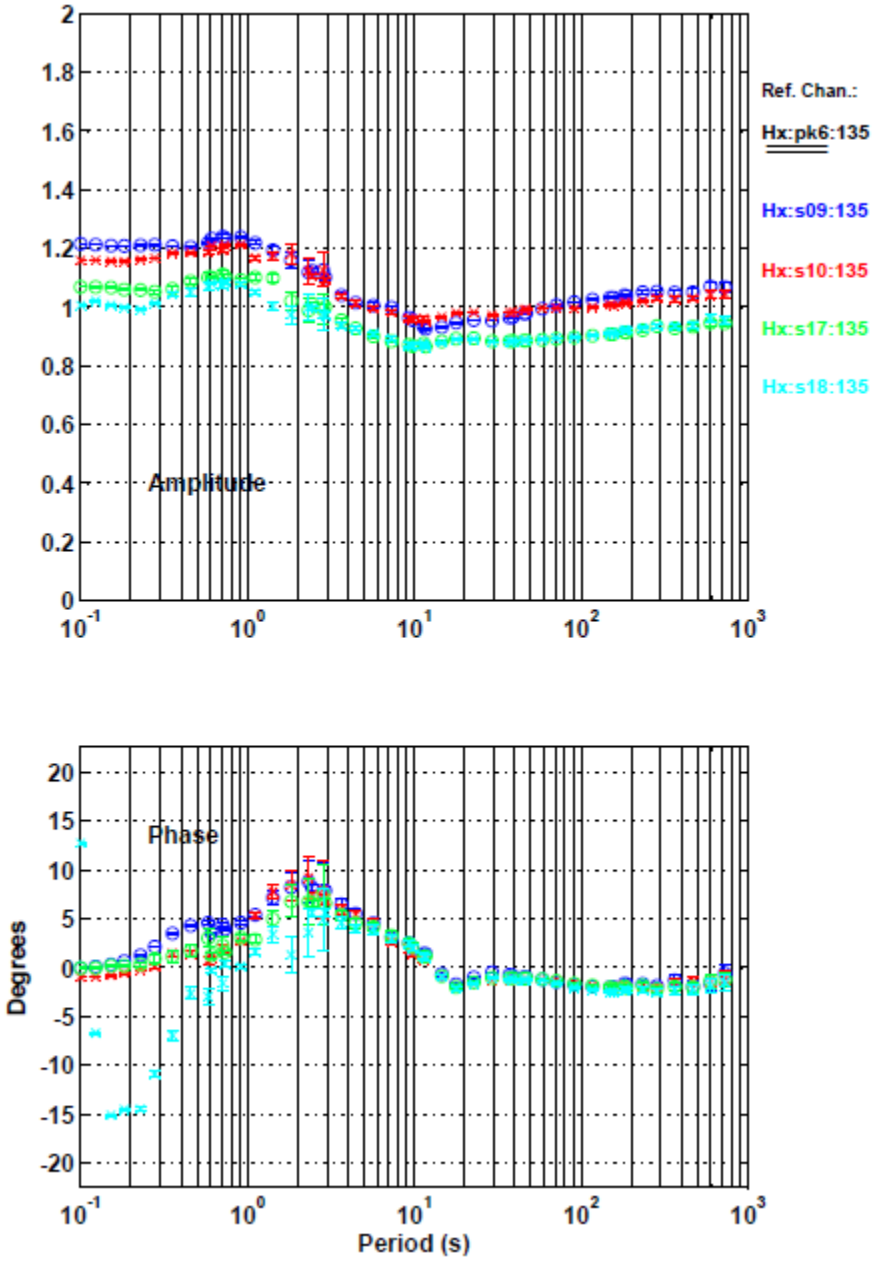
Amplitude
Ref. Chan.:
Hx:pk6:135
Hx:s09:135
Hx:s10:135
Hx:s17:135
Hx:s18:135
Phase
Degrees
Period (s)

Figure 22a

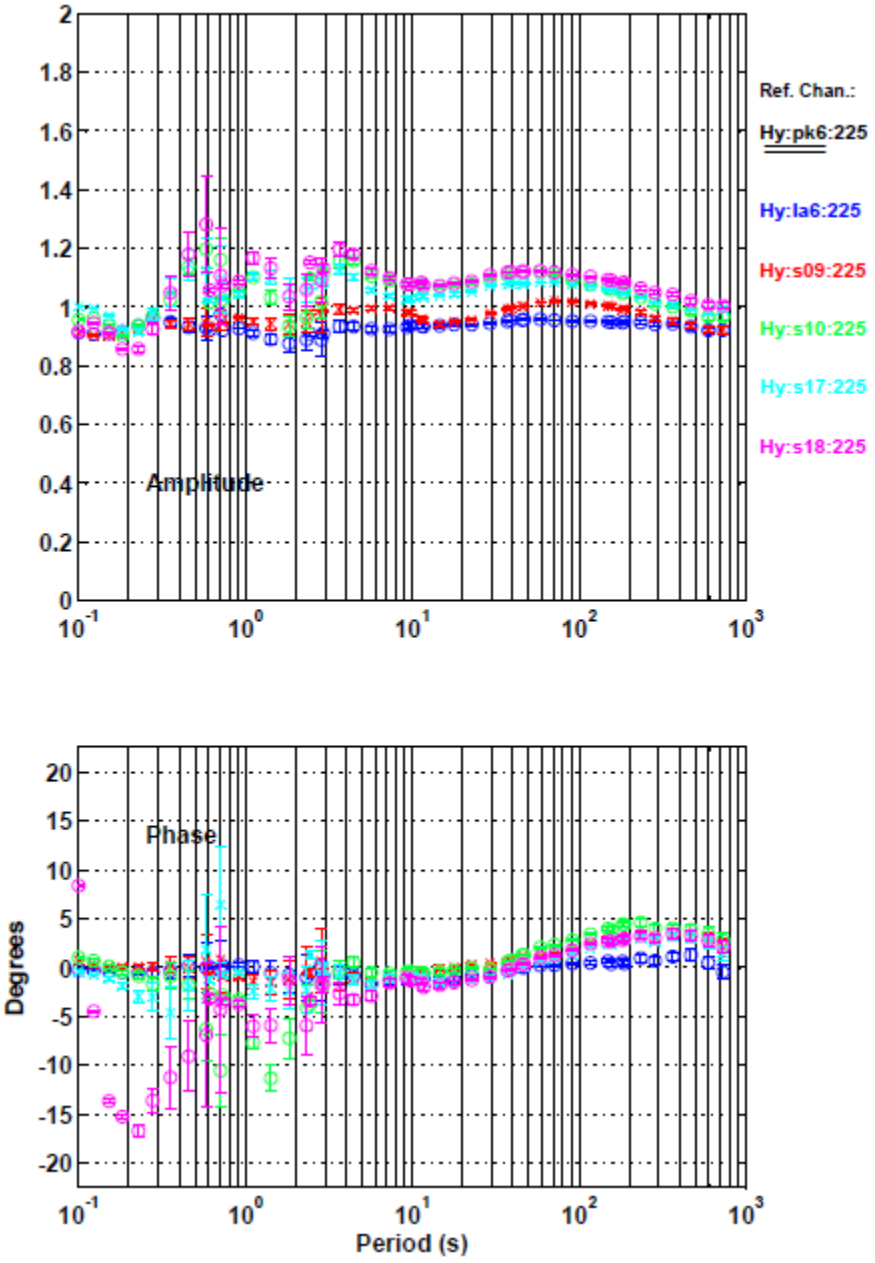
Amplitude
Phase
Degrees
Period (s)
Ref. Chan.:
Hy:pk6:225
Hy:la6:225
Hy:s09:225
Hy:s10:225
Hy:s17:225
Hy:s18:225

Figure 22b

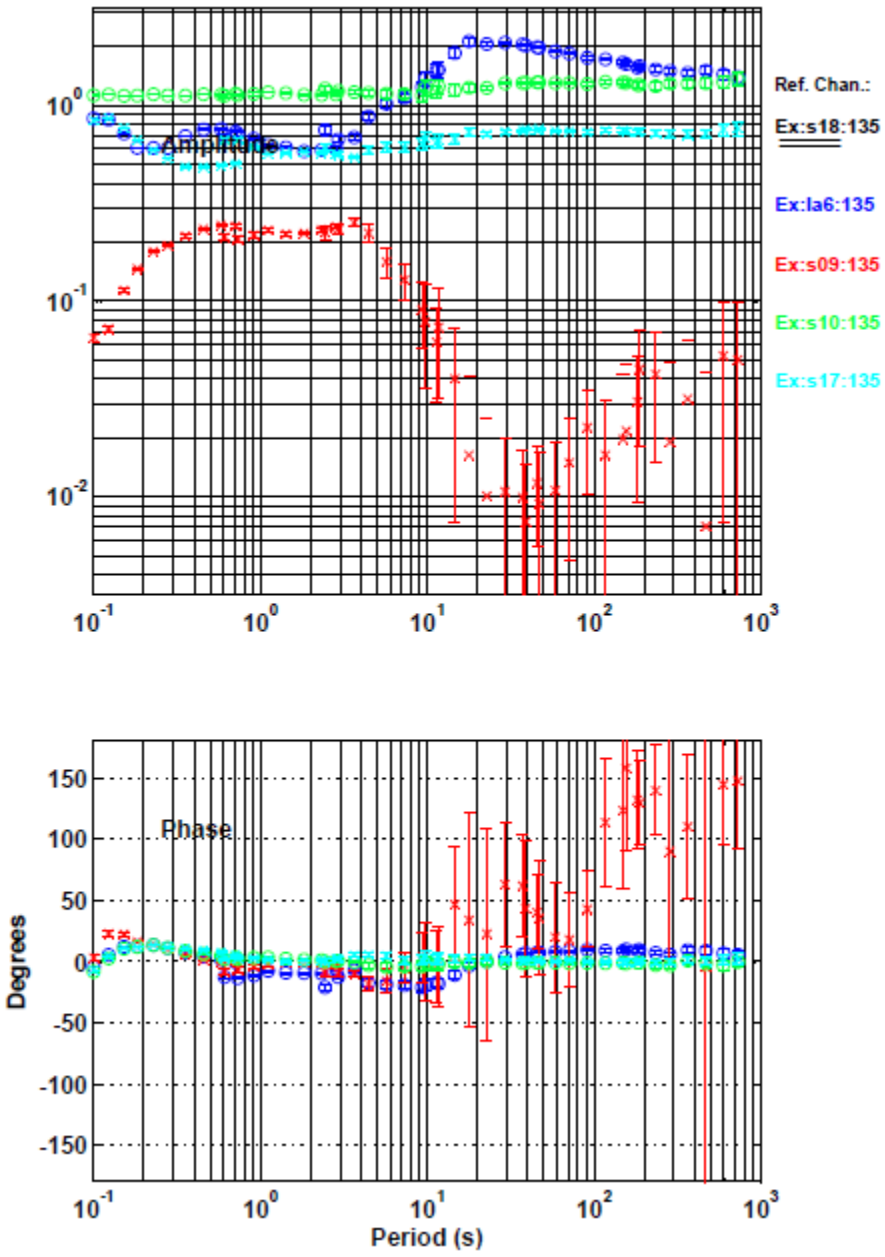
Amplitude
Ref. Chan.:
Ex:s18:135
Ex:la6:135
Ex:s09:135
Ex:s10:135
Ex:s17:135
Phase
Degrees
Period (s)

Figure 22c

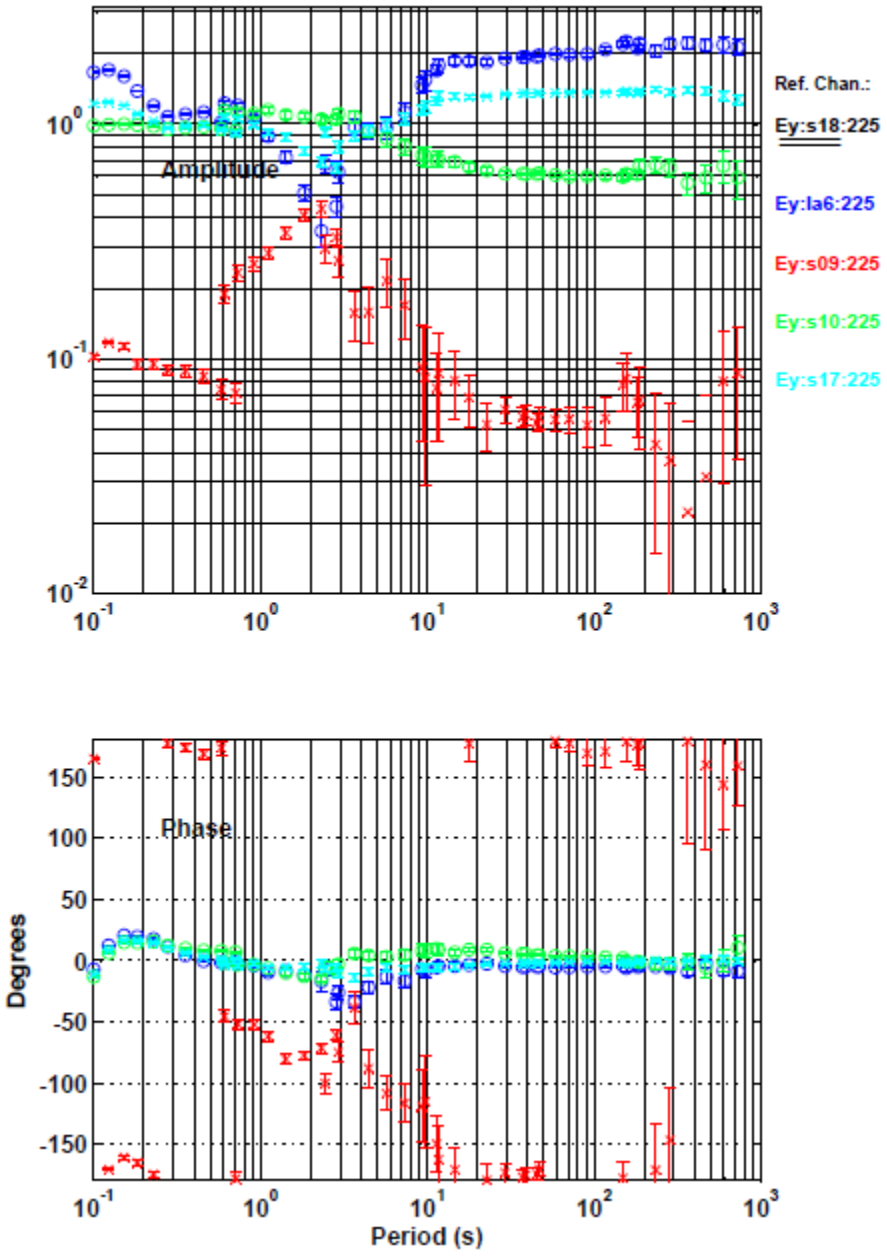
Amplitude
Phase
Degrees
Period (s)
Ref. Chan.:
Ey:s18:225
Ey:la6:225
Ey:s09:225
Ey:s10:225
Ey:s17:225

Figure 22d

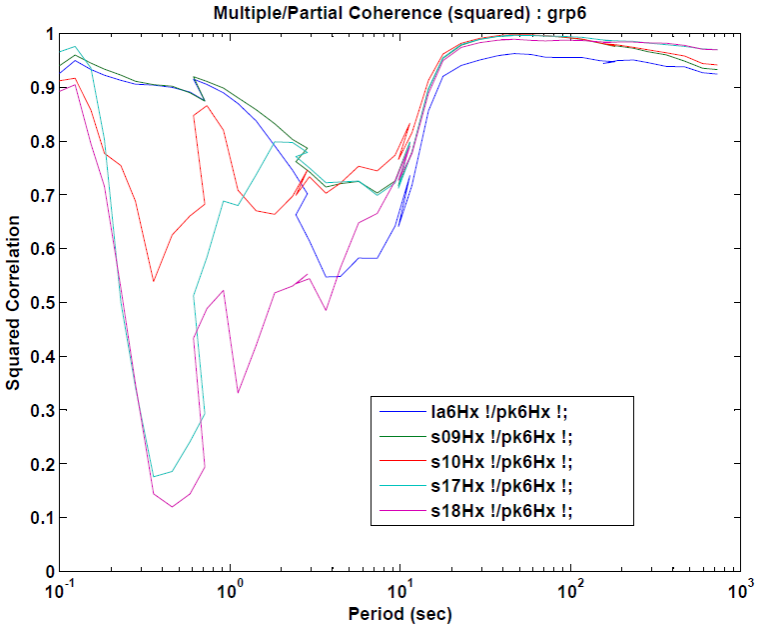

Figure 23a

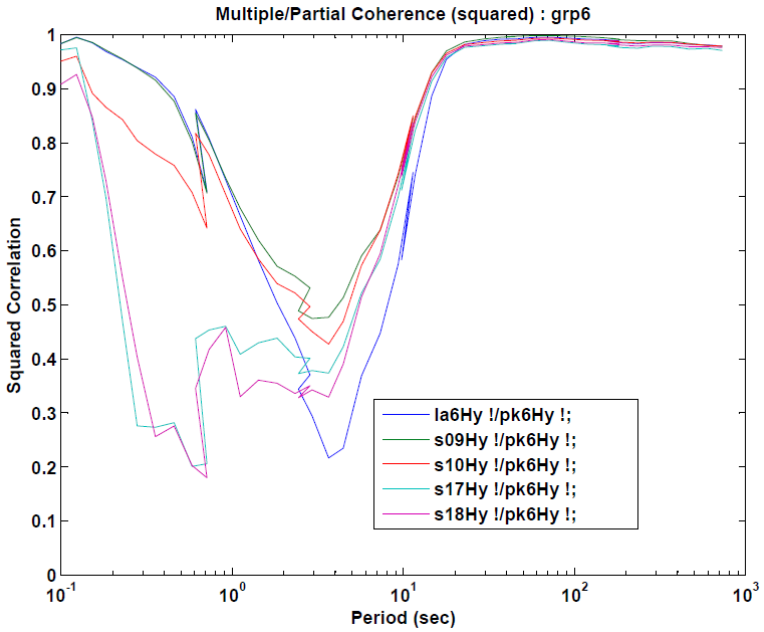

Figure 23b

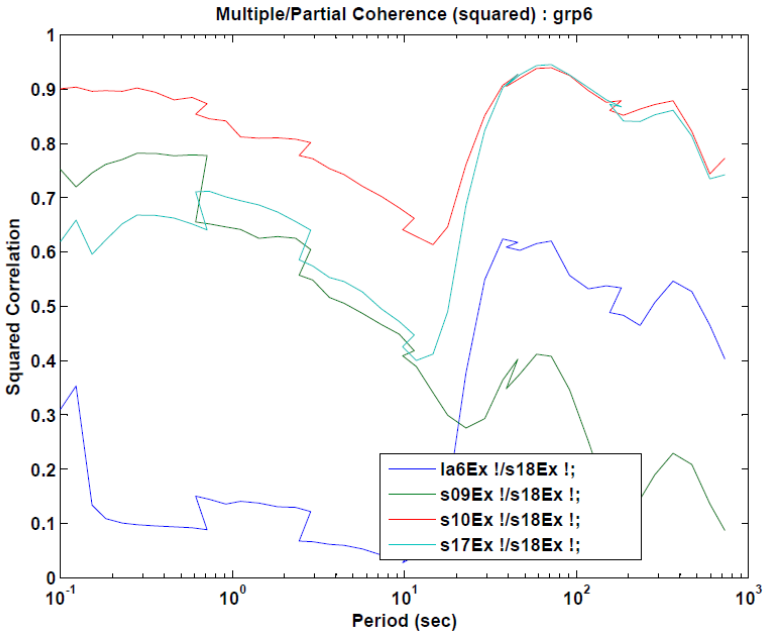

Figure 23c

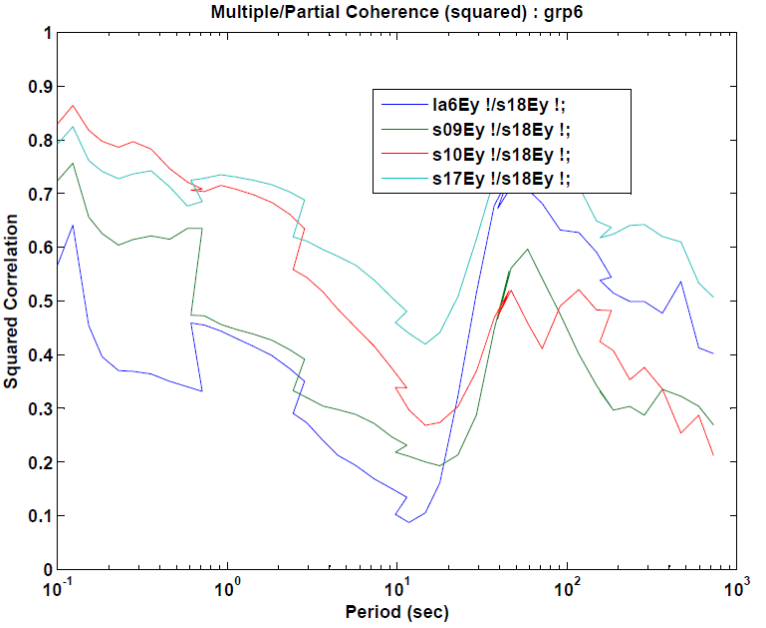

Figure 23d

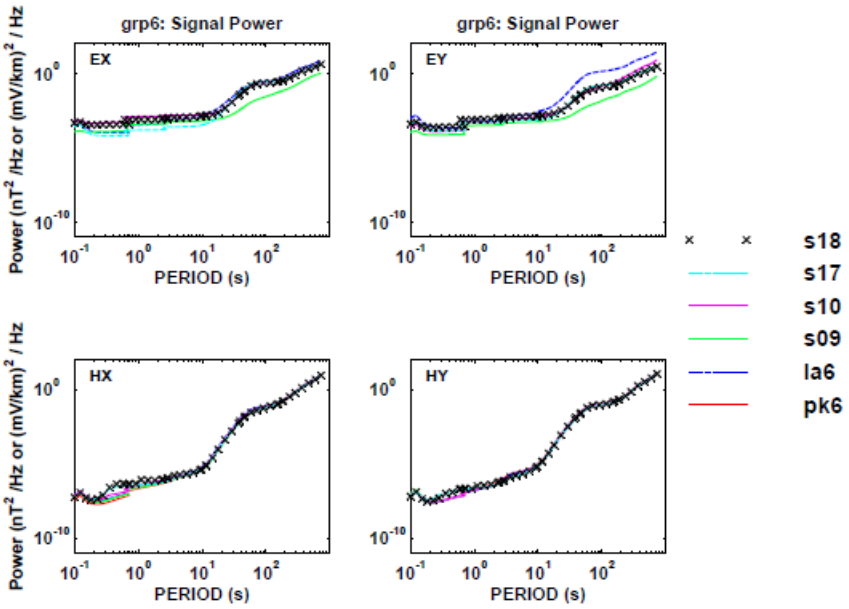

Figure 24a

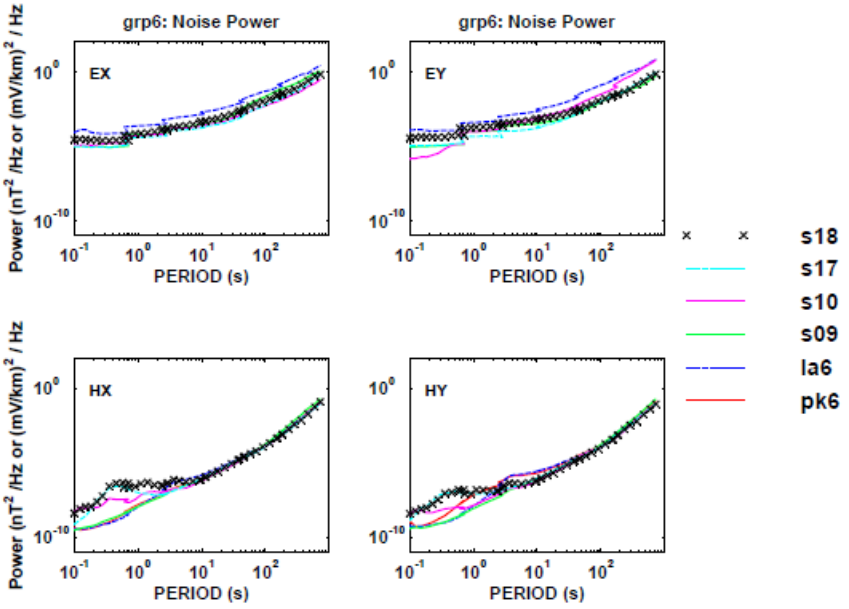

Figure 24b

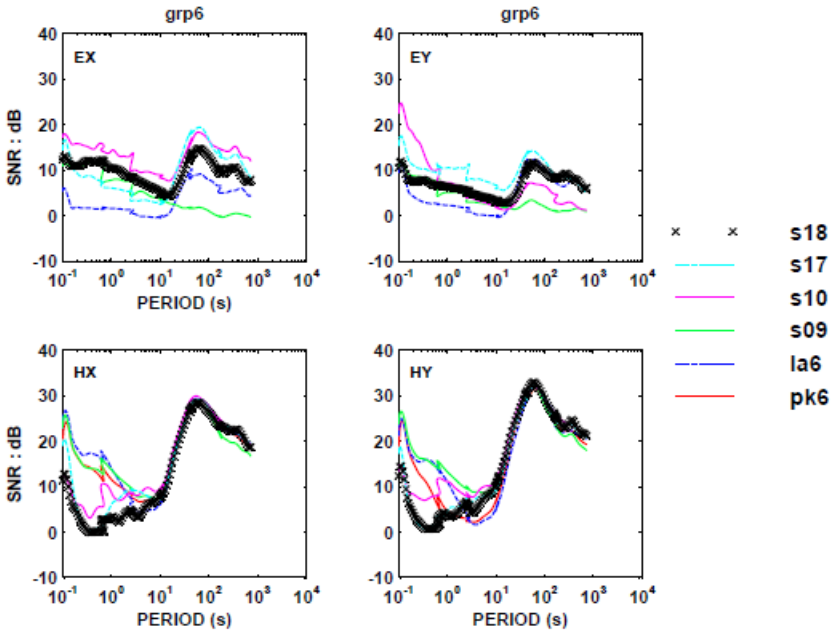

Figure 24c

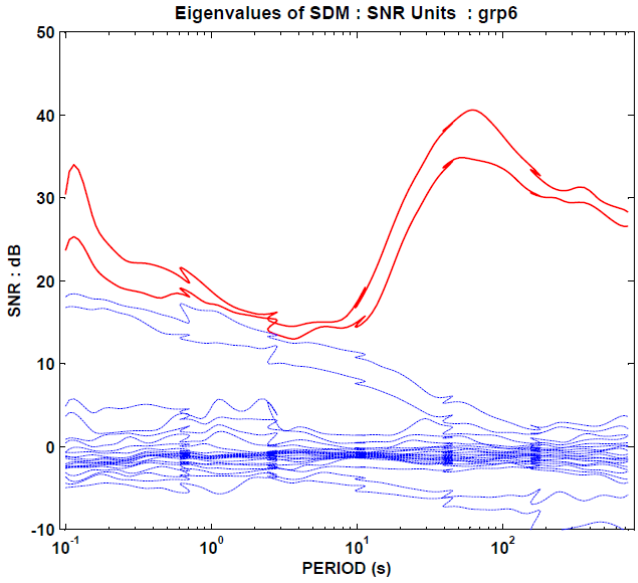

Figure 25

In addition to these 6 groups data at sta05 were collected with parallel setups at two different times separated by ~1 week using hkml4 and hkml6 respectively as remotes. Only data for times larger than 10 s (below 0.1 Hz) have high coherences between the local and remote site. Signals at hkml4 were very low for all channels and therefore didn't provide an ideal reference. Ex channels were coherent at low frequencies (below 0.1 Hz) between all sites, while the coherence was very low at high frequencies (Figure 26a) between hkml6 and sta05. The coherence of Ey channels was high between two parallel setups at sta05, but low when compared with the remote site (Figure 26b).

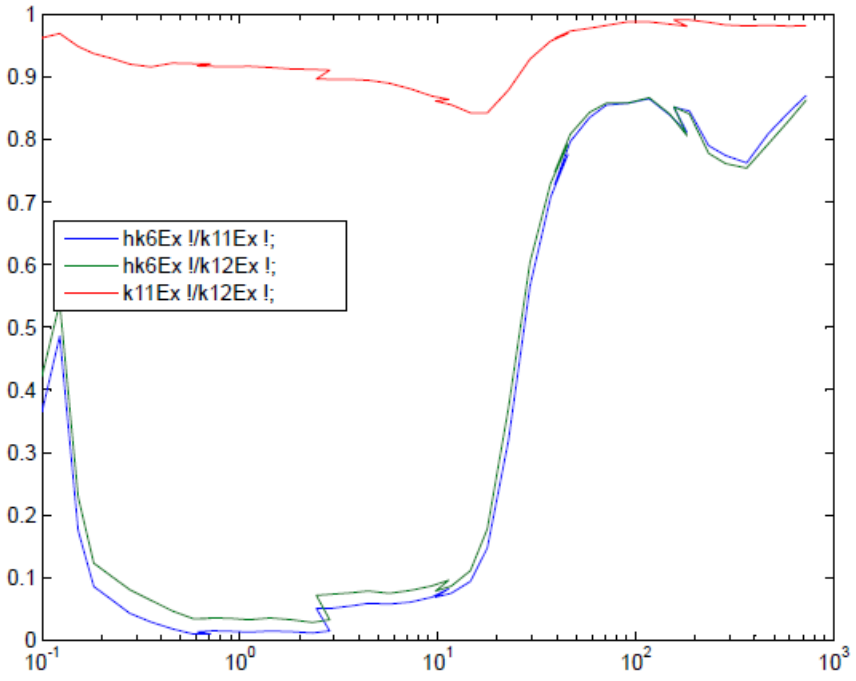

Time (s)

Figure 26a

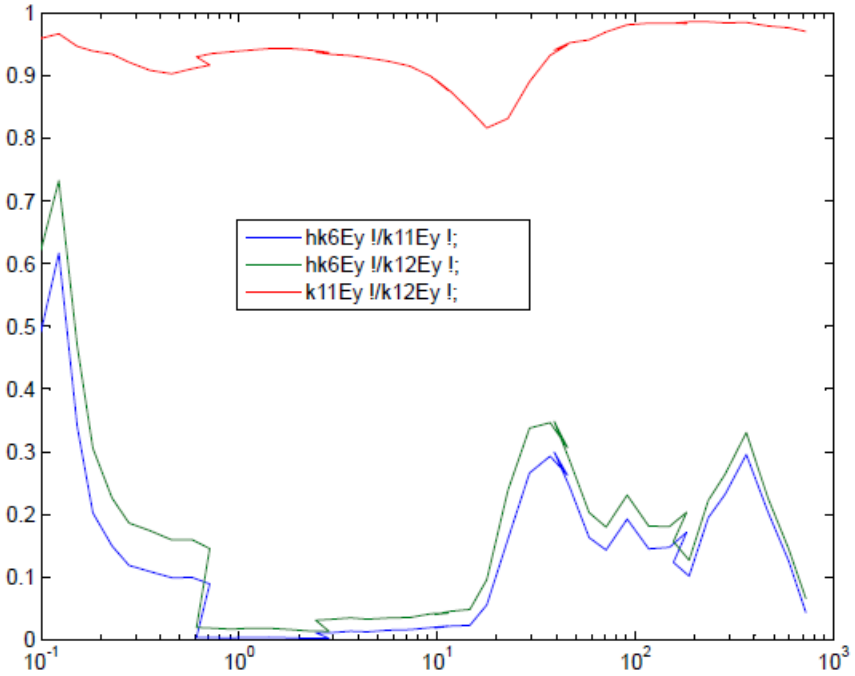

Time (s)

Figure 26b

Similar pattern is observed in Hx and Hy fields as shown in Figure 26c and 26d. High coherencies for Hx component among all the sites at low frequencies, and low between sta05 and remote at high frequencies. The Hy component has very low coherency between the sta05 and remote through all frequencies, while signal at two setups at sta05 is highly coherent through the whole frequency range.

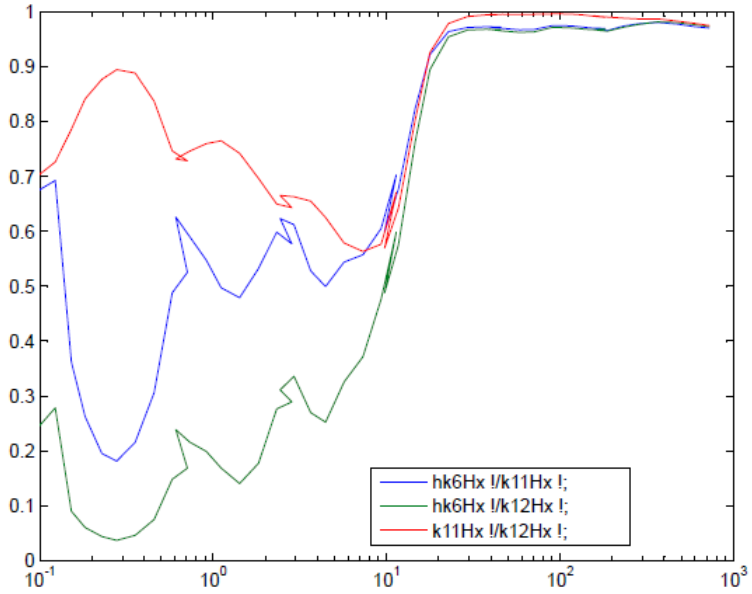

Time (s)

Figure 26c

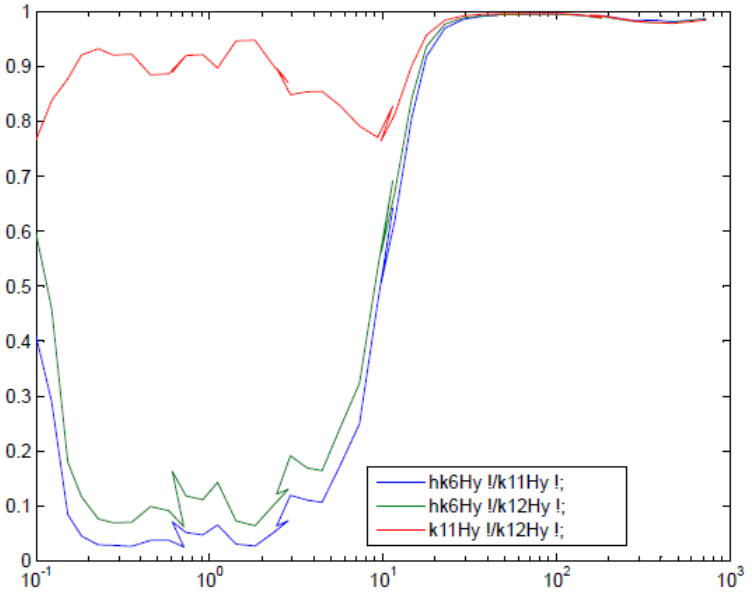

Time (s)

Figure 26d

Figure 27 shows the eigenvalues and coherence for sta05 and remaining group of channels (magnetics at the parallel site and the remote). Red color is used for first and second eigenvalues that are representative of MT portion of the signal, while blue colors are used for higher eigenvalues that represent signals that can't be explained by a plane-wave response. Coherence plot shows how similar the signals are across the two groups. Increased third and fourth eigenvalues in the upper left panel of Figure 27 with low values of coherence at the bottom left panel of Figure 27 indicate presence of signals that are specific to this site and we associate them with a possible fluid flow movement.

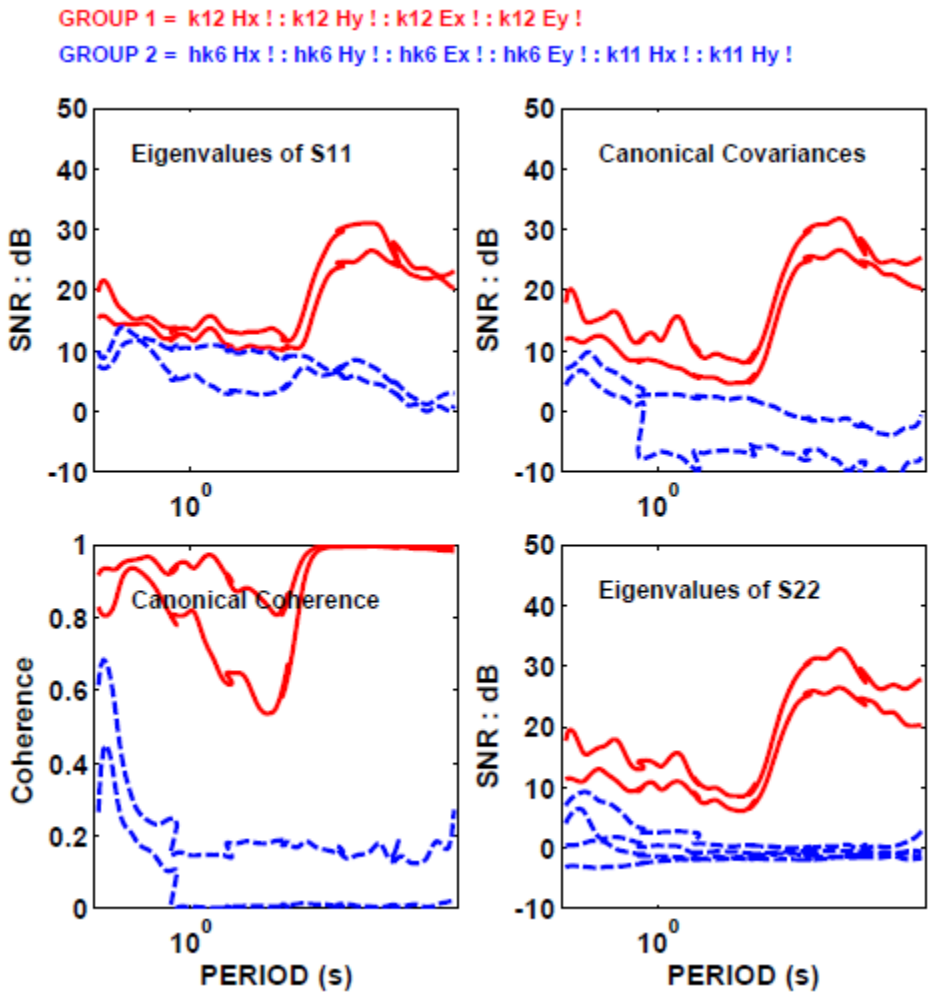

Figure 27

Analysis of 2003 MT dataset

2003 3D MT survey was not designed to look for anomalous signals that are the subject of this research, and therefore not all stations were recorded with both electric and magnetic fields sensors, and a group of acquiring data simultaneously could have as few as three stations. For these reasons some of the stations couldn't be used for a multicomponent analysis. Such stations are sta01, sta08, sta10, sta17, and sta18, which were recorded only with electric field channels, and no other station in their vicinity was recorded with the magnetic coils, so we were unable to estimate if there are any anomalous signals to those sites without having an accurate estimate of the plane-wave MT response. Stations sta07 and sta09 were each a part of groups of too noisy stations, and therefore not suitable for this analysis. However, these data suggested that the SSP signal is present at areas with a fluid flow movement. We developed our approach using this data set and applied it to 2012-2013 data set.

The apparent resistivity and phase curves for each of the stations for both surveys are attached in the appendix. In general the response at low frequencies (below 0.1 Hz) didn't change significantly during the last 10 years. However the higher frequencies are noisier in 2012 perhaps due to various eruptive activities around the Kilauea caldera. As an example, Figure 28 shows apparent resistivity and phase vs. frequency plots for sta05.

The circles represent 2012 data while crosses represent 2003 data. The 2003 data are much quieter than 2012 data between 2 and 0.7 Hz most likely to no activity around this site 10 years ago, while the low frequency response is identical for both years.

For stations were data had acceptable noise levels, stations sta01, sta04, sta05, sta06, sta10, sta11, sta12 show either both or yx-mode only resistivity at 2012 lower than 2003, while sta03, sta04, sta18 show higher xy-mode resistivity in 2012 than 2003. Sta13 and sta19 show lower xy-mode resistivity in 2012 than in 2003. Sta08 responses are different for two different groups in 2012 field campaign and are different from the 2003 response, and therefore need further investigation.

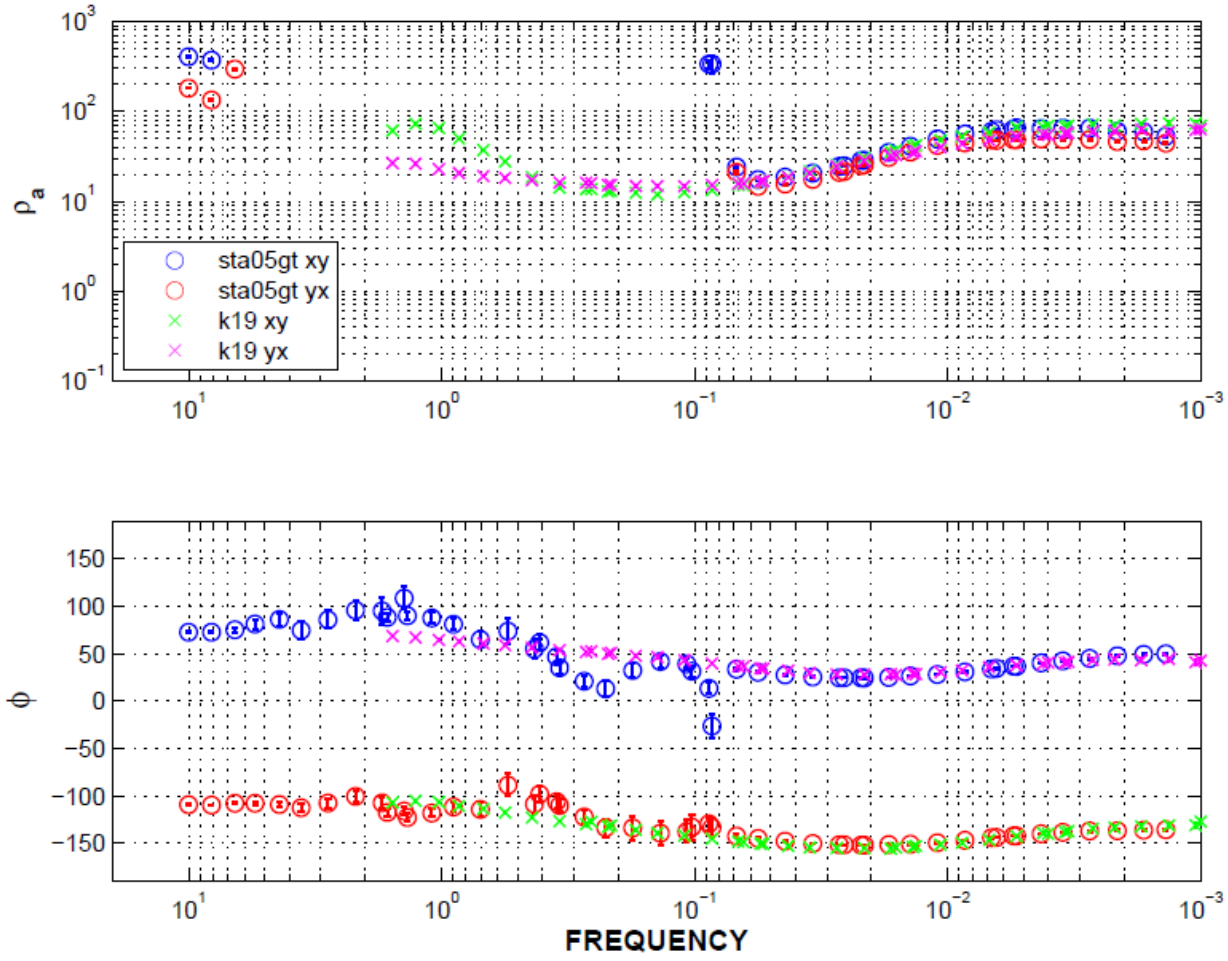

Figure 28

When 2003 data were processed in order to identify anomalous signals that could be related to fluid flow of lava flow activities, the result for sta05 (Keller) show increased values of EV3 with low coherency values between the groups (Figure 29a) between 0.15 and 0.005 Hz (7-200 s). When the movement stopped and SSP signal disappeared, the EV3 and coherency plots are shown in Figure 29b. EV3 values are close to zero and coherency of the signal between the two groups in higher, indicating that this signal is common to both and couldn't be attributed to a local phenomenon. Figure 30 shows the value of EV3 and coherence as a function of time, with the increased value and SSP signal present the first 12 hours of recording, while it was not

present the rest of the time. The increased values of EV3 between 30 and 36 hours of recording at lower frequencies are correlated with high coherency values and therefore they are due to other sources/processes than we are looking for.

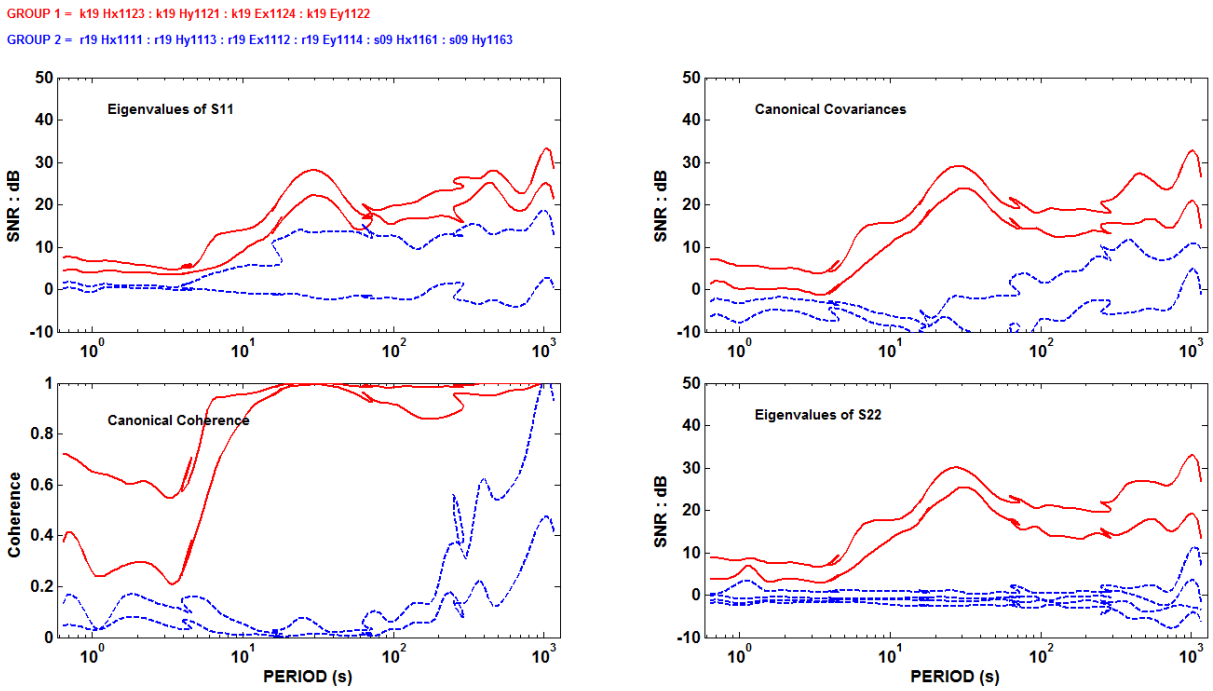

Figure 29a

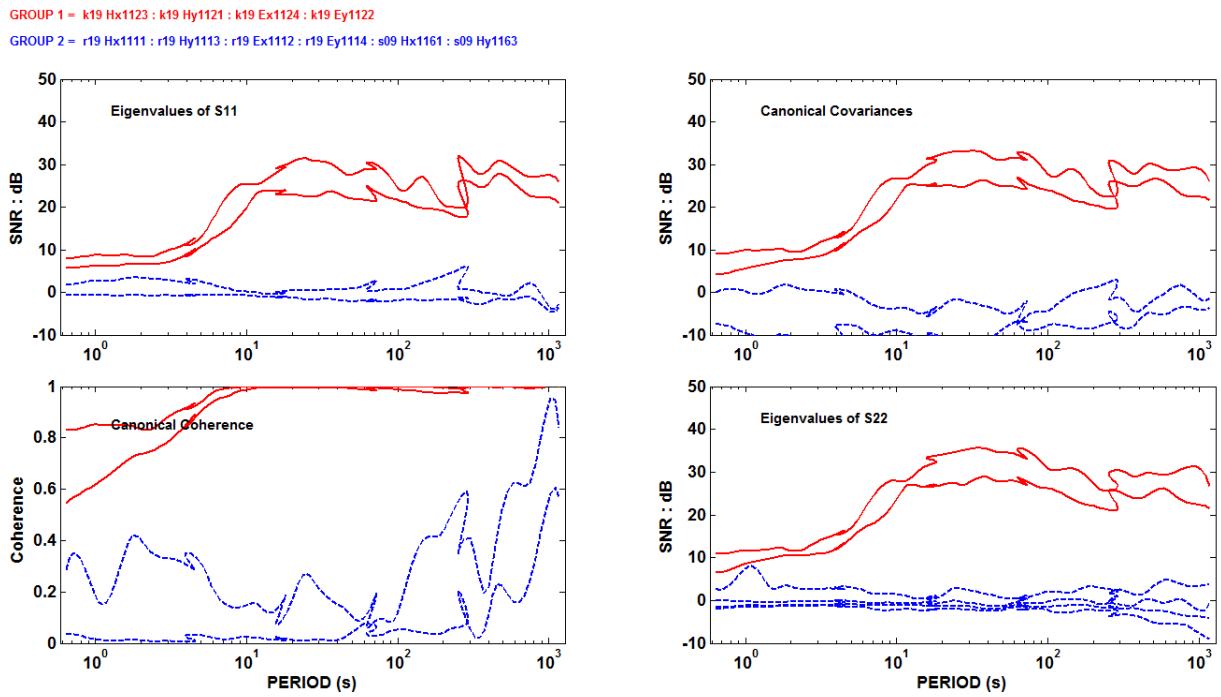
GROUP 1 = k19 Hx1123 : k19 Hy1121 : k19 Ex1124 : k19 Ey1122
GROUP 2 = r19 Hx1111 : r19 Hy1113 : r19 Ex1112 : r19 Ey1114 : s09 Hx1161 : s09 Hy1163
Eigenvalues of S11
Canonical Covariances
Canonical Coherence
Eigenvalues of S22
SNR : dB
Coherence
PERIOD (s)

Figure 29b

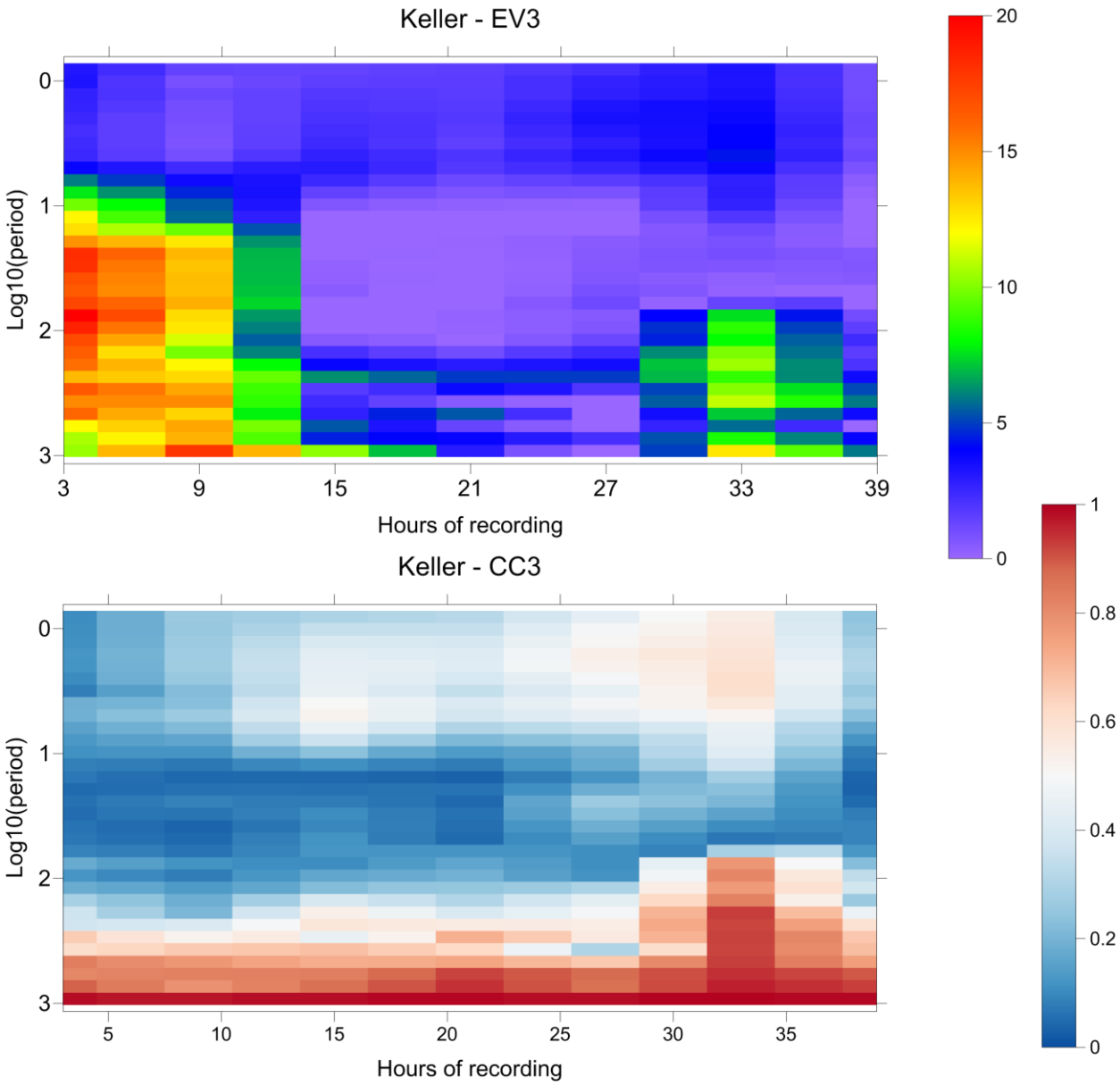

Figure 30

Another two stations where we observed increased values of EV3 while coherency values were low were stations sta12 and sta13, which are located on the eastern edge of the Kilauea caldera. Figure 31 shows increased EV3 values in the upper left panel, and low coherencies of EV3 at the bottom left panel for periods between 10 and 100 s (frequencies between 0.1 and 0.001 Hz) for sta13 and sta12, while the remaining three stations away from the caldera shown in the bottom right panel don't exhibit increase in EV3.

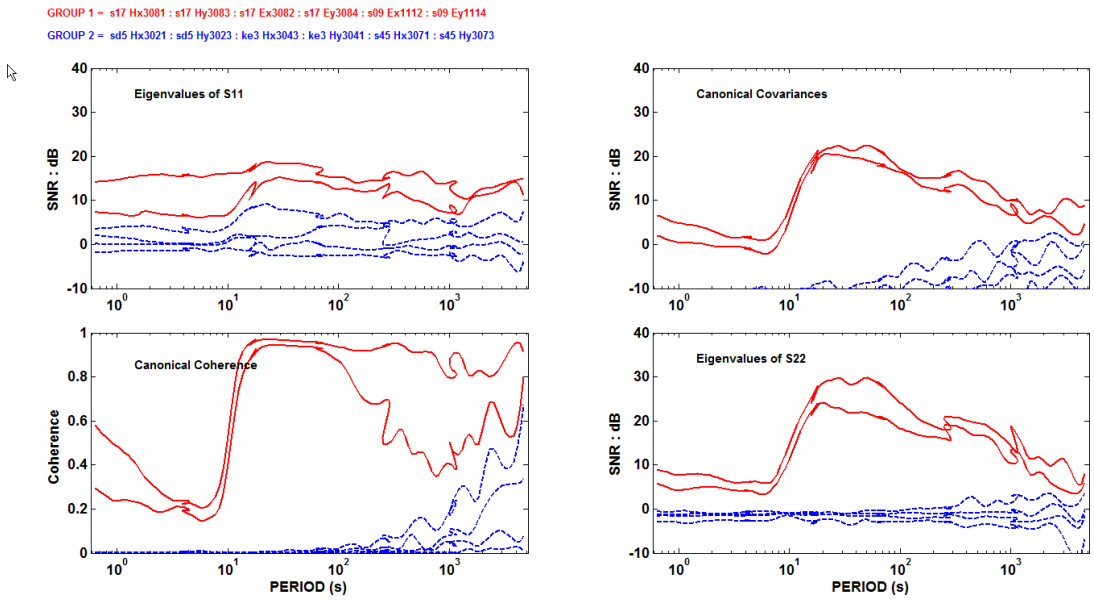

Figure 31

Figure 32 shows variations in EV3 and its coherency as a function of recording time on the x-axis and the period on the y-axis (this is x-axis in Figure 31). Data were processed in 6-hour segments and the color interpolation might cause some smearing, but this Figure shows that EV3 values between 10 and 100 s (1 and 2 on the y-axis) are increased the first ~10 hours (green colors), then they increase even further for next ~ 5 hours, then they disappear for ~ 10 hours, and then they come back but only in the range of 30 – 100 s (1.5 -2 on the log y-scale). The increase of EV3 values around 15th hour of recording are associated with increased values of coherency in the bottom plot, which would indicate that on the top of the EV3 signal observed earlier, there is another signal that is shared between all stations but it is not associated with the fluid movement that causes the EV3 increase in earlier times. This time fluctuation in EV3 values could be associated with magma movement in and outside the caldera.

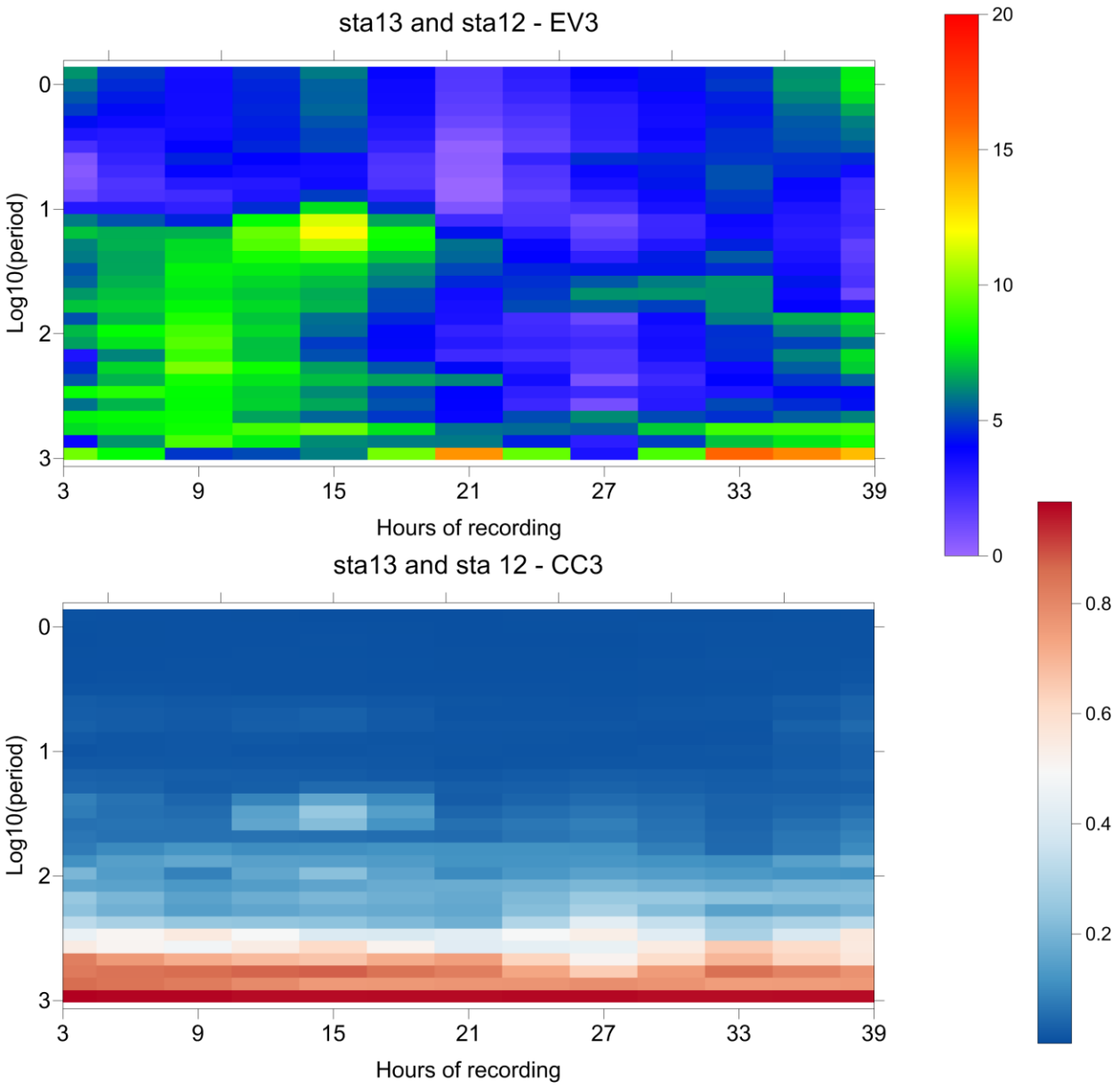
sta13 and sta12 - EV3
Log10(period)
0
1
2
3
3
9
15
21
27
33
39
Hours of recording
20
15
10
5
0
sta13 and sta 12 - CC3
Log10(period)
0
1
2
3
3
9
15
21
27
33
39
Hours of recording
0.8
0.6
0.4
0.2

Figure 32

Figure 33 and 34 show increased EV3 values and the low coherence between 20 and 200 s periods at stations sta11 and sta15, respectively.

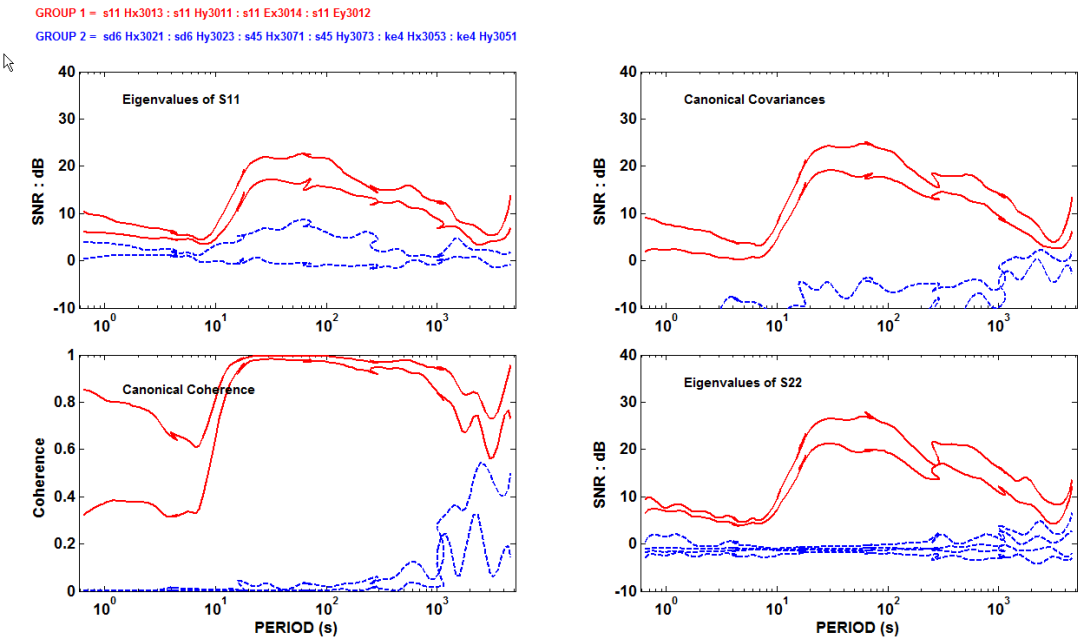

Figure 33

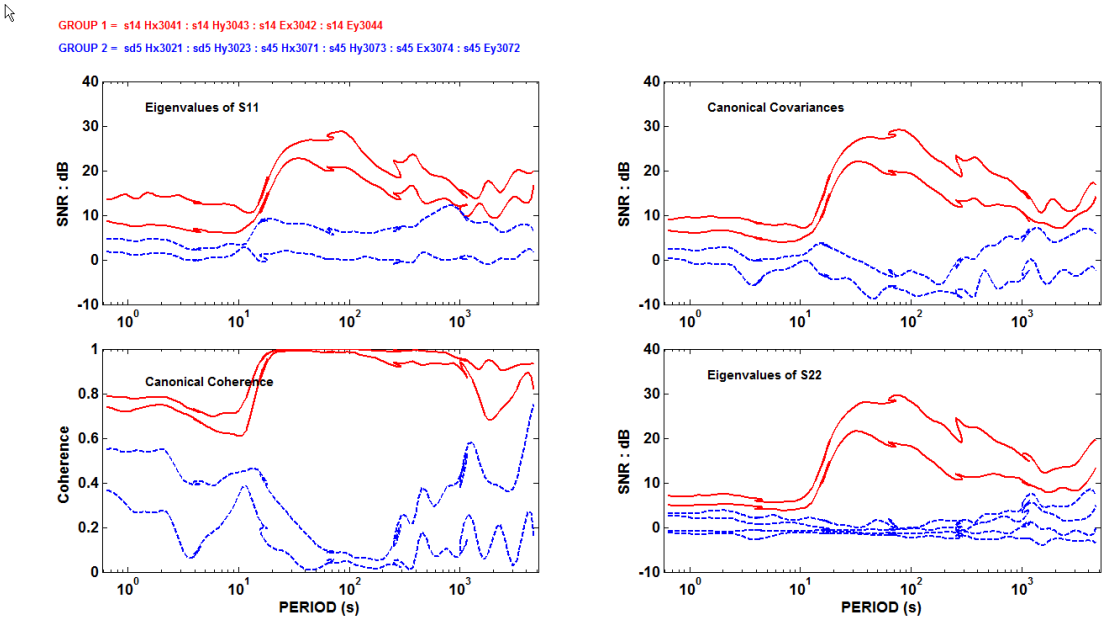

Figure 34

While neither station sta08 or sta10 had magnetic sensors, they are only about 1 km apart, so if we group electric fields of these two stations into one group and study the relationship to the rest of the channels we observe increased EV3 values and low coherency for periods of 2-1000 s (Figure 35). More detailed analysis shows that the electric fields from sta10 affect more two dominant EV values, while Ex component at sta08 is the main contributor to the EV3. Both stations are SE of the Kilauea caldera and sta08 west of the close by steam vents.

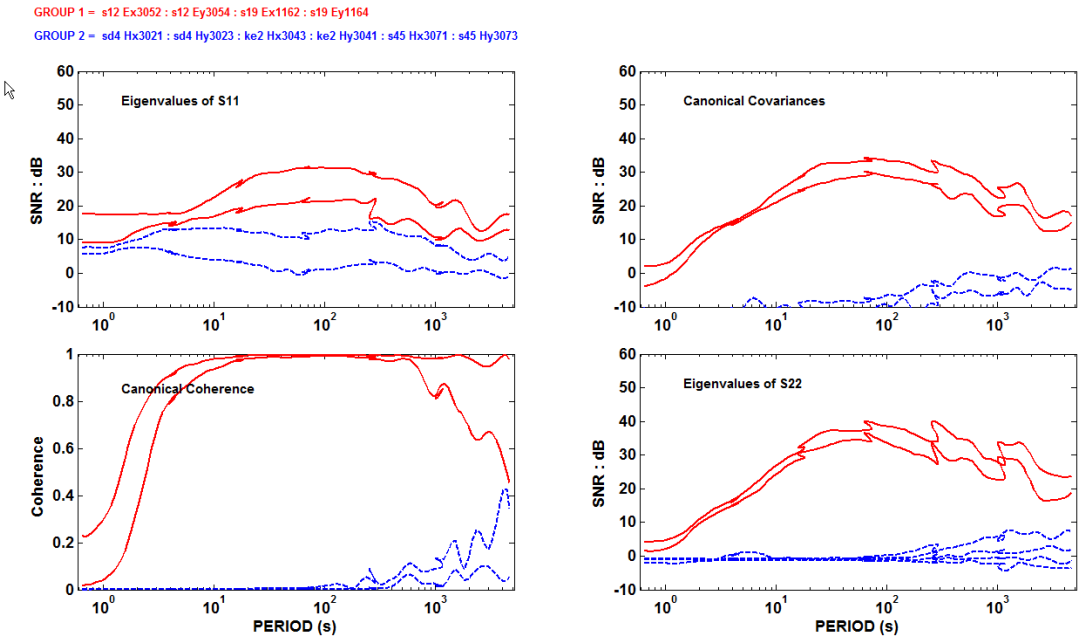

Figure 35

For stations sta03 and sta04 a sequence of four plots (Figure 36a – 36d) shows an increase of EV3 at periods above 200 s (top left) for sta04 (labeled as s65), but high coherence values (bottom left) in that range regardless which combination of channels is used, which suggest that those are related to some other processes that are common to the local and remote sites. This is a group of three stations only with station sta03 (cal) having only electric field measurements.

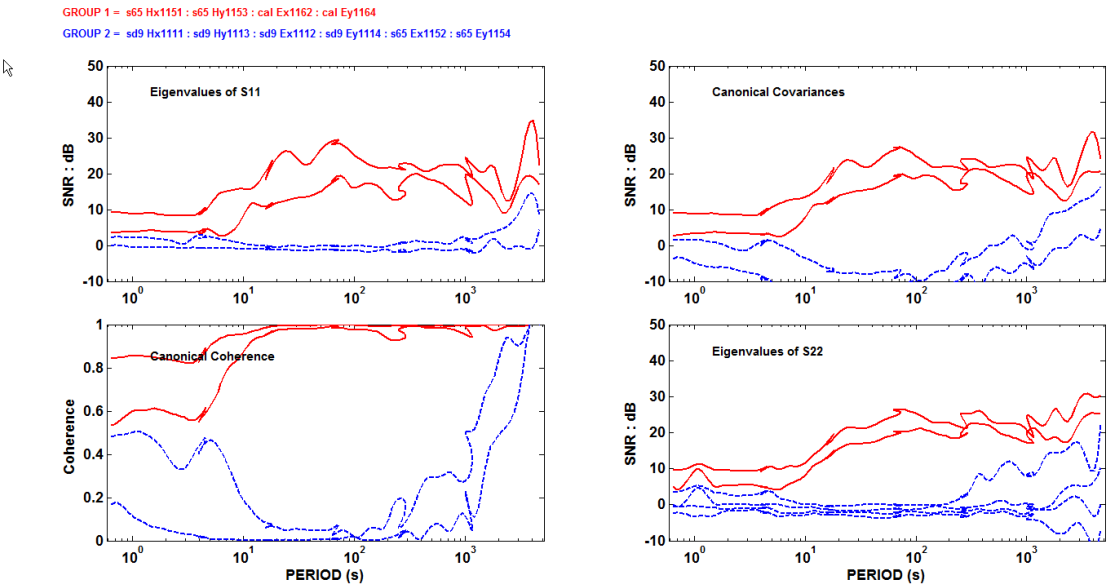

Figure 36a

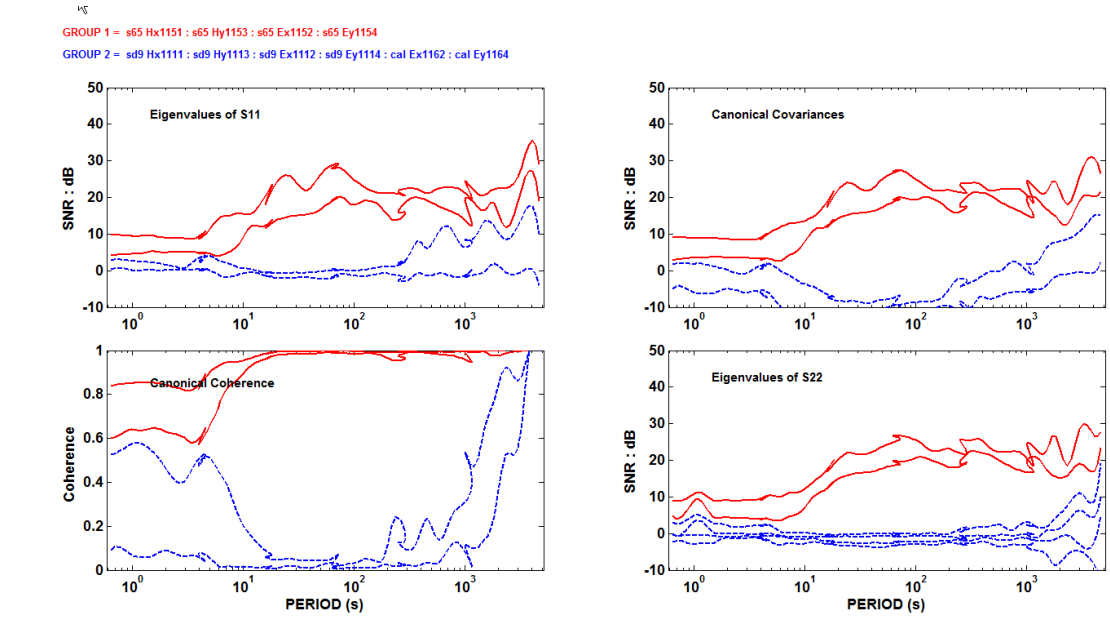

Figure 36b

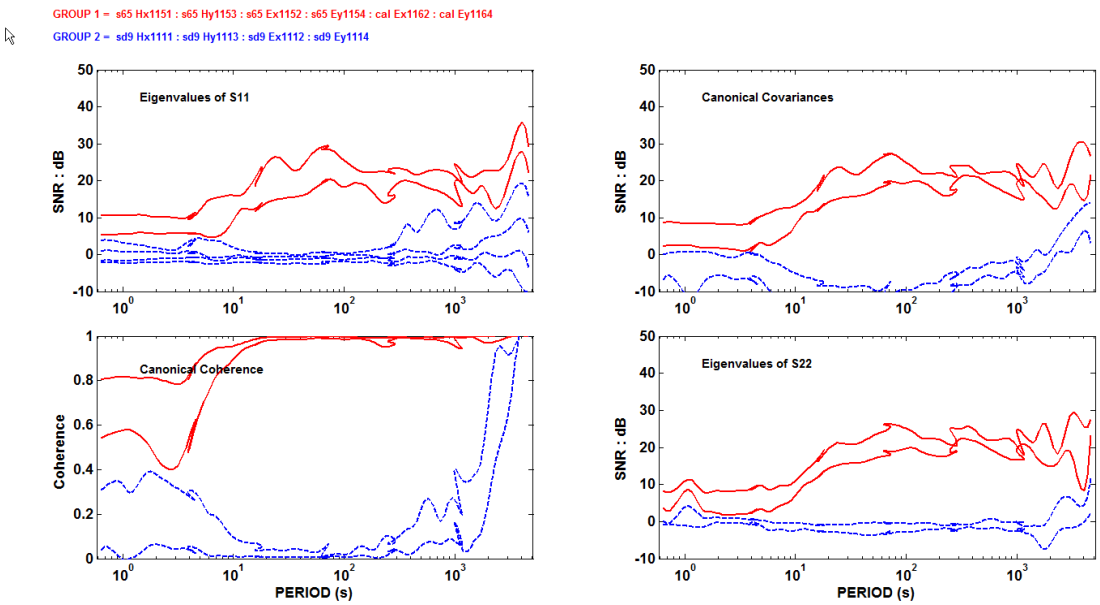

Figure 36c

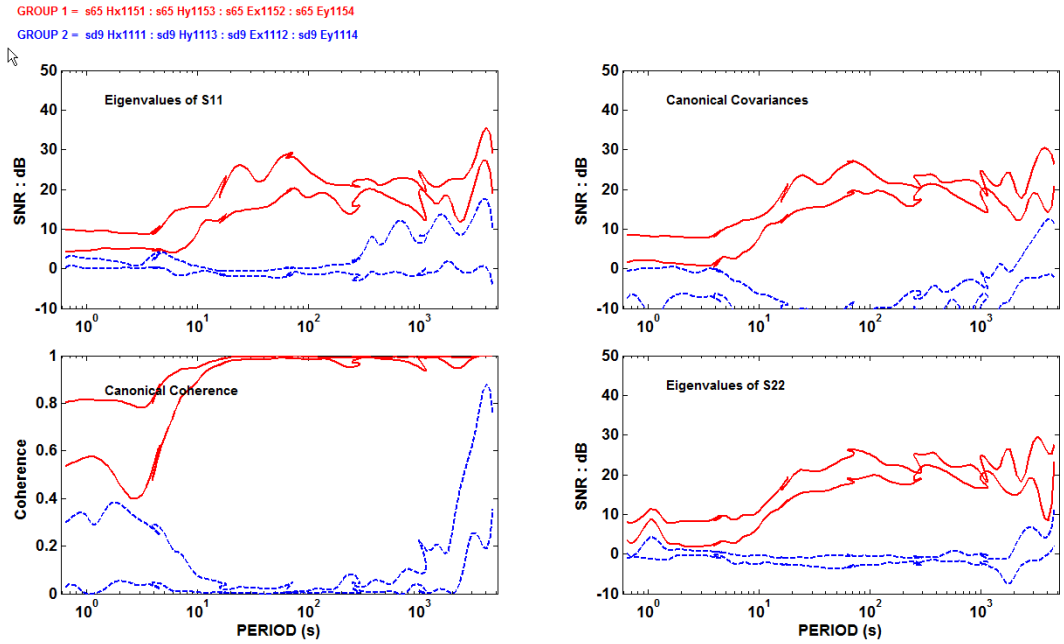

Figure 36d

Stations sta06 (Figure 37) and sta19 (Figure 38) showed no anomalous EV3 values.

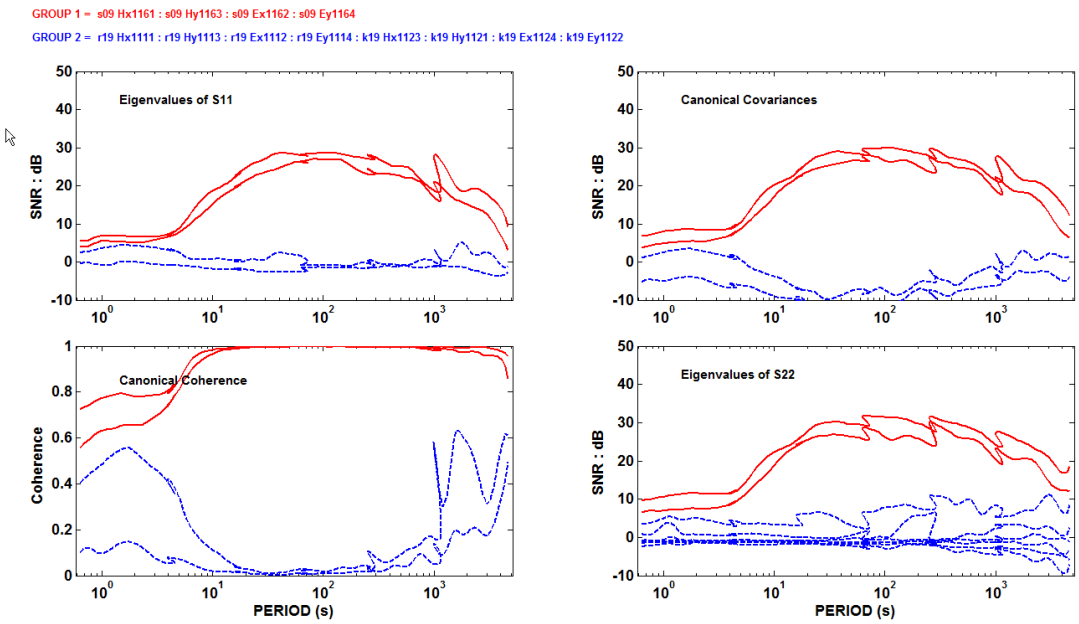

Figure 37

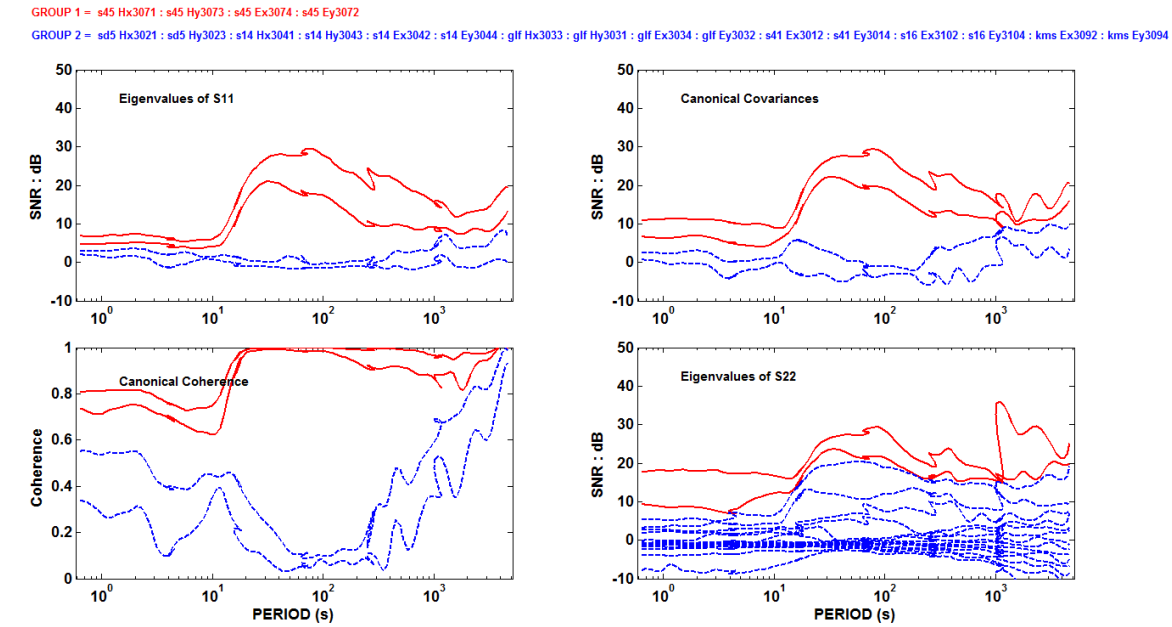

Figure 38

In 2003 data set we identified anomalous EV3 values at stations sta13, sta12, sta11, sta10, and sta08, which are all to the east and southeast of the Kilauea caldera. On the west and southwest of the caldera, sta15 and sta05 also showed increased EV3. These results illustrate and suggest that we are able to identify areas of magma movement, in this case, outline of the caldera. If we assume an intrinsic magma resistivity of 1-3 Ohm-m, using a skin depth calculation and frequencies with anomalous SSP response, it would put us to 1.5 – 3 km depth range, which is assumed to be the depth of the shallow magma reservoir.

Figures 30 and 32 illustrate that these fields or SSP signals vary in time and this kind of processing would be useful and important in the later stage of a geothermal field development, when injection and production, and creating new pathways need to be monitored. In the exploration stage, however, first and foremost, locations where these anomalous SSP signals are present need to be identified. While having a limited data and experience, we believe that if the activity/processes happen frequently enough or are large enough, they would show as anomalous SSP responses as presented in the analysis here (Figures 29 – 38, excluding previously discussed Figures 30 and 32).

Analysis of 2012-2013 data set

In general, the period range (x-axis) can be divided into two intervals: (1) up to 10 s (left side of the plot) is the range that includes the 'dead-band' that is characterized by very low natural EM signals and hence signal-to-noise ratio (SNR) is very low, and (2) above 10 s (the ride side of the plot) where the natural EM signals are much stronger and SNR is very high, indicating that the signals are well above the noise floor of the system and the site. As the separation between the noise and the signal grows (higher SNR values), the parameter estimates from those signals are more accurate and have smaller uncertainties/error bars.

Group 6:

Station sta09 had so low signals (or SNR) that wasn't suitable for the analysis (Figure 39).

Electric fields at sta18 produce increased EV3 at periods higher than 20 s (Figure 40a). These fields, with increased values of EV3, are coherent with electric fields at sta17 at periods 0.1-10 s (Figure 40b), as well as with sta10 and sta09 (Figure 40c). The same high coherence is observed for E-fields at sta10 and sta09 (Figure 41a). The same pattern is observed between sta10 and sta17 (Figure 41b). This flat EV3 value of ~10 db is common to all stations at periods 0.1-10 s. H-field contribution of the local stations for periods 0.1-8 s is ~5 db (Figure 42a), and it appears to be larger at sta17 and sta18 (Figure 42b) than at sta10 and sta09 (Figure 42c).

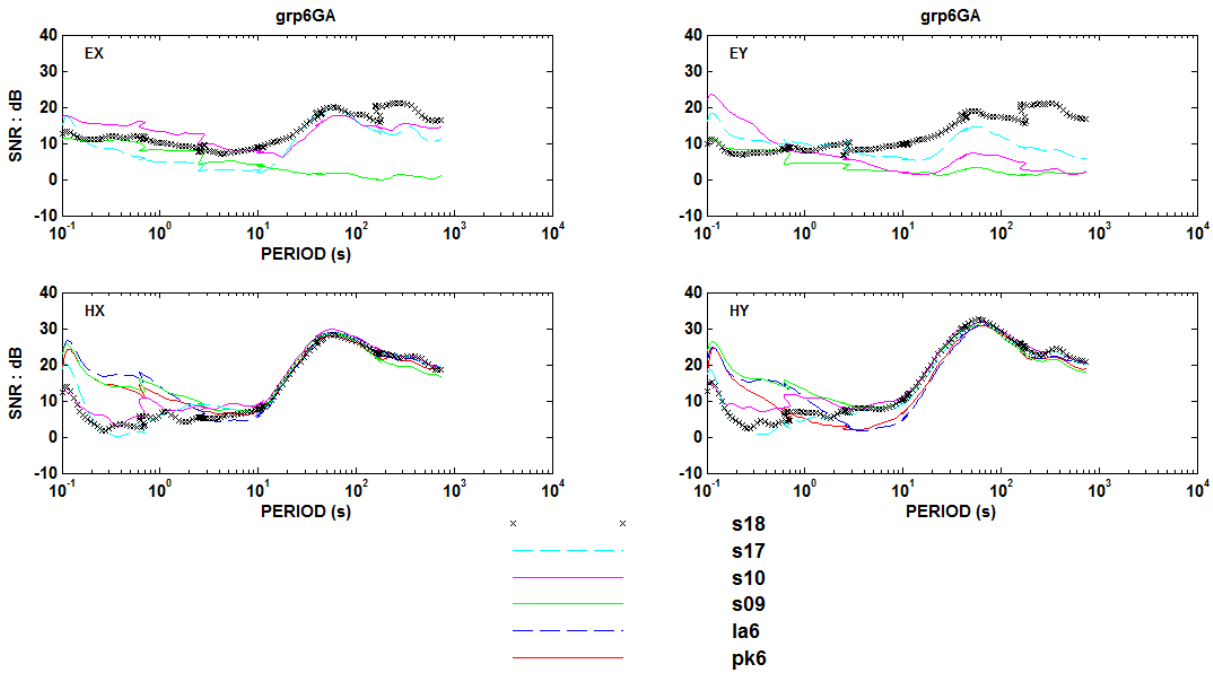

Figure 39

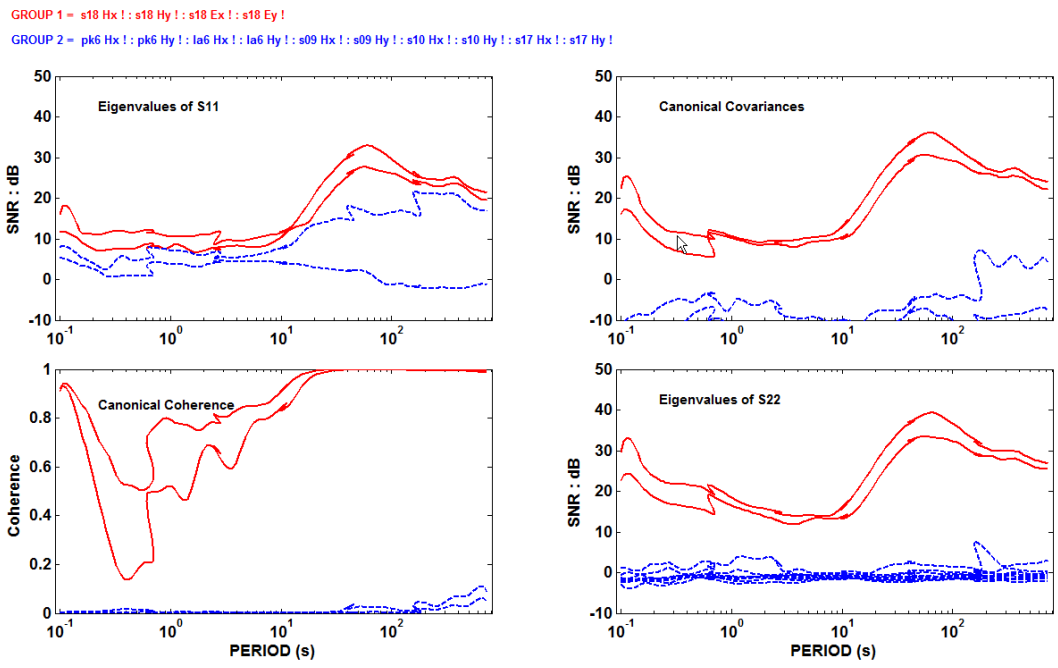

Figure 40a

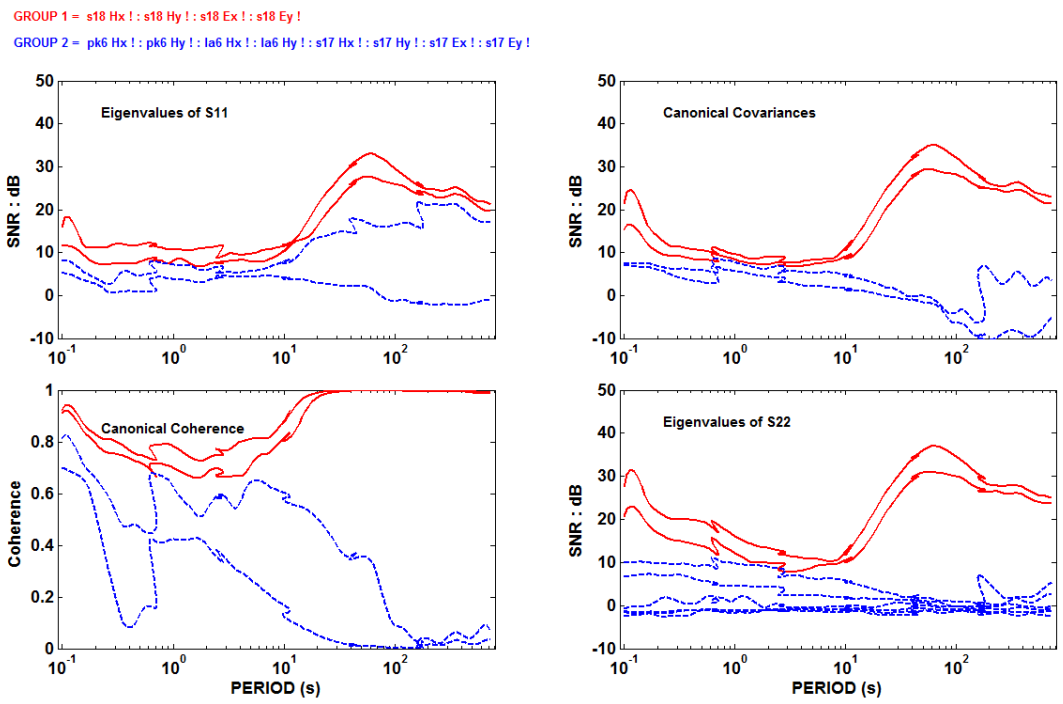

Figure 40b

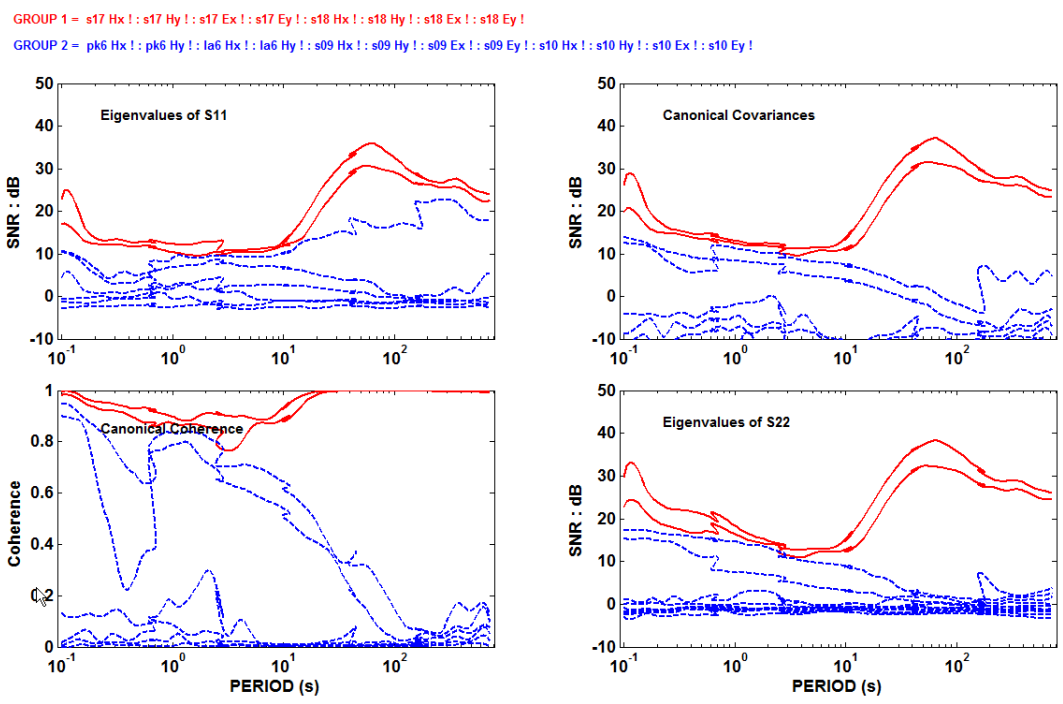

Figure 40c

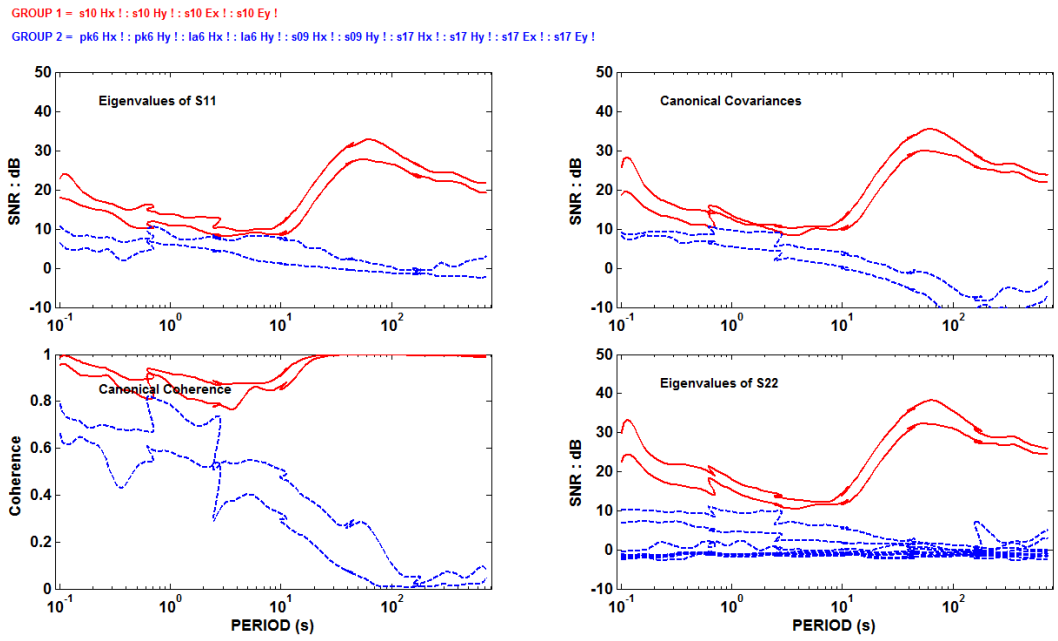

Figure 41a

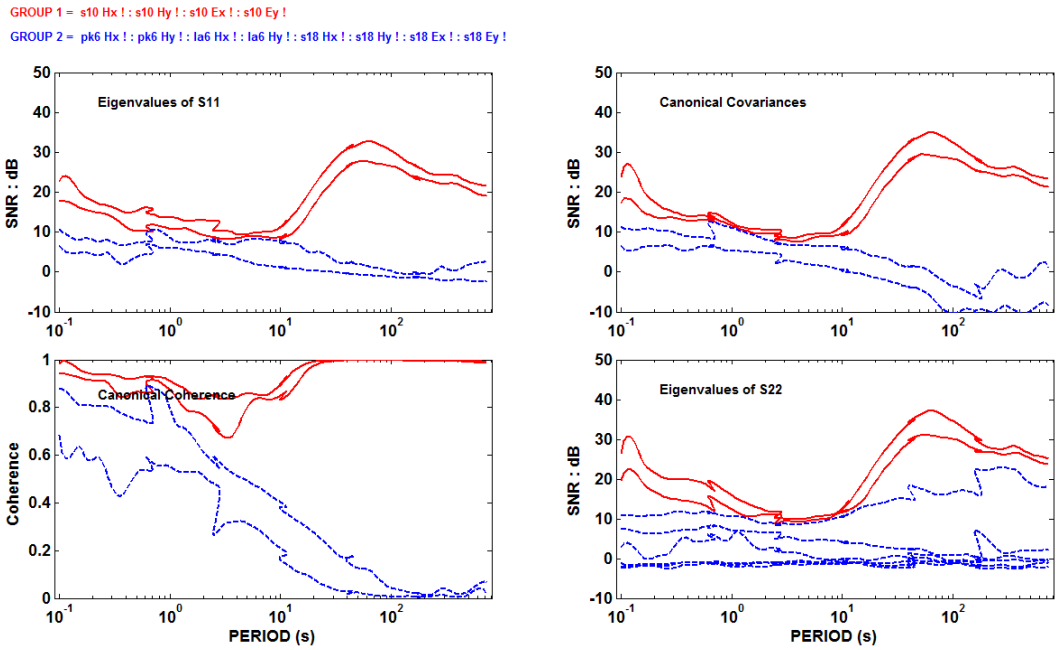

Figure 41b

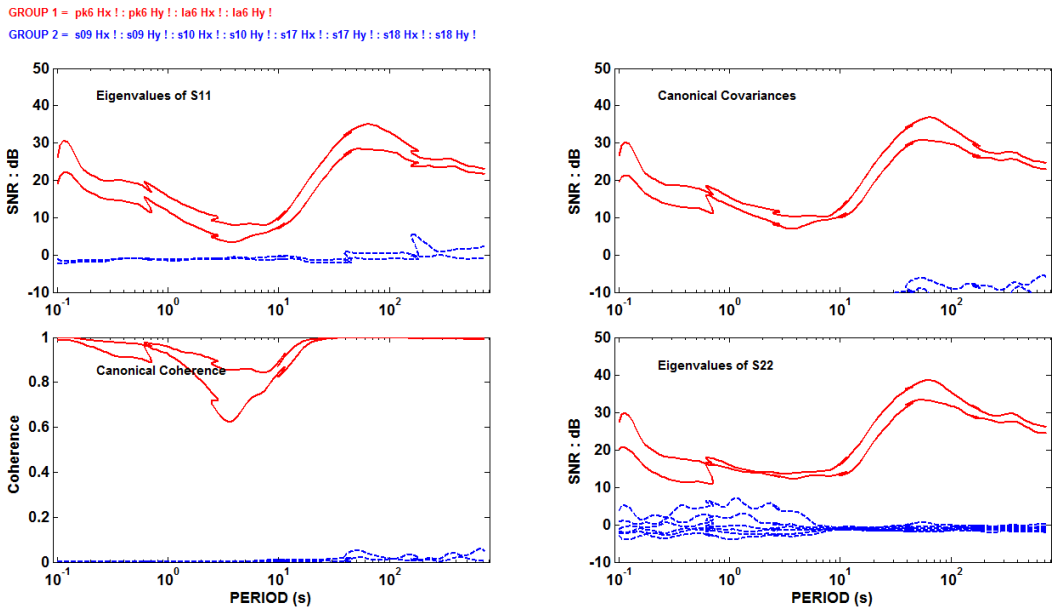

Figure 42a

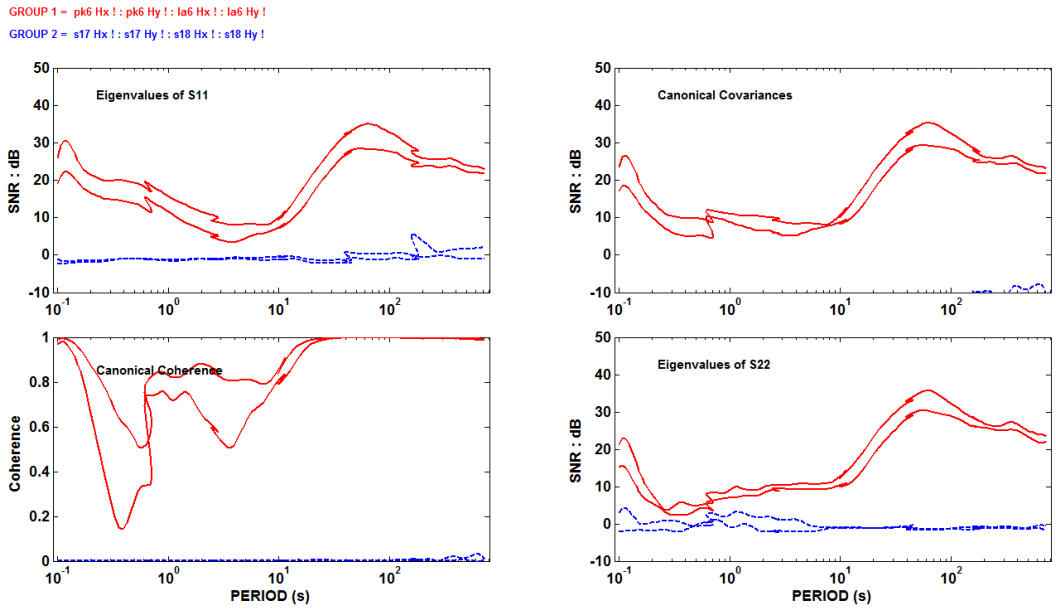

Figure 42b

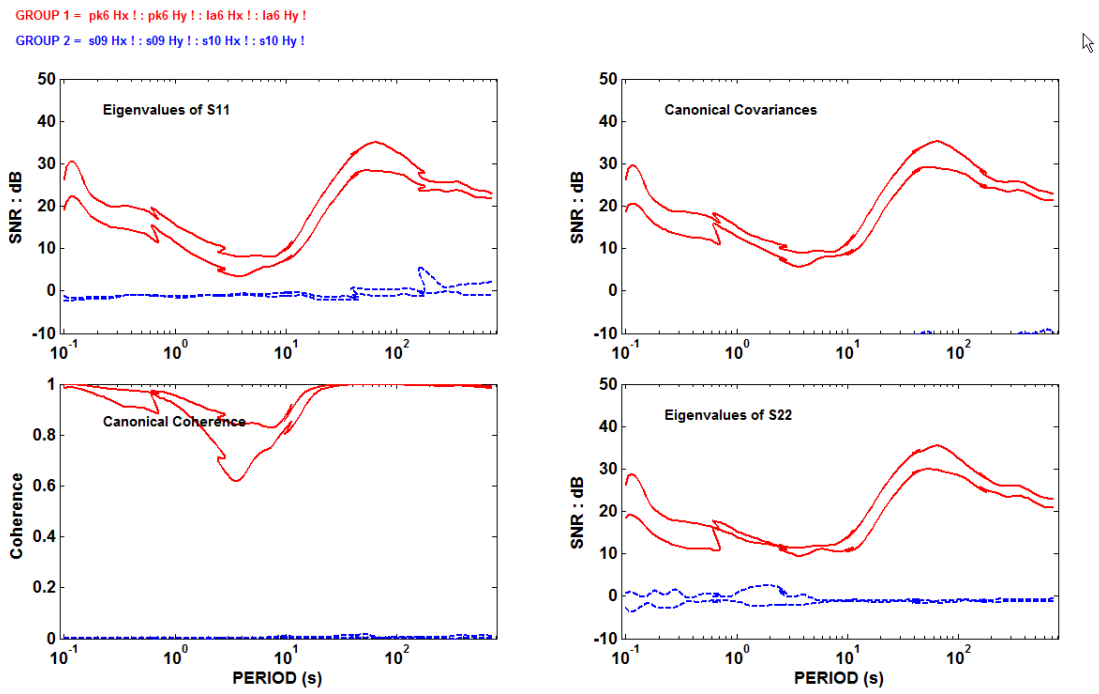

Figure 42c

Group 5:

Except of the H-field signal at the dead-band, and E-fields at sta08, SNR values are reasonable for this group of stations (Figure 43). H-field contribution to the EV3 value is about the same as in group 6. H-fields at sta07 (Figure 44) and E-fields at sta08 (Figure 45) have such a low signal level (low SNR) that the coherence of EV2 is very low, and that means that the plane-wave response is not well resolved. Sta11 (Figures 46 and 47) and sta08 (Figures 45 and 47) show increased EV3 values in periods 0.1-20 s.

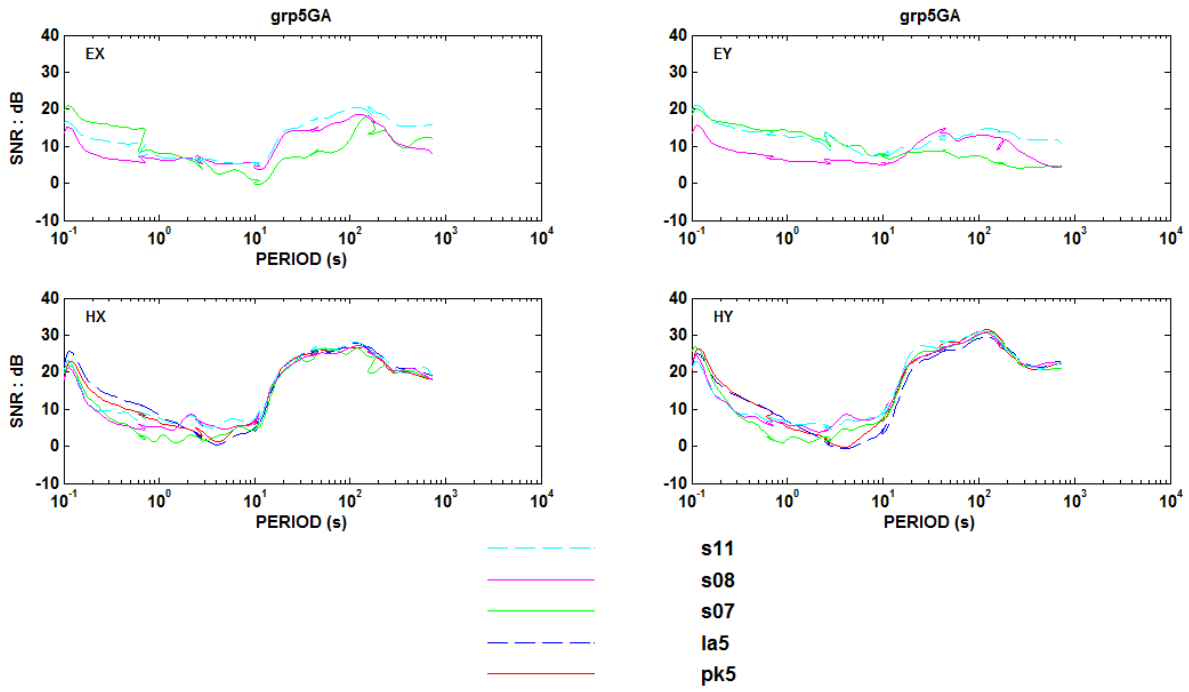

Figure 43

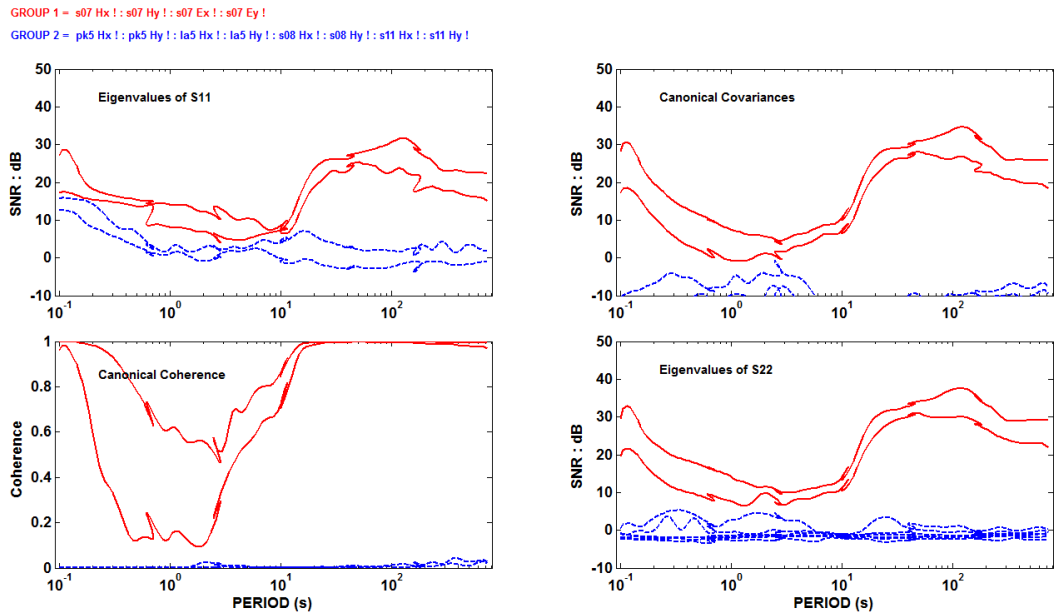

Figure 44

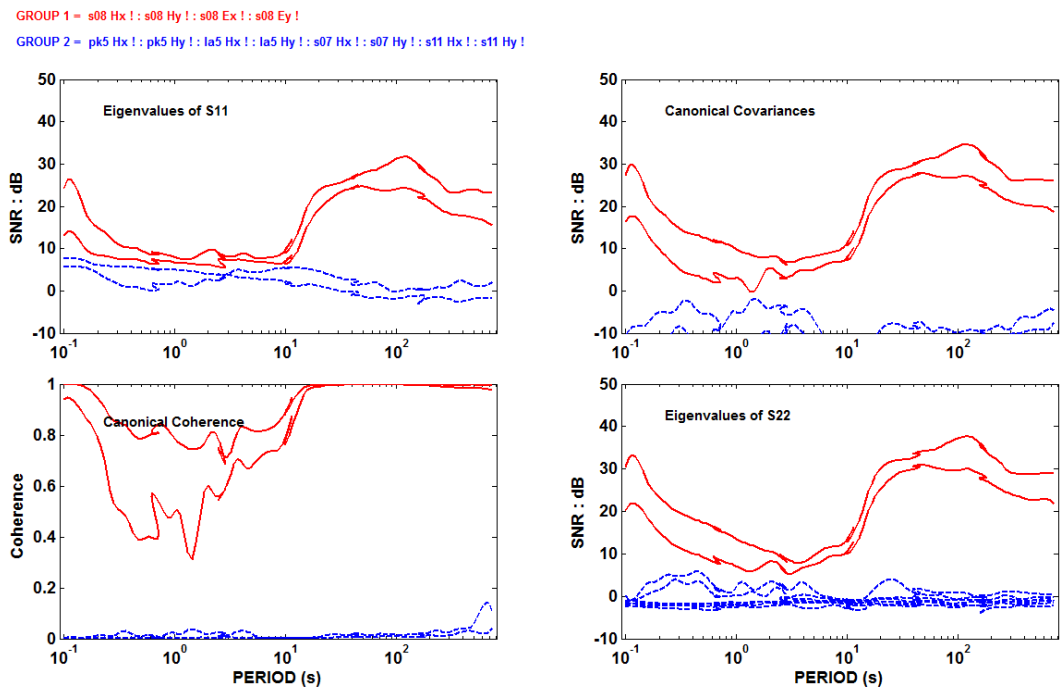

Figure 45

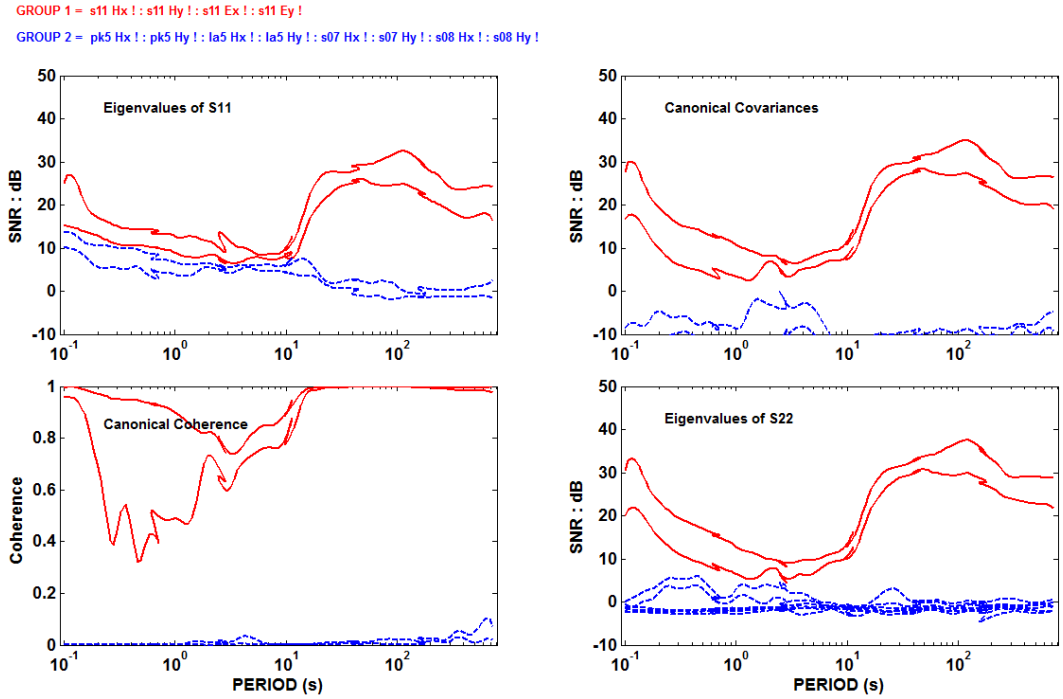

Figure 46

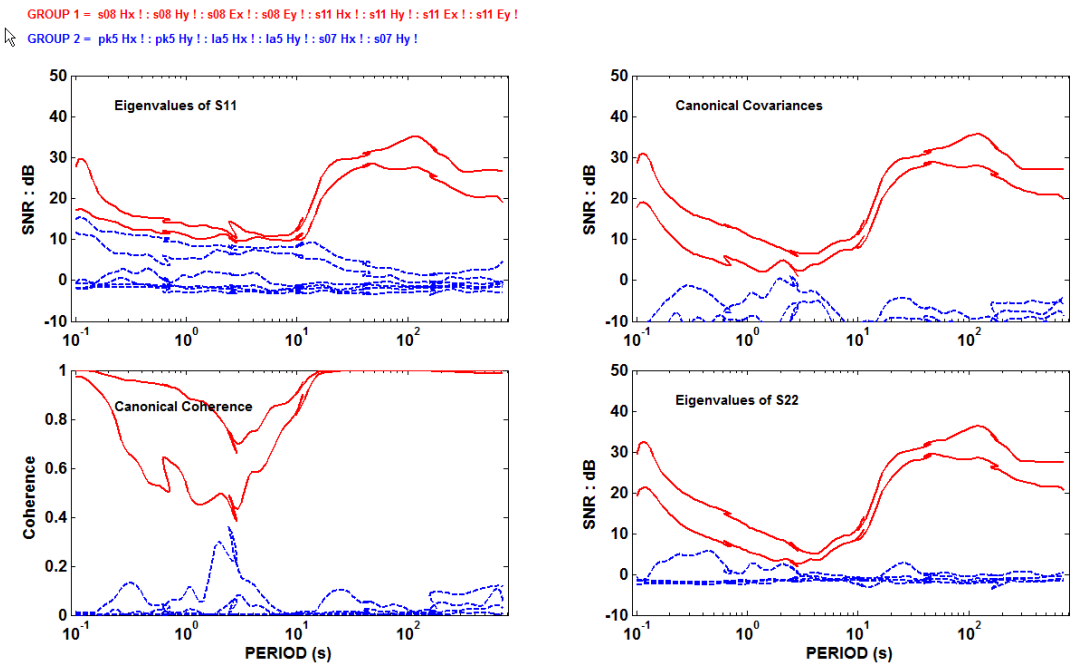

Figure 47

Group 4:

Signal levels (or SNR) for sta08, sta01 for all channels except Ex, and Hy at sta06, for periods up to 10 s, are so low that those can't be used for reliable estimates of EV3 values (Figure 48). This shows as low coherence of the EV1 and/or EV2 values. Only sta06 has high enough signals in this window that could be used for the EV3 evaluation. Therefore, for the periods up to 10 s we don't have enough channels above the noise floor to establish where the anomalous EV3 values could come from. Contribution of H-fields into increased EV3 value is ~3 db for the periods up to 3 s (Figure 49). At higher periods Ey-fields at sta01 and sta06 are very low and therefore should be excluded from the analysis. For periods above 10 s none of the three stations shows anomalous EV3 values (Figures 50a, 50b, and 51).

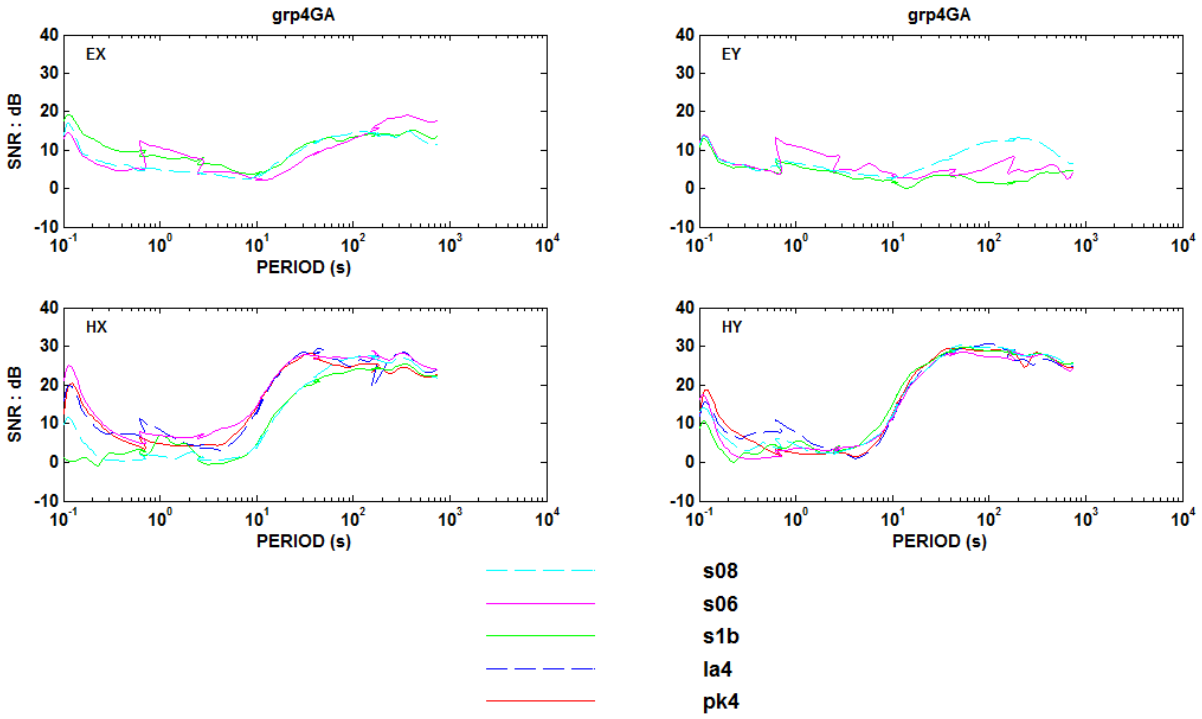

Figure 48

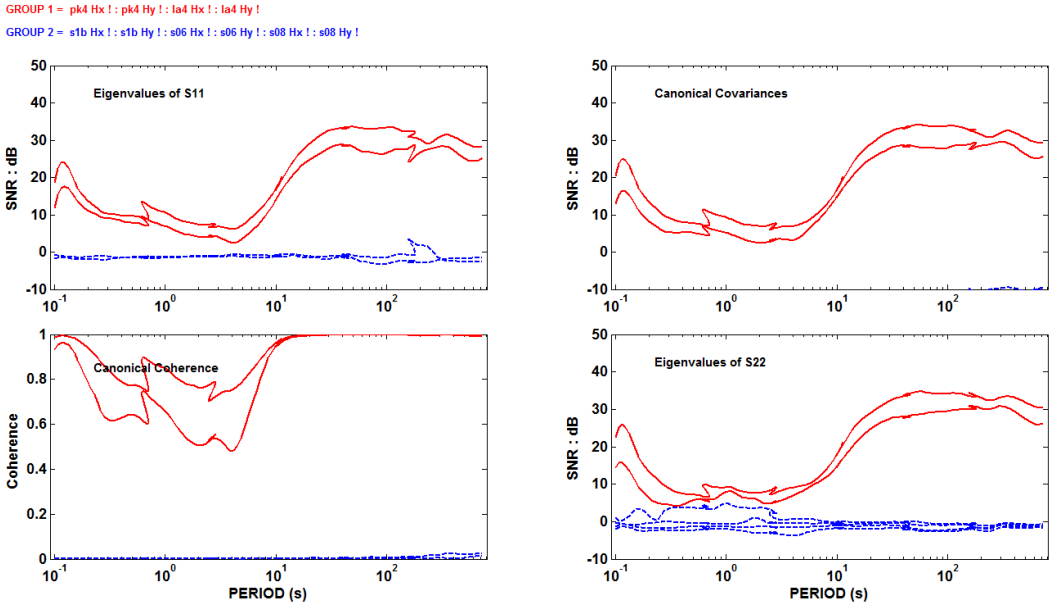

Figure 49

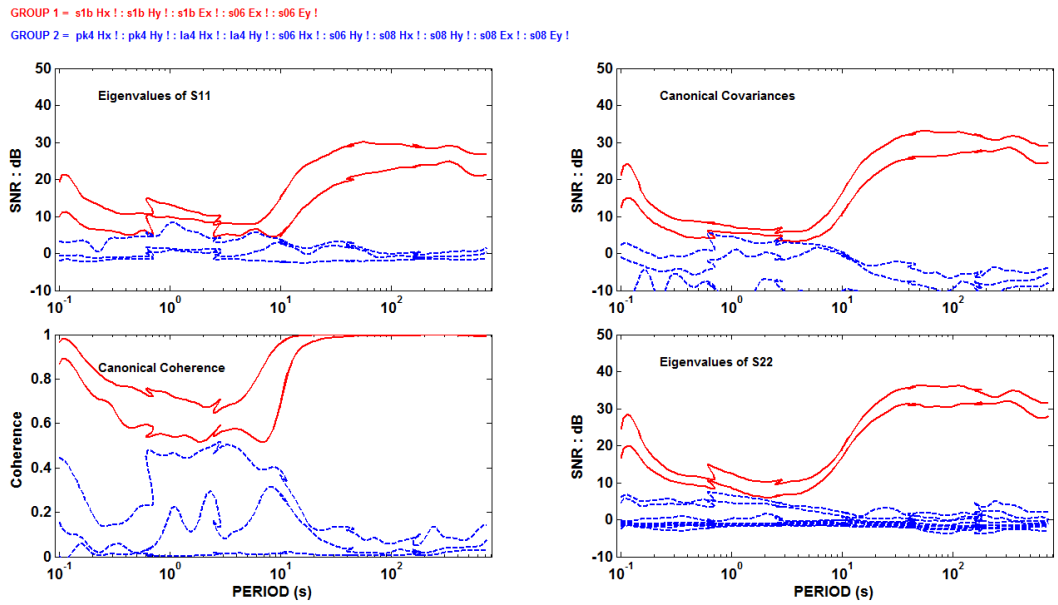

Figure 50a

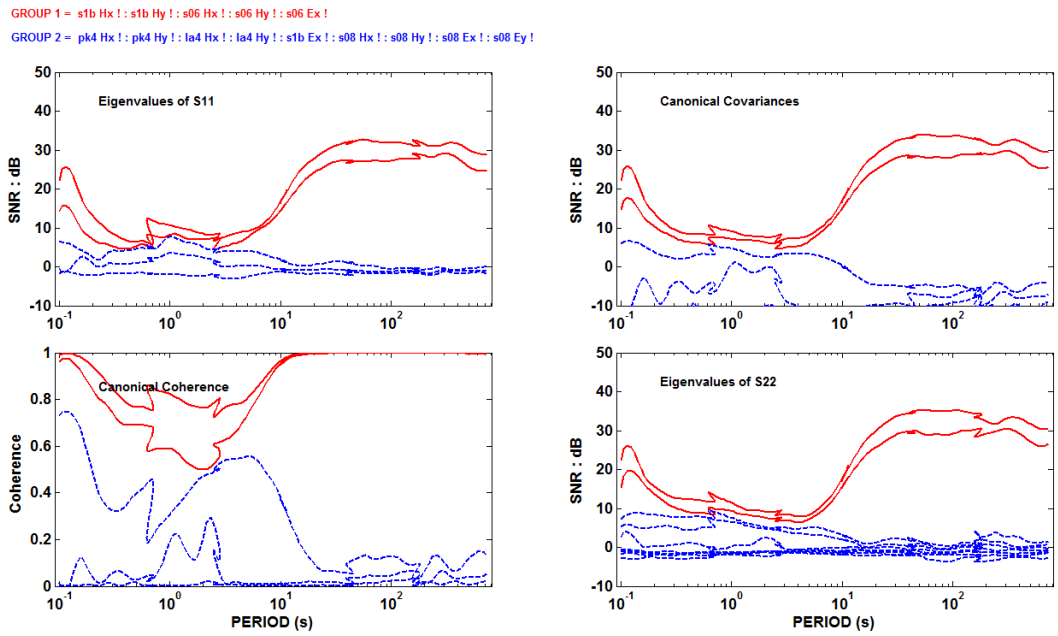

Figure 50b

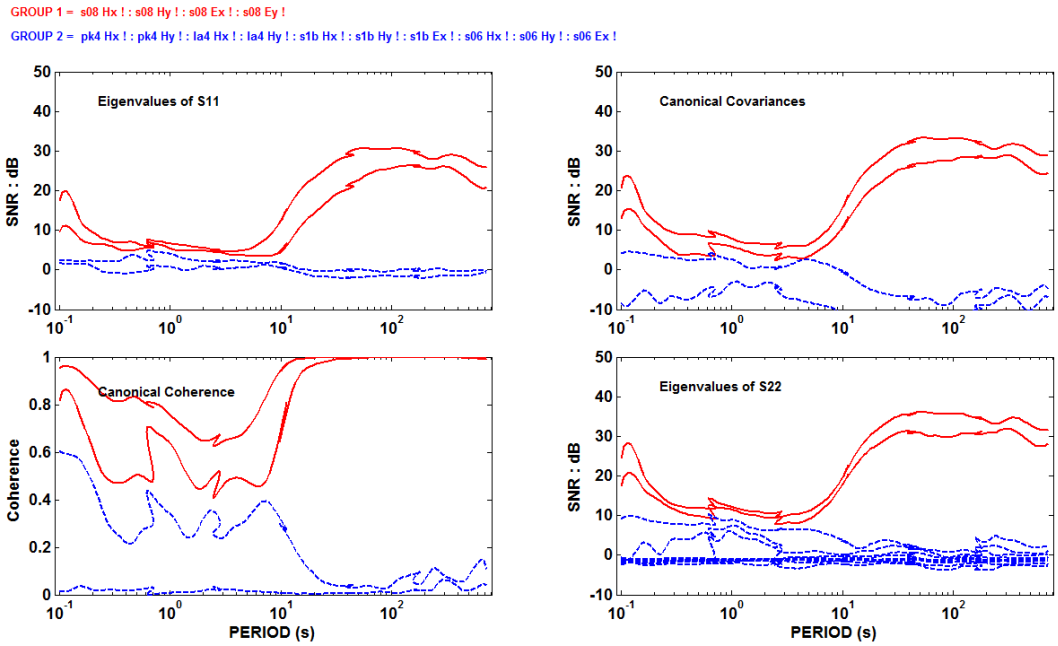

Figure 51

Group 3:

Figure 52 shows SNR values of E and H-fields in this group. Contribution of H-fields into EV3 is largest from sta12b for the periods up to 3 s (Figure 53). To get estimates of E-fields contribution to EV3 values is challenging here, as all three stations are located in the area that is affected by the same processes and therefore from the signal processing of view the signal of interest might be cancelled out. Despite of that, all three stations (Figures 54-56) show increased EV3 for periods up to 10 s, although that is also the interval where the signal is very low and the major components are not resolved well (low EV2). Sta13 (Figure 56) shows anomalous EV3 throughout the whole period range (low periods as well as high periods).

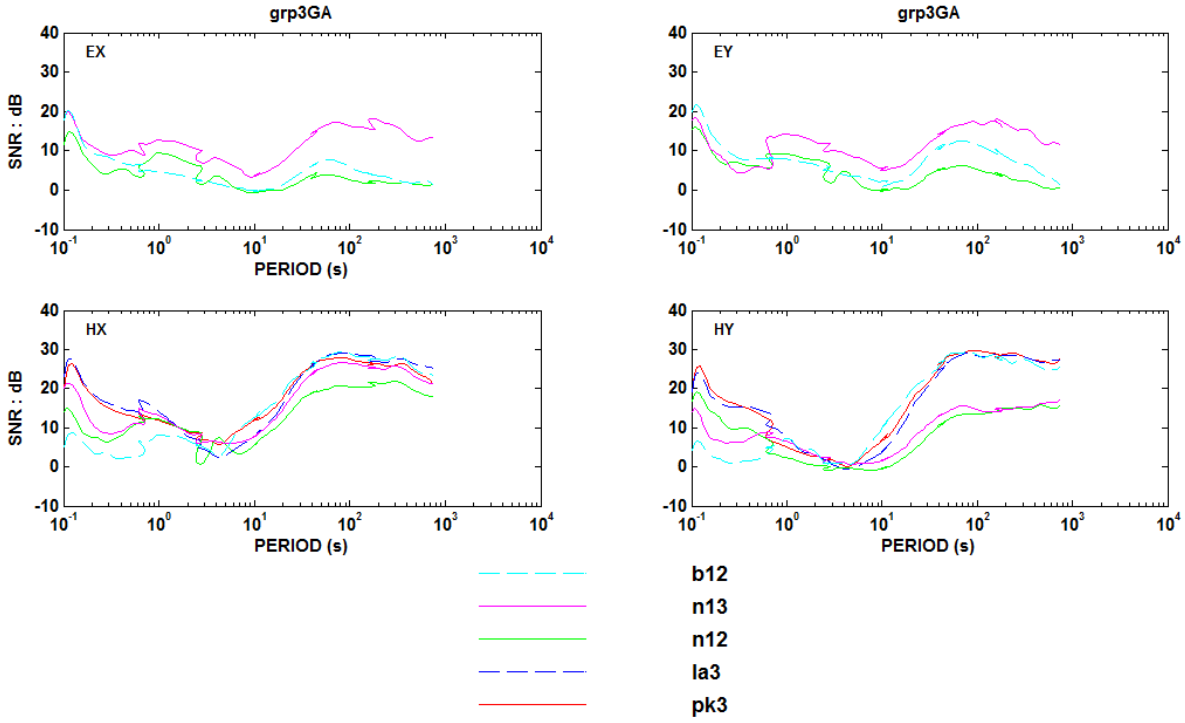

Figure 52

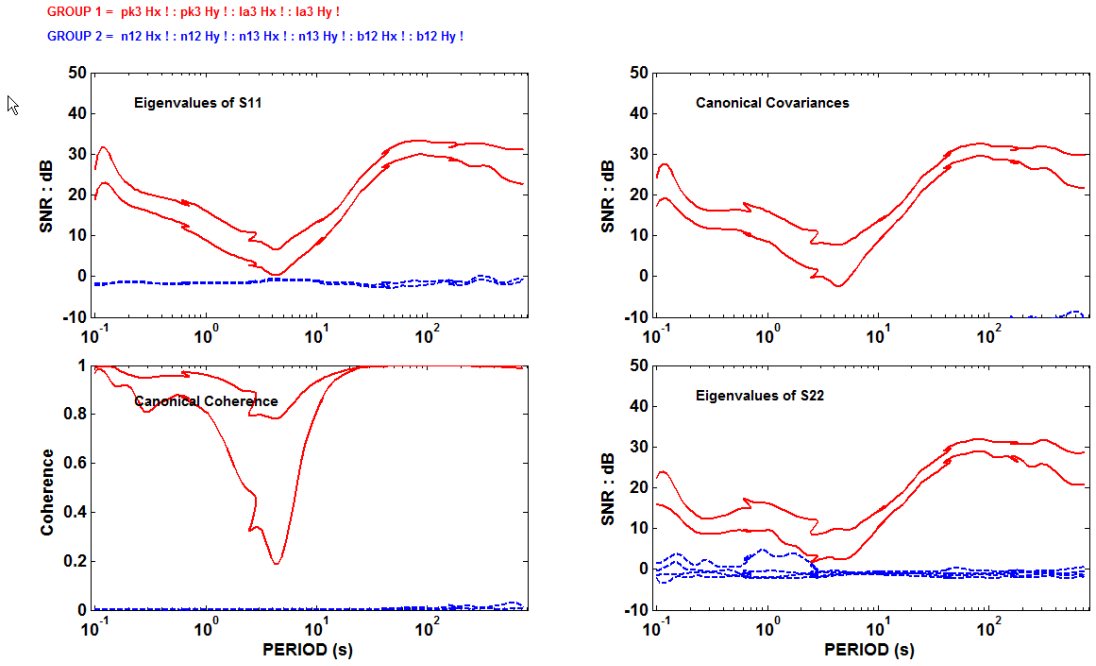

Figure 53a

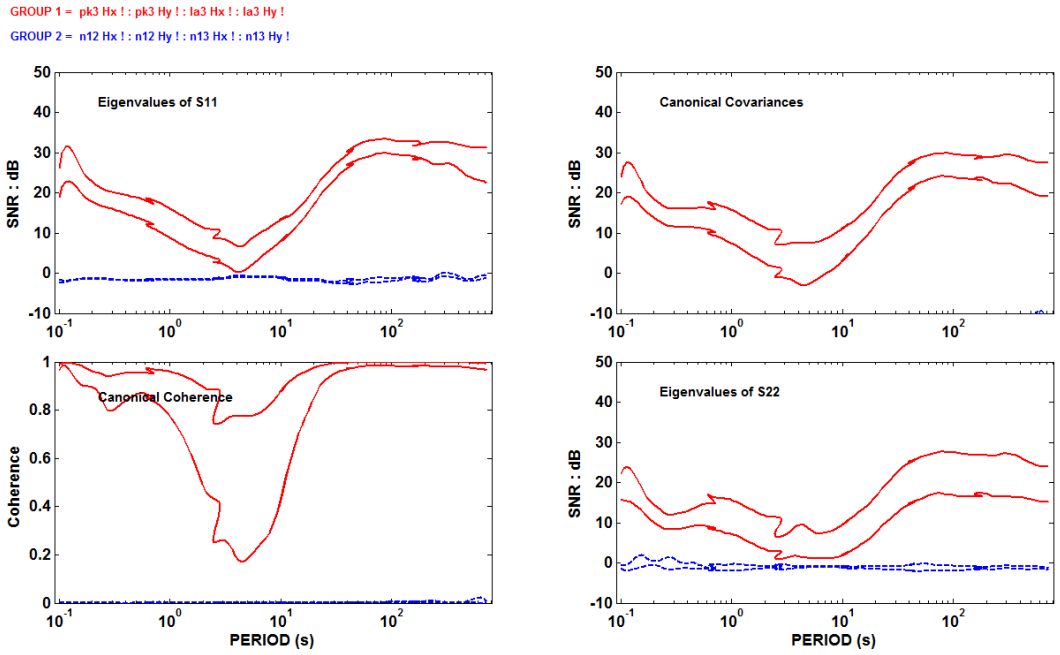

Figure 53b

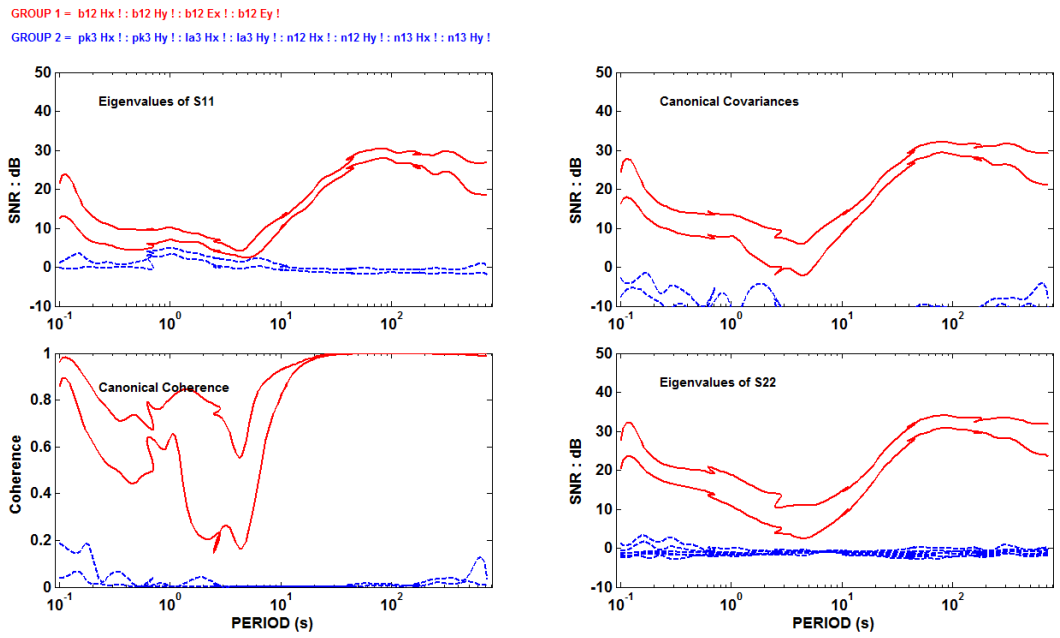

Figure 54a

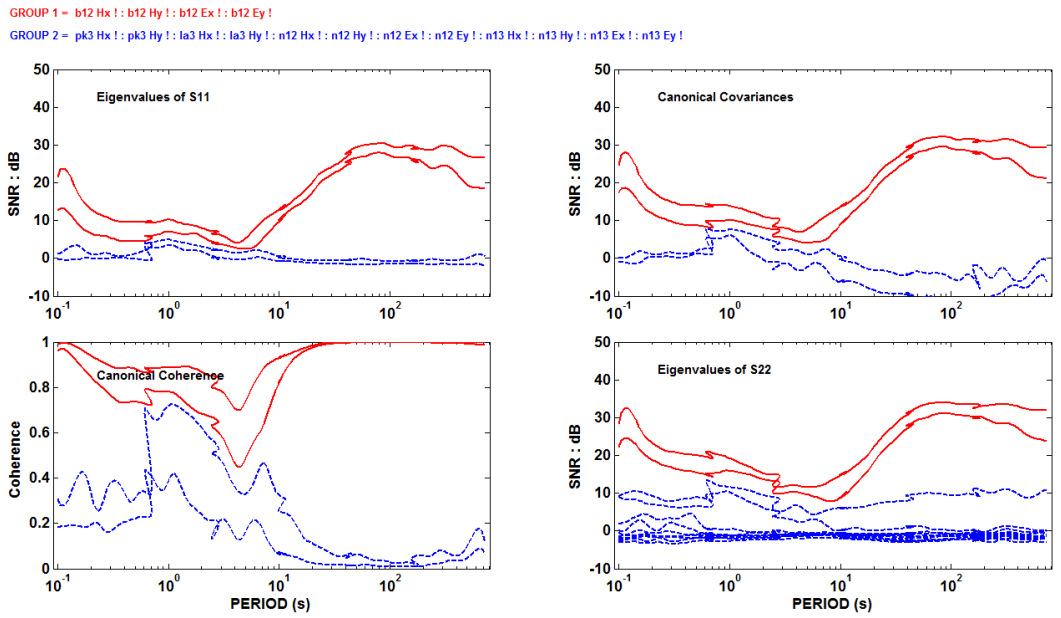

Figure 54b

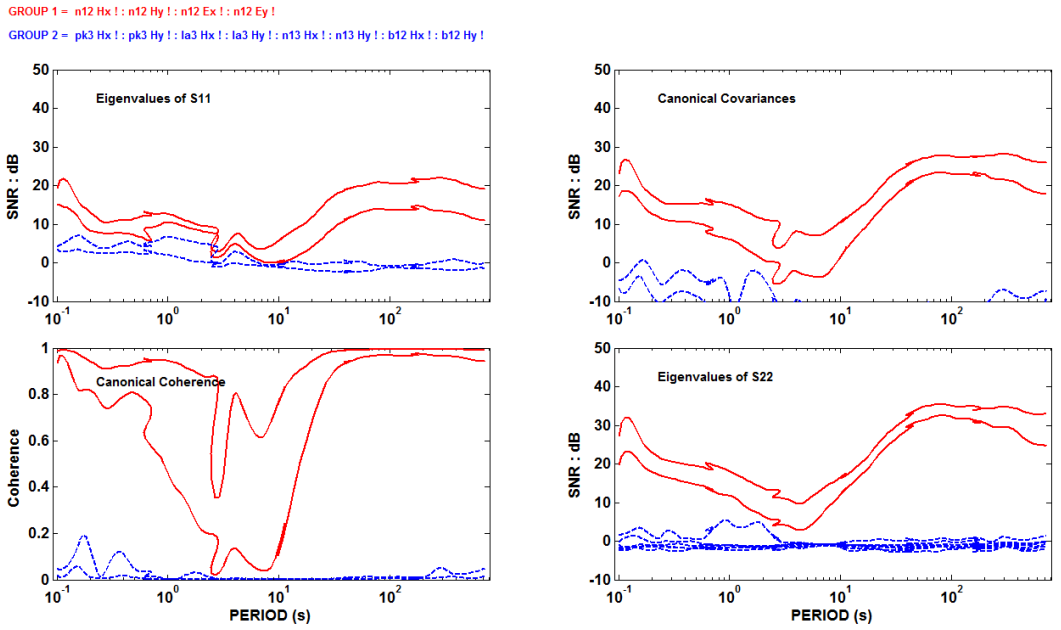

Figure 55

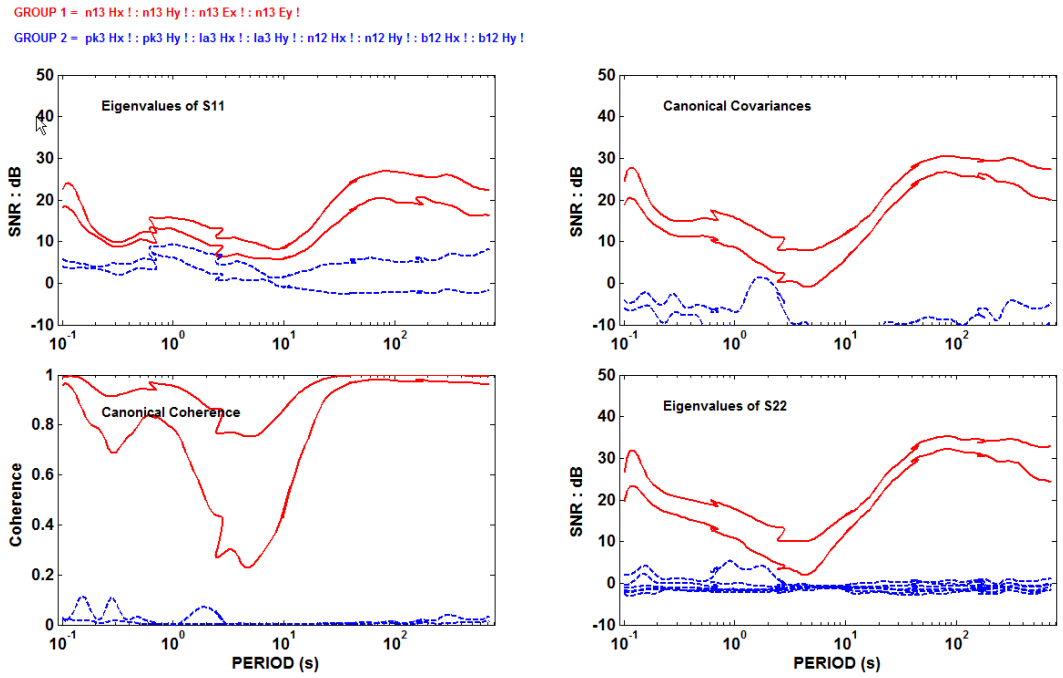

Figure 56a

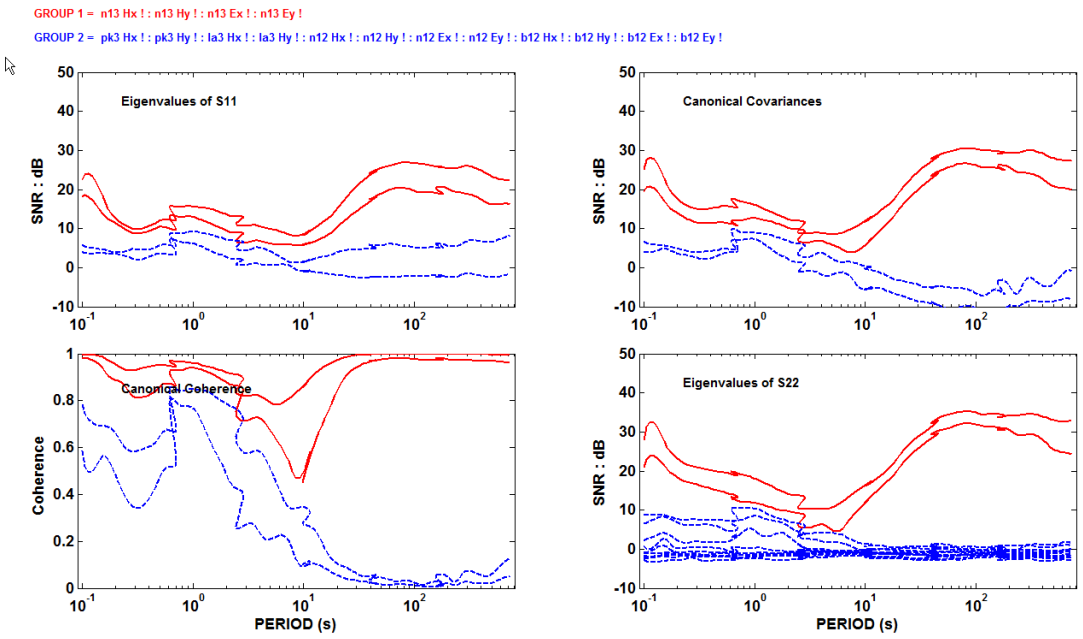

Figure 56b

Group 2:

Figure 57 shows SNR values of E and H-fields in this group. E-fields at stations sta12 and sta13 were very low and therefore these stations were repeated as a part of group 3. At least one of the components of H-fields at sta01 and sta15 at periods up to 5 s was low, which affects estimates of the main EV values and therefore increases uncertainty in the estimates of higher order EV values. Sta01 was repeated in group 4.

Sta01 shows increased EV3 values at periods 1-100 s when compared to a group of stations containing only H-field channels (Figure 58a). Bottom right plot in Figure 58a shows that H-fields at other sites make contribution to increased EV3 values at periods 1-10 s. These responses are highly coherent with the sta15 responses (Figure 58b). When compared with the response at sta13 (Figure 58c) the increased values of EV3 at sta13 are present only up to periods of 10 s, and are somewhat coherent with the sta01 responses, with the note that the major EV components are not estimated well due to low signals of sta13 E-fields and sta01 H-fields. Similar relationship is observed between sta01 and sta12 (Figure 58d), except that the increased value of EV3 at sta12 in present at periods 10-100 s with low coherency with those at sta01, suggesting two independent sources causing these responses. When sta01 is compared to all of the other stations (Figure 58e), the reader can observe cumulative responses of all the contributions described above.

Figure 59 shows that sta15 has increased values of EV3 for periods up to 100 s (upper left plot), with a low coherence values for EV2 at periods 0.2-2 s and a low coherence of higher EV components with H-field components at other stations (bottom left plot), and increased EV3 values for periods 0.4-10 s (bottom right plot) due to H-fields at the other stations.

Figure 60a shows that sta12 has increased EV3 values both at lower periods (0.5-5 s) as well as higher periods (10-100 s) with low coherence values when estimated using all H-field channels at other sites. This group of stations exhibits increased EV3 value due to H-fields in periods 0.5-50 s, with the signal being low around 10 s. Figure 60b shows that the increased EV3 values at sta12 are due to E-fields, as there is no significant contribution of H-fields to that value.

Figure 61a shows that increased EV3 values at sta13 are present only at lower periods (0.5-5 s), which is highly coherent with the signal at sta12 (Figure 61b).

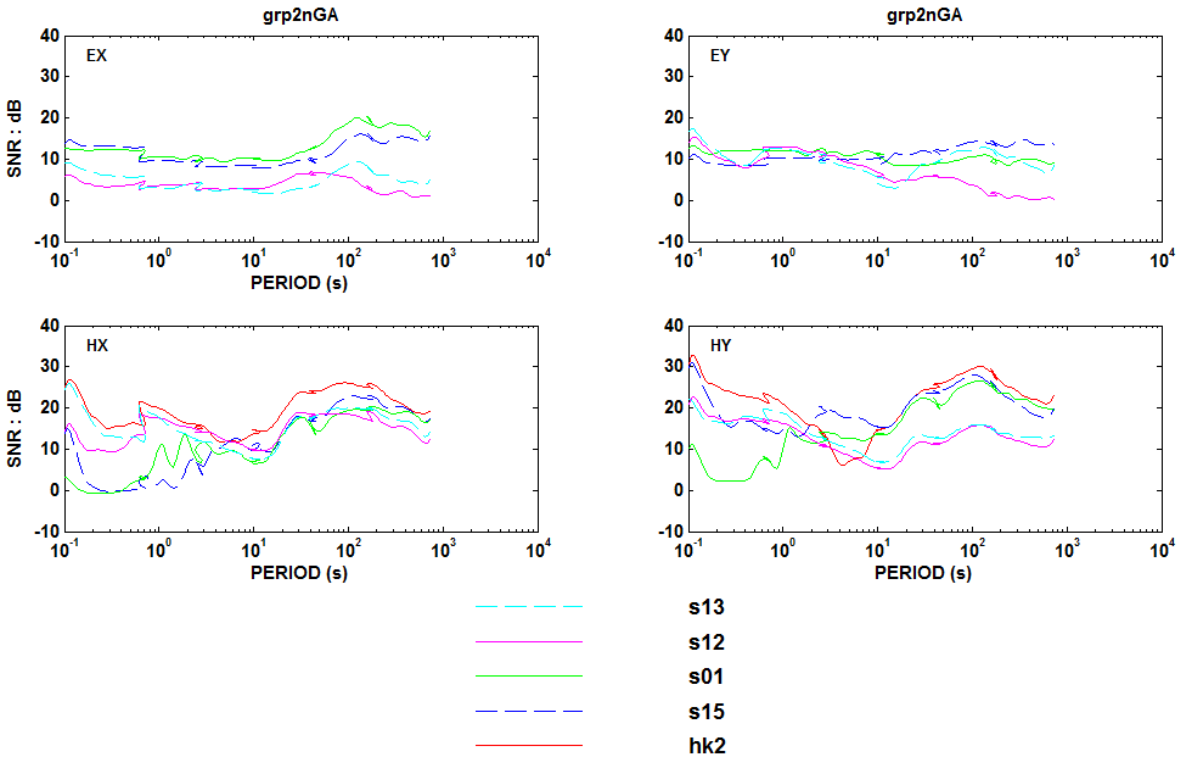

Figure 57

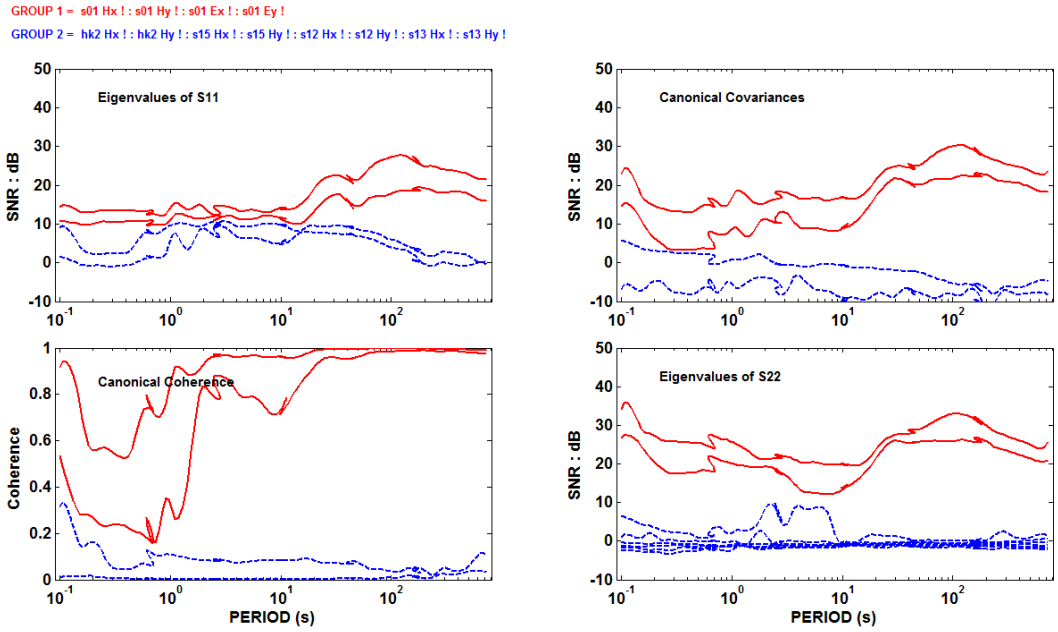

Figure 58a

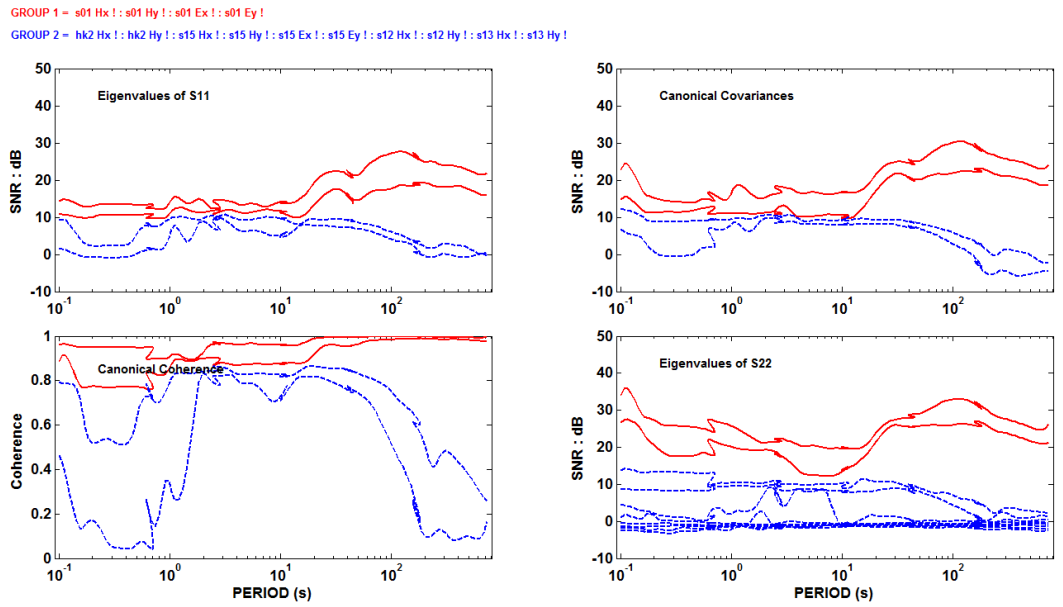

Figure 58b

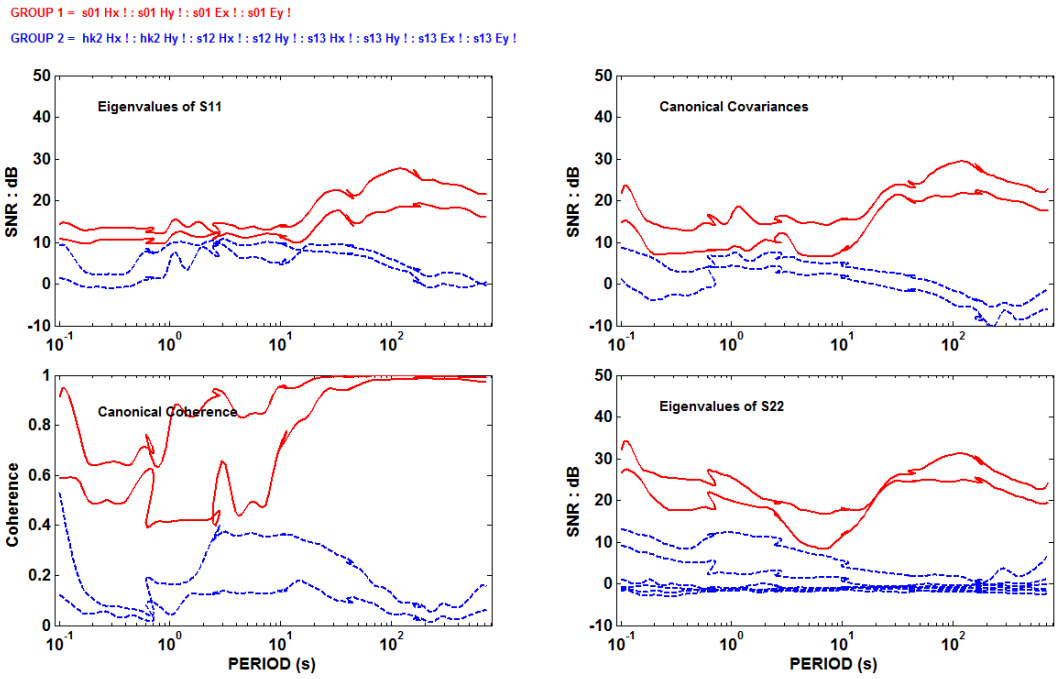

Figure 58c

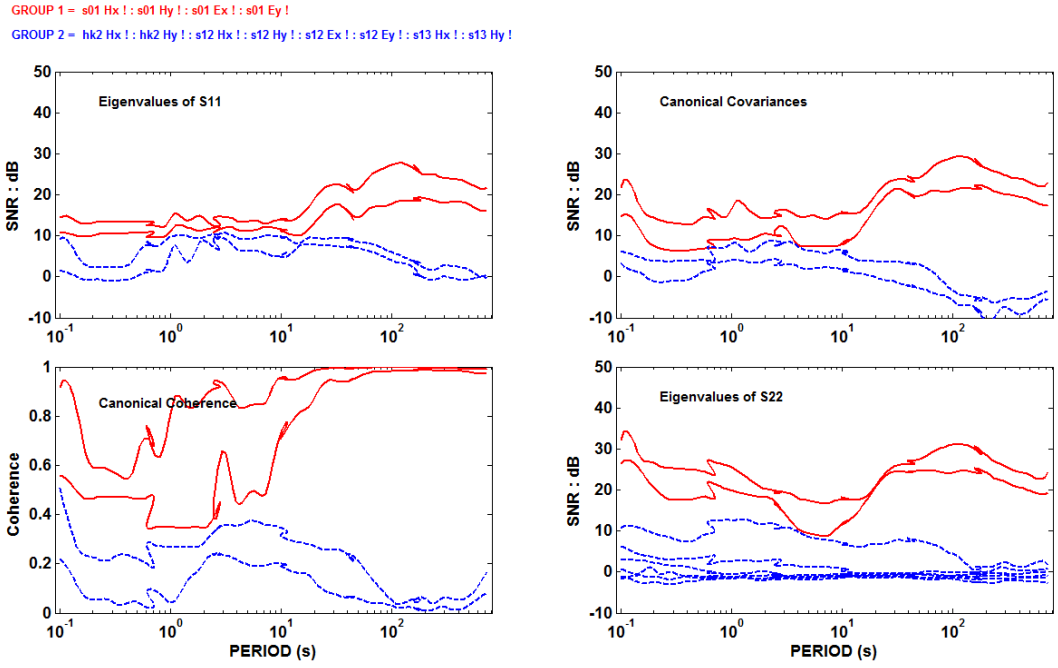

Figure 58d

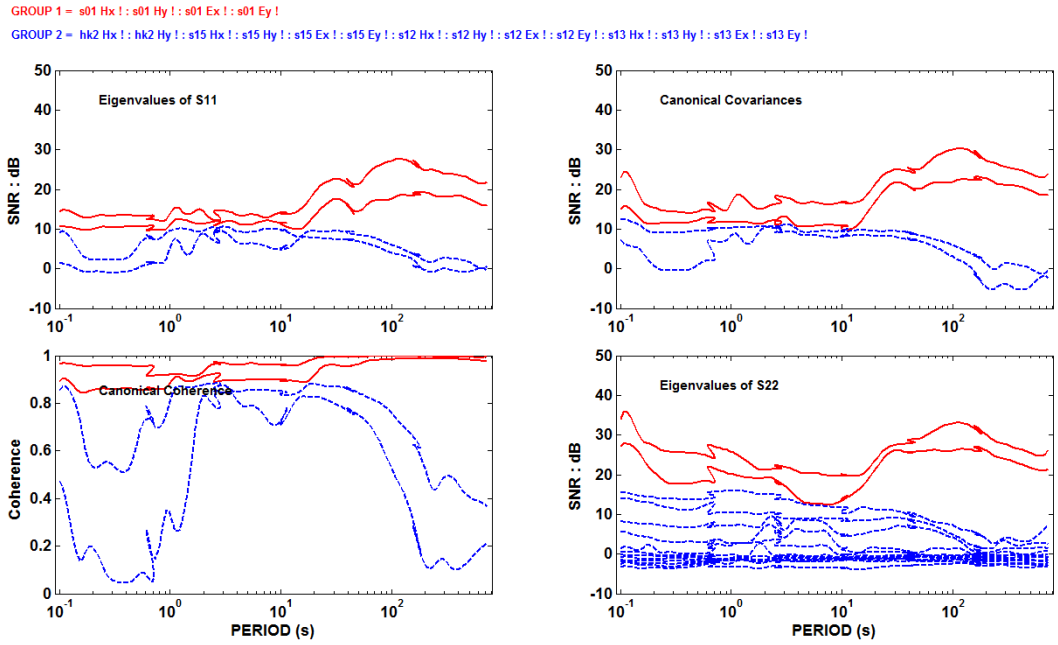

Figure 58e

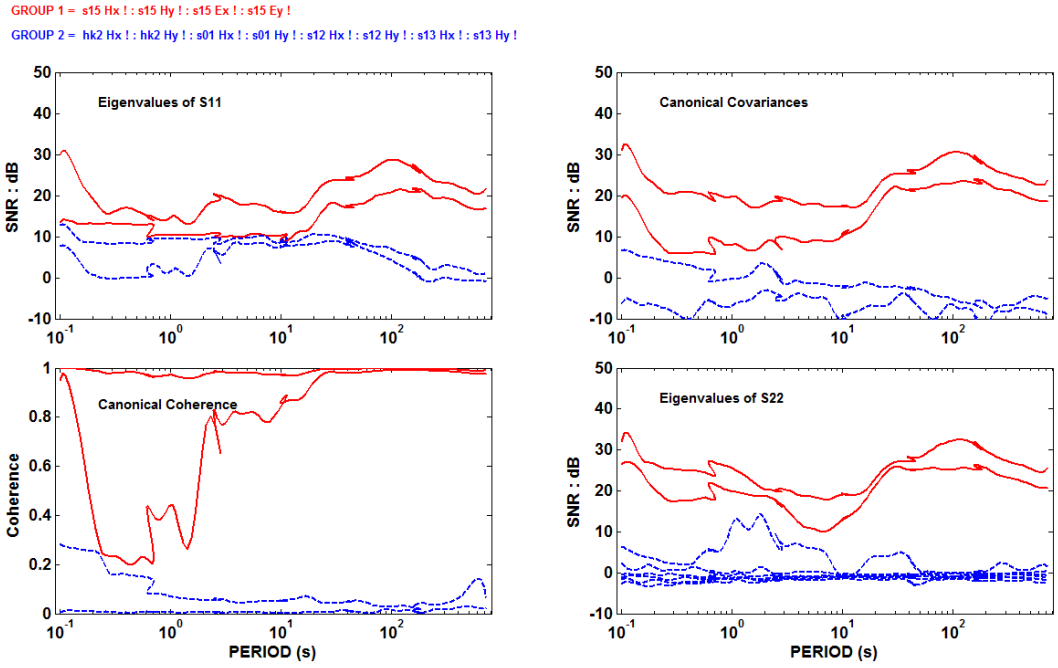

Figure 59

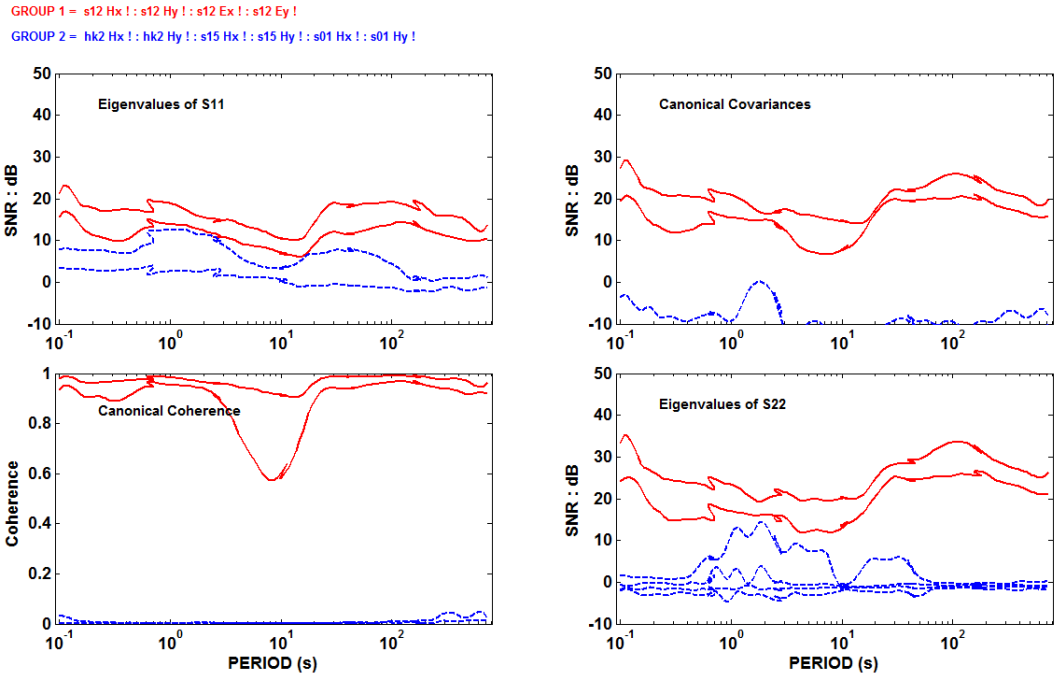

Figure 60a

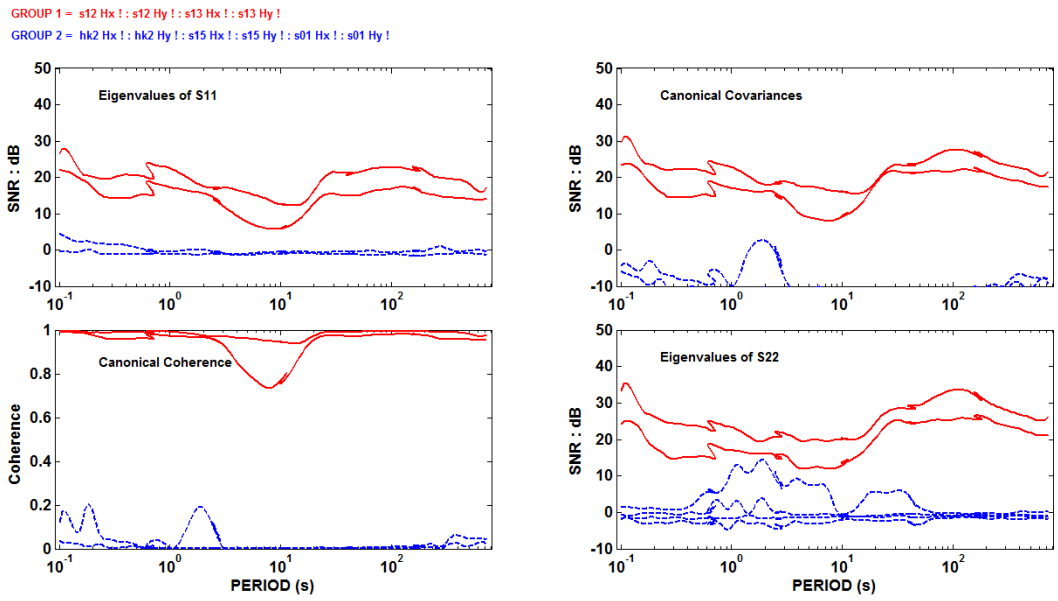

Figure 60b

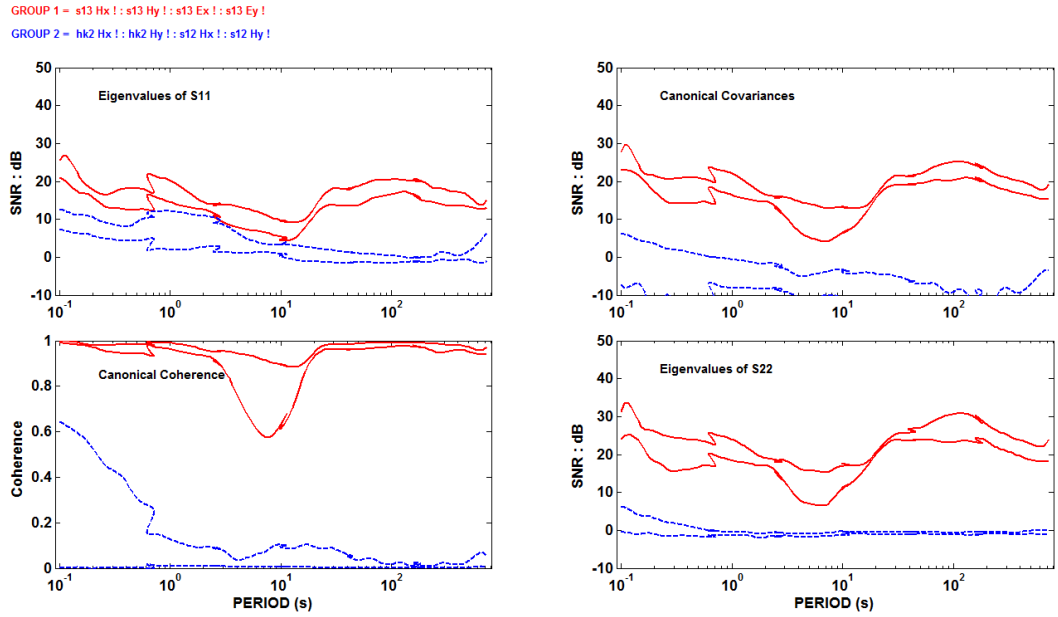

Figure 61a

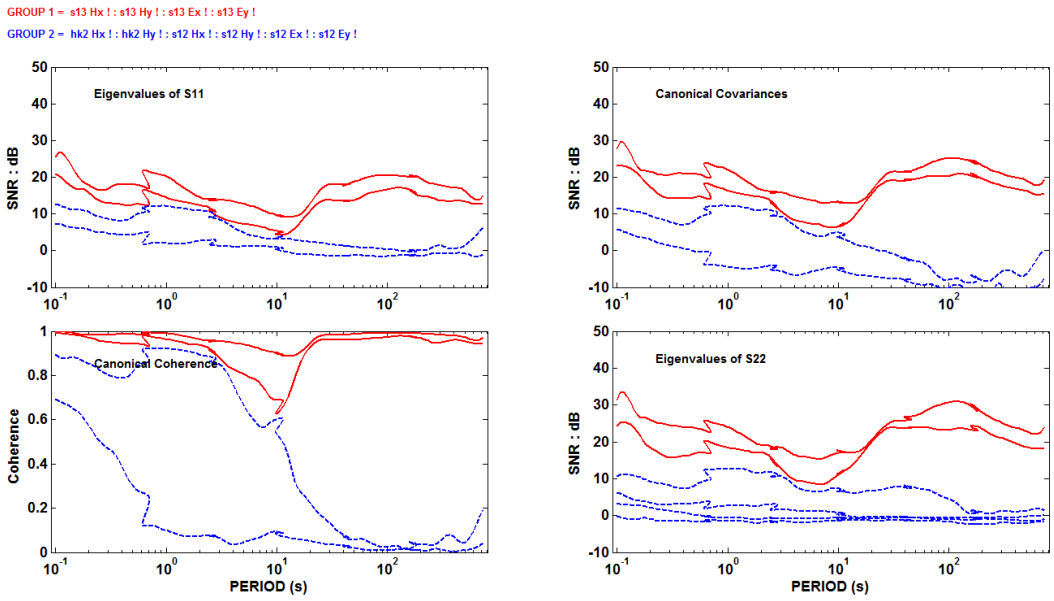

Figure 61b

Group1:

Figure 62 shows SNR values of E and H-fields in this group. Contribution to EV3 from H-fields (Figure 63) on the order of 5 dB at the periods up to 10 s is evident for sta04 (Figure 65) and sta19 (Figure 66). Sta03 has increased EV3 values when only E-fields at other two stations and H-fields from the remote site are used (Figure 64).

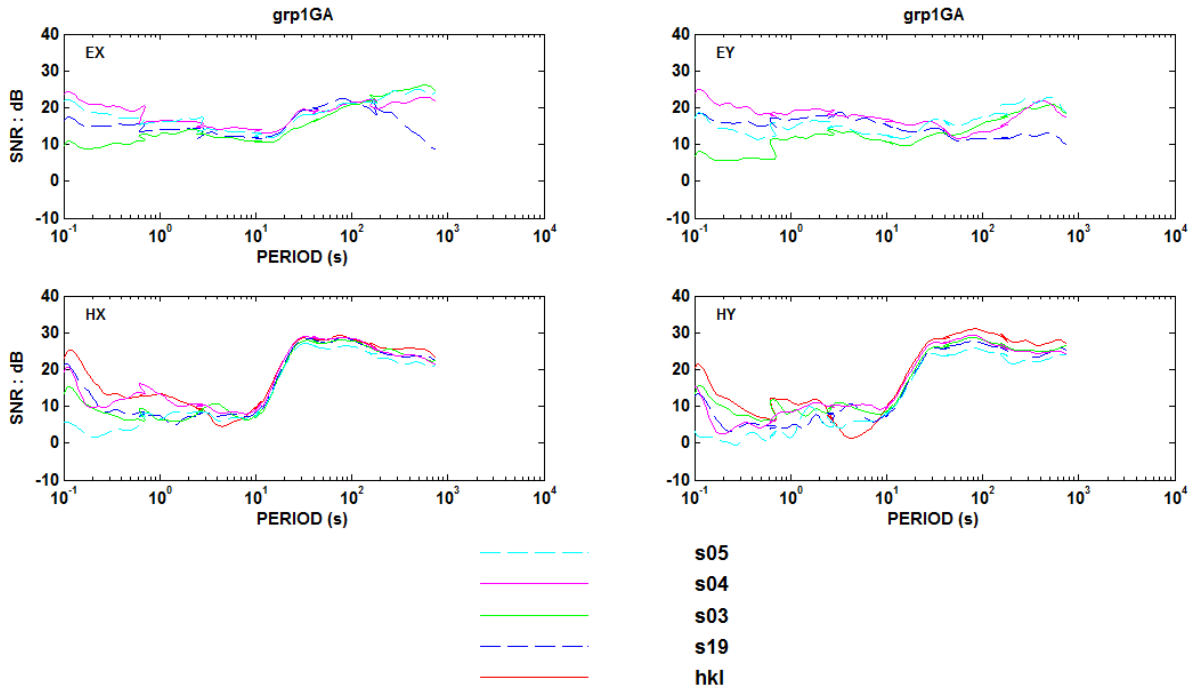

Figure 62

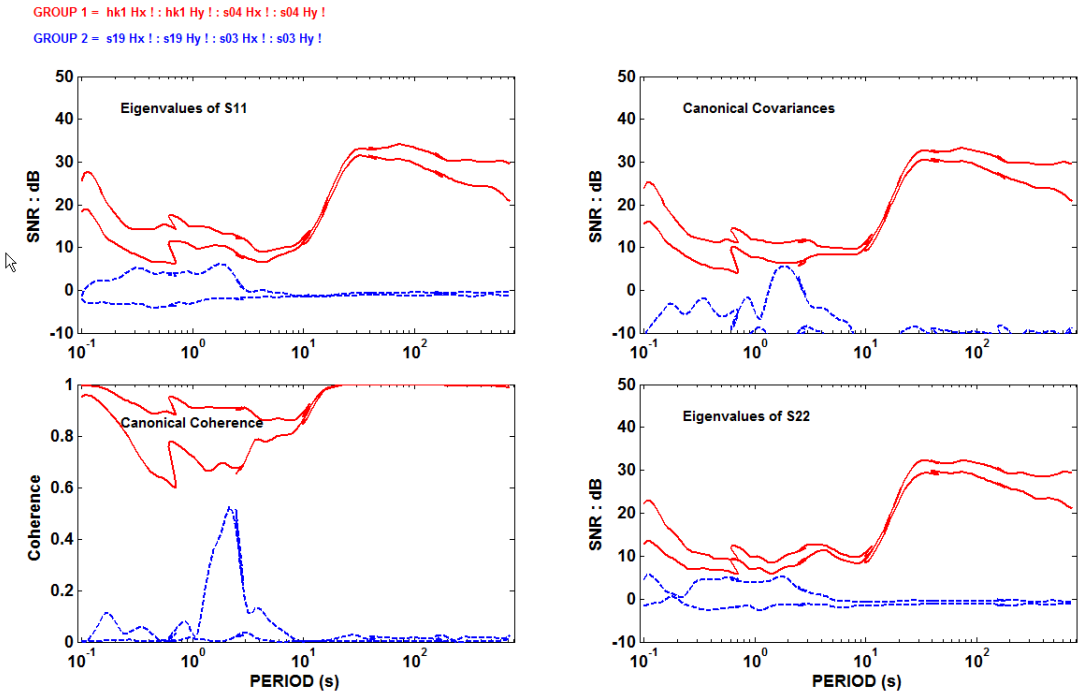

Figure 63a

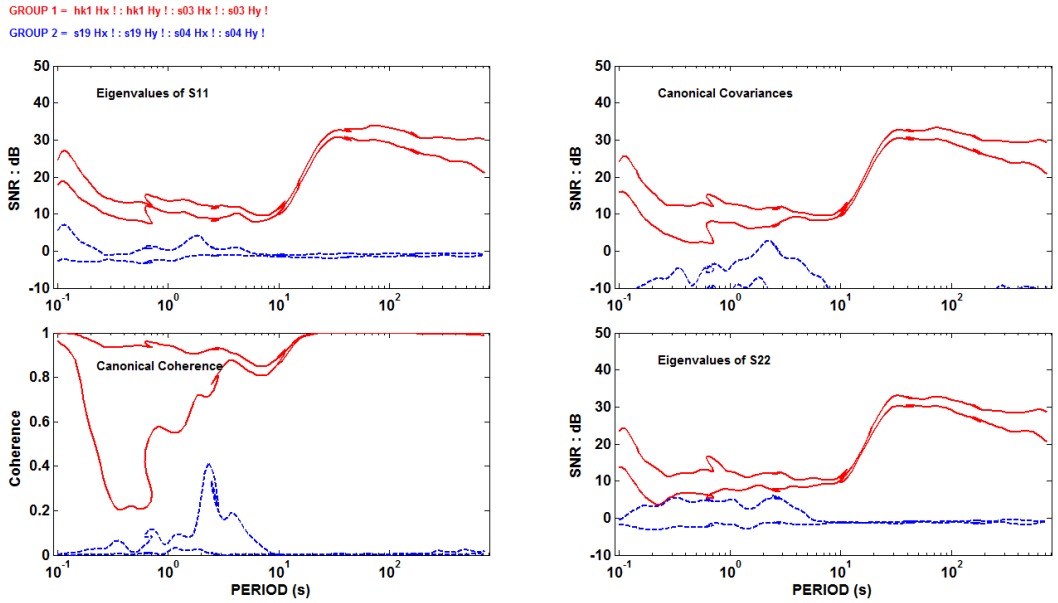

Figure 63b

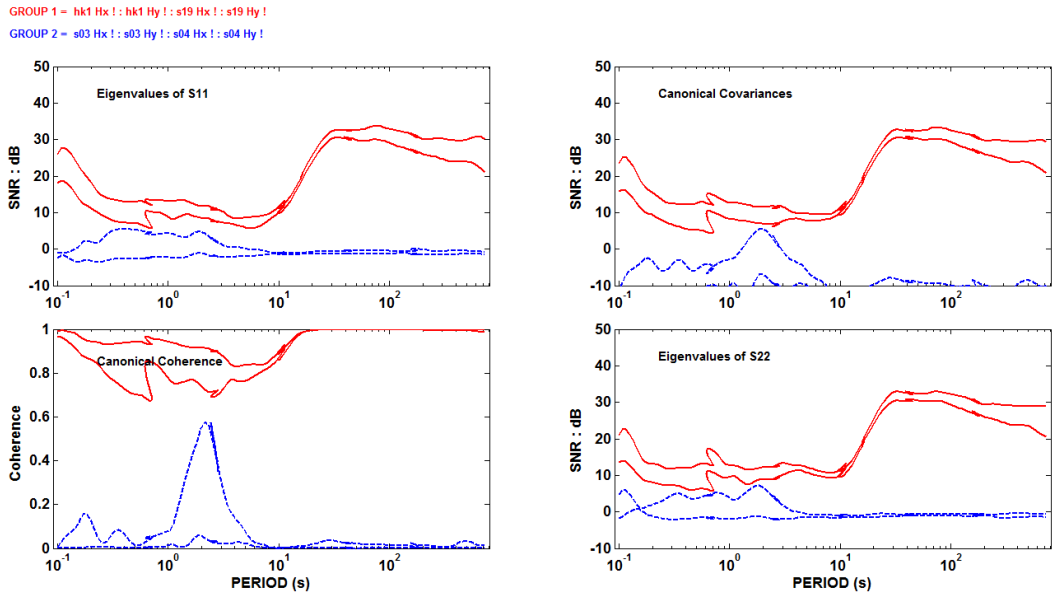

Figure 63c

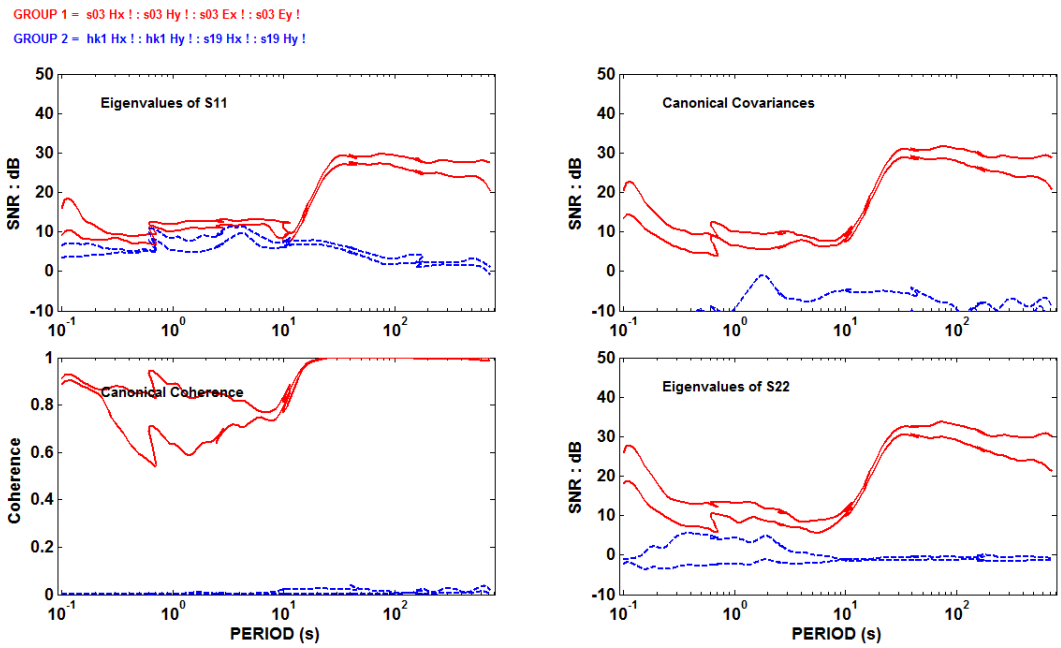

Figure 64a

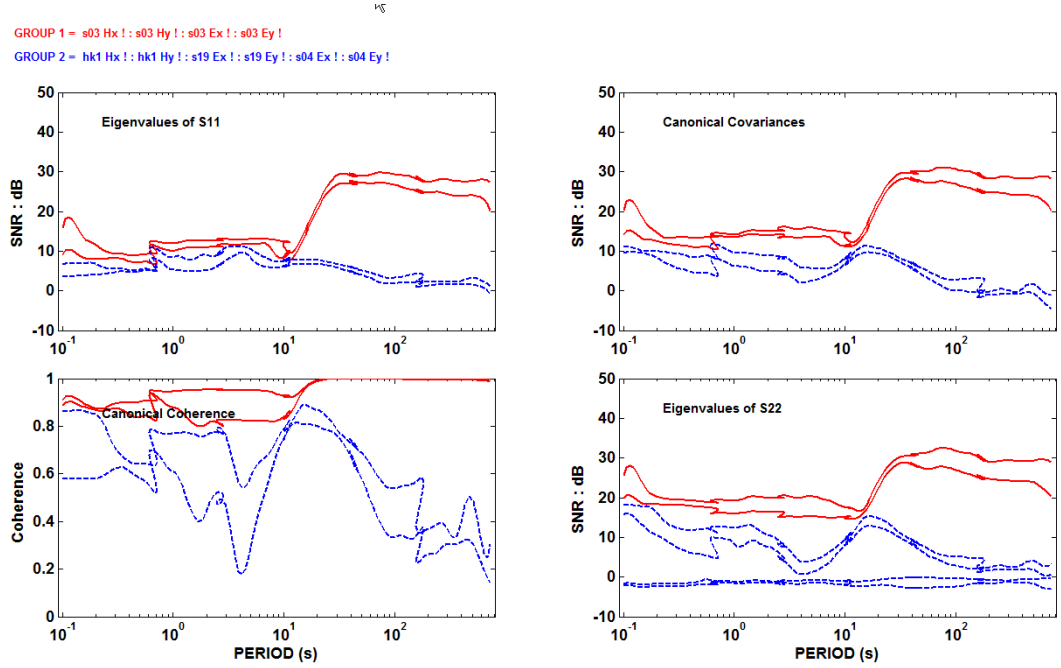

Figure 64b

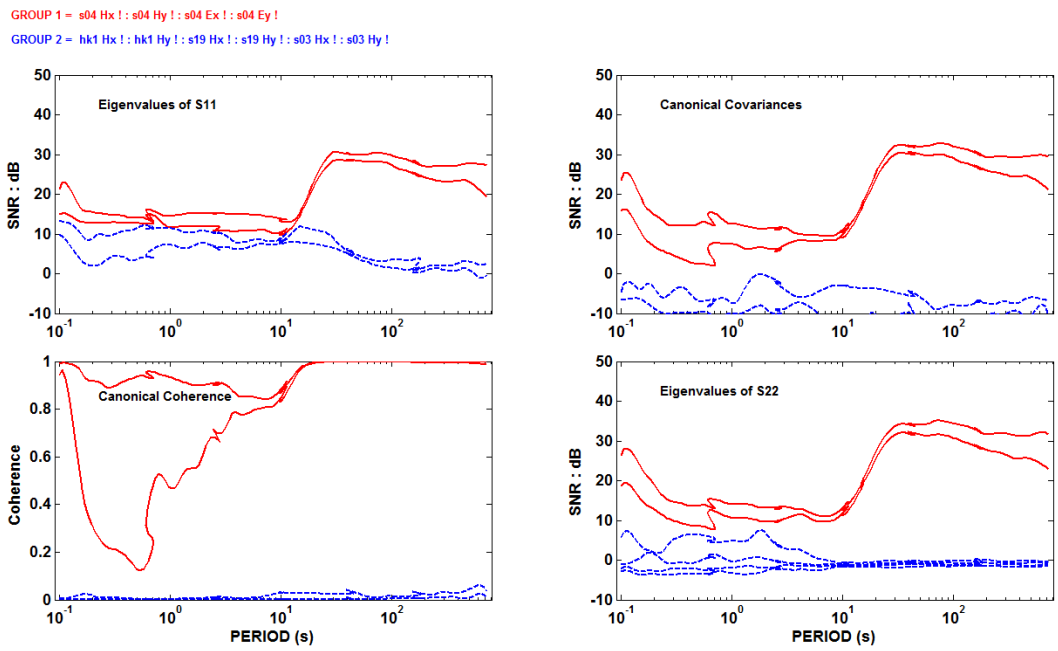

Figure 65

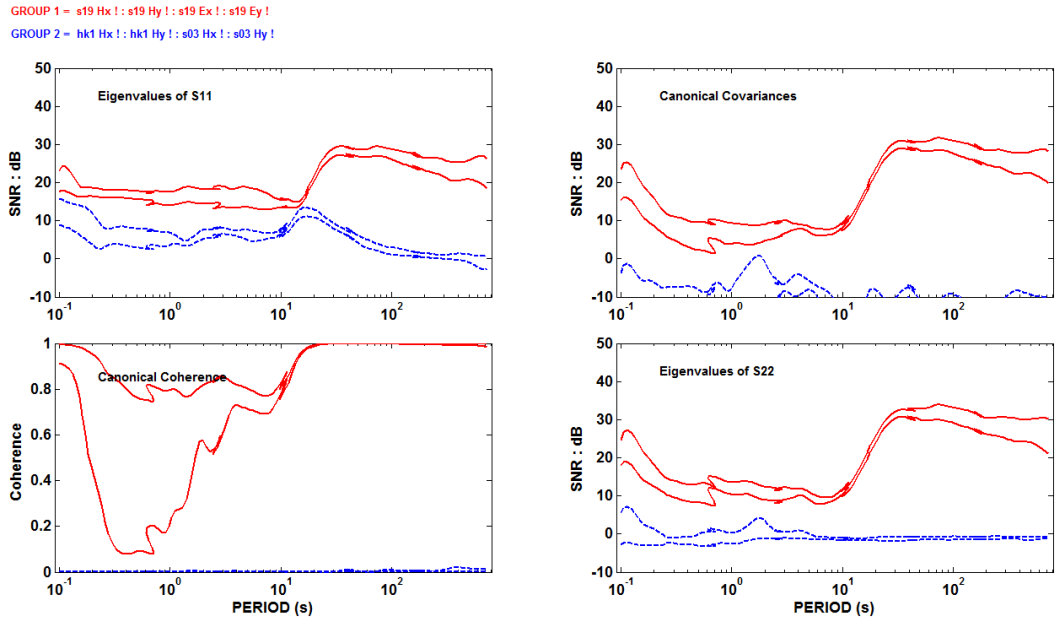

Figure 66

Summary

The MT field survey at the Hawaii National Park during 2012 and 2013 was challenging because of difficult conditions at the Park, and a required escort to all of the stations. For that reason the choice of stations that were acquired simultaneously might not been the most optimal. In order to detect an anomalous signal related to a fluid/lava flow, it is necessary to have data from both areas where no such activity happens and areas that such processes might exist. This wasn't the case for all the groups in our survey. Furthermore, because of continuous eruptive activity around the Kilauea higher noise levels and low signals in the dead-band were major factors that effected our processing. The new MT system is capable of acquiring MT data in all frequencies of interest, although in this particular survey we were not able to use high-frequency data. The field crew was learning how to use the new system and synchronizing high-frequency acquisitions at distant sites proved to be a challenge.

Stations that exhibit higher EV3 values that we associate with the processes of interest, which cause variations in E-fields were: sta15, sta01, sta05, sta13, sta12, sta11, sta10, sta08, and are located on the perimeter of the Kilauea caldera. This illustrates that this approach can qualitatively locate the areas with the fluid flow. While in 2003 dataset these anomalous SSP signals were recorded in higher periods, in 2012-2013 data these signals were observed in lower periods, which suggests that the magma moved into shallower depths in this region.

Additional anomalous SSP signals were observed at sta03, while in the old data set there is no indication of such signals. Sta18 and sta17 also exhibit anomalous responses. These stations are located in the vicinity of the Southwest Rift Zone, and it is possible that these signals are generated by processes in this region. Further study is required to establish what's causing them, and whether these processes are related to those around the Kilauea caldera.

As a part of future research we will also analyze these anomalous signals in the actual field units, which would allow for a spatial correlation between them. When processed in terms of SNR, the strength of the actual fields between different groups of stations may vary, which in turn would effect the amplitude of the anomalous signals. This approach would presumably lead into identification if these anomalous signals come from the same source or if they are caused by multiple sources, where the response is largest, and make our analysis more quantitative. Plotting directions of the anomalous E-fields would also help in identifying flow directions.

The analysis in the actual field units would also address data repeatability. There were four stations – sta01, sta08, sta12, and sta13 that were repeated, and hence acquired as a part of two different groups of stations. Current results suggest that they are different or not repeatable. There are at least three reasons that might cause that. First, the main reason of repeating the station were low signal levels, and therefore if the second acquisition shows much better signal

strengths, it is understandable that those two data sets may produce different results. The second reason is that because of the grouping the anomalous signal amplitudes might be different and therefore seemingly unrelated. The last reason is that the stations are in the locations of episodic processes and depending on time of recording they may or may not be present.